Application of Effective Medium Theory to the Analysis of Integrated Circuit Interconnects

Sonia M. Holik

A Thesis presented for the degree of
Doctor of Philosophy
in
Electronics and Electrical Engineering
at the
University of Glasgow
Glasgow, UK

February 2010

Declaration of Origin

The work described in this Thesis was carried at the University of Glasgow under the supervision of Dr Timothy D. Drysdale, Department of Electronics and Electrical Engineering, in the period October 2006 to September 2009.

The author hereby declares that the work described in this Thesis is her own, except where specific references are made. It has not been submitted in part or in whole to any other university for a degree.

Sonia Holik
Glasgow, February 2010

Abstract

The design and physical verification of contemporary integrated circuits is a challenging task due to their complexity. System-in-Package is an example of generally congested electronic components and interconnects which in the initial design process rely on computationally intensive electromagnetic simulations. Hence the available computer memory capacity and computational speed become meaningful limitations. An alternative method which allows the designer to overcome or reduce the limits is desired.

This work represents the first demonstration of the application of effective medium theory to the analysis of those segments of the entire integrated system where the interconnect networks are more dense. The presented approach takes advantage of the deep subwavelength characteristic of interconnect structures. In order to achieve the aim of defining the homogeneous equivalent for the interconnect grating structure a few steps were followed towards proving the homogenisation concept and finally presenting it by an analytical formulation. A set of parameters (metal fill factor, aspect ratio, dielectric background and period-to-wavelength ratio) with values related to typical design rules were considered. Relating these parameters allows the empirical models to be defined. In order to show the relationship between existing effective medium theories and those developed in this Thesis, the presented empirical models are defined in terms of the Maxwell-Garnett mixing rule with an additional scaling factor. The distribution of the scaling factor was analysed in terms of the calculated reflection and transmission coefficients of the homogenised structures that are equivalent to a given grating geometry. Finally the scaling factor, for each empirical model, was expressed by an analytical formula and the models validated by their application to the numerical analysis of grating structures.
The numerical validation was carried out by comparing the reflection and transmission coefficients obtained for the detailed and homogenised structures. In order to

ensure the empirical models can be broadly employed, the performance of the model in the presence of non-normally incident plane wave was evaluated. For the range of angles $\pm 30^{\circ}$ the model is accurate to 5%. The impact of the shape of the grating, specifically the case of a tapered profile, typical of actual fabricated interconnects was also considered, with sidewall tapers of up to 5° giving the same error not higher than 5%.

Experimental validation of the application of the homogenisation concept to the analysis of interconnects is desired for two main applications: for the reflectivity estimation of a whole chip in a System-in-Package and for the performance estimation of interconnects on lower metal layers in an interconnect stack. For the first, free-space measurements are taken of a grating plate with copper rods aligned in parallel illuminated by a plane wave in the X-band ($8.2 - 12.4\,\text{GHz}$). For the second, S-parameters are measured for microstrip waveguides with a number of metal rods embedded in the substrate between the signal line and ground plane. The good agreement with the simulations validates the homogenisation approach for the analysis of interconnects.

Preface

This dissertation describes research undertaken in the Department of Electronics and Electrical Engineering at the University of Glasgow between October 2006 and September 2009. I am grateful to my supervisor Timothy D. Drysdale for suggesting the topic of research and co-supervisor John M. Arnold for additional supervision during the study.

Aspects of the work described in this Thesis has been published in following papers:

S. M. Holik, T. D. Drysdale. Effective medium approximation for electromagnetic compatibility analysis of Integrated Circuits. *Proc. 2nd International Congress on Advanced Electromagnetic Materials in Microwaves and Optics*, Pamplona, Spain, September 2008, pp. 413 - 415.

S. M. Holik, J. M. Arnold, T. D. Drysdale. Simplified approach to package-level electromagnetic modelling of on-chip interconnects. - submitted to *Elsevier Metamaterials Journal*.

S. M. Holik, T. D. Drysdale. Simplified model for on-chip interconnects in electromagnetic modelling of System-in-Package. - accepted for invited talk at *International Conference on Electromagnetics in Advanced Applications*, Sydney, Australia, September 2010.

S. M. Holik, T. D. Drysdale. Toward an efficient FDTD boundary condition for integrated circuit applications. *PG Conference*, June 2008.

Acknowledgments

I would like to take the opportunity to express my thanks towards all the people that have contributed to this work and who sincerely earn my gratitude.
First and foremost, I would like to thank my supervisor Timothy D. Drysdale and co-supervisor John M. Arnold for their ideas, assistance and guidance throughout this study. Further, I appreciate the fruitful discussions with members of the research group, namely, Tomasz Stefański, Horacio Cantú, Griogair Whyte - for his help with the HFSS software, and Fraser Twaddle. A special thanks go to my other colleagues Lai Bun Lok and Ian McGregor for showing me the practical side of the measurement set-up and system calibration, and for helping me to understand circuit design. Further, I would like to thank Ian McGregor and Fatemeh Aghamoradi for the courteousness in running more computationally demanding simulations on their computers. I do appreciate the effort from Ian McGregor who read the chapters and helped to correct the grammar.
I would also like to convey thanks to the Engineering and Physical Sciences Research Council for providing financial support.
Technical staff ware instrumental in fabricating and preparing the measurement equipment, especially Kaz Piechowiak and the mechanical workshop, namely Wilson MacDougall for the set of grating boards and dielectric lenses and James Kelly for designing and making the holder as well as Stuart Fairbairn who fabricated sets of PCBs.

I owe much gratitude to my family, friends and relatives for their assistance and understanding during this demanding time of study.

Finally, I would like to thank all who have shown interest in my work by reading this Thesis. I sincerely hope that the introduction to the application of effective medium theory to the analysis of integrated circuit interconnects will encourage new ideas for further research and applications.

Notation

AR	aspect ratio
c	speed of light in a vacuum, 2.998×10^8 m/s
$\boldsymbol{E}$	electric field vector
f	metal fill factor
F	Farad
$\boldsymbol{H}$	magnetic field vector
H	Henry, or magnitude of magnetic field depending on context
k	wavenumber
$\boldsymbol{K}$	grating vector
m	metre
n	refractive index
n_{eff}	effective refractive index
r	reflection coefficient
R	reflectivity
s	second
t	transmission coefficient
T	transmissivity
xyz	Cartesian coordinate system with group of equivalent planes
Z_0	characteristic impedance of microstrip line
ϵ_0	permittivity of free space, 8.854×10^{-12} F/m
ϵ_r	relative permittivity, $\epsilon_r = \epsilon/\epsilon_0$
ϵ_{eff}	effective permittivity
η_0	intrinsic impedance of free space, $376.6\,\Omega$
λ	wavelength
λ_0	free space wavelength

Λ	period
μ_0	permeability of free space, $4\pi \times 10^{-7}\,\mathrm{H/m}$
μ_r	relative permeability, $\mu_r = \mu/\mu_0$
ν	frequency
θ	angle of incidence
Ω	resistance or impedance, Ohms
ξ	focal length
Ψ	scaling factor

Glossary

CMOS	Complementary Metal-Oxide-Semiconductor
DUT	Device Under Test
EMT	Effective Medium Theory
FDTD	Finite Difference Time Domain
FEM	Finite Element Method
GHz	GigaHertz (10^9 Hz)
HFSS	High Frequency Structure Simulator
IC	Integrated Circuit
ISM	Industrial, Scientific and Medical band of frequencies
ITRS	International Technology Roadmap for Semiconductors
PCB	Printed Circuit Board
PBC	Periodic Boundary Condition
PEC	Perfect Electric Conductor
PML	Perfect Matched Layer
RCWA	Rigorous Coupled Wave Analysis
SiP	System-in-Package
SoC	System-on-Chip
SLOT	Short Load Open Through calibration
SMA	SubMiniature version A connector
TE	Transverse Electric
TEM	Transverse Electric and Magnetic
TEMPEST	FDTD code from University of California, Berkeley
TM	Transverse Magnetic
TRL	Through Reflect Line calibration
WGP	Wire Grid Polariser
X-band	Band of frequencies between $8.2 - 12.4$ GHz

Contents

List of Figures

List of Tables

Chapter 1

Introduction

1.1 On-Chip Interconnects for Integrated Circuits

For over four decades the evolution of electronic technology has followed Moore's law [1] where the number of transistors in an integrated circuit (IC) approximately doubles every two years. This naturally increases the number of internal interconnections needed to complete the system. The increase in chip complexity is achieved by a combination of dimensional scaling and technology advances. A variety of chip types exist, including memory, microprocessors and application specific circuits such as System-on-Chip (SoC). Since it is expensive to fabricate the large and simple passive components such as on-chip capacitors and inductors on the same die as the active circuits, it is desirable to fabricate these on separate dies then combine them in System-in-Package (SiP). The main advantage of SiP technology is the ability to combine ICs with other components, including passive lumped elements already mentioned but also antennas, high speed chips for radio frequency communication etc., into one fully functional package. The high complexity of SiP brings many challenges to the design process and physical verification of the system. In many cases the design process relies on detailed 3-D numerical electromagnetic simulations that tend to be slow and computationally demanding [2, 3, 4] in many cases limited by the available computer memory capacity and computational speed. Therefore, directly including the detail of the dense interconnect networks into the numerical model is impractical.

Large problems are usually solved by adapting a 'divide and conquer' approach such as diakoptics [5, 6]. Such approaches are appropriate when the problem can be decomposed into small pieces each of which can be readily solved. However, in the

System-in-Package example considered in this Thesis, there is an interest in the case of communication across entire dies, between dies and from one side of the package to another. This involves modelling microwave waveguides (whether deliberately or inadvertently created) that are influenced by the precise nature of the immediate environment. Modelling even a single such waveguide requires much detail and therefore approaches which reduce the computational intensity are desirable.

The presented approach is aimed towards two main applications. First, estimating the reflectivity of a whole chip for use in System-in-Package electromagnetic interference modelling, as illustrated in Fig 1.1. The concept of *aggressor* and *victim* chips in SiP where one chip emits a signal that disrupts the other is depicted in Fig. 1.1(a) with a cross-sectional diagram of a simple SiP and the close-up of the detail of the interconnect stack in the victim. The representation of the proposed homogenisation method where the interconnect is replaced by an equivalent homogenised medium is shown in Fig. 1.1(b).

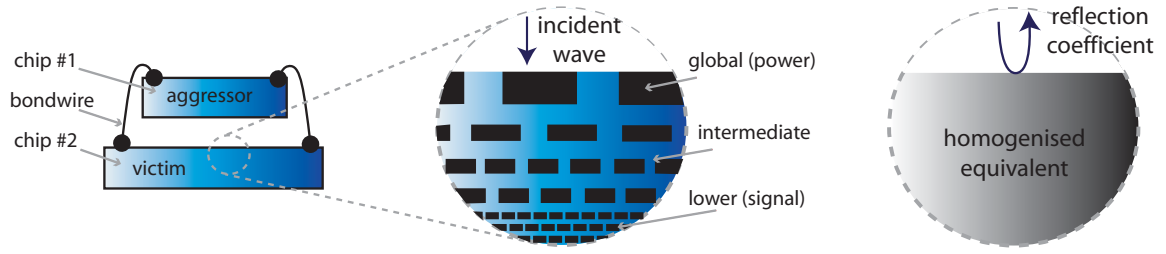

(a) *System-in-Package diagram* (b) *homogenisation concept*

Figure 1.1: *Application of integrated circuit (IC) electromagnetic compatibility analysis (a) diagram of the concept of aggressor and victim chips in SiP with the close-up of the detail of the interconnect stack in the victim chip; (b) representation of the proposed homogenisation approach. (note only one layer is homogenised in this Thesis)*

The second application is based on estimating interconnect performance in the presence of interconnects on lower metal layers. The homogenisation approach is based on the calculated S-parameters for a microstrip prototype with interconnects embedded in the dielectric substrate illustrated in Fig. 1.2(a) and the homogenised equivalent structure in Fig. 1.2(b).

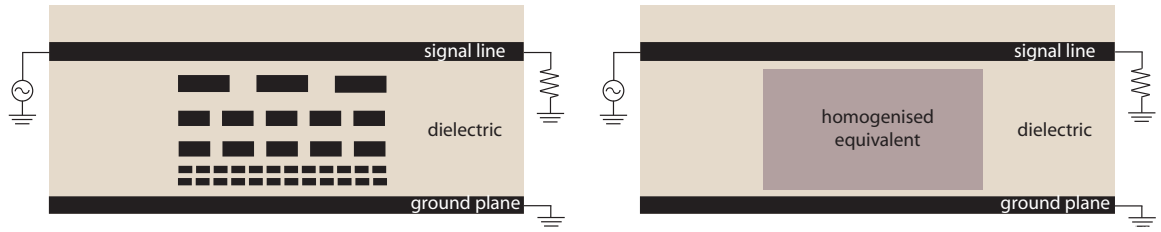

(a) *lower metal layers* (b) *homogenisation concept*

Figure 1.2: *Application of integrated circuit (IC) electromagnetic compatibility analysis (a) diagram of the concept of interconnects at lower metal layers based on the microstrip structure; (b) representation of the proposed homogenisation approach. (note only one layer is homogenised in this Thesis)*

1.1.1 Interconnect Technology Overview

In this Section the design, fabrication and performance of contemporary on-chip interconnects is described. On-chip interconnects are the wiring that connect the transistors. A cross section of a typical CMOS chip is shown in Fig. 1.3 with a transistor formed in the substrate with interconnects formed above in Fig. 1.3(a). Figure 1.3(b) shows a scanning electron micrograph of the interconnect layers in an actual chip, here a $65\,\text{nm}$ process from Intel [7], where the smallest feature in the interconnect stack has $210\,\text{nm}$ pitch. The on-chip interconnects can be classified into Metal 1, intermediate, semiglobal and global lines, depending on their position in the substrate.

The continuous process of down-scaling the IC components defines the size of the wiring pitch at each level of interconnect layers. The graphical illustration of this process based on the forecast published in International Technology Roadmap for Semiconductors (ITRS) 2008 Update [8] is given in Fig. 1.4. In the most recent ITRS forecast the minimum global wiring pitch can have a size in between the value for intermediate and semiglobal lines. Such a trend was not predicted a few years ago where for the same technology nodes the minimum global wiring pitch was affirmed to be larger than the lower levels pitches [9].

The term 'technology node' was typically used with respect to the size of transistor gate length and half pitch of the Metal 1 line. Since the half pitch value stopped decreasing as aggressively as it did in the past generations of ICs and was forecast in ITRS a few years ago, the number for technology node is going to stand more for the commercial name of the logic used than to correspond to the size of half of the pitch. The actual parameter values and the predicted time for their implementation in mass

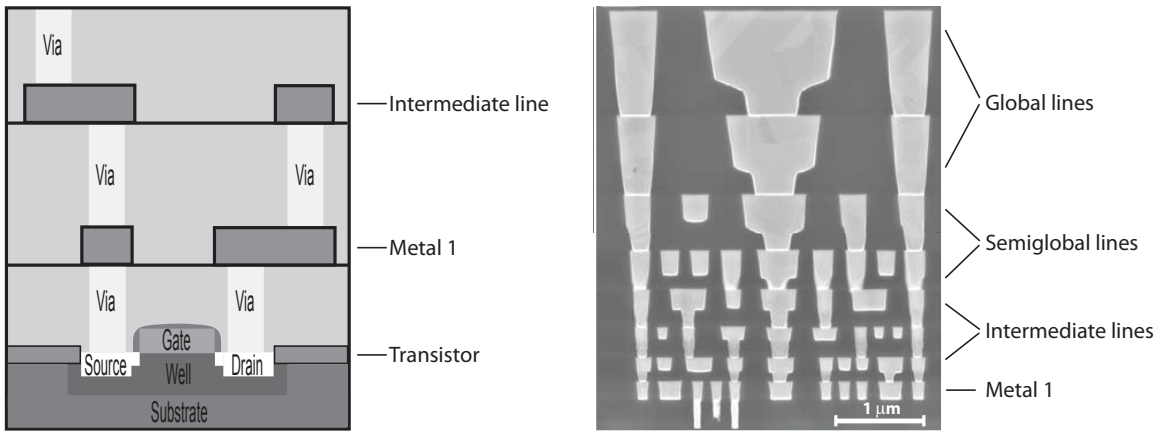

(a) *transistor and interconnects above* (b) *Interconnect layers*

Figure 1.3: *Diagram of typical CMOS integrated circuit showing (a) transistor formed in the substrate and interconnect layers formed above, (b) scanning electron micrograph with cross section of the Intel 65nm 8 layer interconnect stack (reproduced from Bai et al.).*

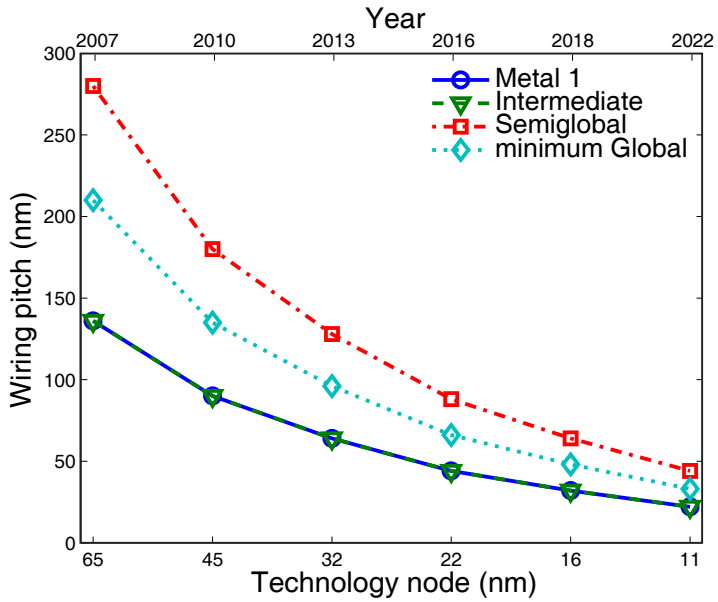

Figure 1.4: *Trend of the wiring pitch size for on-chip interconnects (After ITRS).*

production is typically different from that predicted in ITRS and strongly depends on the semiconductor companies [10].

Since SoC and SiP usually involve at least one and sometimes hundreds of processor cores, it is appropriate to discuss interconnect technology in terms of the microproces-

sor section in the ITRS [8] rather than the memory section.
The earliest generations of microprocessors were generally required only three metal levels whereas contemporary designs, in which more transistors are used, requires additional layers of metal interconnects. The present microprocessors in mass production contain up to 12 metal levels. The ITRS predicts that by the year 2022 the demand for the number of interconnect layers will be within $13 - 15$. Such a large number of layers and continuous downscaling of the pitch involves scaling of the chip wiring, with the result that the interconnect performance dominates the overall chip performance. This is because the interconnect's performance worsens as they shrink, unlike transistors. Specifically, the miniaturization of the metal interconnections increases the resistance, due to the decrease in the cross-sectional area, and typically also increases the capacitance due to an increase in aspect ratio and hence metal height with respect to conductor spacing. Hence, in integrated circuit design and verification, it is important to understand how much parasitic resistance R and capacitance C is introduced by interconnects. While this sort of analysis is peripheral to the goal of this Thesis, a brief overview is given in the rest of this Section.

In an advanced integrated circuit the RC delay is dominated by the performance of the global wires used to interconnect the on-chip components [11]. While the interconnect delay is proportional to the square of its length, and the local and intermediate interconnects tend to scale in their length, their influence on the signal latency is not as significant. Solutions for reducing the delay include the insertion of buffers into long interconnect lines and reverse scaling [12]. Lines longer than the optimal length are usually buffered by repeaters. The optimal length is determined by Rent's rule [13] which relates the number of elementary components in a subcircuit and the number of external connections and is used to estimate the interconnect length. Adding repeaters results in additional power consumption as well as loss of part of the active silicon and routing area, which in turn implies a larger wiring area is required or a more congested layout with interconnect levels may result. On the other hand, reverse scaling is based on reducing the delay by using widely spaced and large wires on the top global metalisation levels. This also improves power handling, reduces the loss and allows more dense wiring at the lower metal layers. However, such a procedure results in a larger size of microprocessor.

Other recognized issues in the analysis of interconnect performance include crosstalk

and power supply quality (elimination of ground bounce and voltage sag), as well as the power dissipation [14]. Power dissipation is of interest for local and intermediate metal levels because the length of local and intermediate interconnect layers generally scales with the implementation of a new technology process. Hence, the reduction of the RC delay at those layers is less important than crosstalk reduction. Crosstalk which occurs as the propagation of a signal to a neighbouring wire is closely related to the total capacitance of the electronic component. It increases in relation to the ratio of the line-to-line capacitance to the total capacitance, while power dissipation and delay are proportional to the total capacitance. Therefore, the optimisation of the overall interconnect system needs to consider both the line-to-line and the total capacitance. However, scaling the wire size increases the resistance in the wire in proportion to the square of the scaling factor. The current density is proportional to the scaling factor as is illustrated in Table 1.1 [15]. These increases in resistance and current density result in an increase of the RC delay and heating. Therefore, power and heat generation are the limiting factors of the downscaling process.

	Local wiring		**Global wiring**	
	ideal scaling	quasi-ideal scaling	ideal scaling	constant dimension scaling
line width and spacing	S	S	S	1
wire thickness	S	$\sqrt{S}$	S	1
interlevel dielectric thickness	S	$\sqrt{S}$	S	1
wire length	S	S	$1/\sqrt{S}$	$1/\sqrt{S}$
resistance per unit length	$1/S^2$	$1/S^{3/2}$	$1/S^2$	1
capacitance per unit length	1	~ 1	1	1
RC delay	1	$\sqrt{S}$	$1/S^3$	$1/S$
current density	$1/S$	$1/\sqrt{S}$	$1/S$	S

Table 1.1: *Interconnect scaling methodologies for local and global wiring (reproduced from Sylvester et al.).*

These consequences can be balanced by changing the typically used aluminum wiring to copper [16] which has lower a resistivity and combining it with low-k dielectric insulation [8]. Some low-k dielectric materials are already used in manufacturing pro-

cesses where the bulk permittivity is $2.5 \leq \epsilon \leq 2.9$ and according to the ITRS forecast is going to decrease to $1.5 \leq \epsilon \leq 1.8$ by the year 2022 if practical issues with their adoption are overcome. There are two ways to implement low-k dielectrics: either as solid materials with low permittivity or by deposition of porous materials. Porosity reduces the bulk permittivity, but also reduces the mechanical strength of the material. Due to the thermal and mechanical weakness of low-k materials, integration and reliability concerns have slowed down their adoption. There are also some efforts toward using air-gaps (ultra low-k material) with copper metalisation in advanced IC technologies (22 nm technology node and below) [17, 10].

The overall performance of an IC can be evaluated in a number of ways such as power consumption, number of operations per second or even clock speed. Using clock speed is not a perfect measure because two chips with the same clock speed can have very different power consumption and processing capacity if they have different designs. However, for the purpose of this Thesis, it will suffice. The on-chip local speed, which is determined by the transistor switching speed as well as the speed of the signal propagation from one component to the next, is currently about 5 GHz and is predicted to rise to approximately 15 GHz by the year 2022 [8] although this may be an ambitious target given the power dissipation issues discussed here. As the interconnect network becomes more and more complex the signal delay becomes a meaningful issue which also influences the entire switching time and the maximum clock speed. The trend in reducing the growth rate in clock frequency and chip size can be observed [10].

The other factor that deserves designers' attention is the aspect ratio (AR) of the metal wires defined as a ratio of the wire thickness to the wire width. The achievable aspect ratio is determined by the technology process and, to some extent, is limited by the fabrication process (etching, cleaning, metal deposition process) and by the properties of the low-k dielectric insulator (thermal and mechanical losses during the fabrication process, fragility, dielectric erosion, chemical interactions). The ITRS forecast with respect to the reliable metal aspect ratio for the current and next generation technology processes are in the range of $1.7 - 2.3$ and are going to increase to $2.1 - 2.9$ in the highly advance 11nm technology node process. The lower bound of the range applies to the lower metalisation levels (Metal 1 wiring and intermediate layers) whereas the upper bound to the global lines.

In the timing analysis and verification of an IC the density of the metalisation on the layout needs to be considered. The interconnect pattern density is initially limited by the design rules within $20\% - 80\%$ [18]. The pattern density is defined as the proportion of the area occupied by metal to the entire area being considered, also called metal volume fraction or metal fill factor. A statistical analysis of the pattern density of a real chip showed that, typically, the maximum pattern density does not exceed 60% in regions where the random logic is separated from the memory blocks [19]. Since the future generations of technological progress are predicted to mainly require scaling of the components whilst keeping a similar pattern density on a given layout this upper limit on the metal pattern density can be assumed to be applicable over the pending technological generations.

1.2 Aim and Scope of Thesis

The aim of this Thesis is to develop empirical effective medium theory models which allow interconnects to be accurately replaced by homogeneous material slabs in electromagnetic simulations containing integrated circuits. Replacing interconnects with a homogeneous equivalent drastically reduces the complexity of the numerical model, whilst simultaneously retaining the precise nature of the influence of those interconnects on nearby waveguides.

The specific aims of this work are:

- consider electromagnetic behaviour of a canonical structure of on-chip interconnects and evaluate validity of replacing detailed structure with an equivalent homogeneous material;
- develop a compact formula or formulas for the prediction of the effective permittivity of such a homogeneous slab;
- conduct experiment to validate that the model can predict the reflection coefficient of a single layer of interconnects;
- extend model to deal with interconnects in the vicinity of a typical interconnect carrying a high frequency signal, and conduct experimental validation.

Some specific limitations on the scope of the work are as follows.
First the main focus is on the performance of a single layer of interconnects in the presence of other interconnects. Since the approach of applying the effective medium theory specifically to the analysis of interconnects has not been presented in the literature prior to this work, it was considered prudent to concentrate on a straightforward canonical structure, that of a single layer of interconnects. It can be reasonably expected that such an analysis can be extended to describe the performance of multilayered arrangements of wires in an interconnect stack. However, such an analysis is out of the scope of this Thesis.
Two frequency ranges, $1-10\,\text{GHz}$ and $30-200\,\text{GHz}$, are targeted. The first, $1-10\,\text{GHz}$, corresponds to typical on-chip signals frequency and the second, $30-200\,\text{GHz}$, is related to high frequency applications and includes several of the Industrial, Scientific and Medical (ISM) bands.
A single layer of interconnects is not unlike a grating structure. A wave propagating through a grating structure with a deep subwavelength period behaves macroscopically the same as if it was travelling through a homogeneous medium. Effective medium theory correlates the critical grating parameters with the dielectric properties of effective homogeneous medium. Despite metals having negative permittivities, metal-dielectric gratings are well known to have positive effective permittivities. In this work only nonmagnetic materials are considered; although these have been considered elsewhere for other applications [20], they are not directly of interest here.

1.3 Thesis Outline

This Section provides an outline of the contents and organisation of the remainder of the Thesis. Generally, the work in this Thesis (Chapter 4-6) is presented in the order in which it was performed.

Chapter two presents the background to the effective medium theory. The theory of artificial dielectrics and metamaterials, form birefringence and subwavelength gratings is provided. It is explained that the effective medium theory gives mathematical tools to analyse the dielectric and metal-dielectric gratings. A selection of mixing rules, with an emphasis on the Maxwell-Garnett rule, are discussed.

Chapter three provides a review of the analysis and simulation techniques. The analytical method - characteristic matrix method - is presented, along with the three numerical methods used to generate the data - finite difference time domain method, rigorous coupled wave analysis and finite element method. The numerical techniques are validated against the analytical method.

Chapter four introduces the canonical structure for which the empirical mixing models are defined. The analytical formulation of the empirical model for on-chip signals band and the empirical model for ISM frequency band are presented together with their validation. Furthermore, the validity of the empirical model for a range of incident angles of the plane wave and change in the grating profile is discussed in the context of theoretical bounds observations. A comparison with other empirical models reported in the literature is also provided.

Chapter five details the X-band ($8.2 - 12.4\,\text{GHz}$) free-space measurements with a description of experimental design and equipment. Detailed accounts of the calibration procedure and measurement accuracy are also presented. The measurement results for the TM polarisation are discussed.

Chapter six deals with the microstrip analysis and measurements. The experimental design and numerical analysis along with the homogenisation procedure and results are presented. The measurements of the prototype microstrip lines are described along with the discussion of the results.

Chapter seven is the last in this Thesis and provides conclusions and plans for further work.

Chapter 2

Background

2.1 Introduction

Effective medium theory (EMT) has been studied since 1892 by such scientists as Lord Rayleigh[21], Lorentz[22] and Maxwell-Garnett[23, 24]. Experimental and theoretical studies of periodic structures show that they behave as homogeneous media if the characteristic period Λ is small compared to the illumination wavelength λ_0; typically $\Lambda < \lambda_0/4$. Replacement of the periodic structure by an equivalent homogeneous medium is a process known as 'homogenisation' and is based on an effective medium theory. The equivalent thin layer has an effective index that can be calculated as some average from the geometry and material properties of the periodic structure. Homogenisation often simplifies the analysis of the structure by creating a new artificial material. Another term often encountered in effective medium theory literature is 'metamaterial', although this requires careful definition. One of the best known examples of effective medium theory is the Maxwell-Garnett mixing rule. This rule is of particular interest here and is described in this Chapter.

2.2 Artificial Dielectrics and Metamaterials Theory

The first porous antireflection surfaces were presented by Fraunhofer[25] and were obtained by etching a glass surface with an acid solution. The upper layer comprised a mixture of air and glass and had a reduced macroscopic refractive index. Consequently, reduced reflections were observed due to the reduced index mismatch at the interface. Further reductions can be obtained with more regular porosity, with

dimensions smaller than the wave length of the illuminating wave which together form a continuous gradient in the refractive index through the thickness of the layer. Considerable experimental work has been done on the reduction of reflections by using porous layers of Gaussian profile [26] - thus validating the EMT approach.

A biological antireflection surface was discovered in the eye of the nocturnal moth and analysed by Bernhard[27, 28]. For the purpose of camouflage the corneas of nocturnal moth eyes are covered with a regular hexagonal array of protuberances of about $200\,\mathrm{nm}$ depth and spacing with a cross section which is approximately sinusoidal. As the scale of the structure is significantly smaller than visible wavelengths, the incoming visible light cannot resolve the details and instead the light 'sees' a material with a smoothly graded refractive index that gradually transitions the refractive index from that of air to that of the cornea. The smoothly graded dielectric constant of the surface does not exist independently of the illumination and is therefore called an artificial dielectric. Early attempts to reduce the surface reflection of the visible spectrum were based on the principle of the effect observed in the moth-eye and is often called the moth-eye-type antireflection coating [29]. Nowadays this effect is used in the mass production of antireflective coatings as an inexpensive alternative to the quarter wave coating.

The rapidly growing research area of artificially obtained media with positive or negative permittivity and permeability is commonly described as metamaterials[1]. The literature relating to the negative index media is neglected here because it is out of the scope of this Thesis. Metamaterials are created artificially by combining inhomogeneous media or patterning an homogeneous material in order to obtain an effective macroscopic response. The two main requirements for metamaterial properties are that they should not be observed both in the constituent materials and are not naturally formed by nature [30]. Hence metamaterial is a man-made, fabricated material engineered to somehow disregard or fulfill the natural phenomena. They are desired for application in new apparatus, systems and materials.

With reference to a discussion on the difference between artificial dielectrics and metamaterials [30], it is worth noting that the moth eye structure [27, 28], when occurring naturally in nature, is an artificial dielectric but not a metamaterial. Were that structure to then be mimicked in a man-made process (e.g. using semiconductor fabrication

[1] meta = beyond, after

technologies) only then it would also qualify as a metamaterial. Similarly, photonic band gap structures found in butterfly wings [31] are not metamaterials whereas a duplicate man-made structure will be.

Properties of artificially created materials depend on both internal and external factors [30]. Internal factors include the composite materials comprising the mixture. Specifically, their shape, alignment (periodicity), separation, volume fractions, etc. External factors include the interaction with the outer 'world' e.g. illumination frequency and wave characteristics. There is a requirement of homogeneity for a material to be called a 'material'. It means that the created inhomogeneous mixture needs to be a disordered or periodic structure with unit cell much smaller that the length of the incident wave to behave as an homogeneous medium. Hence periodic structures are easier to manufacture, are more repeatable and are therefore of main interest in the engineering of metamaterials.

Wire grid polarisers (WGP) have been studied extensively as subwavelength structures consisting of periodically aligned wires which reflect one polarisation of incident wave (electric field polarised parallel to the direction of the wires) while transmitting the other (electric field polarised perpendicular to the direction of the wires). They are mainly utilized as polarisers or polarising beam splitters. The effectiveness of grid polarisers depends on the relationship between the grating periodicity and the illumination wavelength. The spacing between the metallic wires and their widths specify the wavelengths at which the polariser can be used. The grating period should be smaller than the wavelength of the illumination wave. For correct operation of the WGP over the entire range of visible light the grating period should be less than $150\,\text{nm}$.
The incident electromagnetic wave polarised along the wire direction induces the free movement of electrons along the length of the wire. The physical response of the wire grid is similar to that of a thin sheet of metal. The current is generated on the metal surface and some energy is lost due to joule heating whereas the rest of the wave is reflected. In the case of the incident wave polarised perpendicular to the wires, the electrons' mobility is limited by the width of the wires. There is a small amount of the energy both lost and reflected. Thus most of the incident wave is transmitted through the grid. The electric field components parallel to the wires are absorbed or reflected. Therefore, the transmitted wave has its electric field component perpendicular to the wires - a linearly polarised wave. For the considered polarisation, and from form bire-

fringence theory, the wire grid behaves analogously to a homogeneous slab of dielectric.

A schematic diagram of the WGP is shown in Fig. 2.1. Material properties are represented by their refractive indices: n_1 is the complex refractive index for the metallic wires, n_2 is the refractive index of the dielectric medium; f stands for the metal fill factor, Λ is the grating period ($\Lambda << \lambda$, λ - wavelength of illumination wave) and h is the grating height.

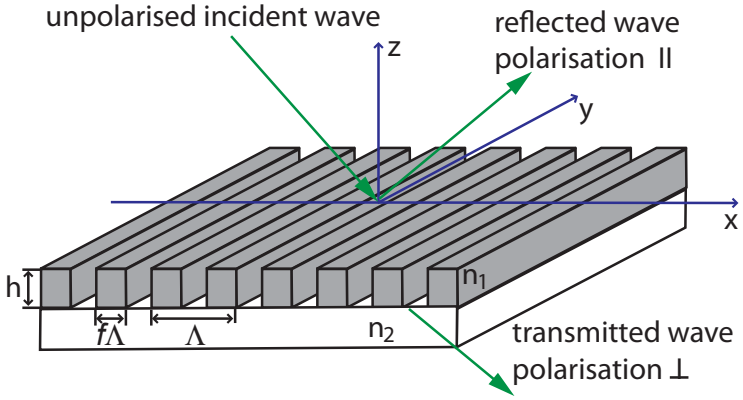

Figure 2.1: *Diagram representing the subwavelength wire grid polariser. When unpolarised wave incident on the polariser, polarisation with electric field parallel (∥) to wire grid is reflected and polarisation with electric field perpendicular (⊥) to the wire grid is transmitted.*

The first attempt to apply the effective medium theory to the analysis of WGP was reported by Yeh *et al.* [32] and Yeh [33, 34]. The authors proposed that a periodic layered medium consisting of layers of different homogeneous and isotropic materials following in sequence behaves as a uniaxial birefringent medium. The effective refractive indices of this composite structure are given by [33]

$$n_{TE} = \left(f n_1^2 + (1-f) n_2^2\right)^{1/2}, \tag{2.1}$$

$$n_{TM} = \left[\frac{f}{n_1^2} + \frac{(1-f)}{n_2^2}\right]^{-1/2} \tag{2.2}$$

The lower indices TE and TM correspond to the polarisation of the electromagnetic field with respect to the orientation of the metallic wires. This will be described in Section 2.3. Note that Eq. (2.1)-(2.2) are equivalent to the zeroth-order approximation of Eq. (2.17)-(2.18) and to the Wiener bounds of Eq. (2.32)-(2.33).

The simplified model of WGP which is based on the effective medium approximation was used in the analysis of polarisers operating at infrared [35], visible [36, 37, 38] and ultraviolet [38] wavelengths. The performance and optimisation of the polarising beam splitter [35] and the wire grid polariser in the vicinity of the volume plasmon frequency (fundamental frequency of a free oscillation of the electrons in the metal) [38] was studied by the straightforward application of formulas Eq. (2.1)-(2.2) in the quasi-static limit. In [35] a detailed study of the zeroth-order diffraction efficiency is conducted for a single wavelength of $1550\,\text{nm}$ (infrared light) and varying grating depth with fixed period $\Lambda = 1069\,\text{nm}$. It is demonstrated that the zeroth-order diffraction efficiency of the transmitted TM polarised wave is a periodic function of grating depth h. The form birefringence approximation theory, Eq. (2.1)-(2.2), can be simply and efficiently applied to the analysis of dielectric gratings [39, 40]. Nevertheless, for metallic gratings, this model is not accurate enough [37]. In [37] it is demonstrated that, in some cases, use of the form birefringence method to calculate optical properties (transmission and reflection coefficient) of the WGP does not yield accurate results. The analysis was performed for the grating with parameters: $\Lambda = 150\,\text{nm}$, $h = 180\,\text{nm}$, metal fill factor $f = 0.55$ and the incident wave with wavelength $\lambda = 543.5\,\text{nm}$ (visible range). For the wave polarised perpendicular to the wires, the form birefringence approximation gives up to 80% error in the reflection coefficient. This is shown in Fig. 2.2(a) and Fig. 2.2(b) for the transmission and reflection coefficients respectively. The deviation of the form birefringence from the experimental results is small for the incident wave polarised parallel to the wires. This is illustrated in Fig. 2.2(c) and Fig. 2.2(d). In Fig. 2.2(c), both rigorous calculations and form birefringence differ from the measured data by very small percentages that are related to the experimental uncertainty. Since the form birefringence approach is not accurate when applied to the analysis of a single metallic gratings illuminated by waves polarised in the direction perpendicular to the wires, either rigorous calculations are required or an alternative effective medium approximation would need to be defined. Hence in this Thesis, classical mixing models are considered.

The effective medium approximation was employed for the extensive modelling of liquid-crystal displays (LCD) by replacing the metal grid with a homogeneous equivalent block [36]. The form birefringence method was used as a starting point to estimate the effective properties. The calculated effective refractive indices were then corrected by fitting two parameters to ensure agreement with experimental data. The first pa-

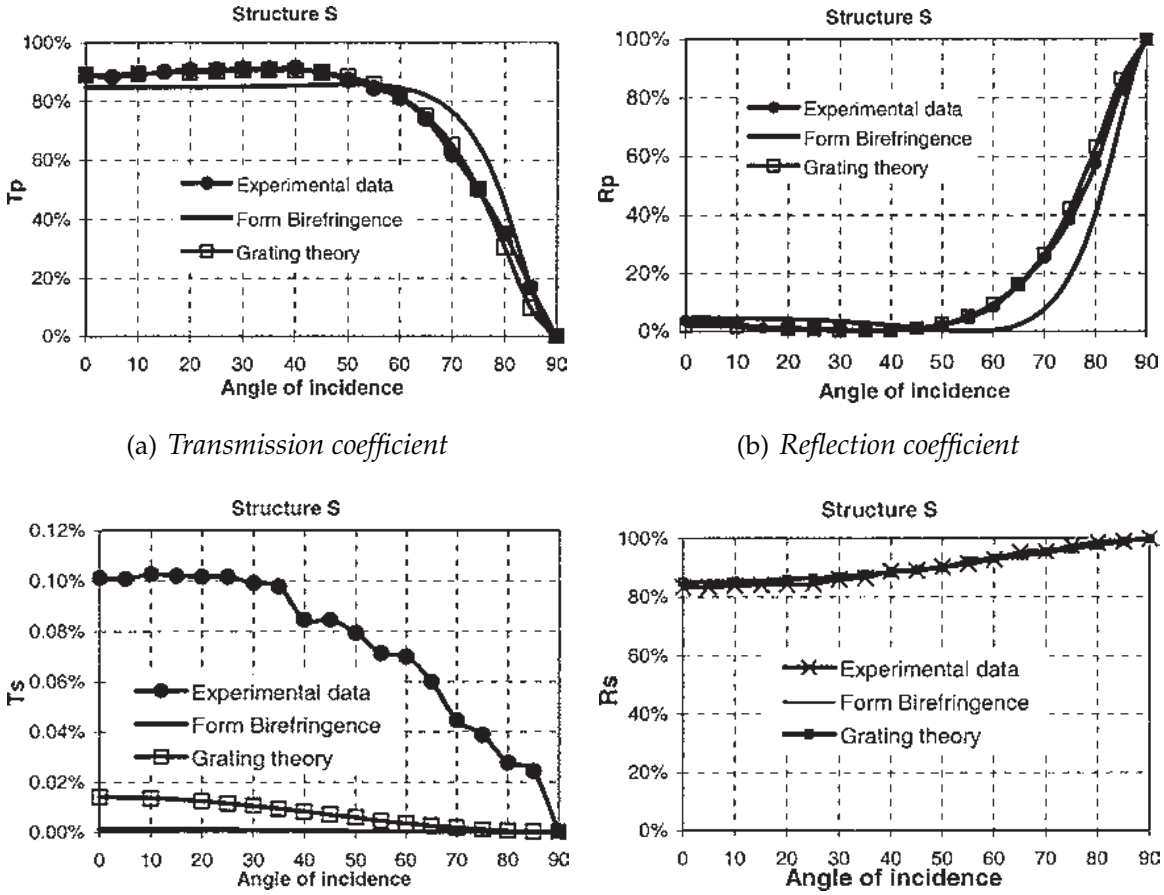

(a) *Transmission coefficient*

(b) *Reflection coefficient*

(c) *Transmission coefficient*

(d) *Reflection coefficient*

Figure 2.2: *Comparison between experimental and simulated data for incident wave polarised perpendicular to wire grids: (a) transmission coefficient, (b) reflection coefficient. The values obtained for incident wave polarised parallel to wire grids: (c) transmission coefficient, (d) reflection coefficient. (reproduced from Yu et al., Fig. 3,4,5,6.)*

rameter is the thickness of the effective medium; the second is the absorption coefficient. Note that the absorption coefficient is dispersive and changes with wavelengths. The authors of [36] provide effective refractive indices for the two polarisations of the incident light in the visible range ($\lambda = 400 - 700\,\text{nm}$). These can be used in the analysis of LCD structures. However the effective refractive indices are only valid for two specific combinations of gating parameters and substrate, and do not go for enough to suffice for the applications considered in this Thesis.

For the subwavelength metallic gratings illuminated by a plane wave, the peak value

of the transmitted wave can be observed at Brewster's angle [41]. The magnitudes of the transmitted and reflected waves incident at this angle are related to the grating parameters and are determined by the horizontal and vertical surface resonances occurring in the metallic periodic structures [42, 43, 44]. For TM polarised plane waves incident on the metallic grating, the resulting zeroth-order diffracted wave excites horizontal surface resonances (surface plasmons) on the upper and lower surface of the periodic structure. The coupling between the upper and lower surface plasmons results from the propagating guided wave in the dielectric part of the grating. The vertical surface resonances arises from the coupling of the two surface waves and corresponds to the Fabry-Pérot resonances of the TM guided wave in the grating slits. The interplay between the two types of resonances causes the outgoing propagating plane wave to be transmitted with high efficiency. For the multilayered structure, such a wave will penetrate into the lower layers, thus the lower layers can also affect the total amount of reflection. Therefore, even though a wire grid polariser are well studied it is necessary to consider a new approach that can be readily extended to multilayers structures, after validation single layer structures.

A metallic periodic structure, when illuminated by electromagnetic incident radiation of required wavelength, can be called an artificial dielectric or metamaterial [45, 46, 47, 48] because the structure's macroscopic metal properties exhibit dielectric characteristics which do not exist in readily available natural materials. Metallic periodic structures composed of copper grids have the properties of metameterial [45]. Such an arrangement of the metal wires can be used, for example, to control the emission of photonic-crystal-based antennas. Even though the crossing-wires structure behave as a metamaterial it does not adequately represent the metal wires found in interconnect stacks.
The metal-dielectric film composites [46] have been successfully applied to improve the performance of near-field superlenses where the negative permittivity is of main interest. The range of wavelengths at which the lens can operate is controlled by the metal fill factor. These structures are characterised by a negative permittivity which is not related to the interconnect structure.
The Maxwell-Garnett rule [23] was generalized for the calculation of the effective properties of a granular metal-dielectric mixture in terms of the size and distribution of the metal particles [47, 48]. Since this effect was studied only for round-corner inclusions the derived formulation cannot be applied straightforwardly to the analysis of mix-

tures with sharp-corner inclusions like those found in an interconnect stack.

2.3 Form Birefringence

When analysing a grating structure its properties strongly depend on the direction of the illuminating wave. Hence, the transverse electric (TE) and transverse magnetic (TM) polarisation of the linearly polarised electromagnetic plane wave is defined with respect to the grating vector ***K*** which is orthogonal to the grating. The TE polarisation is a linear polarisation with the electric field perpendicular to the grating vector, as illustrated in Fig. 2.3(a), and the TM polarisation is a linear polarisation with the electric field parallel to the grating vector, as depicted in Fig. 2.3(b).

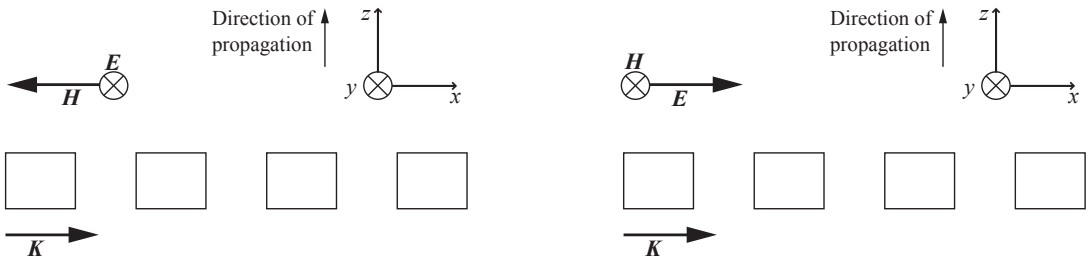

(a) *TE polarisation* (b) *TM polarisation*

Figure 2.3: *Representation of the transverse electric (TE) and transverse magnetic (TM) polarisations of the normally incident linearly polarised electromagnetic waves. These are defined with respect to the grating vector* ***K****: (a) TE - electric field perpendicular to* ***K****, (b) TM - electric field parallel to* ***K****.*

Structures comprising regular parallel plates of isotropic materials with small thicknesses relative to the illumination wavelength behave anisotropically, a phenomena known as form birefringence [49]. Form birefringence is created in surfaces characterised with different grading of the refractive index for TE and TM polarised waves. In such structures the effective dielectric constant depends on the direction of the electric field vector.

Dielectric grating structures forming birefringence have already been extensively analysed in the literature such as the 2-D examples shown in Fig. 2.4. The dielectric constants of the two materials forming the grating structure are denoted by ϵ_1 and ϵ_2; f stands for the fill factor of medium with ϵ_1, and Λ is the structural period. The fill factor is defined as the ratio of the width of the dielectric portion to the grating period,

such that the value of $f\Lambda$ is equal to the plate thickness. In this Thesis, gratings for which ϵ_1 represents a metal and ϵ_2 a dielectric.

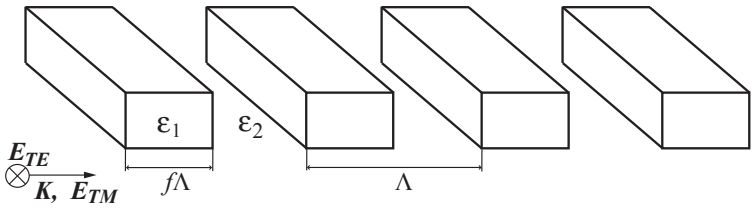

Figure 2.4: *Perspective diagram of a grating structure that creates a birefringence surface, such as might be seen in the analysis of a single layer of interconnects.*

2.4 Subwavelength Gratings

A periodic subwavelength grating is similar to a diffractive structure but does not produce propagating diffracted waves in the far field because the period is small compared to the illuminating wave. The only propagated order is the zero reflected and zero transmitted order in the incident and substrate medium, respectively, while the other higher diffraction orders are evanescent [50]. Figure 2.5 illustrates the geometry of the profile of a 1-D grating surface. The critical dimensions of the grating structure are depicted. Specifically, grating vector $\mathbf{K}$, grating period Λ, the transmitted and reflected higher diffraction orders T_m, T_{-m} and R_m, R_{-m} respectively, and the transmitted and reflected zero-orders $T_0,\ R_0$ respectively. The incident and substrate medium have dielectric refractive indices n_i and n_s respectively.

The grating equation determines whether a given order propagates or not and is given by

$$n_s \sin\theta_m - n_i \sin\theta_i = \frac{m\lambda}{\Lambda}, \tag{2.3}$$

where θ_i is the angle of incidence measured from the normal to the grating surface and θ_m is the angle of the m^{th} diffracted order, λ is the wavelength of the incident wave in free-space.

If the only propagated order is to be $m = 0$ in either the substrate or the incident medium then θ_m needs to be complex for all diffraction orders $m \neq 0$. Equation (2.3) can be transformed to give an upper bound for the period-to-wavelength ratio. For

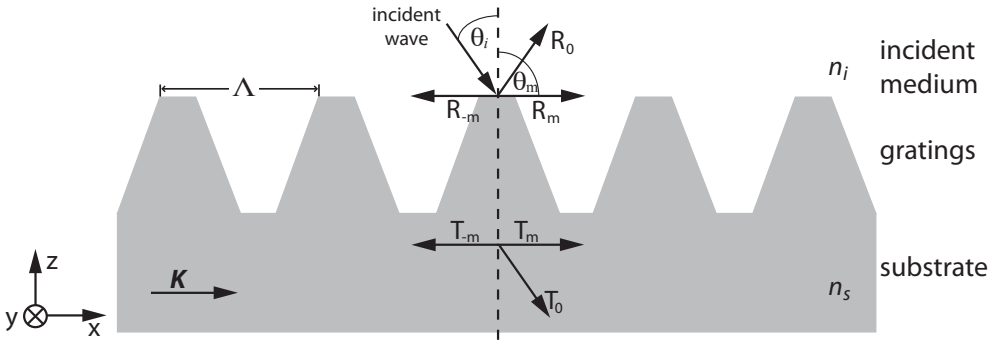

Figure 2.5: *Transmitted and reflected diffraction orders for an artificial dielectric grating of arbitrary profile. (After Raguin et al., Fig. 1)*

the artificial dielectrics the first evanescent order is set to be for $m = 1$ and $\theta_m = \pi/2$. Hence Eq. (2.3) becomes

$$n_s - n_i \sin\theta_i = \frac{\lambda}{\Lambda}. \tag{2.4}$$

The limit of the zero-order regime on the period is given by

$$\Lambda_c = \frac{\lambda}{n_s - n_i \sin\theta_i}, \tag{2.5}$$

where Λ_c is the cutoff limit period above which the higher evanescent orders propagate. The upper limit on the grating period Λ is set by the minimum value of the cutoff limit period Λ_c. For the case when $n_s > n_i$ the minimum value of Λ_c is obtained when $\theta_i = -\frac{\pi}{2}$, $\theta_i \in \left[-\frac{\pi}{2}, \frac{\pi}{2}\right]$ and is equal to $\Lambda_c = \frac{\lambda}{n_s + n_i}$. However, for $n_s < n_i$ the Λ_c as a function of the incident angle θ_i is undefined for $\theta_d = arcsin\left(\frac{n_s}{n_i}\right)$. The limit period Λ_c for $\theta_i > \theta_d$ has negative values $\Lambda_c < 0$ therefore the domain in which Λ_c is defined is $\theta_i \in \left[-\frac{\pi}{2}, \theta_d\right]$.

In order to minimise the cutoff limit period and account for the discontinuity in $\Lambda_c(\theta_i)$ the denominator might be transformed to $\max[n_s, n_i] + n_i \sin\theta_i$. This gives the maximum value of the denominator for given values of n_i, n_s, λ and angle of incident θ_i. Hence the upper limit on Λ becomes $\Lambda < \Lambda_c$ and

$$\Lambda_c = \frac{\lambda}{\max[n_s, n_i] + n_i \sin\theta_i}, \tag{2.6}$$

with the discontinuity angle being $\theta_d = arcsin\left(-\frac{\max[n_s, n_i]}{n_i}\right)$ which always has a negative value. Since $\Lambda_c(\theta_i)$ is monotonically decreasing function in the domain $\theta_i \in \left[\theta_d, \frac{\pi}{2}\right]$ for both cases, when $n_s > n_i$ and $n_s < n_i$, the minimum value of $\Lambda_c(\theta_i)$ is obtained for

the maximum angle of incidence θ_{max}. Therefore, the upper limit on the grating period is

$$\Lambda < \frac{\lambda}{\max[n_s, n_i] + n_i \sin\theta_{\text{max}}}, \tag{2.7}$$

and restated in terms of the period-to-wavelength ratio is

$$\frac{\Lambda}{\lambda} < \frac{1}{\max[n_s, n_i] + n_i \sin\theta_{\text{max}}}, \tag{2.8}$$

where max[] is equal to the maximum value of its arguments.

The above inequality indicates that, for only the zeroth diffraction order to propagate in the grating structure, the structural period needs to be smaller than the incident wavelength. This upper bound on the structural period and the length of illumination wave is a practical way to determine whether or not the grating structure may be considered as an artificial dielectric and, therefore, whether the man-made material with an effective refractive index is a metamaterial with properties that do not exist in nature.

2.5 Dielectric Gratings

This Section focuses on the propagation of electromagnetic waves through periodic laminated structures of dielectrics. However, similar principles apply to other materials. The Rytov [51] and Clogston [52] formulas admit both permittivity ϵ and permeability μ. Nevertheless, in this Thesis it is assumed that the dielectric layers have nonmagnetic properties ($\mu_r = 1$) and the main concern is the permittivity.
Hence, Clogston [52] investigated conductor-dielectric stacks for reducing losses in waveguides and derived the following formula for the effective permittivity

$$\epsilon_{eff} = \epsilon_d \left(1 + \frac{\mathcal{W}}{\mathcal{T}}\right), \tag{2.9}$$

where $\mathcal{W}$ is the thickness of the conducting layers, $\mathcal{T}$ is the thickness of the dielectric layers, and ϵ_d is the permittivity of the dielectric layers.

A more detailed analysis of the laminated stack of dielectrics, in particular in terms of the ratio of the structural period to the wavelength [51, 53, 54], will now be presented.

In [51] Rytov analysed properties of a stratified media consisting of two arbitrary homogeneous dielectrics following in sequence. A schematic diagram of the structure studied by Rytov with alternating layers is shown in Fig. 2.6. The first dielectric layer has permittivity ϵ_1, permeability μ_1 and thickness a, and the second - permittivity ϵ_2, permeability μ_2 and thickness b.

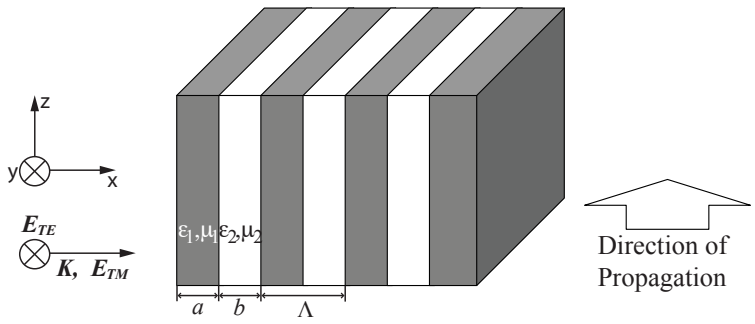

Figure 2.6: *Diagram of the stratified electromagnetic medium with alternating layers analysed in Rytov's paper.*

In order to solve for the field direction characterised by TE and TM polarisation, which are of the interest for the analysis of the grating structure representing a single layer of interconnects, a uniform plane wave was applied to the structure. The TE and TM polarisations are defined with respect to the grating vector **K** as it is specified in Fig. 2.6.

The approach is based on averaging the electromagnetic field in the laminated stack by calculating some average value of the dielectric properties over the period $\Lambda = a + b$. The averaged value gives the effective permittivity and permeability. For metamaterials comprising materials with $\mu_r = 1$ it is not necessary to consider the effective permeability explicitly since its effective value remains $\mu_{eff} = 1$. The method proposed by Rytov [51], and explained in the following, can be applied only under the assumption that there is a slow change of the field along distance Λ in the direction of propagation. This condition is formulated as

$$k\Lambda|n| \ll 1 \tag{2.10}$$

where $k = \omega/c = 2\pi/\lambda$ and n is the effective refractive index of the medium for a given polarisation and direction of propagation, and is similar to that given in Eq. (2.8) in intent.

The effective permittivity for the TE polarisation, ϵ_{TE}, is the root of

$$\frac{\alpha_2}{\mu_2}\tan\frac{\alpha_2 b}{2} = -\frac{\alpha_1}{\mu_1}\tan\frac{\alpha_1 a}{2} \tag{2.11}$$

where

$$\alpha_1 = k\sqrt{\epsilon_1 - \epsilon_{TE}}, \tag{2.12}$$

$$\alpha_2 = k\sqrt{\epsilon_2 - \epsilon_{TE}}. \tag{2.13}$$

The effective permittivity for the TM polarisation, ϵ_{TM}, is the root of

$$\frac{\alpha_2}{\epsilon_2}\tan\frac{\alpha_2 b}{2} = -\frac{\alpha_1}{\epsilon_1}\tan\frac{\alpha_1 a}{2} \tag{2.14}$$

where

$$\alpha_1 = k\sqrt{\epsilon_1 - \epsilon_{TM}}, \tag{2.15}$$

$$\alpha_2 = k\sqrt{\epsilon_2 - \epsilon_{TM}}. \tag{2.16}$$

The derived Eq. (2.11)-(2.16) does not give a close form solution for the effective permittivities for each polarisation. Nevertheless, for the structures where the illumination wave length is much longer than the structural period (quasi-static limit), the arguments of the tangents become small ($|\alpha_1 a| \ll 1$ and $|\alpha_2 b| \ll 1$) and a zeroth-order approximation can be applied. Hence, the tangents are replaced by their arguments and the zeroth-order effective permittivities for TE and TM polarisations are as follows

$$\epsilon_{TE}^{(0)} = f\epsilon_s + (1-f)\epsilon_i, \tag{2.17}$$

$$\epsilon_{TM}^{(0)} = \Big[\frac{f}{\epsilon_s} + \frac{(1-f)}{\epsilon_i}\Big]^{-1} \tag{2.18}$$

where ϵ_s is the permittivity of a substrate medium, ϵ_i stands for the permittivity of an incident medium, and the fill factor f represents the fraction of substrate material within a period Λ. Formulas Eq. (2.17) and Eq. (2.18) depict the difference between effective permittivities calculated for TE and TM polarisations for 1-D grating structure. Hence, they also show the effect of form birefringence in considered structure.

For the subwavelength grating structures, with larger period, that do not meet the long wave limit ($\Lambda/\lambda \ll 1$, note that this is a simplified form of Eq. (2.10) but still represents the limit adequately), it is required that a correction factor is added to the

zeroth-order approximations. The obtained second-order effective permittivities for each polarisation are

$$\epsilon_{TE}^{(2)} = \epsilon_{TE}^{(0)}\left[1 + \frac{1}{3\epsilon_0\epsilon_{TE}^{(0)}}\left(\pi(\epsilon_s - \epsilon_i)\frac{\Lambda}{\lambda_0}f(1-f)\right)^2\right], \tag{2.19}$$

$$\epsilon_{TM}^{(2)} = \epsilon_{TM}^{(0)}\left[1 + \frac{\epsilon_{TE}^{(0)}}{3\epsilon_0}\left(\pi\frac{\epsilon_{TM}^{(0)}(\epsilon_s - \epsilon_i)}{\epsilon_i\epsilon_s}\frac{\Lambda}{\lambda_0}f(1-f)\right)^2\right]. \tag{2.20}$$

Rytov states that Eq. (2.19)-(2.20) are valid only when the correction term is small.

The limiting value of Λ/λ for which the homogenisation approach of EMT agreed with rigorous calculations was studied by Bell *et al.* [53]. For both TE and TM the limit for lamellar gratings (gratings with rectangular profile) is $\Lambda/\lambda < 1/40$. Typical interconnect structures have $\Lambda/\lambda < 1/10^6$ and are thus well within the limit of the theory, under the assumption the metal is represented by a dielectric constant via Drude model.

The above formulations for the estimation of the effective permittivities were derived under the assumption that the stratified medium is infinite in the in-plane direction. For that reason the case of shallow gratings was analysed in more detail and presented by Lalanne *et al.* [54] from which the remainder of the equations in this Subsection are obtained. An analytical solution of Maxwell's equations in the small-depth limit shows that the effective permittivities of subwavelength gratings are strongly dependent on the grating depth and the refractive indices of the media surrounding the gratings. These need to be accounted for, especially if the subwavelength gratings have a depth smaller than two wavelengths. Expressions for the effective permittivities, for TE and TM polarised incident wave, of the shallow gratings obtained by applying Fourier expansion technique are given below

$$\epsilon_{TE}(h) = \epsilon_0 + \sum_{p\neq 0}\frac{\epsilon_p\epsilon_{-p}}{2|p|}\left(\frac{\Lambda}{\lambda}\right)hk + O(h^2k^2), \tag{2.21}$$

$$\epsilon_{TM}(h) = \epsilon_0 - \sum_{p\neq 0}\frac{|p|\epsilon_p\epsilon_{-p}}{\epsilon_s + \epsilon_i}\left(\frac{\lambda}{\Lambda}\right)hk + O(h^2k^2) \tag{2.22}$$

where h is the grating depth, ϵ_0 is the effective relative permittivity, $\epsilon_p,\ \epsilon_{-p}$ are the coefficients of the complex Fourier expansion of the permittivity profile, and p is the number of terms included in the complex Fourier expansion. The effective permittivity obtained for TE polarisation of 1-D gratings depends only on the grating parameters

whereas for the case of TM polarisation the effective index is also influenced by the dielectric properties of the surrounding media. Furthermore, the achievable value of ϵ_{TM} is to some extent limited by the grating profile. The effective permittivity of a discontinuous grating profile in the TM polarisation cannot be analysed using this Fourier expansion method because the coefficient p in the numerator of the sum causes the formula to be undefined.

In the paper [54] Lalanne *et al.* derived and validated an approximate formulation for the effective permittivity in terms of the depth of the grating. The resulting equation was based on arctangent dependency and satisfies the three following conditions: the effective permittivity for the zero depth grating is equal to the zero-frequency component in the Fourier expansion ($\epsilon(0) = \epsilon_0$); the effective permittivity for the infinitely deep grating is equal to the second-order EMT ($\epsilon(\infty) = \epsilon^{(2)}$); for the gratings with depth within those limits the change of the permittivity with respect to the change in grating depth and wavenumber is equal to η_1 ($d\epsilon/d(hk) = \eta_1$), where

$$\eta_1^{TE} = \sum_{p\neq 0} \frac{\epsilon_p \epsilon_{-p}}{2|p|} \left(\frac{\Lambda}{\lambda}\right) hk, \tag{2.23}$$

$$\eta_1^{TM} = \sum_{p\neq 0} \frac{|p|\epsilon_p \epsilon_{-p}}{\epsilon_s + \epsilon_i} \left(\frac{\lambda}{\Lambda}\right) hk. \tag{2.24}$$

The permittivity for a given polarisation and varying depth h of the subwavelength gratings can be calculated from

$$\epsilon(h) = \epsilon_0 + \frac{2}{\pi}(\epsilon^{(2)} - \epsilon_0) \arctan\left(\pi^2 \frac{\eta_1}{\epsilon^{(2)} - \epsilon_0} \frac{h}{\lambda}\right). \tag{2.25}$$

The effective permittivity obtained from Eq. (2.25) was compared with rigorous computations and showed good agreement for the TE polarisation of 1-D gratings. However, for the TM polarisation of the 1-D gratings with non-continuous relative permittivity profile (e.g. rectangular gratings) this equation is not valid. It is not valid due to the method applied to derive equations Eq. (2.23)-(2.24) where the Taylor series expansion was used. Thus, in Eq. (2.24) the summation over p becomes increasingly large. Hence, a different method needs to be used in order to calculate the effective properties of rectangular gratings.

2.6 Dielectric-Metal Gratings

The most common approach to engineering artificial materials is to align the constituents in a periodic manner. This has the advantage of being highly repeatable. Nevertheless, there are naturally created mixtures which are of interest to researchers such as geostructures, biological tissues, etc. that have a random distribution of particles [55]. For such mixtures with random alignment of inclusions the classical mixing rules can be used in original or modified form.

In this Section the Maxwell-Garnett mixing rule is described and an argument presented that the modified classical mixing rules, such as Maxwell-Garnett rule, can be used for calculation of the effective permittivity of composites where the initial conditions for the validity of the original rule are not fully satisfied. In other words, the classical mixing rules are more widely applicable than first expected.

2.6.1 Maxwell-Garnett Mixing Rule

The classical mixing rule for estimating the effective permittivity of a mixture was defined by Maxwell-Garnett in 1904 [23, 24] and with its original formulation is valid for mixtures with dilute conductive constituents under the following assumptions [55, 56]:

- the mixture is electrodynamically isotropic,
- none of the mixture's fundamental parameters depend on the intensity of electromagnetic field (linear mixture),
- the parameters do not vary in time with changing external factors, e.g. electrical, mechanical forces (non-parametric mixture),
- the randomly aligned spherical inclusions do not touch each other,
- the distance between neighboring inclusions is much larger than the radius of spheres,
- the inclusions are small with respect to the illumination wavelength,
- the conductive inclusions are concentrated with a density lower than that specified by the percolation threshold.

A schematic diagram of a typical composition with dielectric spheres, with permittivity ϵ_i, randomly embedded in the dielectric background host (environment), with permittivity ϵ_e, is shown in Fig. 2.7.

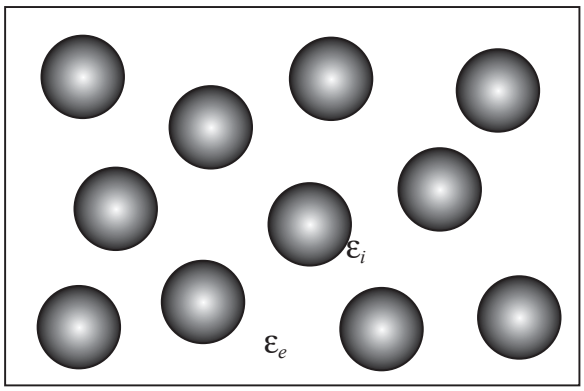

Figure 2.7: *Schematic diagram of the dielectric mixture with randomly distributed spherical inclusions embedded in a dielectric background environment.*

Assuming that the effective permittivity ϵ_{eff} of such a mixture relates the average electric field $\boldsymbol{E}$ with flux density $\boldsymbol{D}$ [55]

$$\boldsymbol{D} = \epsilon_{\text{eff}}\boldsymbol{E} \tag{2.26}$$

and weighting these values with the related inclusion volume fraction f

$$\boldsymbol{D} = f\epsilon_i\boldsymbol{E}_i + (1-f)\epsilon_e\boldsymbol{E}_e, \tag{2.27}$$

$$\boldsymbol{E} = f\boldsymbol{E}_i + (1-f)\boldsymbol{E}_e \tag{2.28}$$

where $\boldsymbol{E}_i$ is the internal field, $\boldsymbol{E}_e$ is the external field, and $\boldsymbol{E}_e$, ϵ_e are constant.
Further, from Eq. (2.26)-(2.28) the effective permittivity is

$$\epsilon_{\text{eff}} = \frac{f\epsilon_i A + \epsilon_e(1-f)}{fA + (1-f)} \tag{2.29}$$

where A relates the internal and external fields $\boldsymbol{E}_i = A\boldsymbol{E}_e$.
For the spherical inclusions, which by definition do not touch each other, and when the distance between neighboring inclusions is much larger than the radius of the sphere the ratio A is

$$A = \frac{3\epsilon_e}{\epsilon_i + 2\epsilon_e} \tag{2.30}$$

and the effective permittivity can be calculated from the Maxwell-Garnett mixing rule formulated below

$$\epsilon_{\text{eff}} = \epsilon_e + 3f\epsilon_e \frac{\epsilon_i - \epsilon_e}{\epsilon_i + 2\epsilon_e - f(\epsilon_i - \epsilon_e)}. \tag{2.31}$$

The effective permittivity does not depend on the radius of the inclusions as long as the radius is small with respect to the illumination wavelength. The geometrical size of the spheres can vary.

For the compound of the two dielectrics the effective permittivity calculated from Eq. (2.31) has to fall in between the following bounds [55, p. 153]

$$\epsilon_{\text{eff,max}} = f\epsilon_i + (1-f)\epsilon_e, \tag{2.32}$$

$$\epsilon_{\text{eff,min}} = \frac{\epsilon_i \epsilon_e}{f\epsilon_e + (1-f)\epsilon_i}. \tag{2.33}$$

These bounds are also called Wiener bounds [57, 55][2]. The upper limit for the effective permittivity $\epsilon_{\text{eff,max}}$ is defined for a layered material with boundaries between inclusions and host dielectric parallel to the field vector. The lower bound $\epsilon_{\text{eff,min}}$ is obtained for the case where the field vector is perpendicular to the boundaries between inclusions and host.

Since the Wiener bounds, Eq. (2.32) and Eq. (2.33), are defined for anisotropic mixtures, stricter bounds, Hashin-Shtrikman bounds [55, p. 153], have been defined for the statistically homogeneous, isotropic and three dimensional mixtures. The upper and the lower bounds are as follows

$$\epsilon_{\text{eff,max}} = \epsilon_i + \frac{1-f}{\frac{1}{\epsilon_e - \epsilon_i} + \frac{f}{3\epsilon_i}}, \tag{2.34}$$

$$\epsilon_{\text{eff,min}} = \epsilon_e + \frac{f}{\frac{1}{\epsilon_i - \epsilon_e} + \frac{1-f}{3\epsilon_e}}. \tag{2.35}$$

where it is assumed that $\epsilon_i > \epsilon_e$.
The lower limit corresponds to the Maxwell-Garnett mixing rule whereas the upper limit is the Maxwell-Garnett rule for the complementary mixture obtained by transferring the constituents: $\epsilon_i \to \epsilon_e$, $\epsilon_e \to \epsilon_i$, $f \to 1-f$.

[2]Note that the original paper [57] is in German

2.6.2 Selection of Mixing Rule

In the literature, many different mixing rules have been proposed to describe the effective properties of different types of mixtures [55]. Most of the current studies based on numerical analysis of 2-D and 3-D structures with two constituents show that the effective properties of the mixture strongly depend on the inclusion volume fraction, its geometrical profile, and spatial orientation in periodic or random arrangements [58, 59]. The contrast between the permittivity and conductivity of the host material and inclusions determine the complex effective permittivity, which in turn depends on the shape of the inclusions [60]. Hence, such a composite allows the designer to tune as well as control the physical properties by varying the size and shape of the inclusions. Since the mixtures with rounded shape inclusions, such as spherical, ellipsoidal or rodlike shapes, have been studied by many researchers and to some extent the mathematical formulas for the effective properties calculation have been defined [55]. The effective properties of the metal-dielectric mixtures [46, 47] or lossy composite materials [61, 55] have been explored mainly in terms of inclusions with round corners [47]. In contrast, the composites with sharp corners have not been as thoroughly investigated [59, 62, 63]. Studies of the effect of randomly and periodically arranged square inclusions in host media showed that for the case of having low contrast between the two mixed media the effective permittivity is not affected by the inclusions' distribution. Whereas for composites with high contrast between constituents the disorder and concentration of the particles strongly differentiate the effective properties of the mixture [59]. Since the classical mixing rules need to be used carefully when the initial conditions are not fully satisfied, in many cases the most appropriate analysis for cubical inclusions are full numerical calculations. The numerical calculations can then be explained by the classical mixing rules scaled by an appropriate constant value fitted to the particular type of studied composites [62, 64, 65, 66].

In [65] Karkkainen *et al.* used the fitting method to define an empirical mixing model that has been validated for the analysis of random dielectric mixtures. The created model was based on numerical results obtained from simulations for a range of mixture of two dielectrics with two different types of configuration. First, where the inclusion permittivity was higher than the host permittivity $\epsilon_i > \epsilon_e$ (so-called 'raisin pudding' mixture), and the second covering the case when $\epsilon_i < \epsilon_e$ (so-called 'Swiss cheese' mixture). The v-model [55, p. 172] was used to build the representation of studied structures. The key advantage of the v-model is that it unifies three widely used mix-

ing models: the Maxwell-Garnett rule, which is the most relevant to this work, and two other related models - Bruggeman rule and Coherent Potential. All three models are described in reference [55]. The v-model is defined for mixtures with isotropic spherical inclusions of permittivity ϵ_i immersed in an isotropic environment ϵ_e and given by

$$\frac{\epsilon_{\text{eff}} - \epsilon_e}{\epsilon_{\text{eff}} + \epsilon_e + v(\epsilon_{\text{eff}} - \epsilon_e)} = f\frac{\epsilon_i - \epsilon_e}{\epsilon_i + \epsilon_e + v(\epsilon_{\text{eff}} - \epsilon_e)}. \tag{2.36}$$

The Maxwell-Garnett rule is obtained for $v = 0$, the value $v = 1$ gives the Bruggeman rule, and for $v = 2$ the Coherent Potential approximation is formulated. Since the Maxwell-Garnett mixing rule has already been introduced in a previous Subsection, a brief presentation of the two other rules is given below.

The Bruggemen rule [55, p. 161] assumes absolute equality between the constituents constructing the mixture. Hence the difference between environment and inclusions is neglected and the homogenised medium is treated as background with respect to which the polarisations in terms of the environment and inclusions are measured. Further, it considers the inclusions and the environment symmetrically, thus mixtures with transfered material properties ($\epsilon_i \to \epsilon_e,\ \epsilon_e \to \epsilon_i,\ f \to 1 - f$) have the same effective permittivity.

The Coherent Potential formula [55, p. 163] is based on Green's function for the field in the mixture, seen as an effective medium, without considering the inclusions and environment separately.

The parameter v can be set to other values, hence defining new mixing models. In [65] the empirical mixing model was defined fulfilling the two dimensional parameter space by varying the inclusion volume fraction and the permittivity contrast calculated as the ratio ϵ_i/ϵ_e.

The Maxwell-Garnett mixing rule will be of main interest in the presented work. Focus on this particular mixing formula is motivated by the fact that the Maxwell-Garnett mixing rule gives a qualitatively correct prediction of the effective properties of a composite with conducting inclusions (e.g. metallic) [55, p. 80]. The other reason for the interest in the Maxwell-Garnett rule is that, for the case of having a dilute mixture with inclusions separated from each other and satisfying the condition $\epsilon_i > \epsilon_e$, this formula gives a good enough approximation to the effective permittivity [65]. At one end of the range of the considered fill factors in the interconnect grating structure the dilute mixtures ($f < 0.3$) are included. As shown in Fig. 2.8, the Bruggemen model does not

approximate the numerical data very well and it would appear that it gets even worse as the fill factor increases beyond $f = 0.3$.

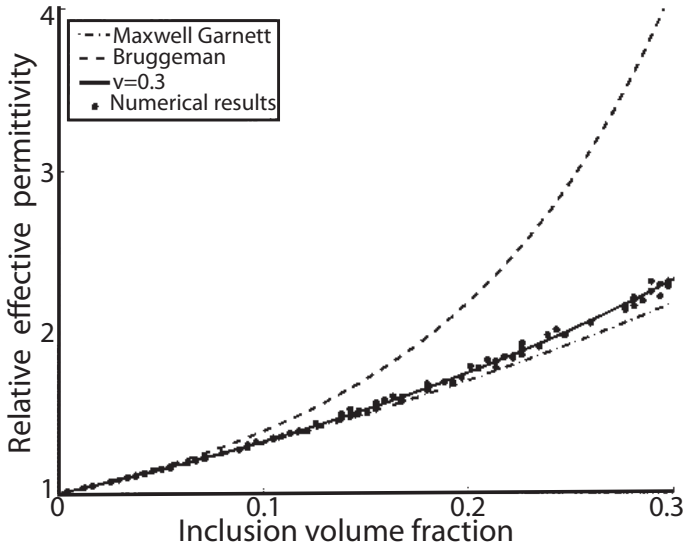

Figure 2.8: *Mixing models are plotted with numerical results for the mixture with permittivity contrast $\epsilon_i/\epsilon_e = 51$ without clustering (reproduced from Karkkainen et al., Fig. 9).*

2.7 Summary

This Chapter has provided coverage of the background material relating to the interconnects analysis investigated in this Thesis. A brief description of artificial dielectrics and metamaterials has been presented along with the effective medium theory. The formulation of the effective medium theory defined by Rytov for the periodic laminated structure and explored by other researchers has been reported. An overview of the related work where the modified classical mixing rules were used to define the effective properties of a mixture with constituents specific to the analysed problems, was presented. An evaluation of the accuracy of the various mixing rules when dealing with structures having parameters similar to on-chip interconnects indicates that the Maxwell-Garnett rule (or a modified form of it) is most likely to yield a suitable effective medium theory for interconnects.

Chapter 3

Interconnects Simulation

3.1 Introduction

There are many practical engineering problems involving the analysis of the electromagnetic behavior inside a system which require the solution of Maxwell's equations. However, for many problems obtaining the exact solution is a hard if not impossible task. These difficulties may be ascribed to the complexity of the problem itself or to the issues in defining the boundaries and initial conditions. Nevertheless, the available numerical techniques, implemented either in commercial software or by the user, give the possibility of computing the solution with good accuracy. An advantage of the analytical solution over a numerical algorithm is that it demonstrates an understanding of the physics of the problem whereas a numerical model can produce highly detailed and accurate field data without necessarily enhancing the users understanding of the operation of the system. Nonetheless, numerical methods are extremely valuable, particularly when it is desirable to simulate complex structures that do not readily yield to analytical methods. Often, numerical methods begin by developing a discrete mesh representing the geometry of interest. Hence, the first initiative operation, known as discretization, for any numerical method is based on dividing the domain of interest into a number of subsections and mesh points (nodes).

This Chapter presents a review of the analysis and numerical methods used in generating the data that underpin the effective medium models presented in this Thesis. A brief description of the boundary conditions used in the models is also presented. The Chapter includes the validation of presented techniques against analytical calculations of the reflection and transmission coefficients for a canonical structure.

3.2 Review of Analysis and Simulation Techniques

This Section reviews three widely used numerical methods for solving periodic structures in terms of electromagnetic phenomena. Namely, finite difference time domain method (FDTD), finite element method (FEM), and rigorous coupled wave analysis (RCWA). The analytical technique applicable to the solution of wave equations propagating through a planar stratified medium, the characteristic matrix method, is presented first.

3.2.1 Characteristic Matrix Method

The characteristic matrix method is a straightforward analytical technique used for the solution of wave equations in the case of a plane wave incident on a stack of films (multilayered structure) placed between planar, homogeneous regions. It is assumed that the stack of dielectrics is normal to the z-axis, the direction of propagation, and that the field within one layer can be characterised by a superposition of a forward and backward traveling wave with magnitudes E_f, E_b respectively, and propagation constant k defined in the medium on both sides of the interface k_f and k_b respectively,

$$E(z) = E_f e^{-\mathrm{j}k_f z} + E_b e^{\mathrm{j}k_b z}. \tag{3.1}$$

The optical properties of a plane, time-harmonic electromagnetic wave (monochromatic wave) propagating through a stratified medium, can be fully described by a 2×2 matrix $\boldsymbol{M}$ [49, p. 61]. Matrix $\boldsymbol{M}$ is called the characteristic matrix of the stratified medium and expresses the relationship between the electric and magnetic fields propagating through an individual layer. The matrix is formulated as

$$\boldsymbol{M}(h) = \begin{bmatrix} \cos\beta & -\frac{\mathrm{j}}{p}\sin\beta \\ -\mathrm{j}p\sin\beta & \cos\beta \end{bmatrix} \tag{3.2}$$

where $\beta = k_0 n h \cos\theta$, $k_0 = 2\pi/\lambda_0$ is the propagation constant calculated for the free-space wavelength λ_0, $n = \sqrt{\epsilon\mu}$ is the dielectric refractive index of the layer and $\epsilon = \epsilon_0\epsilon_r$ is the material permittivity ($\epsilon_0 = 8.85 \times 10^{-12}\,\mathrm{Fm}^{-1}$ - permittivity of vacuum, ϵ_r - permittivity of medium), $\mu = \mu_0\mu_r$ is the permeability ($\mu_0 = 4\pi 10^{-7}\,\mathrm{Hm}^{-1}$ - permeability of vacuum, μ_r - permeability of medium), h denotes the thickness of the layer, θ is the angle between the direction of propagation of the wave and the z-axis, and $\mathrm{j} = \sqrt{-1}$ denotes an imaginary number.

A schematic diagram of the propagation of an electromagnetic wave through a system with a dielectric medium interfaced between two other media is depicted in Fig. 3.1, where n_1, n_2, n_3 are the refractive indices of the three media, h stands for the thickness of the dielectric layer, and θ, θ_r, θ_t are the angles of incident, reflected and transmitted wave, respectively.

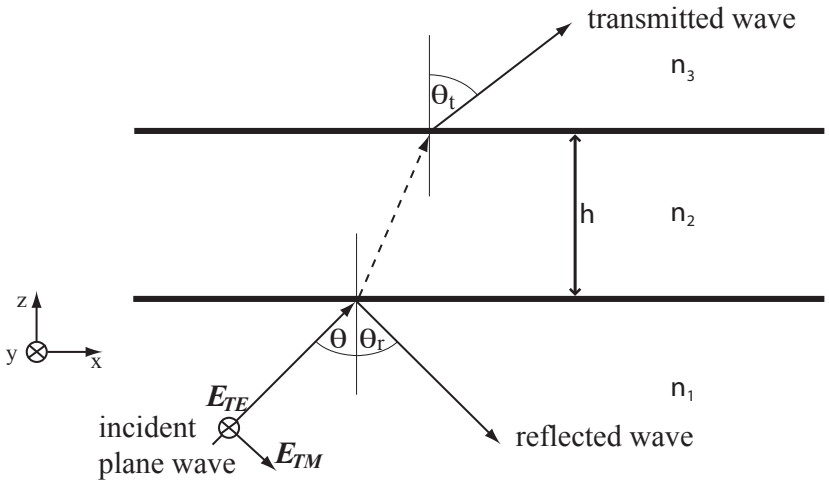

Figure 3.1: *Propagation of an electromagnetic wave through a homogeneous layer.*

The characteristic matrix formulated by Eq. (3.2) can be applied to the analysis of the two special cases of linearly polarised illumination wave. For the transverse electric wave (TE) with electric vector perpendicular to the plane of incidence the factor p is defined

$$p_{TE} = \sqrt{\frac{\epsilon}{\mu}} \cos\theta, \tag{3.3}$$

whereas for the transverse magnetic wave (TM) with magnetic vector perpendicular to the plane of incidence

$$p_{TM} = \sqrt{\frac{\mu}{\epsilon}} \cos\theta. \tag{3.4}$$

The stratified medium composed of m homogeneous layers can be described by the characteristic matrix of the complete system obtained by multiplication of the characteristic matrices of each layer $\boldsymbol{M}_i$, where $i = 1, 2, \ldots, m$ and denotes the succession of stratified media from the first to the last layer and is defined by

$$\boldsymbol{M} = \prod_{i=1}^{m} \boldsymbol{M}_i. \tag{3.5}$$

The reflection r and transmission t coefficients of the layered system is related to the elements of the matrix $\boldsymbol{M}$ by

$$r = \frac{(m_{11} + m_{12}p_l)\, p_1 - (m_{21} + m_{22}p_l)}{(m_{11} + m_{12}p_l)\, p_1 + (m_{21} + m_{22}p_l)}, \tag{3.6}$$

$$t = \frac{2p_1}{(m_{11} + m_{12}p_l)\, p_1 + (m_{21} + m_{22}p_l)}, \tag{3.7}$$

where p_1, p_l are the values calculated for the first and the last medium through which the wave propagates.

The reflectivity and transmissivity are calculated in terms of the complex r and t

$$R = |r|^2, \tag{3.8}$$

$$T = \frac{p_l}{p_1} |t|^2. \tag{3.9}$$

The phase change on reflection ϕ refers to the first surface of discontinuity and is expressed in the form

$$\phi = \arctan\left(\frac{\mathrm{Im}(r)}{\mathrm{Re}(r)}\right). \tag{3.10}$$

Here, it is assumed that each of the layers comprising the structure is of a nonmagnetic dielectric material, hence the relative permeability of the medium is $\mu_r = 1$.

The reflection coefficient is the ratio of the electric field magnitude of the reflected wave $\boldsymbol{E}_r$ to the magnitude of the incident wave $\boldsymbol{E}_0$

$$r = \frac{\mathbf{E}_r}{\mathbf{E}_0}. \tag{3.11}$$

Similarly, transmission coefficient is defined as the ratio of the electric field magnitude of the transmitted wave $\boldsymbol{E}_t$ to the magnitude of the incident wave $\boldsymbol{E}_0$

$$t = \frac{\mathbf{E}_t}{\mathbf{E}_0}. \tag{3.12}$$

3.2.2 Finite Difference Time Domain

The finite difference time domain (FDTD) method is a popular computational technique for the full wave analysis of electromagnetic phenomena [67]. It offers many advantages because of the simplicity of the algorithm both in conception and in terms

of implementation. The FDTD method solves the electromagnetic field simultaneously with respect to space domain and time variations and provides a useful tool for the visualization of physical interactions present in an analysed structure. Even though the FDTD method can solve complicated problems it is generally computationally expensive due to the large memory requirement and long computational time.

The standard FDTD algorithm solves Maxwell's two curl equations (Faraday's and Ampere's laws) in the time domain

$$\nabla \times \boldsymbol{E} = -\mu \frac{\partial \boldsymbol{H}}{\partial \boldsymbol{t}}, \tag{3.13}$$

$$\nabla \times \boldsymbol{H} = \sigma \boldsymbol{E} + \epsilon \frac{\partial \boldsymbol{E}}{\partial \boldsymbol{t}}, \tag{3.14}$$

and is based on central difference approximations.
The first electromagnetic FDTD algorithm was proposed by Kane Yee in 1966 [68]. That algorithm employs the first order central difference approximations of the temporal and spatial derivatives of Maxwell's curl equations and gives second order accuracy. The space derivatives can be expressed as

$$\frac{\partial A^n(i,j,k)}{\partial x} = \frac{A^n(i+1/2,j,k) - A^n(i-1/2,j,k)}{\Delta x} + O(\Delta x^2) \tag{3.15}$$

and the time derivative is indicated as

$$\frac{\partial A^n(i,j,k)}{\partial t} = \frac{A^{n+1/2}(i,j,k) - A^{n-1/2}(i,j,k)}{\Delta t} + O(\Delta t^2), \tag{3.16}$$

where the space point in the rectangular grid is $(i,j,k) = (i\Delta x, j\Delta y, k\Delta z)$, any function of time and space is defined as $A^n(i,j,k) = A(i\Delta x, j\Delta y, k\Delta z, n\Delta t)$, Δx, Δy, Δz are the grid space increments in x, y, z Cartesian coordinate directions, Δt is the time increment and i, j, k, n are integers.
Applying these approximations to Eq. (3.13)-(3.14) for each electric and magnetic field component an explicit update scheme can be derived. The simulation domain is discretized with respect to space and time and the electric and magnetic fields are therefore staggered both in space and time. As the lattices are offset by a half grid in all dimensions the solution of the difference equations for the 'future' fields is calculated in terms of the 'past' field. Namely, the field solution at time $(n+1/2)\Delta t$ is obtained in terms of field at time $n\Delta t$ or $(n-1/2)\Delta t$. Such evaluation of the field at alternate half

time steps is known as a leap-frog manner.
An exemplar update expression for the E_x field component is as follows

$$\begin{aligned} E_x^n(i+1/2,j,k) &= E_x^{n-1}(i+1/2,j,k) \\ &+ \frac{\Delta t}{\epsilon \Delta y}\left[H_z^{n-1/2}(i+1/2,j+1/2,k) - H_z^{n-1/2}(i+1/2,j-1/2,k)\right] \\ &+ \frac{\Delta t}{\epsilon \Delta z}\left[H_y^{n-1/2}(i+1/2,j,k+1/2) - H_y^{n-1/2}(i+1/2,j,k-1/2)\right]. \end{aligned} \tag{3.17}$$

The cell size and the time step are the two main factors which determine the accuracy and computational time for the problem being solved although the boundary conditions need to be chosen with caution. The size of the cell must be small enough to accurately represent the simulated problem at the highest frequency of interest. A rule often applied is

$$\Delta x \leq \lambda_n/10 \tag{3.18}$$

where Δx is the size of the cubic grid ($\Delta x = \Delta y = \Delta z$) and λ_n is the smallest wavelength at given frequency in entire simulated domain. Hence, λ_n is the length of the wave propagated through the media with the highest refractive index in the domain ($\lambda_n = \lambda_0/n_{\text{max}}$, where λ_0 is the free-space wavelength at the highest frequency of interest). The maximum size of the time step is determined by two factors. Firstly, the electromagnetic wave cannot propagate in free-space faster than the speed of light. Secondly, the wave cannot propagate between any two nodes faster than the equations are updated. The criterion is set by the Courant-Friedrichs-Lewy (CFL) constraint [69, 67]

$$\Delta t \leq \frac{\Delta x}{\sqrt{n} \cdot c_0} \tag{3.19}$$

where n is the dimension of the simulation and c_0 is the speed of light. This constraint is valid under the assumption that the space increment in each direction of the domain is equal and is easily modified for the case of non-cubic mesh cells.

The two types of boundary conditions used in this Thesis are the perfect matched layer (PML) and periodic boundary conditions. The PML is defined as an artificial, anisotropic material used in order to truncate the computational region. For the FDTD simulation domain the requirement for the thickness of the absorbing layer is $4 - 16$ nodes (here 10 nodes were used). The distance between the nearest material interface and PML surface needs to be at least half of the wavelength for the lowest frequency of interest, as the performance of this implementation of PML is not predictable in the presence of evanescent fields.

The periodic boundary condition (PBC) allows for the reduction of an infinite or repeating geometry to a single unit cell size. This boundary is useful for grating structures which, from their definition, are periodic. In the software available in this study, TEMPEST FDTD Electromagnetic Simulation Program (University of California, Berkeley), the PBC are defined as default boundaries on all six sides of the computational domain. The metal part of the simulation domain was defined as a perfect electric conductor (PEC). The electric and magnetic fields are equal to zero inside a geometry with material specified as PEC. This material can also be used as a boundary condition in structures where the total reflection is required.

Here the FDTD method was used for the analysis of grating structures. The reflection and transmission coefficients were extracted from the steady state field values.

3.2.3 Rigorous Coupled Wave Analysis

The rigorous coupled wave analysis (RCWA) was initially formulated by M. G. Moharam and T. K. Gaylord [70, 71] for the analysis of electromagnetic wave diffraction by periodic structures. It is an exact and at the same time straightforward, noniterative and deterministic method for solving Maxwell's equations. The technique can be succesfully applied to the analysis of both holographic and surface-relief grating structures such as those which can be found in an interconnect stack.

The algorithm is implemented over a domain which is divided into three parts: a grating layer located between two semi-infinite regions called the superstrate and substrate. For the surface-relief gratings the grating region is defined as a stack of binary layers (gratings with rectangular profile). Also, gratings with continuous profile can be analysed by this method. Then the procedure for approximating the continuous profile by a number of sufficiently thin binary layers needs to be employed. The construction of the binary geometry performed by the commercial software GSolver for a given grating is illustrated in Fig. 3.2.

In the RCWA algorithm the permittivity profile in the grating region is expanded in a Fourier series. Then the field is calculated by solving the wave equation in each of the three regions and matching the tangential electric and magnetic fields at the two boundaries to satisfy the continuity requirement. The boundary conditions are applied

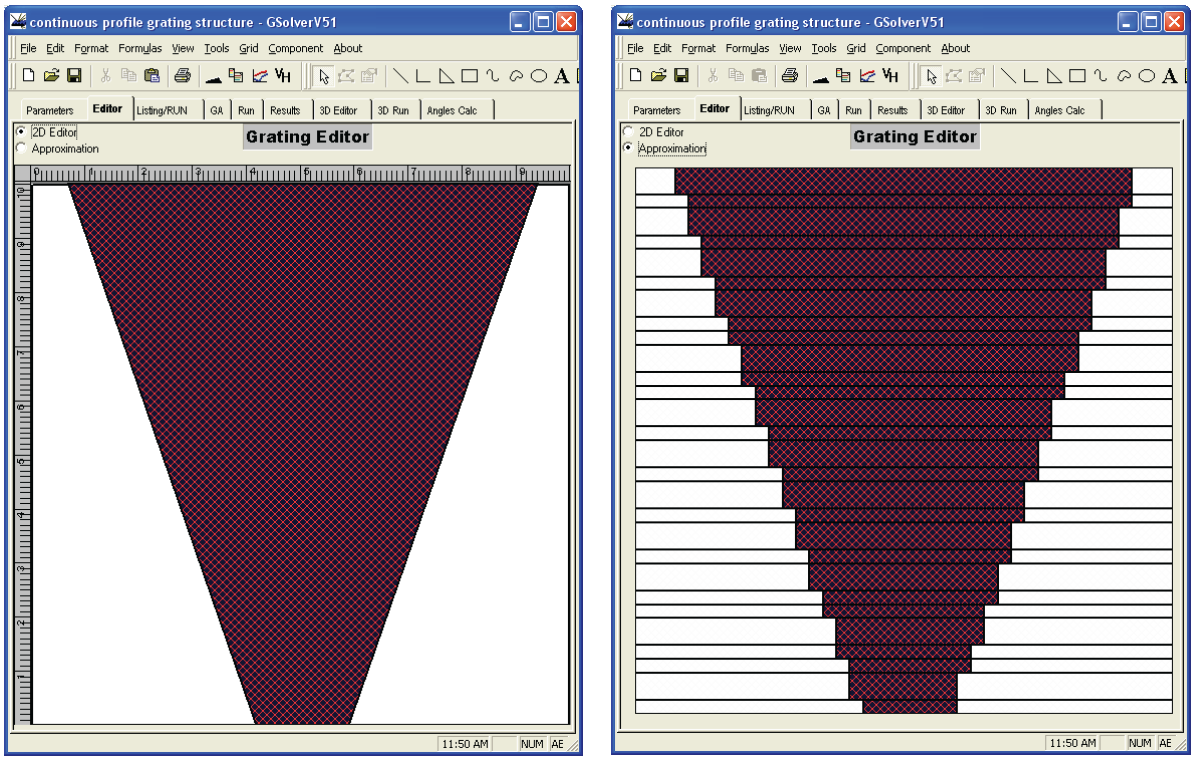

(a) *2-D model* (b) *Binary approximation*

Figure 3.2: *The GSolver V5.1 user interface (a) 2-D grating structure editor, (b) continuous profile approximation.*

successively in the input region, where the backward-diffracted waves exist, between the individual grating layers, and finally in the output region, where the forward-diffracted waves are present. Employing this algorithm, the reflected and transmitted diffracted field amplitudes and the diffraction efficiencies are obtained. This technique always involves the zero diffracted order in the calculations therefore it can be successfully applied to the analysis of subwavelength gratings.

The accuracy of the solution depends on the number of terms retained in the calculations satisfying the criterion of energy conservation. For each propagating order some evanescent orders need to be retained. For 1-D metallic gratings the convergence rate is slow for the TM polarisation [72] which is of the main interest in the presented work. In the case of metallic gratings the field is more rapidly varying and the higher order evanescent field magnitudes decay slowly. Hence, for a given propagated order more evanescent orders need to be retained.

This algorithm is particularly useful for the analysis of periodic structures for which there is no effective medium theory (EMT) defined. Since it is an accurate and efficient method it was the one which was mainly used in this work for the purpose of generating the numerical data for defining the empirical models presented in Chapter 4. Although the analysis was based on studying the metal-dielectric gratings (lossy gratings) illuminated by a plane wave with TM polarisation where up to 70 orders had to be retained in the calculations, it was still a less time consuming algorithm compared with others which were available to the author. The commercially available software GSolver, developed by David Fluckiger of the Grating Solver Development Company [73], which implement the RCWA technique was used.

The energy (E) of a photon is defined as the product of reduced Planck's constant ($\hbar = \frac{h}{2\pi}, h = 6.62606896 \times 10^{-34}$ [$J \cdot s$]) and the angular frequency (ω) of the associated electromagnetic wave

$$E = \hbar\omega \ \ [J]. \tag{3.20}$$

The metal parts in the unit cell of the simulation domain were defined by frequency dependent dielectric function expressed by a Drude model [74][55, p. 201]

$$\epsilon(\omega) = 1 - \frac{\omega_p^2}{\omega(\omega + \mathrm{j}\gamma)}, \tag{3.21}$$

where $\hbar\omega$ is the energy given in electron volts related to the free-space wavelength λ_0 by $\hbar\omega = \frac{1240\times10^{-9}}{\lambda_0}$ [eV] ($1\,eV = 1.60217653 \times 10^{-19}$ [J]), $\hbar\gamma$ is the damping term representing dissipation of the plasmon's energy into the system, and ω_p is the plasma frequency

$$\omega_p = \sqrt{\frac{n_d e^2}{\epsilon_0 m_e}} \ \left[\frac{rad}{s}\right], \tag{3.22}$$

where n_d is the electron density, e is the electric charge, ϵ_0 is the permittivity of free-space and m_e is the mass of an electron.
Despite wide spread use of copper interconnects for the lower levels of interconnect stacks, aluminum is often used for the global wiring, which are of the main concern in this work, and has $\hbar\omega_p = 15$ [eV] and $\hbar\gamma = 0.1$ [eV] [74].

3.2.4 Finite Element Method

Finite element method (FEM) is the second, after finite difference method, most commonly used numerical method for solving electromagnetic phenomena within com-

plex geometries or complex boundary conditions [75, 76]. This technique uses integral equations rather than difference equations, as for the case of FDTD method, to create a system of algebraic equations. The finite element analysis discretizes the solution domain by subdividing the problem into nodes and tetrahedral elements and allows arbitrary 3-D geometries to be meshed. This method enables the enhancement of the mesh in locations with fine geometries without increasing the number of elements in volumes with coarse features. The mesh is iteratively refined by the FEM solver until the solution converges to an acceptable small difference. For electromagnetic problems in 3-D the following wave equation derived from Maxwell's equations is employed

$$\nabla \times \left(\frac{1}{\mu_r} \nabla \times \boldsymbol{E}(x, y, z) \right) - k_0^2 \epsilon_r \boldsymbol{E}(x, y, z) = 0 \tag{3.23}$$

where $\mathbf{E}(x, y, z)$ is the complex electric field within the simulation domain, ϵ_r is the position dependent complex relative permittivity, μ_r is the position dependent complex relative permeability and k_0 is the free-space wavenumber $\omega\sqrt{\epsilon_0 \mu_0}$ where $\omega = 2\pi\nu$ is the angular frequency and ν is the frequency.

The commercial software High Frequency Structure Simulator (HFSS) [77] which utilizes a 3-D full-wave FEM was used to perform the simulations and analysis of the microstrip prototype structure as well as for the validation of the analyses of periodic grating structures performed by the FDTD and RCWA methods.

Four types of boundary conditions were used in the FEM models: radiation boundary, PML, master-slave boundary, and symmetry boundary. The radiation boundary enables the wave to radiate infinitely far into space and it is assigned to an air or vacuum box. The minimum distance between the radiating structure and the boundary should be equal to one quarter of a wavelength of the lowest frequency of interest. The perfect matched layer (PML) is an artificial absorbing layer which absorbs the waves exiting the computational domain with minimal reflection. The PML layer can be defined at the distance of at least one tenth of the longest wavelength of interest from the radiating geometry. The master-slave boundaries enable the modelling of periodic structures with infinite extent. These boundaries enforce the electric field on one surface (slave boundary) to match the electric field at each corresponding point on the other surface (master boundary) to within a phase difference. The only constraint is that the fields on the two boundaries need to have the same magnitudes and the same or opposite direction. The electric field does not have to be tangential or normal to these boundaries.

Finally, the symmetry boundary can reduce the size and complexity of the modelled structure by only requiring part of the structure to be simulated . Therefore the computational time is also minimized. The symmetry boundaries are defined as perfect E when the electric field is normal to the symmetry plane or perfect H in the case of electric field being tangential to the symmetry plane.

3.3 Validating FDTD, RCWA and FEM against Analytical Method

In this Section the three numerical methods reviewed in Section 3.2, namely FDTD, RCWA and FEM are validated against the analytical technique. For this purpose, the simple structure of a solid silicon slab (etalon) surrounded by infinite half-spaces of air was modelled in each of the simulators. The reflection and transmission coefficients were extracted from the numerical data and compared with analytical calculations obtained from the characteristic matrix method. The space increment in FDTD simulations was set to $5\,\mu$m in all directions. For the FEM calculations the mesh operations were restricted to the maximum length of tetrahedral edge which was set to $5\,\mu$m. The good agreement amongst those numerical methods and the analytical approach is illustrated in Fig. 3.3 for a range of depths 0 (free-space only) to $200\,\mu$m, with the agreement for reflection coefficient calculations in Fig. 3.3(a) and the transmission coefficient in Fig. 3.3(b).

The error in the reflection coefficient calculated from numerical solutions when compared with the analytical method is within 0.05% for FDTD and RCWA algorithms and less than 2% for FEM, shown in Fig. 3.3(c). Similar error is obtained for the transmission coefficient calculations, as is illustrated in Fig. 3.3(d), where the FEM gives error lower than 1.1%. Such good agreement amongst these techniques gives confidence in using any one of them in the further analysis presented in this Thesis. The FEM has a larger error which does not decrease with the tightening of the convergence criteria. Therefore, the difference can be attributed to either a small change in the effective size of the slab during the mesh process or to a possible small difference in the performance of the applied boundary conditions.

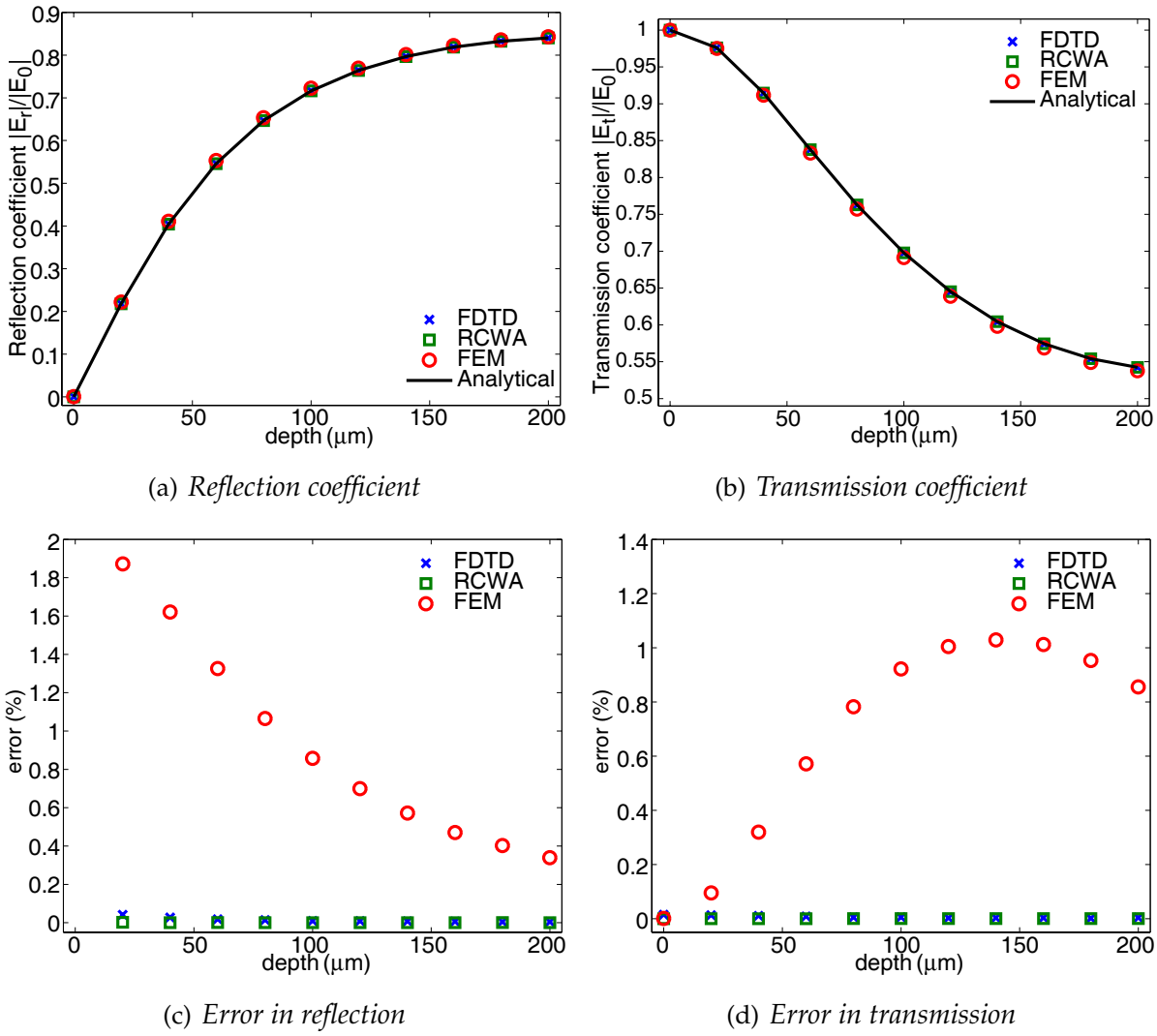

(a) *Reflection coefficient*

(b) *Transmission coefficient*

(c) *Error in reflection*

(d) *Error in transmission*

Figure 3.3: *The magnitude of the (a) reflection and (b) transmission coefficients of a solid silicon etalon surrounded by air calculated by FDTD, RCWA, FEM and characteristic matrix method. The error in: (c) reflection and (d) transmission coefficients calculated for each numerical method relative to the analytical method.*

Error Calculation

The error between two values a and b is calculated from the formula

$$error = \frac{|a-b|}{b} \cdot 100 \quad [\%], \tag{3.24}$$

where a is the first value mention in the text and b is the second. This formula was used throughout this Thesis to calculate relative errors between data sets.

3.4 Summary

A brief review of the analytical method for calculation of the reflection and transmission coefficients of stratified medium and the three numerical techniques: FDTD, RCWA, and FEM, have been presented. Further, the validation of these techniques against the analytical formulation showed that each of the presented algorithms can be used succesfully in the analysis of periodic structures. The FDTD and RCWA calculations of the reflection and transmission coefficients are equally accurate with a minimal error of 0.05% whereas the FEM performs with an acceptable error of 2%.

Chapter 4

Canonical Structure

4.1 Introduction

In this Chapter a detailed study of the reflection and the transmission characteristics of a single layer of interconnects is presented. The analysis is concluded with three empirical models each defined for a canonical structure based on the grating structure of interest. The geometry of the grating structure, which is equivalent to the interconnect arrangement in an IC, along with the homogenisation approach is described in detail. The empirical models are formulated in terms of a modified Maxwell-Garnett mixing rule. The first two models, which correspond to typical on-chip signals [8], are defined for frequency range ($1 - 10\,\text{GHz}$) and the third for emerging applications at higher frequencies including Industrial, Scientific and Medical (ISM) bands in the range ($30 - 200\,\text{GHz}$) [78, 79, 80]. Each model is validated by a comparison of the magnitude of the reflection and transmission coefficients obtained from numerical simulations for the detailed structure against those predicted by the empirical models. It is demonstrated that the presented empirical models are well within the theoretical Wiener bounds. The validity of the canonical structure over a range of tapered metallic inclusions and angles of incidence is discussed. It is also illustrated that, for the low frequency empirical model, the distribution of the values of scaling factor Ψ have a trend similar to those presented in the literature where different mixtures and mixing models are used, although those models could not be used in place of the ones developed here.

4.2 Method

The Maxwell-Garnett mixing rule relates the internal and external fields in a mixture containing spherical inclusions by the ratio A (Eq. 2.30), providing the assumptions stated in Subsection 2.6.1 are valid. The interconnect structure is characterised by distant rectangular (sharp corners) inclusions embedded in dielectric. The inclusion dimensions are much smaller than the wavelength of the signal propagated along the wire. In order to account for the difference in geometry between the inclusions originally considered by Maxwell-Garnett and those studied in this Thesis the approach will be based on introducing an additional scaling factor. Since a typical interconnect stack can be perceived as a mixture with background host ϵ_e being a lossless dielectric and the rectangular interconnects ϵ_i being lossy and conductive metallic inclusions distributed in periodical arrangement. Therefore, it is plausible that the internal and external fields in the developed mixture are also related to each other. This relation is different to that of the spherical inclusions. However, for the subwavelength interconnect structure it is expected that this difference can be accounted for by modifying the ratio A. To denote the modified ratio, symbol Ψ is introduced, giving the modified Maxwell-Garnett mixing rule as

$$\epsilon_{\text{eff}} = \epsilon_e + \Psi f \epsilon_e \frac{\epsilon_i - \epsilon_e}{\epsilon_i + 2\epsilon_e - f(\epsilon_i - \epsilon_e)}. \tag{4.1}$$

where f is the metal volume fraction.

It is expected that Ψ will be sensitive to the precise geometry of the structure so the problem becomes the determination of Ψ as a function of the parameters to which it is sensitive. The first step in determining the parameter space was to make sure that the full range of typical interconnect structures are covered. The details of these structures were described in Section 1.1.1 and are restated here in terms of the parameter space to be explored in this Thesis. Specifically, the change in interconnects separation is defined by the range of considered metal volume fractions in a unit cell and the geometry of the inclusions is determined by the aspect ratio. Further, the dielectric properties of the background medium and the change in frequency of the illuminated plane wave are considered.

The concept of the homogenisation of a single layer of interconnect stack was investigated with the assumption that a series of interconnects are aligned in parallel in a periodic manner. The model was based on analysing the electromagnetic properties

of a grating structure with varying dimensions and material properties for sampled frequencies from considered bands. The grating dimension was defined by the aspect ratio (AR) in the range $AR_{min} \leq AR \leq 3$ and the metal fill factor from set $0.2 \leq f \leq 0.6$ where the minimum value of the aspect ratio (AR_{min}) for each f is presented in Table 4.1. The wide range of aspect ratios studied includes all likely structures defined in typical design rules [8].

f	AR_{min}	AR_{max}
0.2	0.6	3
0.3	0.4	3
0.4	0.4	3
0.5	0.2	3
0.6	0.2	3

Table 4.1: *The lower and upper limits put on the aspect ratio AR for the range of considered metal fill factors f.*

One of the approaches to improve the performance of interconnects in IC is based on introducing low-k dielectrics. Therefore, a wide range of dielectric materials is included in the study: as of the air-gap or ultra low-k materials ($\epsilon_r = 1$) up to silicon dielectric ($\epsilon_r = 11.7$). Since the dielectric permittivity ϵ of a material is related to the dielectric refractive index n by

$$n = \sqrt{\epsilon} \tag{4.2}$$

in the rest of the Thesis the range of considered dielectric backgrounds will be expressed in terms of the refractive index and will include $1 \leq n \leq 3.42$.

The representative frequencies for each of the considered bands are: $1\,\text{GHz}$, $3\,\text{GHz}$, $5\,\text{GHz}$, and $10\,\text{GHz}$ for the first band $(1 - 10\,\text{GHz})$; and $30\,\text{GHz}$, $60\,\text{GHz}$, $100\,\text{GHz}$, $150\,\text{GHz}$, and $200\,\text{GHz}$ for the second band $(30 - 200\,\text{GHz})$. The first band represents a selection of likely on-chip signal frequencies whereas the second band represents signals in ISM bands that chips are likely to be exposed to in the future applications although round figures have been chosen for the frequencies to maintain generality.

4.3 Description of Canonical Structure

The analysis presented here was performed using the RCWA algorithm implemented in GSolver [73] software for TM polarisation only. The TE polarisation has a very high reflectivity of illuminated wave from the grating structure, $R \approx 1$, and the analysis in terms of the modified Maxwell-Garnett mixing rule therefore has no purpose. Thus, the defined canonical structure is valid for grating excited by TM polarised plane wave and, as it will be discussed in due course, for a range of incident angles and grating profiles.

The canonical structure is illustrated in Fig. 4.1 with a diagram of the grating structure shown in Fig. 4.1(a) and its homogenised equivalent in Fig. 4.1(b).

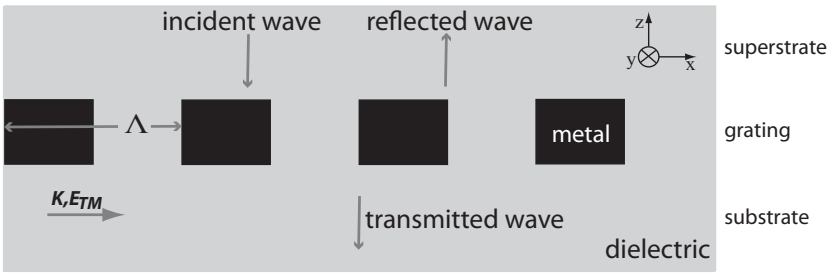

(a) *Grating structure*

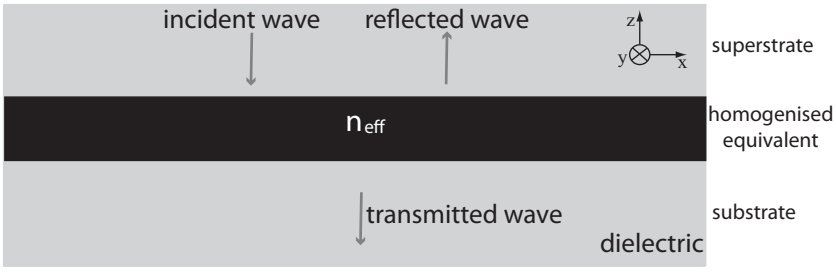

(b) *Homogenised structure*

Figure 4.1: *Canonical grating structure diagrams of (a) grating with period Λ, grating vector **K**, and TM electric field polarisation E_{TM}; (b) equivalent homogenised structure with n_{eff} calculated from modified Maxwell-Garnett mixing rule.*

The structural period Λ of the unit cell is made equal to $100\,\mu$m so that, for the set of considered frequencies, it was well into the deep subwavelength regime $(\Lambda \leq \lambda/4)$ [51]. The TM polarised electric field vector $\mathbf{E}_{TM}$ is parallel to the grating vector **K**. The incident plain wave propagates from the upper infinite half-plane, the reflected and

transmitted waves are also depicted.

4.4 Homogenisation Procedure

In this Section details of the homogenisation procedure are presented. In order to define the canonical structure a set of procedures is followed. Firstly, by using 'brute force' method and calculating reflection and transmission coefficients for a homogenised structure with broad set of n_{eff} values, it was found that it is valid to homogenise the grating structure. Secondly, a mixing model was found to predict the value of n_{eff} for a given structure so that the inefficient 'brute force' method is no longer required. Thirdly, a fitting procedure based on the least squares method (Appendix A) is used to estimate the value of coefficient Ψ and express it by an analytical formula so that the results of this study can be compactly expressed and efficiently communicated to potential users.

The initial approach to the homogenisation process is to calculate the reflection and transmission coefficients for a sample grating structure and compare them with those calculated for a homogeneous layer of the same depth but with a refractive index from a wide range of values. Since the homogenised grating contains a lossy conductive component (metal) the considered refractive indices are defined as a set of complex numbers obtained by averaging the indices of the constituents where the metallic part is defined as aluminum by the Drude model [74].

A diagram of the algorithm used for the 'brute force' fitting for a single structure is presented in Fig. 4.2. The fitting procedure was carried out separately for the estimation of reflection and transmission coefficients.

The algorithm is defined in the following steps. The initial input values are the parameters that define the grating geometry: aspect ratio AR, metal volume fraction f, grating period Λ; material properties of the host $n_e \cong n$ and inclusion n_i composites and frequency ν of the illumination wave. The background dielectric is characterised by its refractive index from the range $1 \leq n \leq 3.42$, whereas the inclusion material is defined as aluminum. The wide set of values within which the parameter Ψ varies is also specified. Then the Maxwell-Garnett mixing model is introduced and a range of effective refractive indices n_{eff} is calculated for all previously defined values of scaling

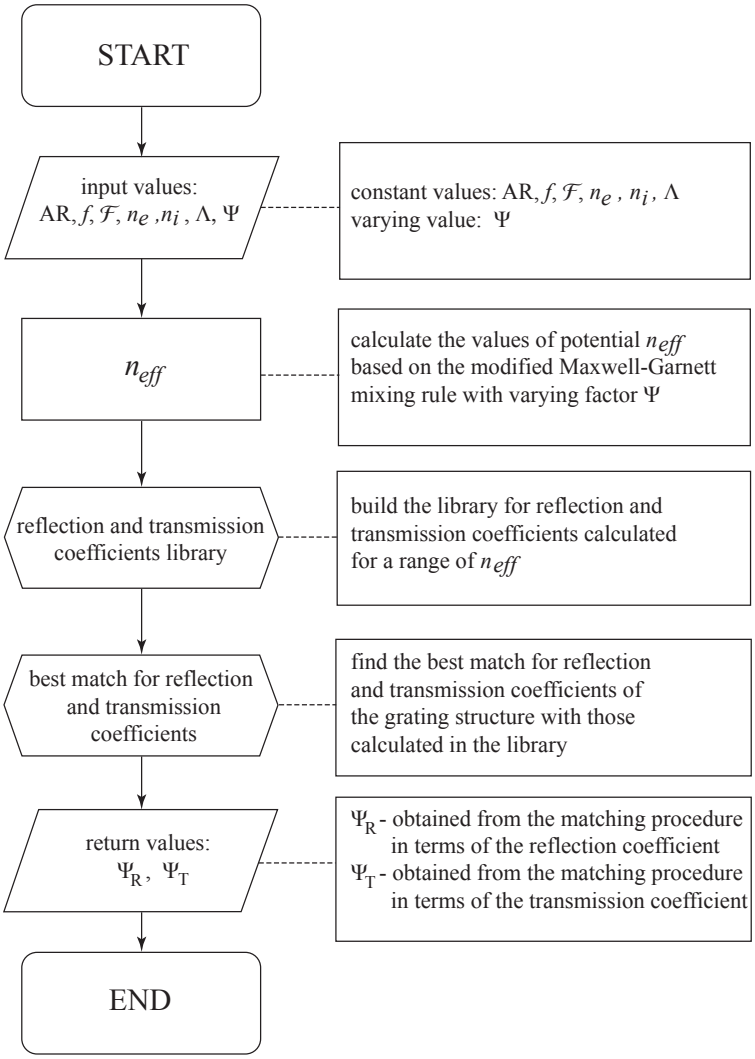

Figure 4.2: *Diagram representing fitting algorithm for a single grating structure. For the input values used to define a single grating structure algorithm returns the value of factors Ψ_R and Ψ_T calculated in terms of the reflection and transmission coefficients respectively.*

factor Ψ. Next, the reflection and transmission coefficients are calculated based on the characteristic matrix method (Section 3.2.1) for a system with dielectric medium characterised by n_{eff} value interface between two other infinite media. At this stage the library for the values of reflection and transmission coefficients for the corresponding homogenised equivalent structures is obtained. Finally, the best match for the reflection and transmission coefficients calculated for the detailed grating structure and the values stored in the library is found. The algorithm returns the values of the factor Ψ that give the best approximation in the homogenisation process. Since the algorithm

is applied separately but in parallel for the reflection and transmission coefficients, it gives two independent values Ψ_R and Ψ_T respectively.

This procedure shows that in the set of effective refractive indices there is one value for which the homogeneous layer gives the same response as the grating, as it is illustrated in Fig. 4.3. Nevertheless, it is shown in Fig. 4.3(a) and Fig. 4.3(b) that the best fit for reflection and transmission was obtained for different n_{eff}.

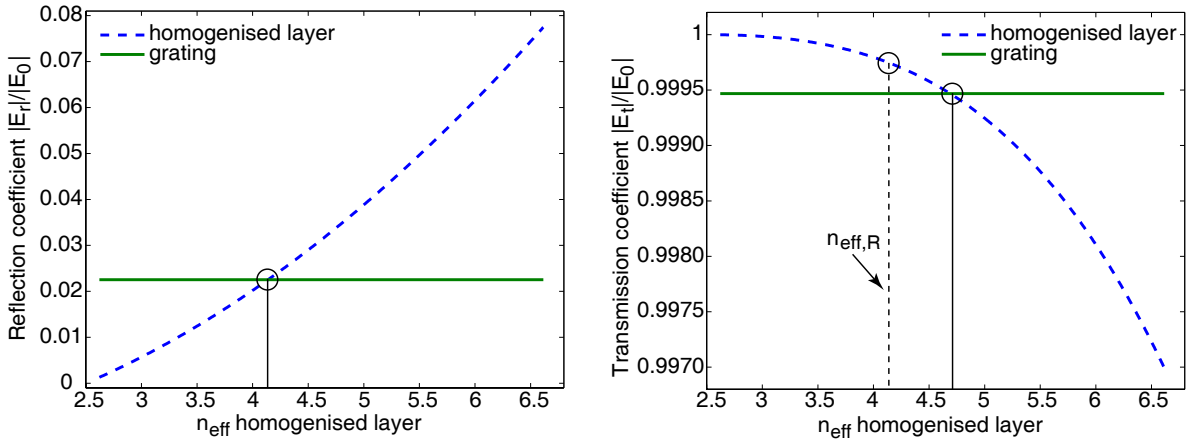

(a) *Reflection coefficient* (b) *Transmission coefficient*

Figure 4.3: *The magnitude of (a) the reflection and (b) transmission coefficients for a grating structure with grating parameters:* $f = 0.5$, $\Lambda = 100\,\mu m$, $AR = 2$, $n = 2.5$, $\nu = 5\,GHz$. *The effective refractive index of the grating can be found in the fitting process. Note that only the real part of the* n_{eff} *is presented.*

Due to the discrepancy in the values of n_{eff}, it was verified and is shown in Fig. 4.4, for sampled grating structure with metal fill $f = 0.4$ and dielectric constant $n = 2$, that the related scaling factors Ψ_R and Ψ_T obtained for reflection and transmission coefficients converge with increase of the applied frequency within $1\,$GHz to $200\,$GHz.
Further, it was confirmed that for both reflection and transmission coefficients estimation scaling factor Ψ_R can be used. A comparison between reflection coefficients calculated for grating structure and its homogenised equivalent obtained by applying mixing rule with Ψ_R is shown in Fig. 4.5(a), and analogous plot for transmission coefficient calculations, where the same value of scaling factor Ψ_R was used, is presented in Fig. 4.5(b). For this particular geometry the corresponding error (calculated from Eq. (3.24)) between grating and homogenised structure obtained for Ψ_R when cal-

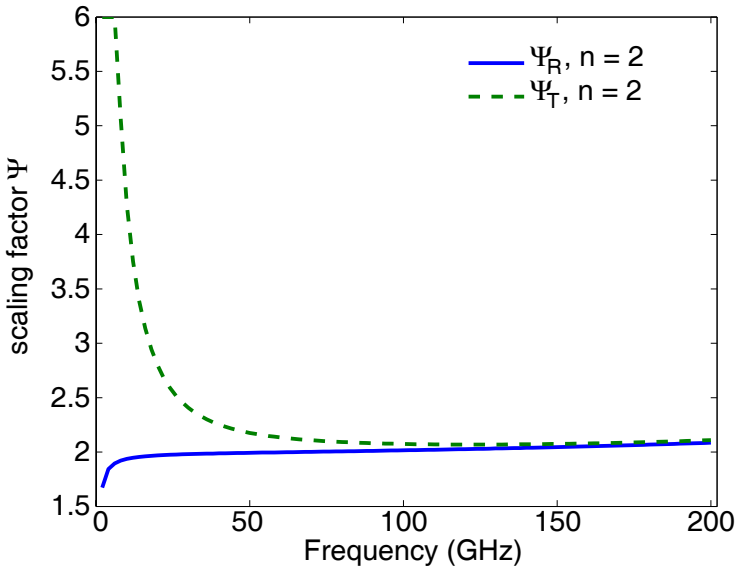

Figure 4.4: *The comparison of the value of the scaling factors Ψ_R and Ψ_T obtained from the fitting algorithm for a grating structure with grating parameters: $AR = 1.6$, $f = 0.4$, $n = 2$, $\Lambda = 100\,\mu m$, $1\,GHz \leq \nu \leq 200\,GHz$. Factors Ψ_R and Ψ_T converge with an increase of applied frequency.*

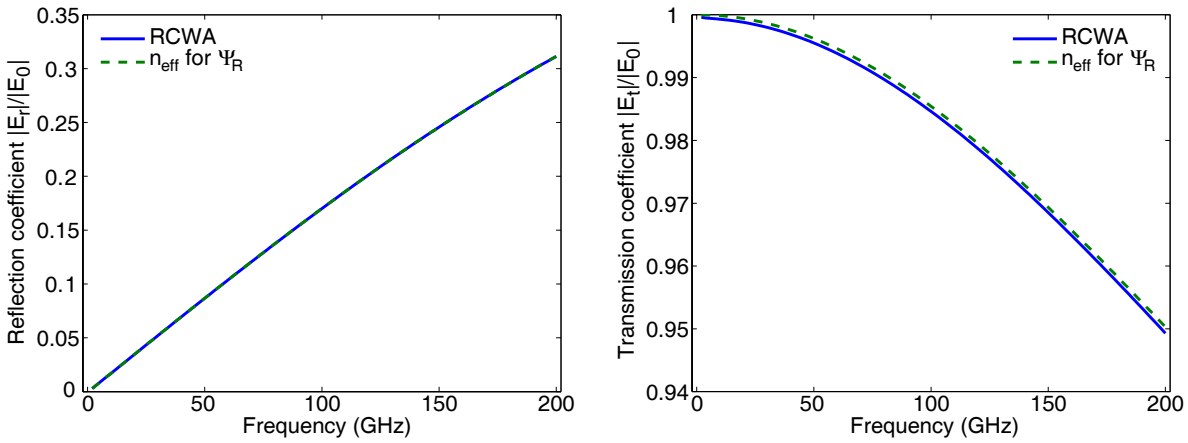

(a) *Reflection coefficient* (b) *Transmission coefficient*

Figure 4.5: *The magnitude of the reflection and transmission coefficients for a grating structure with grating parameters: $AR = 1.6$, $f = 0.4$, $n = 2$, $\Lambda = 100\,\mu m$, $1\,GHz \leq \nu \leq 200\,GHz$. The RCWA results agree with EMT formulation with n_{eff} calculated for scaling factor Ψ_R.*

culated for reflectivity is less than 0.03%, whereas for transmission estimation the error is lower than 0.2%, as illustrated in Fig. 4.6. These errors are close to the maximum ob-

served over the wide range of grating structures analysed. Therefore, given the good accuracy obtained the scaling factor Ψ_R was chosen for the rest of the analysis and its notation was simplified to Ψ.

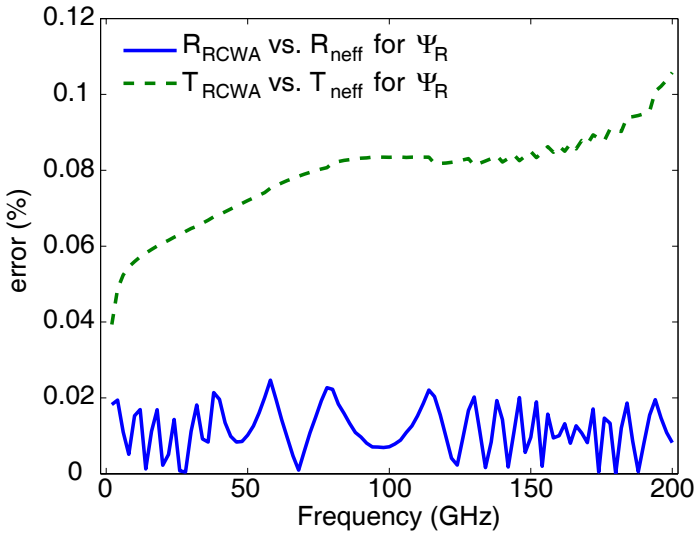

Figure 4.6: *The error (%) in the magnitude of the reflection (continuous line) and transmission (dashed line) coefficient estimation for a grating structure with grating parameters:* $AR = 1.6$, $f = 0.4$, $n = 2$, $\Lambda = 100\,\mu m$, $1\,GHz \leq \nu \leq 200\,GHz$. *The effective refractive index for the homogenised structure is calculated with scaling factor* Ψ_R. *The error between reflection and transmission coefficient of detailed and homogenised structure is at a very low level.*

Due to the four dimensional parameter space specified for the grating structure, the accuracy of the algorithm, at the stage of determining the empirical model, was verified for each of the parameters separately. For the low frequency model, over the range of all studied geometries the reflection coefficient was always estimated with an error less than 0.3%, and the transmission coefficient within 0.005% tolerance. In order to illustrate the exactness of the 'brute force' fitting the reference grating with parameters: $f = 0.5$, $n = 2.5$, $AR = 2$, $\nu = 5\,$GHz; has been chosen. The results are presented for both reflection and transmission coefficients and the corresponding errors in their estimation over varying values in the range defined for each parameter. Figure 4.7 illustrates the data in terms of the changing background dielectric within $1 \leq n \leq 3.42$. Figure 4.8 shows the accuracy with respect to the metal volume fraction in the range of $0.2 \leq f \leq 0.6$. Figure 4.9 presents the data over the range of studied aspect ratios $0.2 \leq AR \leq 3$, and finnaly, Fig. 4.10 depicts the accuracy of the algorithm for the frequency sampled from the set of $1 - 10\,$GHz.

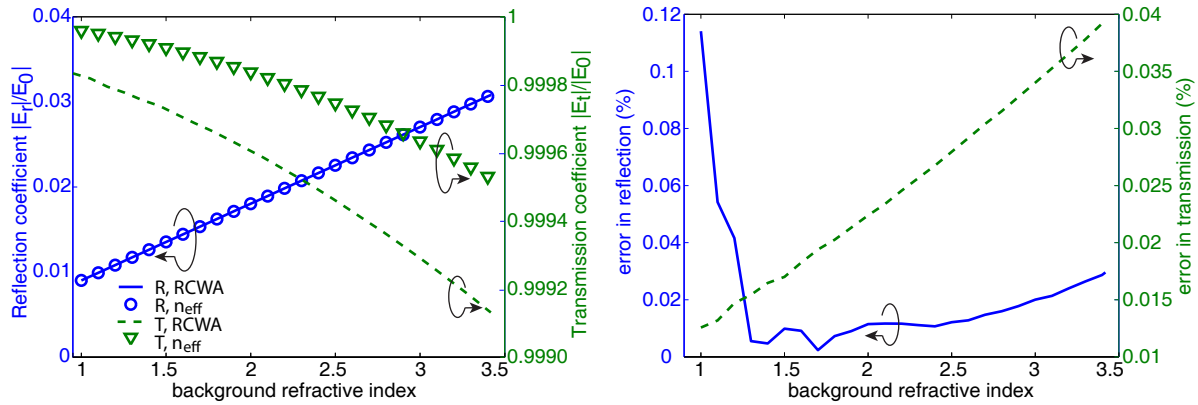

(a) *Reflection and transmission coefficients* (b) *errors*

Figure 4.7: *(a) The magnitude of the reflection and transmission coefficients for a grating structure with grating parameters:* $AR = 2$, $f = 0.5$, $1 \leq n \leq 3.42$, $\Lambda = 100\,\mu m$, $\nu = 5\,GHz$. *(b) The error in reflection and transmission between grating and homogenised layer with* n_{eff} *calculated from the fitting algorithm. The arrows point in the direction of the axis to which the curves belong.*

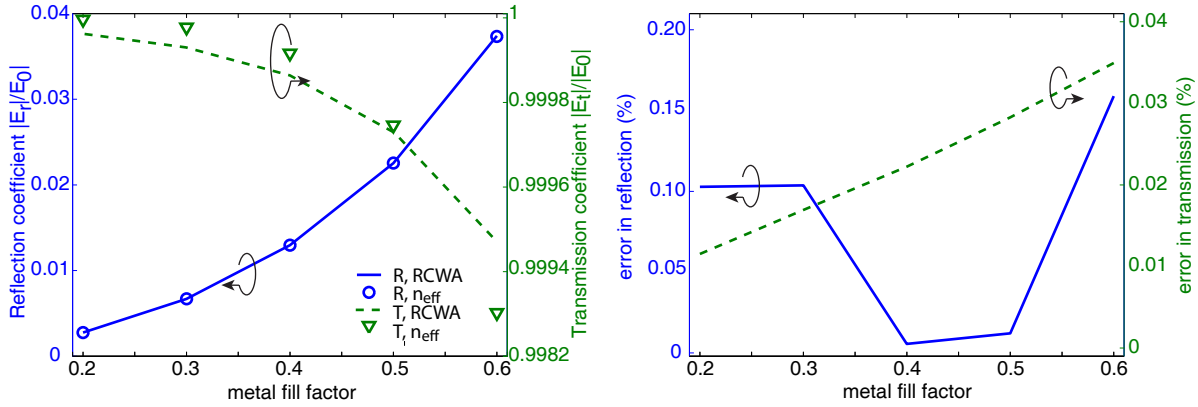

(a) *Reflection and transmission coefficients* (b) *errors*

Figure 4.8: *(a) The magnitude of the reflection and transmission coefficients for a grating structure with grating parameters:* $AR = 2$, $0.2 \leq f \leq 0.6$, $n = 2.5$, $\Lambda = 100\,\mu m$, $\nu = 5\,GHz$. *(b) The error in reflection and transmission between grating and homogenised layer with* n_{eff} *calculated from the fitting algorithm. The arrows point in the direction of the axis to which the curves belong.*

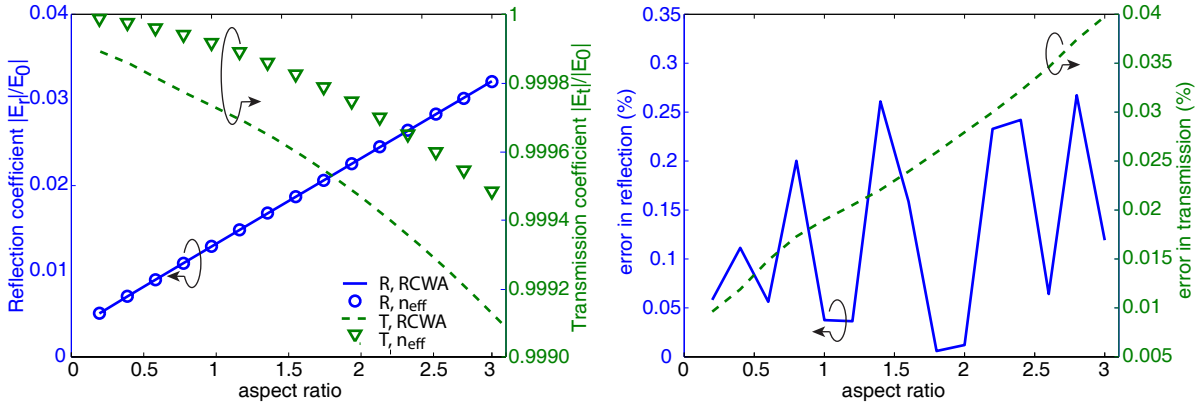

(a) *Reflection and transmission coefficients* (b) *errors*

Figure 4.9: *(a) The magnitude of the reflection and transmission coefficients for a grating structure with grating parameters:* $0.2 \leq AR \leq 3$, $f = 0.5$, $n = 2.5$, $\Lambda = 100\,\mu m$, $\nu = 5\,GHz$. *(b) The error in reflection and transmission between grating and homogenised layer with* n_{eff} *calculated from the fitting algorithm. The arrows point in the direction of the axis to which the curves belong.*

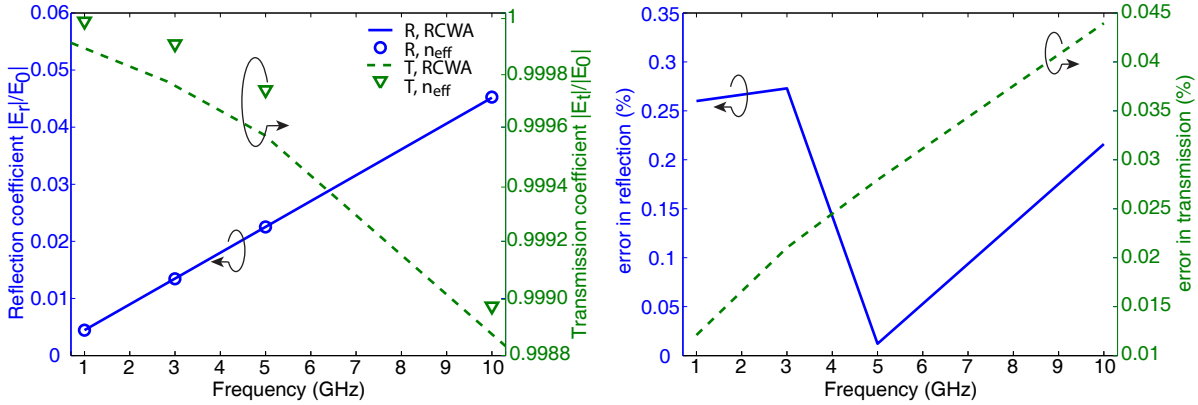

(a) *Reflection and transmission coefficients* (b) *errors*

Figure 4.10: *(a) The magnitude of the reflection and transmission coefficients for a grating structure with grating parameters:* $AR = 2$, $f = 0.5$, $n = 2.5$, $\Lambda = 100\,\mu m$, $1\,GHz \leq \nu \leq 5\,GHz$. *(b) The error in reflection and transmission between grating and homogenised layer with* n_{eff} *calculated from the fitting algorithm. The arrows point in the direction of the axis to which the curves belong.*

The homogenisation approach was also validated by comparing the electric field magnitudes obtained from the FDTD simulations of the detailed and homogenised structure for a set of gratings. A plot of the steady state electric field magnitude of an

exemplar geometry is presented in Fig. 4.11 with the plot obtained for the grating in Fig. 4.11(a), and for the homogenised equivalent in Fig. 4.11(b). In both geometries the strip is between node 110 and 146 giving $36\,\mu$m depth ($\Delta x = 1\,\mu$m). The plain wave is excited at node 250.

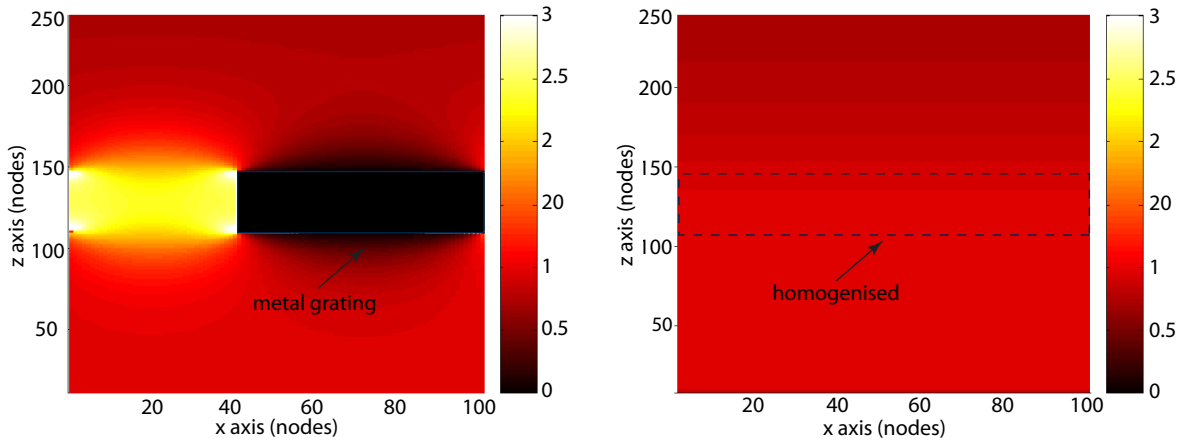

(a) *grating* (b) *homogenised layer*

Figure 4.11: *The magnitude of the steady state electric field for (a) grating and (b) homogenised layer. Grating parameters:* $\Lambda = 100\,\mu m$, $f = 0.6$, $AR = 0.6$, $n = 2.5$, $\nu = 100\,GHz$.

A comparison of the magnitudes calculated at three increasingly distant points from the z axis node 146 (z axis nodes: $180,\ 210,\ 240$) is depicted in Fig. 4.12. These graphs demonstrate that the electric field magnitude of the illumination plane wave reflected from both grating and homogenised layer gradually converges with increasing distance from the structure with the result that very close agreement is obtained in the far field pattern.

4.5 Empirical Model for On-Chip Signals Band

This Section presents two empirical models for the interconnect grating structure of the type presented in Section 4.3 for the frequencies $1 - 10\,$GHz corresponding to the on-chip signals band. The impact of the metal volume fraction on the scaling factor Ψ is discussed in detail. Mathematical formulation for the calculated scaling factor Ψ is presented. The empirical models are validated by applying them to the analysis of the studied geometries.

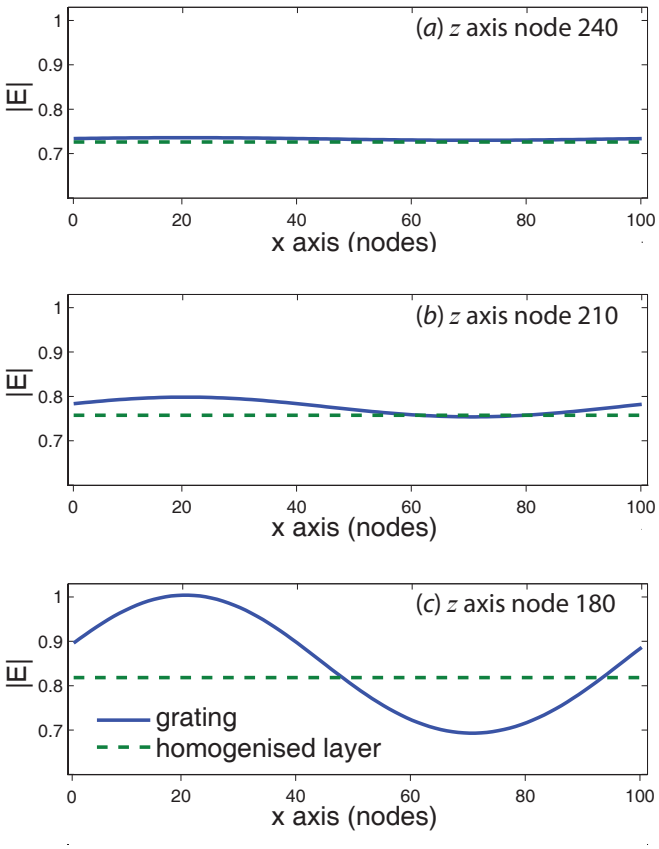

Figure 4.12: *The magnitude of the steady state electric field for grating and homogenised layer calculated at three z axis nodes: (a) 240, (b) 210,* (c) 180. The magnitudes converges in the far field.

4.5.1 Impact of the Metal Fill Factor

The analysis of the grating structure presented in Fig. 4.1 highlighted the impact of metal fill factor on the value of fitted parameter Ψ for a given aspect ratio. Figure 4.13 illustrates that gratings with high metal fill factor ($f > 0.5$) require a lower value of Ψ compared to those where the dielectric part predominate the grating cell. The presented plot was obtained for a homogenised structure illuminated by normally incident wave with free-space wavelength $\lambda = 6\,\text{cm}$ ($\nu = 5\,\text{GHz}$) where the metal bars are embedded in dielectric with refractive index $n = 2.5$. A similar relationship between metal fill factor and scaling factor Ψ was observed for varying dielectric backgrounds. The same tendency occurs for all frequencies over the considered range and is illustrated in Fig. 4.14 for a single aspect ratio $AR = 1.6$. The change in the scaling factor Ψ is presented in terms of the period-wavelength ratio (Λ/λ) for all metal fill factors.

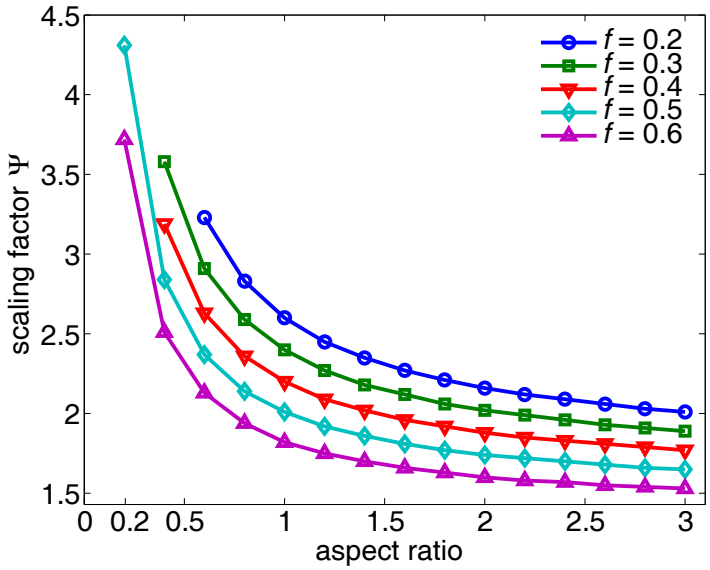

Figure 4.13: *Change in the value of scaling factor Ψ with the change of metal volume fraction f. Grating parameters: $n = 2.5$, $\Lambda = 100\,\mu m$, $\nu = 5\,GHz$, $0.2 \leq AR \leq 3$.*

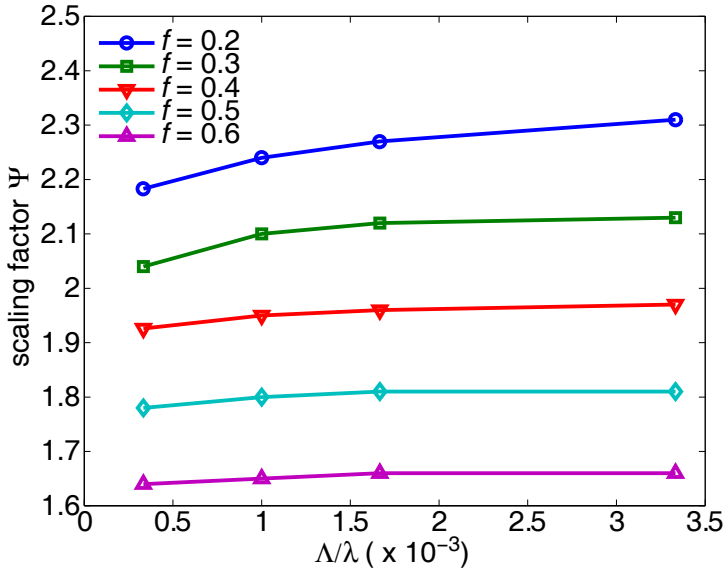

Figure 4.14: *Change in the value of scaling factor Ψ with the change of the metal volume fraction f. Grating parameters: $n = 2.5$, $\Lambda = 100\,\mu m$, $AR = 1.6$, the period-wavelength ratio varies with the change of considered frequency.*

The distribution of the value of coefficient Ψ in terms of the metal fill factor is related to the homogenisation technique chosen to build the model. Detailed study of this issue

will be presented in Subsection 4.6.2 which is devoted to the high frequency empirical model.

In Fig. 4.15 it is demonstrated, for an exemplar structure, that the value of the scaling factor Ψ does not significantly depend on the frequency of illuminating wave. The small difference in the value of Ψ which does occur in the range of studied structures has a tendency to disappear with the increase of the metal fill factor as demonstrated in Fig. 4.15(a) for $f = 0.3$, and in Fig. 4.15(b) for $f = 0.5$. The effective refractive index defined by the modified Maxwell-Garnett mixing rule with the permittivity of metal inclusions calculated from the Drude model [74] accounts for the frequency dependence. The frequency dependence of the value of factor Ψ is smaller for lower metal fill factors and tends to disappear as this factor increases.

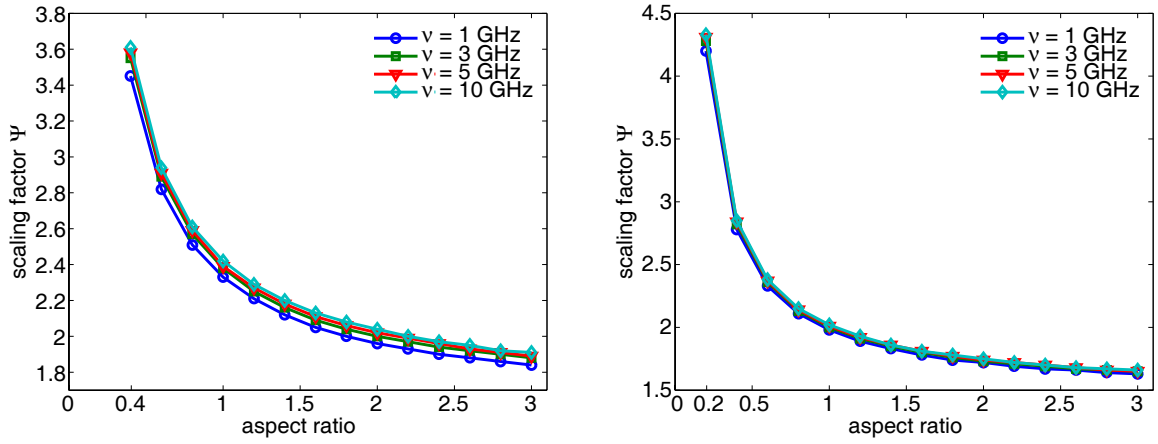

(a) $f = 0.3$ (b) $f = 0.5$

Figure 4.15: *A graph showing that obtained value of scaling factor Ψ does not significantly change with the change of frequency of the illumination wave. Grating parameters: $n = 2$, $\Lambda = 100\,\mu m$, $0.2 \leq AR \leq 3$, and metal fill factor: (a) $f = 0.3$; (b) $f = 0.5$.*

4.5.2 Model Simplification

It was verified and is presented in Fig. 4.16 that for a single frequency and a considered range of aspect ratios the change in the scaling factor Ψ in terms of the varying refractive indices of the dielectric background is minimal (less than 1%). Therefore, it is not necessary to make the scaling factor Ψ dependent on the dielectric constituent as

it is explicitly included in the modified Maxwell-Garnett formula with a single value of $\Psi = 1$. For the sake of clarity, results for structures with background refractive index $n = 2.5$, which is in the middle of the studied range, were chosen for further analysis.

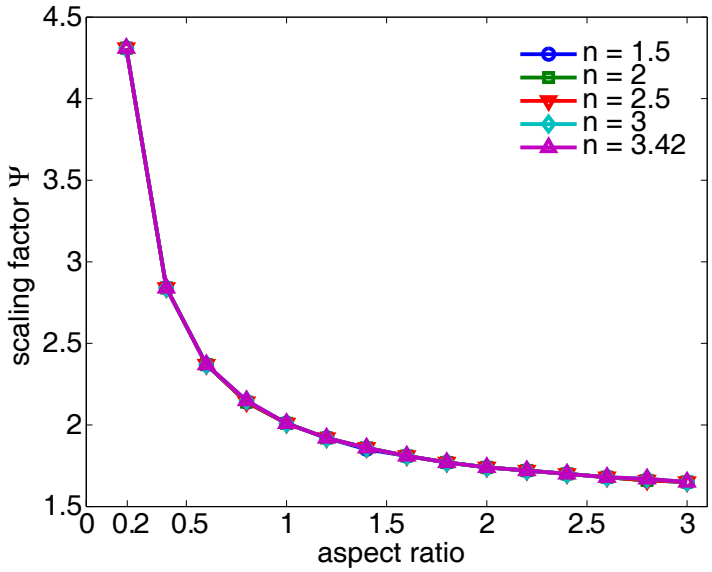

Figure 4.16: *A graph showing that obtained value of scaling factor Ψ does not change with the change of the dielectric constant n. Grating parameters: $f = 0.5$, $\Lambda = 100\,\mu m$, $\nu = 5\,GHz$, $0.2 \leq AR \leq 3$.*

The distribution of the value Ψ versus aspect ratio for a given frequency and metal fill factor has exponential characteristics. This regularity was considered in the fitting procedure where the nonlinear least squares method involving the Taylor series expansion (Appendix A) was used. It was assumed that the studied model can be represented by a nonlinear function which is the sum of two exponential functions with the aspect ratio as variable. Hence, the scaling factor Ψ is defined for every dielectric with refractive index n as a function of varying aspect ratio by formula

$$\Psi(x_{AR}) = \alpha \cdot e^{\beta \cdot x_{AR}} + \gamma \cdot e^{\delta \cdot x_{AR}} \tag{4.3}$$

where x_{AR} is the variable representing aspect ratio with $AR_{min} \leq x_{AR} \leq 3$, and limits for AR_{min} presented in Table 4.1.

Further coefficients α, β, γ, δ are determined by linear least squares method, including expansion in Taylor series (Appendix A.3, A.5), for every n and frequency[1] ν as a

[1]The unit for frequency has been set to GHz

function of varying metal volume fraction f and they are given by

$$\alpha(f) = \alpha_1 \cdot f + \alpha_2 \tag{4.4}$$
$$\beta(f) = \beta_1 \cdot f + \beta_2 \tag{4.5}$$
$$\gamma(f) = \gamma_1 \cdot f + \gamma_2 \tag{4.6}$$
$$\delta(f) = \delta_1 \cdot f + \delta_2 \tag{4.7}$$

for $0.2 \leq f \leq 0.6$. All coefficients α_m, β_m, γ_m, δ_m, where $m = \{1, 2\}$ are well approximated by

$$\alpha_1(\nu) = \alpha_{11} \cdot \nu + \alpha_{12} \tag{4.8}$$
$$\alpha_2(\nu) = \alpha_{21} \cdot \nu + \alpha_{22} \tag{4.9}$$
$$\beta_1(\nu) = \beta_{11} \cdot \nu + \beta_{12} \tag{4.10}$$
$$\beta_2(\nu) = \beta_{21} \cdot \nu + \beta_{22} \tag{4.11}$$
$$\gamma_1(\nu) = \gamma_{11} \cdot \nu + \gamma_{12} \tag{4.12}$$
$$\gamma_2(\nu) = \gamma_{21} \cdot \nu + \gamma_{22} \tag{4.13}$$
$$\delta_1(\nu) = \delta_{11} \cdot \nu + \delta_{12} \tag{4.14}$$
$$\delta_2(\nu) = \delta_{21} \cdot \nu + \delta_{22} \tag{4.15}$$

Coefficients α_{mn}, β_{mn}, γ_{mn}, and δ_{mn} where $m, n = \{1, 2\}$ are given in Table 4.2.

α_{11}	-0.0054	β_{11}	0.0191	γ_{11}	-0.0370	δ_{11}	0.0026
α_{12}	3.0965	β_{12}	-6.3175	γ_{12}	-1.0792	δ_{12}	-0.0558
α_{21}	0.0188	β_{21}	-0.0086	γ_{21}	0.0231	δ_{21}	-0.0015
α_{22}	3.1421	β_{22}	-1.1014	γ_{22}	2.5738	δ_{22}	-0.0513

Table 4.2: *Coefficients α_{mn} and β_{mn}, where $m, n = \{1, 2\}$, for Ψ calculations according to the Eq. (4.3) - (4.15).*

The empirical model can be expressed in the multidimensional Taylor series form (Appendix A.1). The first-order coefficients of the Taylor series are expressed in terms of those presented in Table 4.2 and are given below

$$\begin{aligned}\Psi|_{\mathbf{0}} = {} & [\alpha_{11}\nu_{\mathbf{0}}f_{\mathbf{0}} + \alpha_{12}f_{\mathbf{0}} + \alpha_{21}\nu_{\mathbf{0}} + \alpha_{22}]e^{\beta_{11}\nu_{\mathbf{0}}f_{\mathbf{0}}x_{AR_{\mathbf{0}}} + \beta_{12}f_{\mathbf{0}}x_{AR_{\mathbf{0}}} + \beta_{21}\nu_{\mathbf{0}}x_{AR_{\mathbf{0}}} + \beta_{22}x_{AR_{\mathbf{0}}}} + \\ & [\gamma_{11}\nu_{\mathbf{0}}f_{\mathbf{0}} + \gamma_{12}f_{\mathbf{0}} + \gamma_{21}\nu_{\mathbf{0}} + \gamma_{22}]e^{\delta_{11}\nu_{\mathbf{0}}f_{\mathbf{0}}x_{AR_{\mathbf{0}}} + \delta_{12}f_{\mathbf{0}}x_{AR_{\mathbf{0}}} + \delta_{21}\nu_{\mathbf{0}}x_{AR_{\mathbf{0}}} + \delta_{22}x_{AR_{\mathbf{0}}}}\end{aligned} \tag{4.16}$$

$$\begin{aligned}\left.\frac{\partial\Psi}{\partial\nu}\right|_{\mathbf{0}} &= [\alpha_{11}f_{\mathbf{0}}+\alpha_{21}]e^{(\beta_{11}f_{\mathbf{0}}x_{AR_{\mathbf{0}}}+\beta_{21}x_{AR_{\mathbf{0}}})\nu_{\mathbf{0}}+\beta_{12}f_{\mathbf{0}}x_{AR_{\mathbf{0}}}+\beta_{22}x_{AR_{\mathbf{0}}}} + \\ &\quad [\alpha_{11}\nu_{\mathbf{0}}f_{\mathbf{0}}+\alpha_{12}f_{\mathbf{0}}+\alpha_{21}\nu_{\mathbf{0}}+\alpha_{22}]\cdot[\beta_{11}f_{\mathbf{0}}x_{AR_{\mathbf{0}}}+\beta_{21}x_{AR_{\mathbf{0}}}]\cdot \\ &\quad e^{(\beta_{11}f_{\mathbf{0}}x_{AR_{\mathbf{0}}}+\beta_{21}x_{AR_{\mathbf{0}}})\nu_{\mathbf{0}}+\beta_{12}f_{\mathbf{0}}x_{AR_{\mathbf{0}}}+\beta_{22}x_{AR_{\mathbf{0}}}} + \\ &\quad [\gamma_{11}f_{\mathbf{0}}+\gamma_{21}]e^{(\delta_{11}f_{\mathbf{0}}x_{AR_{\mathbf{0}}}+\delta_{21}x_{AR_{\mathbf{0}}})\nu_{\mathbf{0}}+\delta_{12}f_{\mathbf{0}}x_{AR_{\mathbf{0}}}+\delta_{22}x_{AR_{\mathbf{0}}}} + \\ &\quad [\gamma_{11}\nu_{\mathbf{0}}f_{\mathbf{0}}+\gamma_{12}f_{\mathbf{0}}+\gamma_{21}\nu_{\mathbf{0}}+\gamma_{22}]\cdot[\delta_{11}f_{\mathbf{0}}x_{AR_{\mathbf{0}}}+\delta_{21}x_{AR_{\mathbf{0}}}]\cdot \\ &\quad e^{(\delta_{11}f_{\mathbf{0}}x_{AR_{\mathbf{0}}}+\delta_{21}x_{AR_{\mathbf{0}}})\nu_{\mathbf{0}}+\delta_{12}f_{\mathbf{0}}x_{AR_{\mathbf{0}}}+\delta_{22}x_{AR_{\mathbf{0}}}} \end{aligned} \tag{4.17}$$

$$\begin{aligned}\left.\frac{\partial\Psi}{\partial f}\right|_{\mathbf{0}} &= [\alpha_{11}\nu_{\mathbf{0}}+\alpha_{12}]e^{(\beta_{11}\nu_{\mathbf{0}}x_{AR_{\mathbf{0}}}+\beta_{12}x_{AR_{\mathbf{0}}})f_{\mathbf{0}}+\beta_{21}\nu_{\mathbf{0}}x_{AR_{\mathbf{0}}}+\beta_{22}x_{AR_{\mathbf{0}}}} + \\ &\quad [\alpha_{11}\nu_{\mathbf{0}}f_{\mathbf{0}}+\alpha_{12}f_{\mathbf{0}}+\alpha_{21}\nu_{\mathbf{0}}+\alpha_{22}]\cdot[\beta_{11}\nu_{\mathbf{0}}x_{AR_{\mathbf{0}}}+\beta_{12}x_{AR_{\mathbf{0}}}]\cdot \\ &\quad e^{(\beta_{11}\nu_{\mathbf{0}}x_{AR_{\mathbf{0}}}+\beta_{12}x_{AR_{\mathbf{0}}})f_{\mathbf{0}}+\beta_{21}\nu_{\mathbf{0}}x_{AR_{\mathbf{0}}}+\beta_{22}x_{AR_{\mathbf{0}}}} + \\ &\quad [\gamma_{11}\nu_{\mathbf{0}}+\gamma_{12}]e^{(\delta_{11}\nu_{\mathbf{0}}x_{AR_{\mathbf{0}}}+\delta_{12}x_{AR_{\mathbf{0}}})f_{\mathbf{0}}+\delta_{21}\nu_{\mathbf{0}}x_{AR_{\mathbf{0}}}+\delta_{22}x_{AR_{\mathbf{0}}}} + \\ &\quad [\gamma_{11}\nu_{\mathbf{0}}f_{\mathbf{0}}+\gamma_{12}f_{\mathbf{0}}+\gamma_{21}\nu_{\mathbf{0}}+\gamma_{22}]\cdot[\delta_{11}\nu_{\mathbf{0}}x_{AR_{\mathbf{0}}}+\delta_{12}x_{AR_{\mathbf{0}}}]\cdot \\ &\quad e^{(\delta_{11}\nu_{\mathbf{0}}x_{AR_{\mathbf{0}}}+\delta_{12}x_{AR_{\mathbf{0}}})f_{\mathbf{0}}+\delta_{21}\nu_{\mathbf{0}}x_{AR_{\mathbf{0}}}+\delta_{22}x_{AR_{\mathbf{0}}}} \end{aligned} \tag{4.18}$$

$$\begin{aligned}\left.\frac{\partial\Psi}{\partial x_{AR}}\right|_{\mathbf{0}} &= [\alpha_{11}\nu_{\mathbf{0}}f_{\mathbf{0}}+\alpha_{12}f_{\mathbf{0}}+\alpha_{21}\nu_{\mathbf{0}}+\alpha_{22}]\cdot[\beta_{11}\nu_{\mathbf{0}}f_{\mathbf{0}}+\beta_{12}f_{\mathbf{0}}+\beta_{21}\nu_{\mathbf{0}}+\beta_{22}]\cdot \\ &\quad e^{(\beta_{11}\nu_{\mathbf{0}}f_{\mathbf{0}}+\beta_{12}f_{\mathbf{0}}+\beta_{21}\nu_{\mathbf{0}}+\beta_{22}x_{AR_{\mathbf{0}}})x_{AR_{\mathbf{0}}}} + \\ &\quad [\gamma_{11}\nu_{\mathbf{0}}f_{\mathbf{0}}+\gamma_{12}f_{\mathbf{0}}+\gamma_{21}\nu_{\mathbf{0}}+\gamma_{22}]\cdot[\delta_{11}\nu_{\mathbf{0}}f_{\mathbf{0}}+\delta_{12}f_{\mathbf{0}}+\delta_{21}\nu_{\mathbf{0}}+\delta_{22}]\cdot \\ &\quad e^{(\delta_{11}\nu_{\mathbf{0}}f_{\mathbf{0}}+\delta_{12}f_{\mathbf{0}}+\delta_{21}\nu_{\mathbf{0}}+\delta_{22}x_{AR_{\mathbf{0}}})x_{AR_{\mathbf{0}}}}. \end{aligned} \tag{4.19}$$

Figure 4.17 demonstrates how the defined empirical model approximates the values of the scaling factor Ψ obtained from the 'brute force' algorithm for a single reference grating, at each step of increased complexity. Figure 4.17(a) illustrates the agreement between Ψ obtained from the 'brute force' fitting algorithm illustrated in Fig. 4.2 and that from exponential approximation defined for every n as a function with varying aspect ratio for grating structure with metal fill factor equal to 0.5 illuminated by normally incident wave with frequency $5\,\mathrm{GHz}$. Whereas Fig. 4.17(b) shows the distribution of factor Ψ when coefficients are expressed by linear regression defined for all n and all f as a function with varying aspect ratio compared with the reference data. Figure 4.17(c) demonstrates how the scaling factor Ψ is estimated by the final model. Figure 4.17(d) shows the accuracy in the estimation of Ψ at each of the three steps of building the complex model when all the data are compared with the value obtained from the fitting algorithm. There is minimal absolute difference in the distribution of

value Ψ among all steps followed to estimate that factor. However it is still necessarily to follow these steps in order to include the all four parameters to the final formulation of the scaling factor Ψ.

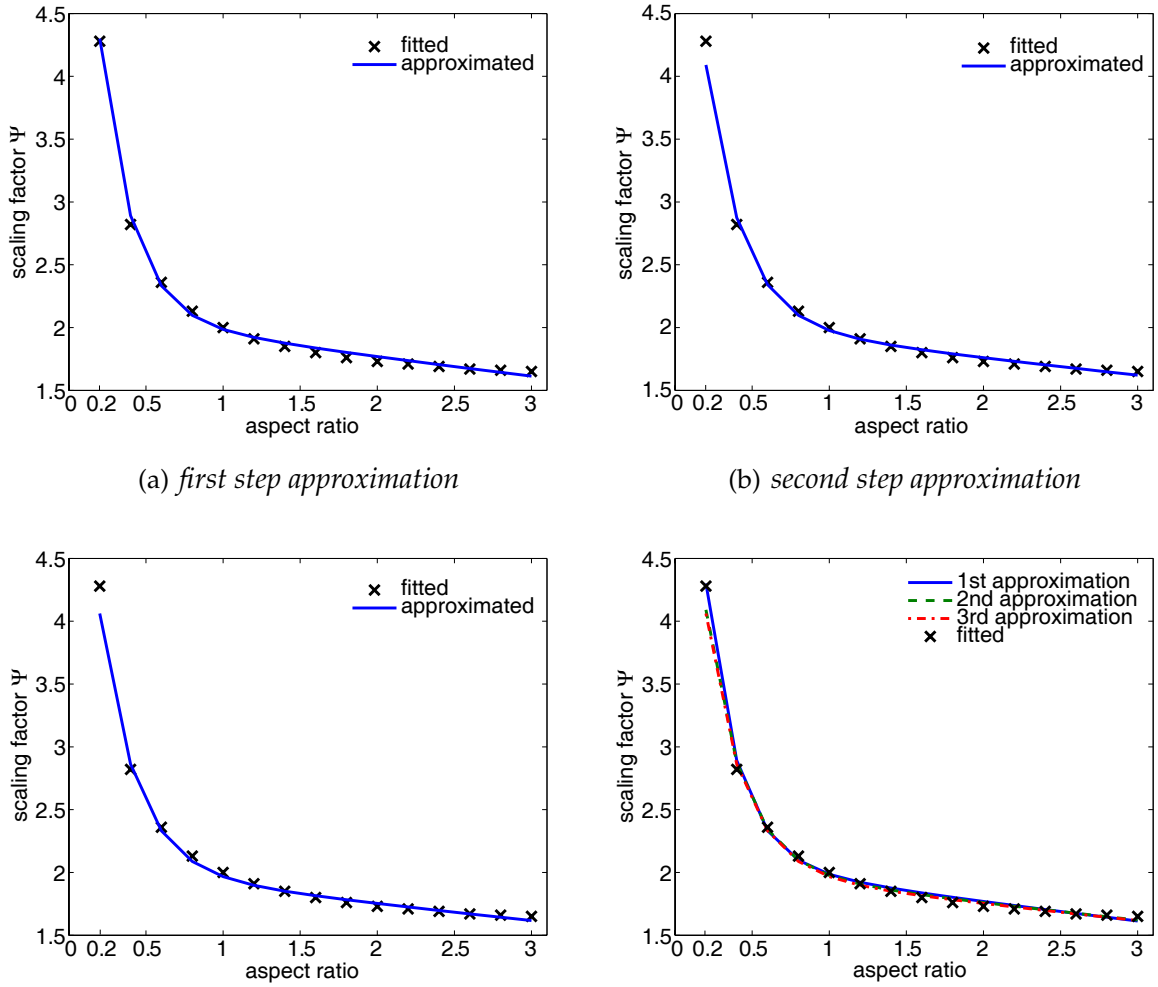

(a) *first step approximation*

(b) *second step approximation*

(c) *third step approximation*

(d) *comparison*

Figure 4.17: *The values of the scaling factor Ψ obtained from the 'brute force' algorithm plotted as crosses against values with scaling factor Ψ defined as a function for: (a) all background dielectrics with varying aspect ratio; (b) all dielectrics and metal volume fractions with varying aspect ratio; (c) all dielectrics, metal volume fractions and frequencies with varying aspect ratio plotted as continuous lines. Figure (d) shows comparison of Ψ for all approximation steps together. Grating parameters: $f = 0.5$, $\Lambda = 100\,\mu m$, $\nu = 5\,GHz$, $n = 2.5$, $0.2 \leq AR \leq 3$.*

Scaling factor Ψ when predicted by the least squares method for all background di-

electrics n, all metal fill factors f, and all frequencies ν as a function of aspect ratio results in an error within $0\% - 2.5\%$ compared to the values obtained from the 'brute force' fitting algorithm. There is a higher error of about $4\% - 6\%$ in the scaling factor for metal volume fraction $f = 0.2$ and aspect ratio within $0.6 - 1$, but the proposed model is aimed to be used for interconnects analysis and the aspect ratio currently predicted in the ITRS [8] is between 1.6 and 3. Hence this error can be neglected here.

4.5.3 Numerical Validation of Analytical Model

The validation of the proposed empirical model was carried out by applying it to the analysis of the studied structure and calculating the errors in reflection and transmission coefficients between detailed and homogenised structures. The reference structure was set to be the grating structure with reflectivity and transmissivity calculated from RCWA. Justification of the homogenisation procedure is achieved in steps related to those taken to build the model. First, in Fig. 4.18(a) it is shown that when the structure is homogenised using the modified Maxwell-Garnett mixing rule with parameter Ψ obtained from the 'brute force' algorithm estimates the reflection coefficient with an error less than 0.3%. Furthermore, exponential approximation defined for all background materials was applied to express the dependence of Ψ in terms of varying aspect ratio as illustrated in Figure 4.18(b). Then in Fig. 4.18(c) it is shown that the same agreement is obtained when the analytical model is defined for all dielectric materials and metal fills in terms of varying aspect ratio. The final analytical model was determined by expressing coefficients from exponential approximation by a set of linear functions defined for all n, all f, and all ν in terms of changing aspect ratio, and the accuracy of this empirical model is illustrated in Fig. 4.18(d).

Simplification of the model after each approximation step results in an error in reflectivity estimation not higher than 2.7% and in most cases less than 1.5%. Estimation of the transmission coefficient was verified after each step was followed to get the final analytical representation of the model. It was calculated that the error between transmission obtained for simulated detailed structure and homogenised one at each level of complexity is not higher that 0.2%. Plots of the transmission coefficient estimation are not shown for brevity.

The difference in the phase of the detailed and homogenised grating structure with

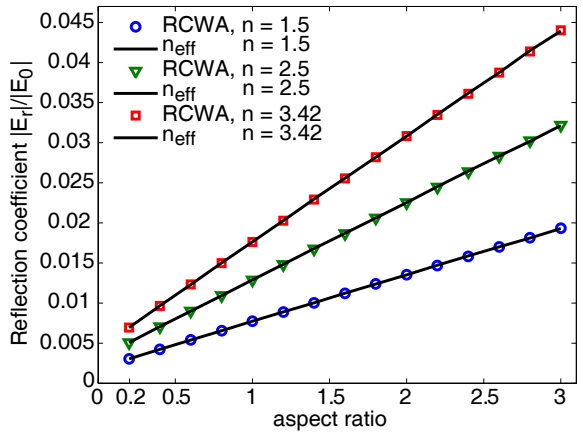

(a) *Reflection coefficient*

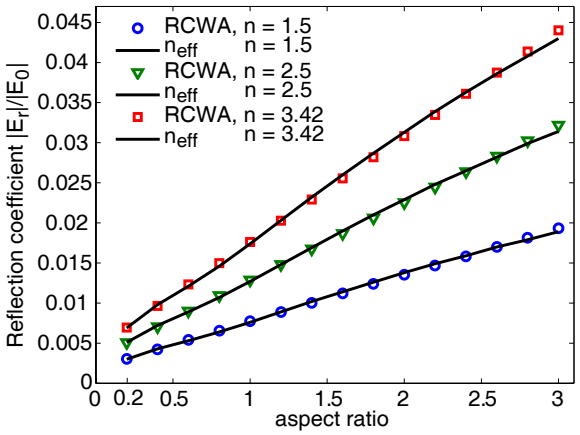

(b) *Reflection coefficient*

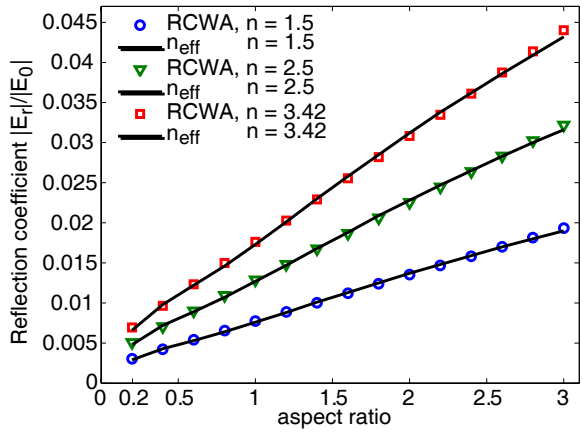

(c) *Reflection coefficient*

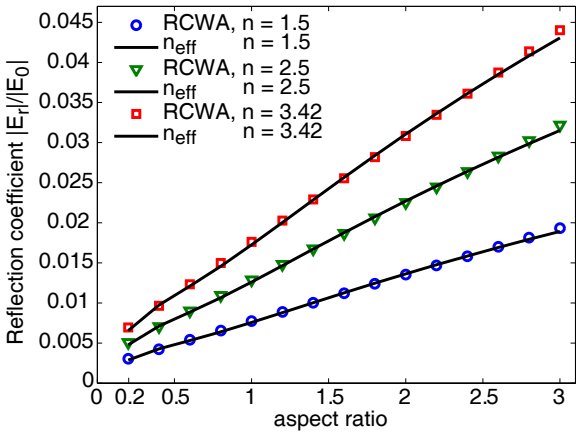

(d) *Reflection coefficient*

Figure 4.18: *The magnitude of the reflection coefficient for a grating structure with grating parameters:* $f = 0.5$, $\Lambda = 100\,\mu m$, $\nu = 5\,GHz$, $n = \{1.5, 2.5, 3.42\}$, $0.2 \leq AR \leq 3$. *The RCWA results are plotted along with the EMA formulation with* n_{eff} *calculated: (a) from 'brute force' algorithm; (b) with scaling factor* Ψ *defined as a function for all background dielectrics with varying aspect ratio; (c) with* Ψ *defined as a function for all dielectrics and metal volume fractions with varying aspect ratio; (d) with* Ψ *defined as a function for all dielectrics, metal volume fractions, and frequencies with varying aspect ratio.*

respect to increasing aspect ratio is also considered. It is illustrated in Fig. 4.19 that the difference in phase is within $0^\circ - 2^\circ$ with tendency to increase with the increase of the background dielectric permittivity. Due to such small deviation in the phase, further analysis will be mainly focused on the reflection and transmission coefficients.

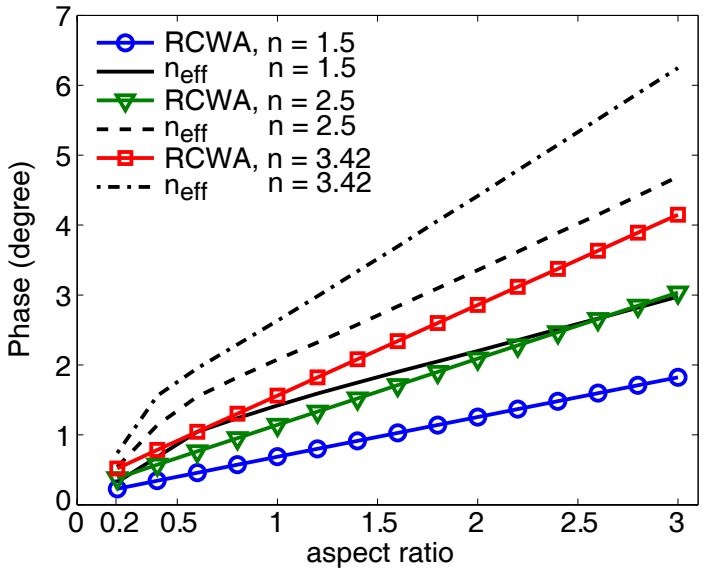

Figure 4.19: *The obtained small change in the phase value. Grating parameters:* $f = 0.5$, $\Lambda = 100\,\mu m$, $\nu = 5\,GHz$, $n = \{1.5, 2.5, 3.42\}$, $0.2 \leq AR \leq 3$.

4.5.4 Further Model Simplification

Further simplification of the model was achieved by reducing the range of aspect ratios to $1.4 \leq AR \leq 3$ in order to reflect the dimensions of typically used interconnects. Over this reduced range, the scaling factor can be represented as a linear function. This observation was considered as a base to define the empirical model presented below.

The least squares method was applied to express the scaling factor Ψ in analytical form. First, the scaling factor Ψ was determined by a linear least squares method, involving expansion in Taylor series (Appendix A.3, A.5), for every refractive index n and every metal volume fraction f as a function of varying aspect ratio $1.4 \leq x_{AR} \leq 3$ by the formula

$$\Psi(x_{AR}) = \alpha \cdot x_{AR} + \beta \tag{4.20}$$

Coefficients α and β are defined by linear regression for every frequency[2] ν as a function of varying metal volume fraction f by

$$\alpha(f) = \alpha_1 \cdot f + \alpha_2 \tag{4.21}$$

$$\beta(f) = \beta_1 \cdot f + \beta_2 \tag{4.22}$$

[2]The unit for frequency has been set to GHz

All coefficients α_1, α_2, β_1, β_2 are well approximated by

$$\alpha_1(\nu) = \alpha_{11} \cdot \nu + \alpha_{12} \tag{4.23}$$

$$\alpha_2(\nu) = \alpha_{21} \cdot \nu + \alpha_{22} \tag{4.24}$$

$$\beta_1(\nu) = \beta_{11} \cdot \nu + \beta_{12} \tag{4.25}$$

$$\beta_2(\nu) = \beta_{21} \cdot \nu + \beta_{22} \tag{4.26}$$

with values of α_{mn} and β_{mn}, where $m, n = \{1, 2\}$ presented in Table 4.3.

α_{11}	0.0064	β_{11}	-0.0341
α_{12}	0.2309	β_{12}	-1.7494
α_{21}	-0.0037	β_{21}	0.0213
α_{22}	-0.2346	β_{22}	2.8473

Table 4.3: *Coefficients α_{mn} and β_{mn}, where $m, n = \{1, 2\}$, for Ψ calculations according to the Eq. (4.20) - (4.26).*

The α-coefficients determine the gradient of the linear function $\Psi(x_{AR})$, whereas β-coefficients are used in y-intercept calculations. Both coefficients are well predicted by linear least squares method at each step in the analytical formulation. The error in the approximation of Ψ, when calculated in terms of the reference data obtained from the 'brute force' algorithm, for the studied range of structures is in the range $0\% - 2.5\%$. Generally, the error reaches its maximum for structures with aspect ratios at either end of the range $1.4 \leq AR \leq 3$, whereas the error is not higher than 1% when the aspect ratio is near the middle of the studied range.

The empirical model can be expressed in the multidimensional Taylor series form (Appendix A.1) and the coefficients are given in Table 4.4

$\Psi\big\vert_{\mathbf{0}}$	β_{11}	$\frac{\partial \Psi}{\partial x_{AR}}\big\vert_{\mathbf{0}}$	α_{22}	$\frac{\partial \Psi}{\partial f}\big\vert_{\mathbf{0}}$	β_{12}	$\frac{\partial \Psi}{\partial \nu}\big\vert_{\mathbf{0}}$	β_{21}
$\frac{\partial^2 \Psi}{\partial x_{AR} \partial f}\big\vert_{\mathbf{0}}$	$2\alpha_{12}$	$\frac{\partial^2 \Psi}{\partial x_{AR} \partial \nu}\big\vert_{\mathbf{0}}$	$2\alpha_{21}$	$\frac{\partial^2 \Psi}{\partial f \partial \nu}\big\vert_{\mathbf{0}}$	$2\beta_{11}$	$\frac{\partial^3 \Psi}{\partial x_{AR} \partial f \partial \nu}\big\vert_{\mathbf{0}}$	$2\alpha_{11}$

Table 4.4: *Coefficients for the Taylor series expansion of Ψ expressed in terms of the coefficients given in Table 4.3.*

Figure 4.20 plots the scaling factor Ψ versus aspect ratio for the data obtained from the 'brute force' algorithm (shown in Fig. 4.2) and the data obtained from the approximation procedure. Figure 4.20(a) shows the data obtained from the 'brute force' algorithm and the data from the approximation procedure when Ψ is defined as a function of n and the aspect ratio. Figure 4.20(b) shows the scaling factor Ψ when defined as a linear function of aspect ratio for all refractive indices n and metal fill factors f. Figure 4.20(c) demonstrates Ψ when calculated by Eq. (4.20)-(4.26). Finally, Fig. 4.20(d) shows a comparison of the scaling factor Ψ calculated from the three approximations. The increase in complexity of the model does not significantly change the distribution of the value Ψ, therefore the correlated error in the reflection and transmission coefficient predicted by the empirical model is relatively low as is discussed further in this Section.

The corresponding results for the reflection coefficient estimation are presented in Fig. 4.21. Numerical data from RCWA for a reference grating structure is plotted along with data obtained from the analysis of the equivalent homogenised structure with effective refractive index n_{eff} obtained from the 'brute force' algorithm in Fig. 4.21(a); n_{eff} calculated from modified Maxwell-Garnett formula with Ψ defined as linear function for all dielectrics from studied range in terms of varying AR in Fig. 4.21(b); and Ψ determined for all dielectrics and all metal fills as a function of changing aspect ratio in Fig. 4.21(c); finally Fig. 4.21(d) demonstrates results obtained when the complex model is used to calculate the value of scaling factor Ψ.

The error in the reflection coefficient predicted by the presented empirical model varies from 0% to 2.5%, nevertheless the transmission coefficient is estimated with an error not exceeding 0.2%. The accuracy of the model for reflectivity calculations tends to improve with an increase of the metal fill factor. For structures with metal fills $0.4 \leq f \leq 0.6$ the error varies between $0 - 1.5\%$.

4.5.5 Application of Model at Other Frequencies

Now that the effectiveness of the empirical model has been demonstrated at the frequency points 1, 3, 5 and 10 GHz, it will be further validated for a different sample frequency from the range $1 - 10$ GHz.
The model was constructed by sampling the numerical response at discreet values of

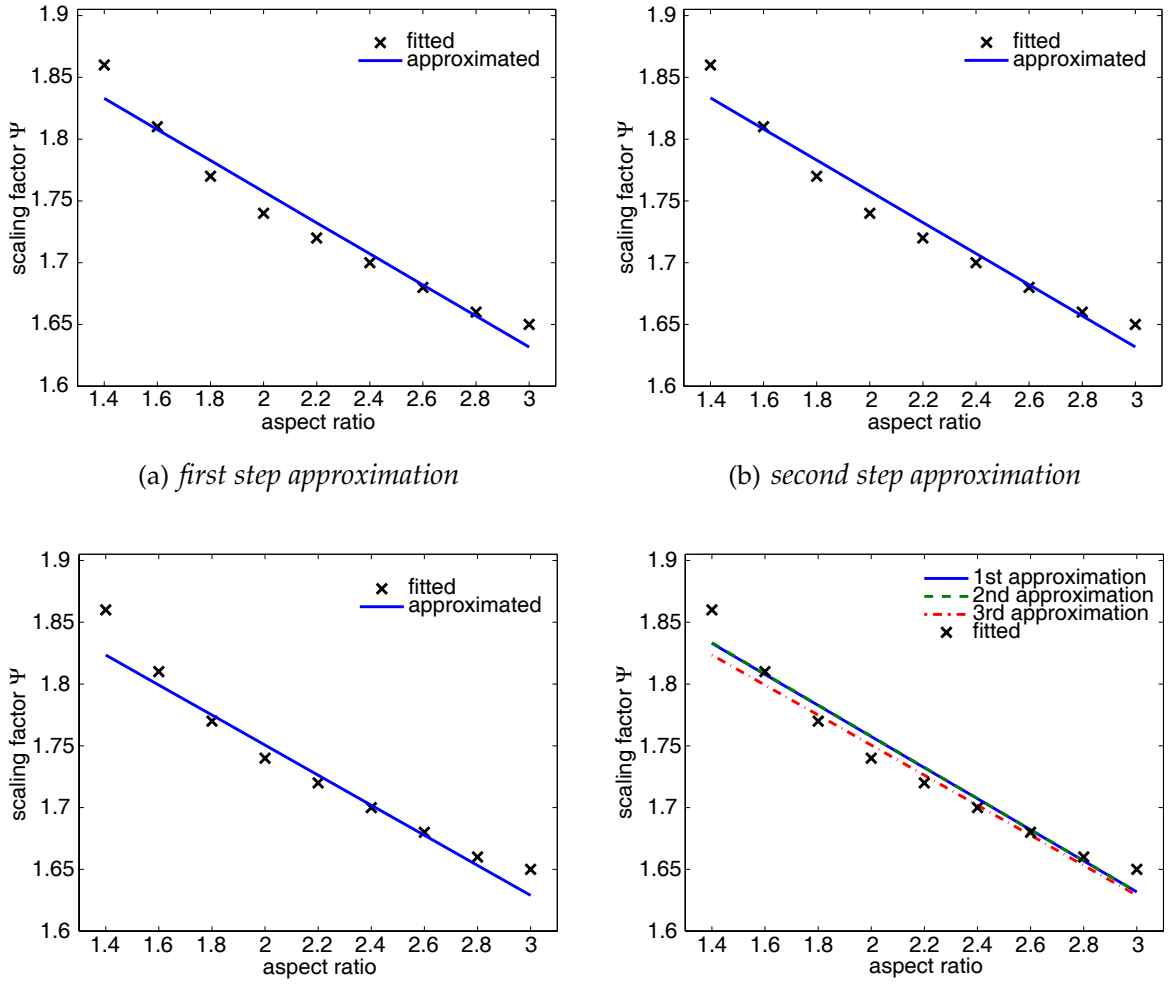

(a) *first step approximation*

(b) *second step approximation*

(c) *third step approximation*

(d) *comparison*

Figure 4.20: *The fitted values obtained from the 'brute force' algorithm plotted as crosses along with approximated values of scaling factor Ψ defined as a function for: (a) all background dielectrics with varying aspect ratio; (b) all dielectrics and metal volume fractions with varying aspect ratio; (c) all dielectrics, metal volume fractions and frequencies with varying aspect ratio plotted as continuous line. Figure (d) shows comparison of Ψ for all approximation steps together. Grating parameters: $f = 0.5$, $\Lambda = 100\,\mu m$, $\nu = 5\,GHz$, $n = 2.5$, $1.4 \leq AR \leq 3$.*

four parameters: aspect ratio, metal volume fraction, background material, and frequency. It was then verified by comparing the numerical data obtained for the detailed grating structure and its homogenised equivalent at a frequency point not used to define the model. Hence, the exemplar frequency of $6\,$GHz was chosen. Detailed grating structures with metal volume fraction of 0.3 and 0.5 and their homegenised equiva-

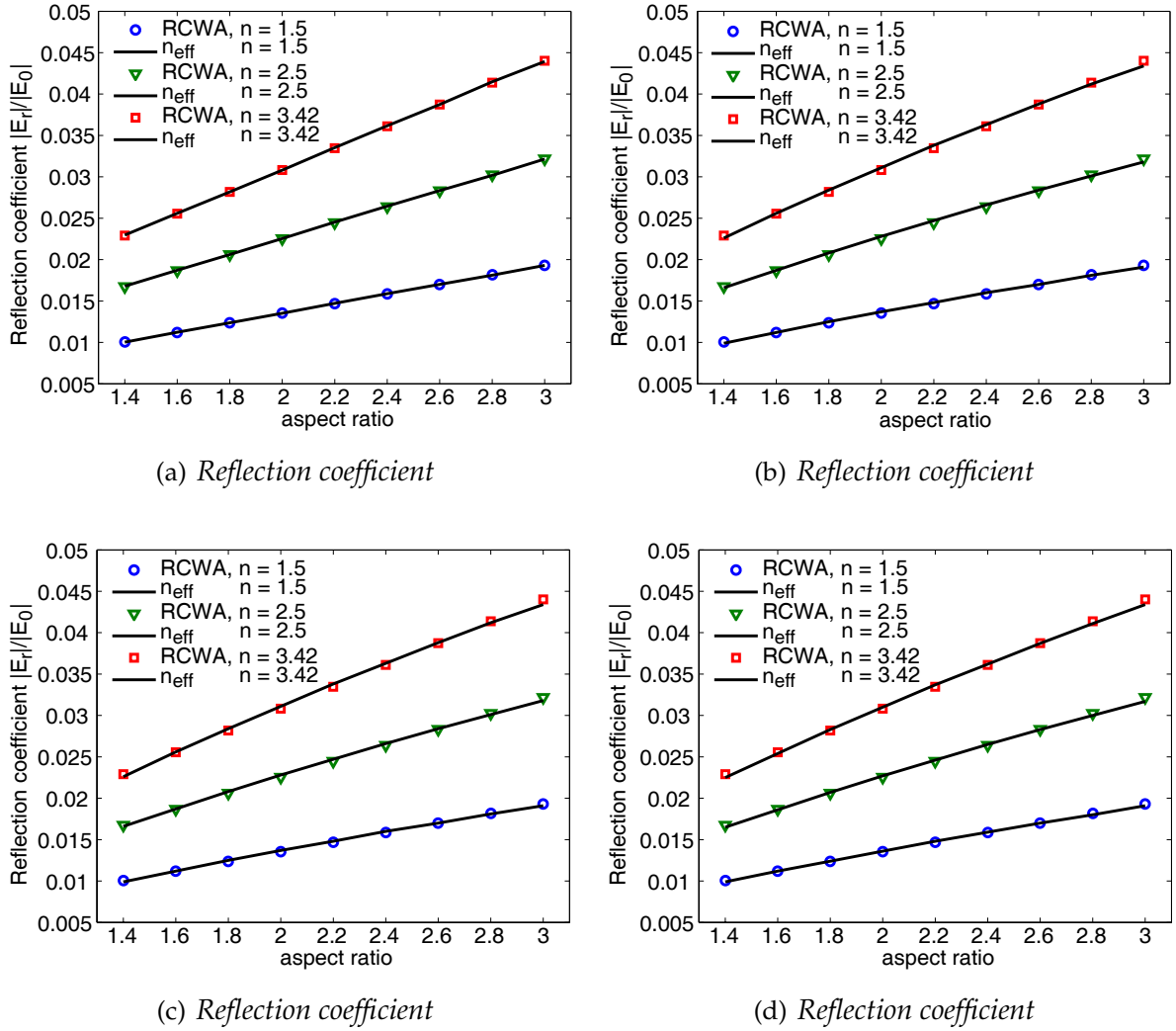

(a) *Reflection coefficient*

(b) *Reflection coefficient*

(c) *Reflection coefficient*

(d) *Reflection coefficient*

Figure 4.21: *The magnitude of the reflection coefficient for a grating structure with grating parameters:* $f = 0.5$, $\Lambda = 100\,\mu m$, $\nu = 5\,GHz$, $n = \{1.5, 2.5, 3.42\}$, $1.4 \leq AR \leq 3$. *The RCWA results are plotted along with the EMA formulation with* n_{eff} *calculated: (a) from the 'brute force' algorithm; (b) with scaling factor* Ψ *defined as a function for all background dielectrics with varying aspect ratio; (c) with* Ψ *defined as a function for all dielectrics and metal volume fractions with varying aspect ratio; (d) with* Ψ *defined for all dielectrics, metal volume fractions and frequencies with varying aspect ratio.*

lents were simulated over a range of varying aspect ratios and background materials. Fig. 4.22(a) shows good agreement between the reflection coefficients of gratings with 30% metal fill and homogenised structures with n_{eff} calculated from defined canonical structure (Section 4.5.4). The error in reflection coefficient estimation is not higher than 1.7% for structures with aspect ratios within the interval $1.6 - 2.8$, whereas

the error for bounded aspect ratios rises up to 3%. Better accuracy is obtained for gratings in which the metal fill factor is 50% or greater. The agreement is illustrated in Fig. 4.22(b) where the error in return loss calculated using the two methods approaches 1.5% for structures with values of aspect ratios from the top and bottom of the considered range and the error lower than 1% when the aspect ratio is from the middle of the considered range. The transmission coefficient for all gratings is always

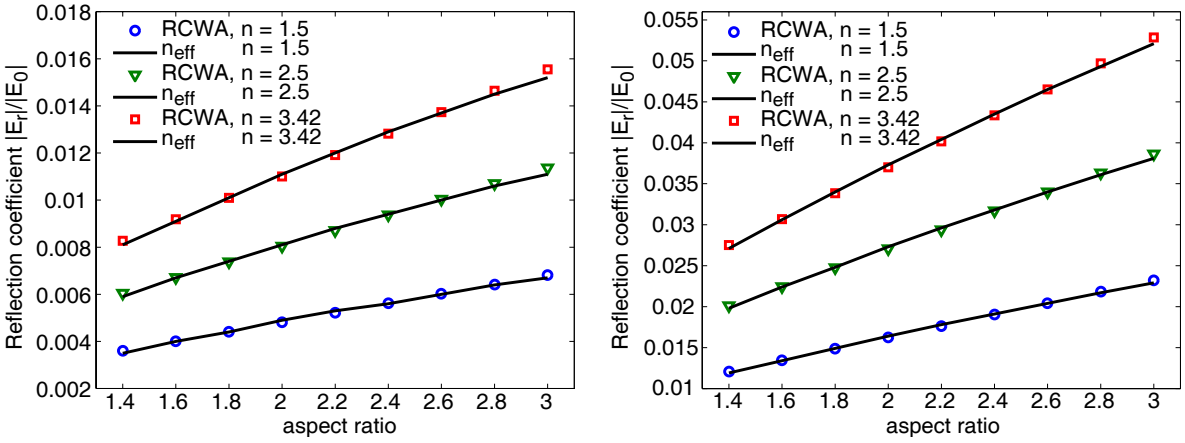

(a) $f = 0.3$ (b) $f = 0.5$

Figure 4.22: *The magnitude of the reflection coefficient for a grating structure with grating parameters:* $\Lambda = 100\,\mu m$, $\nu = 6\,GHz$, $n = \{1.5, 2.5, 3.42\}$, $1.4 \leq AR \leq 3$. *The RCWA results are plotted along with the EMA formulation with* n_{eff} *calculated from modified Maxwall Garnett formula with* Ψ *defined in Section 4.5.4 for gratings with: (a)* $f = 0.3$, *(b)* $f = 0.5$.

estimated with an error less than 0.2%. The accuracy of the presented empirical model is associated with the fact that the modified Maxwell-Garnett mixing rule, with inclusions defined as metal by frequency dependent Drude model, when used to calculate the effective dielectric constant of mixture with constituent having sharp corners appears to predict the effective dielectric constant more accurately when the metal volume fraction increases in the unit grating cell. Some aspects of this relationship have already been discussed in Section 4.5.1 and is demonstrated in Fig. 4.15.

4.6 Empirical Model for ISM Band

So far, empirical models have been investigated for selected frequencies from $1 - 10$ GHz. These are representative of on-chip signal frequencies. As high speed transistor technology develops (including non-CMOS transistors in particular) there is growing use of microwave signals at much higher frequencies. It is expected that the most widely encountered signals will be from the unlicensed bands of which there are several between 30 GHz and 200 GHz. In particular $57 - 66$ GHz, $85 - 110$ GHz, and $122 - 123$ GHz [78, 79, 80]. An empirical model is now developed for these frequencies. The homogenisation procedure to build this model was described in Section 4.4. Analysis of a grating structure with the same dimensions as the structure studied to define previous models shows that as the frequency increases the influence of the dielectric background material on reflectivity and transmissivity becomes significant.

4.6.1 Limitation of the Model

The accuracy of the algorithm use for the 'brute force' fitting of the effective refractive index to the data obtained from the numerical analysis of the grating structure is reduced with increase of applied frequency and, equivalently, the electrical thickness of the structure. Specifically, the distribution of scaling factor Ψ is well behaved up to a particular value of aspect ratio and refractive index of the background material. The smooth curve characterising the values of Ψ rapidly changes direction with values fluctuating in not regular manner. Such a distribution would require a high order polynomial or more complicated model function with a large number of coefficients in order to be represented by an analytical formulation. Moreover, such an approximation would result in high errors in reflection coefficient prediction. The transmission coefficient is always predicted with good accuracy due to its very small variation. Therefore, the presented empirical model was defined with limits related to the values of the aspect ratio and refractive index around which the first 'break' in the Ψ distribution occurs. The shorter the wavelength the more strict the limits of the model for gratings with high aspect ratio and high dielectric constant of background material. Restrictions for considered frequencies and metal fills are given in Table 4.5 for a model valid in terms of the aspect ratio, and in Table 4.6 for a model valid with respect to the background materials.

ν \ f	0.2	0.3	0.4	0.5	0.6
30 GHz	$0.6-3$	$0.4-3$	$0.4-3$	$0.2-3$	$0.2-3$
60 GHz	$0.6-3$	$0.4-3$	$0.4-3$	$0.2-3$	$0.2-3$
100 GHz	$0.6-3$	$0.4-3$	$0.4-3$	$0.2-2.6$	$0.2-1.8$
150 GHz	$0.6-3$	$0.4-3$	$0.4-2.6$	$0.2-1.8$	$0.2-1.2$
200 GHz	$0.6-3$	$0.4-3$	$0.4-2.0$	$0.2-1.4$	$0.2-1.0$

Table 4.5: *Range of aspect ratios considered. Note reduced ranges in shaded cells*

ν \ f	0.2	0.3	0.4	0.5	0.6
30 GHz	3.42	3.42	3.42	3.42	3.42
60 GHz	3.42	3.42	3.42	3.42	3.42
100 GHz	3.42	3.42	3.42	3.1	2.3
150 GHz	3.42	3.42	2.9	2.1	1.5
200 GHz	3.42	3.42	2.3	1.6	1.1

Table 4.6: *Maximum background refractive index. Note reduced ranges in shaded cells.*

The empirical model proposed in this Chapter was based on the numerical data obtained for the grating structure where some initial limitations were put on the aspect ratio. As is presented in Table 4.1, structures with metal fill factor $f = 0.2$ were analysed for aspect ratios above 0.6, while for $f = 0.3$ and $f = 0.4$ that limit was lowered to $AR = 0.4$. Other structures had aspect ratios as low as $AR = 0.2$. The limits were imposed in order to cover the typical interconnect geometry [8] where relatively wide and shallow wires are not very likely to be used.

One tendency observed during the process of collecting and analysing simulation data, but not included in the process of defining the analytical formulation due to limitations as discussed above, is worthy of being presented. Figure 4.23 illustrates the trend which occurs in the studied model of the ratio occupied by metal in the grating structure. In the structure chosen for demonstration there is an aspect ratio at which a continuously varying value of scaling factor Ψ ceases to decrease and begins to increase. It

can be observed for $f = 0.6$ and aspect ratio about 1.4 that a similar trend occurs in the real and imaginary part of the effective refractive index n_{eff} (not shown here). Further, it can be noted that for a structure illuminated by wave with frequency $\nu = 100\,\text{GHz}$, fixed metal fill factor $f = 0.6$ and refractive index $n = 2.3$ there are two structures with different aspect ratios which require very similar values of n_{eff} for the homogenised equivalent. As the magnitudes of the reflection and transmission coefficients of a single grating layer are determined not only by material properties but also by the depth of the layer, it follows that some cases can arise where the effective refractive indices are equal. Therefore the 'brute force' algorithm is still self-consistent.
This changing direction of the value Ψ only occurs when the metal fill factor is within the range 0.3 to 0.6. The location and the magnitude of the minimum values in the characteristic depend on applied frequency, dielectric material and grating depth (related to AR). The higher the frequency, metal fill, and dielectric constant, the lower the aspect ratio for which the discussed trend occurs.

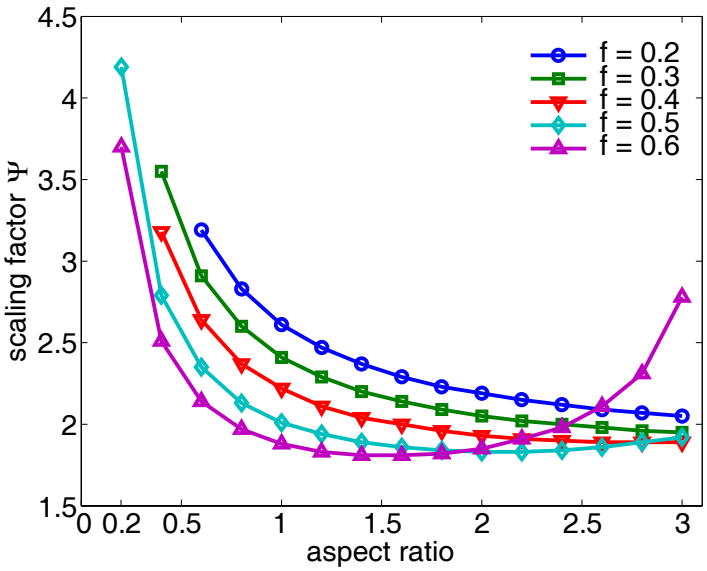

Figure 4.23: *The scaling factor Ψ predicted from the 'brute force' algorithm plotted against the aspect ratio for different values of metal fill factor f. Grating parameters: $n = 2.3$, $\Lambda = 100\,\mu m$, $\nu = 100\,GHz$, $0.2 \leq AR \leq 3$.*

4.6.2 Impact of the Metal Fill Factor

Analysis of grating structures for frequencies from the ISM band within the range $30 - 200\,\text{GHz}$ showed that the general trend in the dependence of the scaling factor Ψ on metal fill factor which was observed in the on-chip signals frequency models is also present. As illustrated in Fig. 4.24(a) and Fig. 4.24(b), within considered limits for a chosen frequency of $100\,\text{GHz}$ and varying aspect ratio, the real and imaginary parts of the effective refractive index n_{eff} of the homogenised equivalent increases gradually with an increase in the proportion of metal part in the grating structure. This trend is observed in all structures from the range of studied dielectric materials and is presented here for dielectric with refractive index $n = 2.3$.

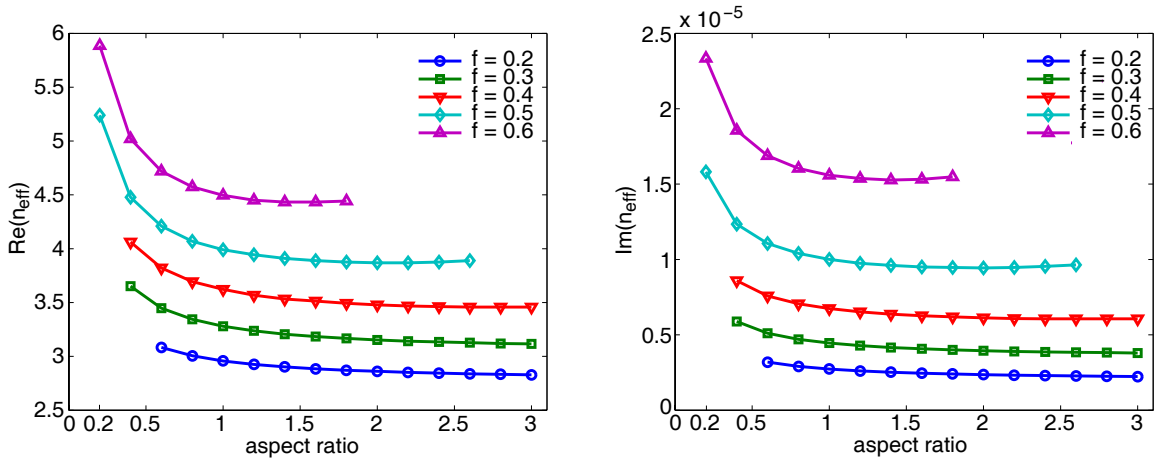

(a) $Re(n_{eff})$ (b) $Im(n_{eff})$

Figure 4.24: *(a) The real part of the effective refractive index $Re(n_{eff})$ and (b) imaginary part $Im(n_{eff})$ plotted versus aspect ratio for different values of metal fill factor f. Grating parameters: $n = 2.3$, $\Lambda = 100\,\mu m$, $\nu = 100\,GHz$, $0.2 \leq AR \leq 3$.*

The distribution of the scaling factor Ψ obtained when the 'brute force' algorithm is used to calculate the effective permittivity is presented in Fig. 4.25. There is an inverse relation in the value of Ψ, and hence n_{eff}, in terms of the metal fill factor for considered aspect ratios - the higher value of metal fill factor f, the lower value of the calculated scaling factor Ψ. This tendency can be explained in terms of established homogenisation technique by the analysis of the stronger electromagnetic field which occurs due to the multiple reflections between metal bars.

To explain this phenomenon numerical calculations for a sample grating structure were

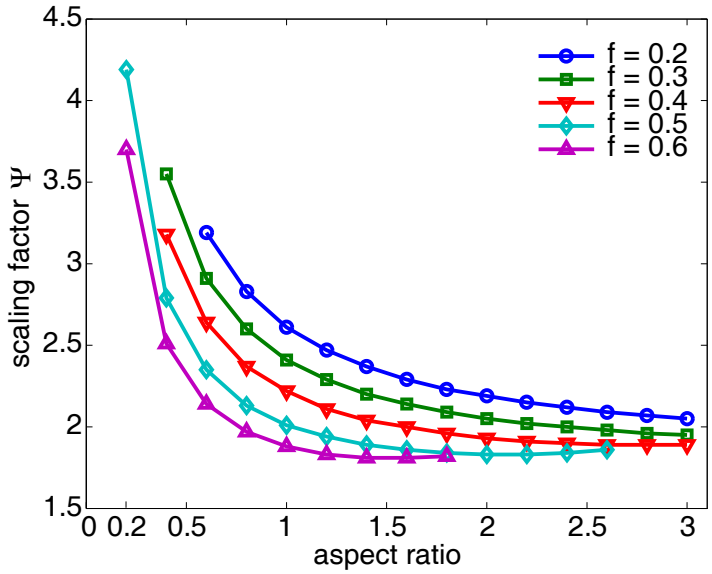

Figure 4.25: *The scaling factor Ψ predicted from the 'brute force' algorithm plotted against the aspect ratio, within considered limits, for different values of metal fill factor f. Grating parameters: $n = 2.3$, $\Lambda = 100\,\mu m$, $\nu = 100\,GHz$, $0.2 \leq AR \leq 3$.*

performed by the FDTD method for a single frequency $\nu = 100\,\text{GHz}$ and range of aspect ratios, metal fill factors, and background materials. For the sake of illustration the reference aspect ratio is chosen as $AR = 1.6$ and the dielectric constant is $n = 2.3$. Two plots of the electric field magnitude are presented in Figure 4.26(a) and Figure 4.26(b), with grating structure occupied by a metal fill in 20% and 60% respectively.
It is assumed that the homogenised equivalent has the same height as the grating part of the model. In such an homogenisation technique the original Maxwell-Garnett mixing formula does not account sufficiently for all changes occurring in the electromagnetic field. For a given aspect ratio of $AR = 1.6$ such a field becomes stronger with a reduction of the distance between metal parts and for the sharp corner inclusions it is partially accounted for in the original Maxwell-Garnett mixing rule which predicts effective dielectric constant in terms of the volume occupied by the metal fills (inclusions) and dielectric properties of the constituents. For gratings with lower metal fill factors such a field, being even weaker, spreads more widely and means that the scaling factor Ψ needs to be proportionally larger.

In Fig. 4.27 it is illustrated for a particular structure that the value of scaling factor Ψ depends on both the frequency of illuminating wave and the metal volume fraction. Grat-

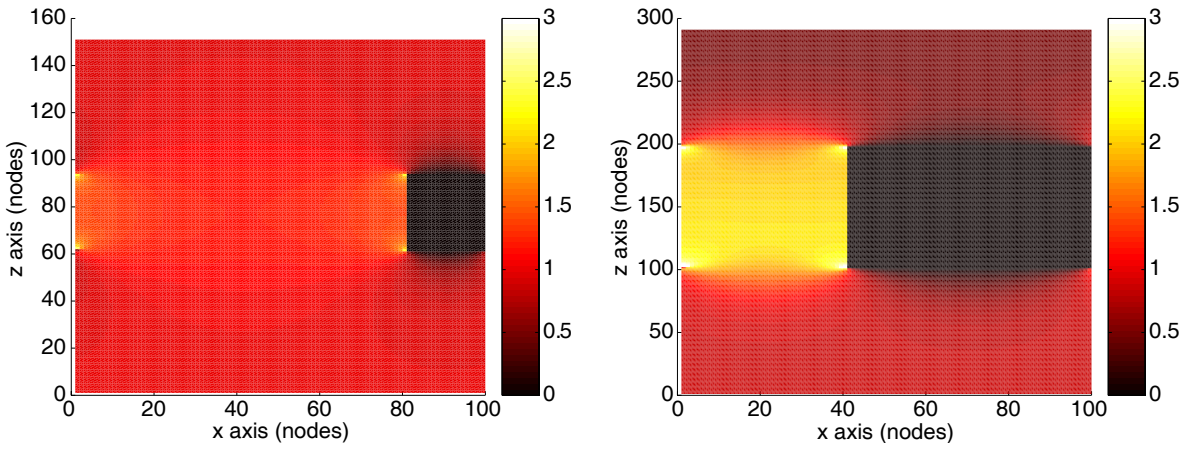

(a) $f = 0.2$ (b) $f = 0.6$

Figure 4.26: *The magnitude of the steady state electric field for a grating structure with grating parameters:* $n = 2.3$, $\Lambda = 100\mu m$, $\nu = 100$ *GHz*, $AR = 1.6$, *and: (a)* $f = 0.2$, *(b)* $f = 0.6$. *Stronger electric field accumulates in the corners of the metal parts of the gratings.*

ing structures with metal fill of 50% or more are represented by the plot in Fig. 4.27(b). These structures are characterised by their value of factor Ψ being significantly influenced by the value of applied frequency. In this case Ψ also tends to increase with the increase of dielectric refractive index of background material (not shown here). For frequencies as high as $100-200$ GHz the electrical thickness of the homogenised equivalent changes significantly and is reflected in a notable difference in the value Ψ which is related to the length of illumination wave and metal volume fraction. Figure 4.27(a) shows this for a grating structure with a metal volume fraction of 30%, and Fig 4.27(b) for a metal volume fraction equal to 50%.

4.6.3 Model Simplification

It was illustrated in Fig. 4.25 that the distribution of parameter Ψ in terms of the aspect ratio for a given metal volume fraction has an exponential characteristic. Nevertheless, for the presented model the analytical formulation is given for the range of aspect ratios $1.4 \leq AR \leq 3$. The lower limit was conveniently increased because typical interconnects tend not to have such low aspect ratios. This also allows the model to be reduced to a linear function. Hence structures with dimensions defined by metal volume fraction $f = 0.5$ illuminated by wave with frequency 200 GHz, and those with

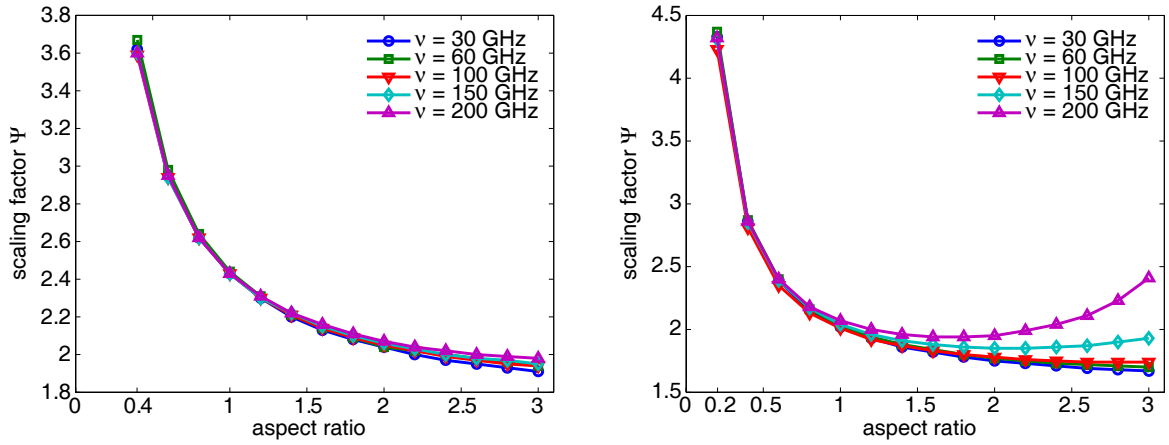

(a) $f = 0.3$ (b) $f = 0.5$

Figure 4.27: *The scaling factor* Ψ *calculated from the 'brute force' algorithm plotted against the aspect ratio for different values of illumination wave frequency. Grating parameters:* $n = 1.5$, $\Lambda = 100\,\mu m$, $0.2 \leq AR \leq 3$, *and metal fill factor: (a)* $f = 0.3$; *(b)* $f = 0.5$.

metal fill $f = 0.6$ excited by signal with frequency $150\,\text{GHz}$ and $200\,\text{GHz}$ according to the limitations set in Table 4.5 are not included in the presented analytical formulation of the model. Analysis of data obtained from numerical simulations of the studied structures showed that all variation in scaling factor Ψ in terms of the varying refractive index n of the background dielectric, metal volume fraction f, and frequency ν can be account for by a linear function of varying aspect ratio.
Hence factor Ψ is given by

$$\Psi(x_{AR}) = \alpha \cdot x_{AR} + \beta \tag{4.27}$$

and it is defined by linear least squares method, involving expansion in Taylor series (Appendix A.3, A.5) for every background material n as a function of varying aspect ratio AR where $1.4 \leq x_{AR} \leq 3$. Coefficients α and β are determined for all refractive indices n and they are represented by

$$\alpha(n) = \alpha_1 \cdot n + \alpha_2 \tag{4.28}$$

$$\beta(n) = \beta_1 \cdot n + \beta_2 \tag{4.29}$$

Both α and β are functions defined by linear regression for every metal volume fraction as a function of varying background material. Coefficients α_1, α_2, β_1, and β_2 are well

approximated for all metal fill factors f by

$$\alpha_1(f) = \alpha_{11} \cdot f + \alpha_{12} \tag{4.30}$$

$$\alpha_2(f) = \alpha_{21} \cdot f + \alpha_{22} \tag{4.31}$$

$$\beta_1(f) = \beta_{11} \cdot f + \beta_{12} \tag{4.32}$$

$$\beta_2(f) = \beta_{21} \cdot f + \beta_{22} \tag{4.33}$$

All coefficients α_1, α_2, β_1, and β_2 are functions determined by linear least squares method for every frequency[3] from considered range as a function of varying metal volume fraction. Coefficients α_{mn} and β_{mn} where $m, n = \{1, 2\}$ are accurately approximated by

$$\alpha_{11}(\nu) = \alpha_{111} \cdot \nu + \alpha_{112} \tag{4.34}$$

$$\alpha_{12}(\nu) = \alpha_{121} \cdot \nu + \alpha_{122} \tag{4.35}$$

$$\alpha_{21}(\nu) = \alpha_{211} \cdot \nu + \alpha_{212} \tag{4.36}$$

$$\alpha_{22}(\nu) = \alpha_{221} \cdot \nu + \alpha_{222} \tag{4.37}$$

$$\beta_{11}(\nu) = \beta_{111} \cdot \nu + \beta_{112} \tag{4.38}$$

$$\beta_{12}(\nu) = \beta_{121} \cdot \nu + \beta_{122} \tag{4.39}$$

$$\beta_{21}(\nu) = \beta_{211} \cdot \nu + \beta_{212} \tag{4.40}$$

$$\beta_{22}(\nu) = \beta_{221} \cdot \nu + \beta_{222} \tag{4.41}$$

Factors α_{mn1}, α_{mn2}, β_{mn1}, and β_{mn2} where $m, n = \{1, 2\}$ are given in Table 4.7.

α_{111}	0.0032	α_{211}	−0.0050	β_{111}	−0.0027	β_{211}	0.0056
α_{112}	−0.0049	α_{212}	0.3236	β_{112}	−0.0335	β_{212}	−2.0725
α_{121}	−0.0005	α_{221}	0.0008	β_{121}	0.0002	β_{221}	−0.0006
α_{122}	−0.0133	α_{222}	−0.2523	β_{122}	0.0287	β_{222}	3.0087

Table 4.7: *Coefficients α_{mn1}, α_{mn2}, β_{mn1}, and β_{mn2} where $m, n = \{1, 2\}$, for Ψ calculations according to the Eq. (4.27) - (4.41).*

The presented model is valid under the assumption that all limitations presented in Subsection 4.6.1 are observed.

The empirical model can be expressed in the multidimensional Taylor series form (Appendix A.1) and the coefficients are given in Table 4.8

[3]The unit for frequency has been set to GHz

$\Psi\big\vert_{\mathbf{0}}$	β_{222}	$\frac{\partial\Psi}{\partial x_{AR}}\big\vert_{\mathbf{0}}$	α_{222}	$\frac{\partial\Psi}{\partial n}\big\vert_{\mathbf{0}}$	β_{122}	$\frac{\partial\Psi}{\partial f}\big\vert_{\mathbf{0}}$	β_{212}
$\frac{\partial\Psi}{\partial \nu}\big\vert_{\mathbf{0}}$	β_{221}	$\frac{\partial^2\Psi}{\partial x_{AR}\partial n}\big\vert_{\mathbf{0}}$	$2\alpha_{122}$	$\frac{\partial^2\Psi}{\partial x_{AR}\partial f}\big\vert_{\mathbf{0}}$	$2\alpha_{212}$	$\frac{\partial^2\Psi}{\partial x_{AR}\partial \nu}\big\vert_{\mathbf{0}}$	$2\alpha_{221}$
$\frac{\partial^2\Psi}{\partial n\partial f}\big\vert_{\mathbf{0}}$	$2\beta_{112}$	$\frac{\partial^2\Psi}{\partial n\partial \nu}\big\vert_{\mathbf{0}}$	$2\beta_{121}$	$\frac{\partial^2\Psi}{\partial f\partial \nu}\big\vert_{\mathbf{0}}$	$2\beta_{211}$	$\frac{\partial^3\Psi}{\partial x_{AR}\partial n\partial f}\big\vert_{\mathbf{0}}$	$3!\alpha_{112}$
$\frac{\partial^3\Psi}{\partial x_{AR}\partial n\partial \nu}\big\vert_{\mathbf{0}}$	$3!\alpha_{121}$	$\frac{\partial^3\Psi}{\partial x_{AR}\partial f\partial \nu}\big\vert_{\mathbf{0}}$	$3!\alpha_{211}$	$\frac{\partial^3\Psi}{\partial n\partial f\partial \nu}\big\vert_{\mathbf{0}}$	$3!\beta_{111}$	$\frac{\partial^4\Psi}{\partial x_{AR}\partial n\partial f\partial \nu}\big\vert_{\mathbf{0}}$	$4!\alpha_{111}$

Table 4.8: *Coefficients for the Taylor series expansion of Ψ expressed in terms of coefficients given in Table 4.7.*

Figure 4.28 illustrates the distribution of the parameter Ψ for exemplar structure with grating part occupied by 50% metal, dielectric background with refractive index $n = 1.5$, and frequency $\nu = 100\,\text{GHz}$, where the reference data obtained from the 'brute force' algorithm are plotted along with those calculated by least squares method at each of the three steps necessary to build the analytical formulation of the complex model. Figure 4.28(a) shows the scaling factor Ψ when approximated by a linear function for all refractive indices n with varying aspect ratio and is compared with the reference data. Further, Fig. 4.28(b) demonstrates the variation in Ψ when approximated in terms of all background dielectrics and metal volume fractions f as a function of aspect ratio plotted with reference data. In Fig. 4.28(c) results for Ψ calculations in terms of all n, all f, and all frequencies ν versus varying aspect ratio are plotted along with data obtained from the developed algorithm. Finally, Fig. 4.28(d) illustrates the accuracy in Ψ estimation obtained for all three steps of building the complex model compared with the value obtained from the fitting algorithm. All three linear regressions are characterised by an error not higher than 2% in scaling factor Ψ estimation.

4.6.4 Numerical Validation of Analytical Model

The validity of the analytical model was examined by an approach analogous to that presented in Subsection 4.5.2. For each of the steps taken to construct the empirical model, the magnitude of the reflection and transmission coefficients calculated for the grating structure and its homogenised equivalent were compared. Figure 4.29 and Fig. 4.30 show the agreement between data obtained from numerical calculations for grating structure using RCWA and calculations of reflection and transmission coefficients using the characteristic matrix method where n_{eff} was obtained from the modified Maxwell-Garnett mixing rule with scaling factor Ψ calculated from Eq. (4.27).

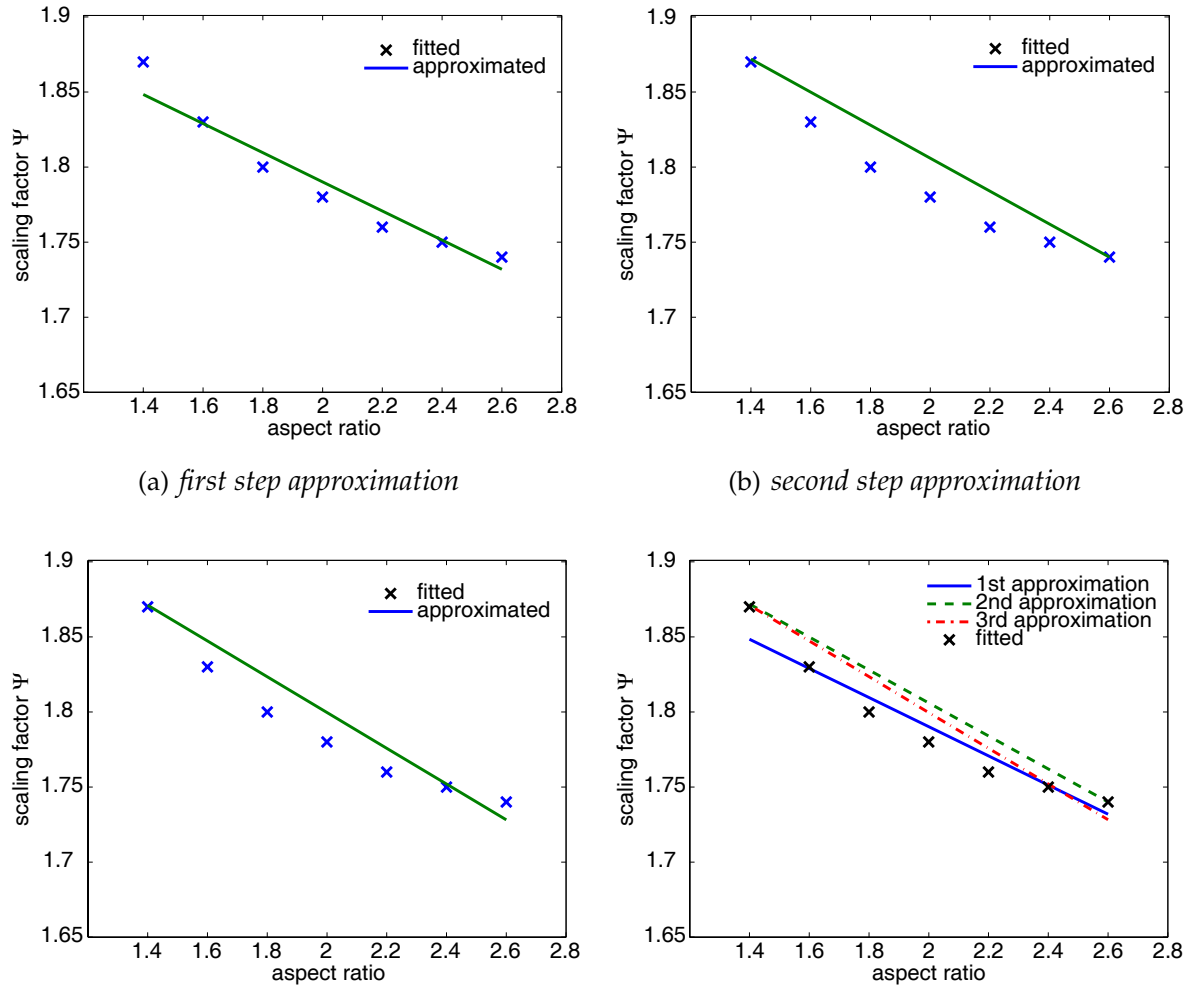

(a) *first step approximation*

(b) *second step approximation*

(c) *third step approximation*

(d) *comparison*

Figure 4.28: *The fitted values obtained from the 'brute force' algorithm plotted as crosses along with approximated values of scaling factor Ψ defined as a function for: (a) all background dielectrics with varying aspect ratio; (b) all dielectrics and metal volume fractions with varying aspect ratio; (c) all dielectrics, metal volume fractions and frequencies with varying aspect ratio plotted as continuous line. Figure (d) shows comparison of Ψ for all approximation steps together. Grating parameters: $f = 0.5$, $\Lambda = 100\,\mu m$, frequency $\nu = 100\,GHz$, $n = 1.5$, $1.4 \leq AR \leq 3$.*

Figure 4.29(a) and Fig. 4.29(b) show the high accuracy in the estimation of the reflection and transmission coefficients when the grating structure is replaced by a homogenised equivalent with n_{eff} obtained from the 'brute force' fitting. The very low errors demonstrated in Fig. 4.6 increase due to the curve fitting procedure applied in order to analytically interpret the changes of each variable in the four dimensional parameter space.

This tendency is expected and the errors for reflectivity estimation at each step of building the empirical model in most structure is within $0-3\%$ and it tends to reach the maximum value for an aspect ratio bounding the considered set whereas in most cases it is less than 1%. On the other hand, transmissivity is always predicted with an error less than 99%.

It was noted that the complex empirical model suffers from an increase in the error in reflectivity estimation when applied to some structures with metal part having an aspect ratio from the upper bound of considered ranges when embedded in dielectric with refractive index $n > 3$. In these cases the error is within $4-8\%$. To address this issue further limitations in terms of the background material can be set as presented in Table 4.9. Since the permittivity of the low-k dielectrics used in the commercial products is predicted to decreas [8] with developing technology the model is likely to satisfy the menufacturable needs.

ν \ f	0.2	0.3	0.4	0.5	0.6
30 GHz	3	3.42	3.42	3.42	3.42
60 GHz	3	3.42	3.42	3.42	3.42
100 GHz	3	3.42	3.42	2.9	2.3
150 GHz	3	3	2.7	2.1	–
200 GHz	3	3	2.3	–	–

Table 4.9: *Maximum background refractive index. Note reduced ranges in shaded cells*

Visual demonstration of the agreement in reflection and transmission coefficients estimation by the model for all steps is presented in the remaining subfigures of Fig. 4.29 and Fig. 4.30. The reference structure is chosen as grating with period $\Lambda = 100\,\mu$m occupied by metal in 50% and background dielectric with refractive indices $n = \{1.5, 2.0, 2.5\}$ illuminated by normally incident wave with free-space wavelength $\lambda = 3\,$mm ($\nu = 100\,$GHz). The reflection and transmission coefficients obtained from the homogenised structure with n_{eff} calculated from modified Maxwell-Garnett mixing rule when factor Ψ is determined by the linear distribution defined for all background materials as a function of varying aspect ratio are plotted along with data obtained for the reference structure in Fig. 4.29(c) and Fig. 4.29(d) respectively. Figure 4.30(a)

and Fig. 4.30(b) illustrate similar agreement when factor Ψ is defined for all background materials and all metal fill factors from studied range as a function of changing aspect ratio. Finally, the empirical model is used to estimate factor Ψ, and consequently n_{eff}, and the reflection and transmission coefficients of the homogenised equivalent; these are shown in Fig. 4.30(c) and Fig. 4.30(d) with calculations for the reference structure.

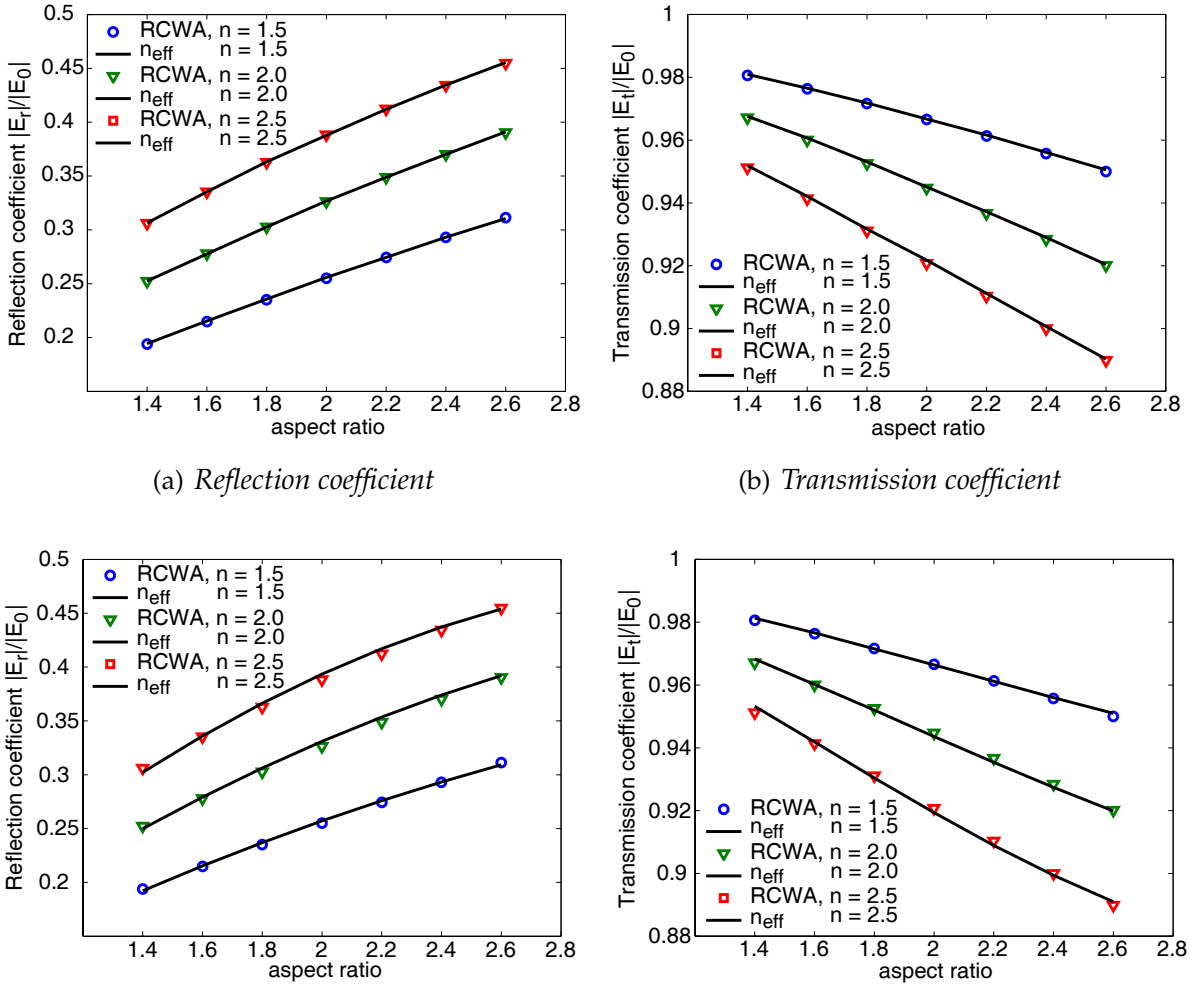

(a) *Reflection coefficient* (b) *Transmission coefficient*

(c) *Reflection coefficient* (d) *Transmission coefficient*

Figure 4.29: *The magnitude of the reflection and transmission coefficients for a grating structure with grating parameters:* $f = 0.5$, $\Lambda = 100\,\mu m$, $\nu = 100\,GHz$, $n = \{1.5, 2.0, 2.5\}$, $1.4 \leq AR \leq 3$. *The RCWA results are compared with the EMA formulation with* n_{eff} *calculated: (a,b) from 'brute force' algorithm; (c,d) with scaling factor* Ψ *defined as a function for all* n *with varying aspect ratio.*

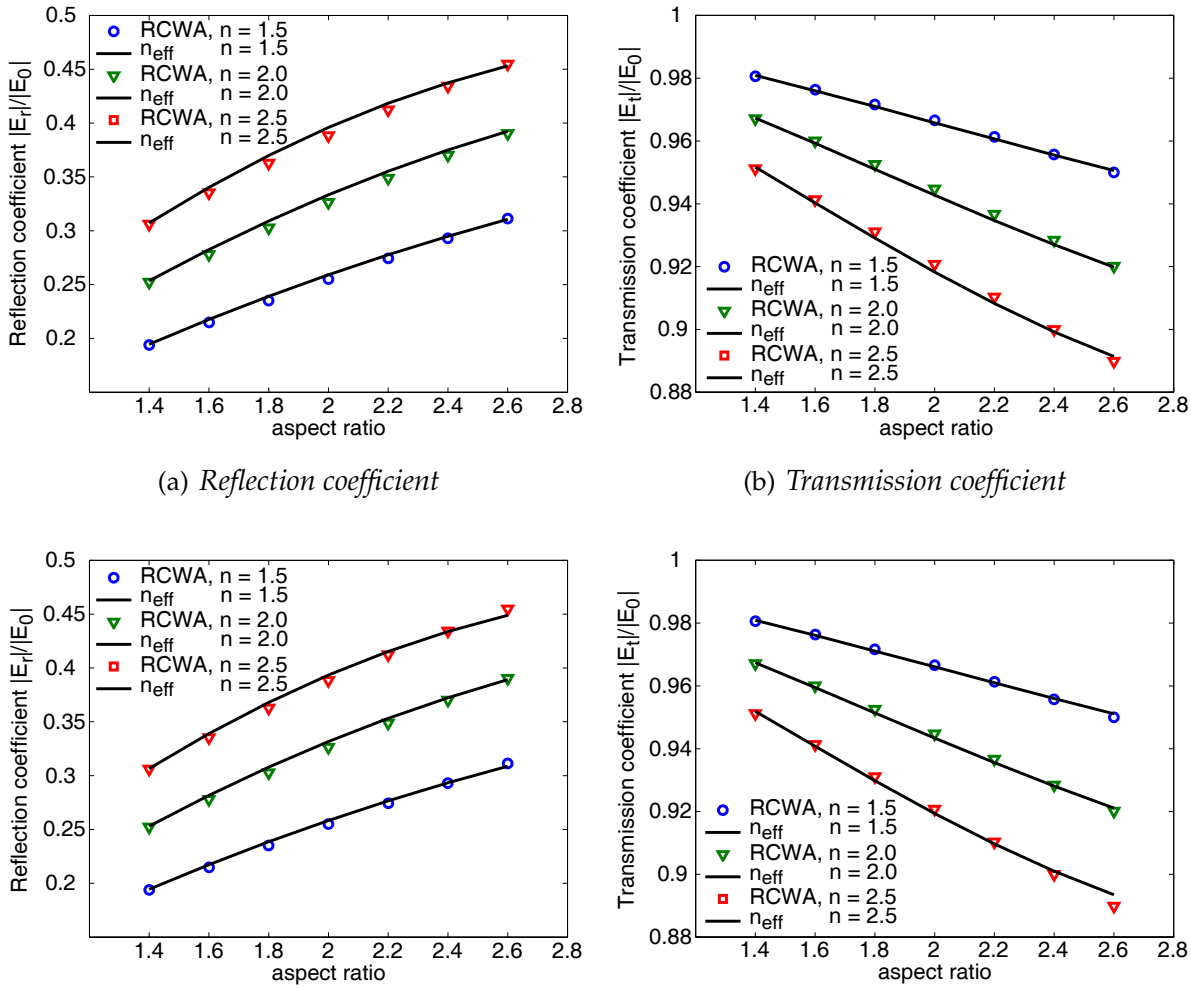

(a) *Reflection coefficient* (b) *Transmission coefficient*

(c) *Reflection coefficient* (d) *Transmission coefficient*

Figure 4.30: *The magnitude of the reflection and transmission coefficients for a grating structure with grating parameters:* $f = 0.5$, $\Lambda = 100\,\mu m$, $\nu = 100\,GHz$, $n = \{1.5, 2.0, 2.5\}$, $1.4 \leq AR \leq 3$. *The RCWA results are compared with the EMA formulation with* n_{eff} *calculated: (a,b) with* Ψ *defined as a function for for all* n *and* f *with varying* AR*; (c,d) with* Ψ *defined as a function for all* n, f, ν *with varying* AR.

4.7 Empirical Model for On-Chip Signals Band Discussion

In this Section the validity of the empirical model for on-chip signal band is explored for non-normal angles of incidence. For broad applicability, it is essential to have a homogeneised equivalent that works for a range of incident angles. The validity of

the model for differently shaped metal inclusions, specifically the case of tapered inclusions, is investigated. The defined empirical model is compared with the empirical mixing model presented by Karkkainen and Sihvola *et al.* in [65]. The bounds that limit the range of predictions for the effective permittivity are considered and presented first.

4.7.1 General Bounds

The calculated effective permittivity varies according to the particular mixing rules used to analyse a given mixture. However, there are theoretical bounds to the range of calculated effective permittivieties, e.g. Wiener and Hashin-Shtrikman bounds (Eq. (2.32)-(2.35)). It was verified that in a set of about 7000 simulations of the grating structure run to define each of the empirical models all effective refractive indices are well within the Wiener bounds. Nevertheless, the predicted n_{eff} has values close to the lower limit. This is related to the specific alignment of the grating structure (single layer of interconnects) and the angle of incidence wave. Such regular and linearly distributed arrangement of the inclusions with the field vector perpendicular to the grating surface results in an effective permittvity from the bottom range of the possible values defined by Wiener bounds, as was stated in Subsection 2.6.1. The upper limit is several orders higher in magnitude, hence even if satisfied, for the purpose of the analyses of this particular grating structure it can be lowered by replacing it with the Hashin-Shtrikman lower limit. It is illustrated in Fig. 4.31, for two random structures, that the real parts of the effective permittivity obtained from the empirical model are within the lower limits of the Wiener and Hashin-Shtrikman bounds.
The more strict Hashin-Shtrikman bounds overestimate the obtained values of n_{eff}. These limits are based on the Maxwell-Garnett mixing rule for the complementary mixtures with transfered constituents ($\epsilon_i \rightarrow \epsilon_e$, $\epsilon_e \rightarrow \epsilon_i$, $f \rightarrow 1 - f$), Subsection 2.6.1, and the lower limit is just the classical Maxwell-Garnett rule with $\epsilon_i > \epsilon_e$. Therefore, for the analysed interconnect grating structure it can be assumed that the upper bound for the effective permittivity is the classical Maxwell-Garnett rule whereas the lower bound is the Wiener lower limit.

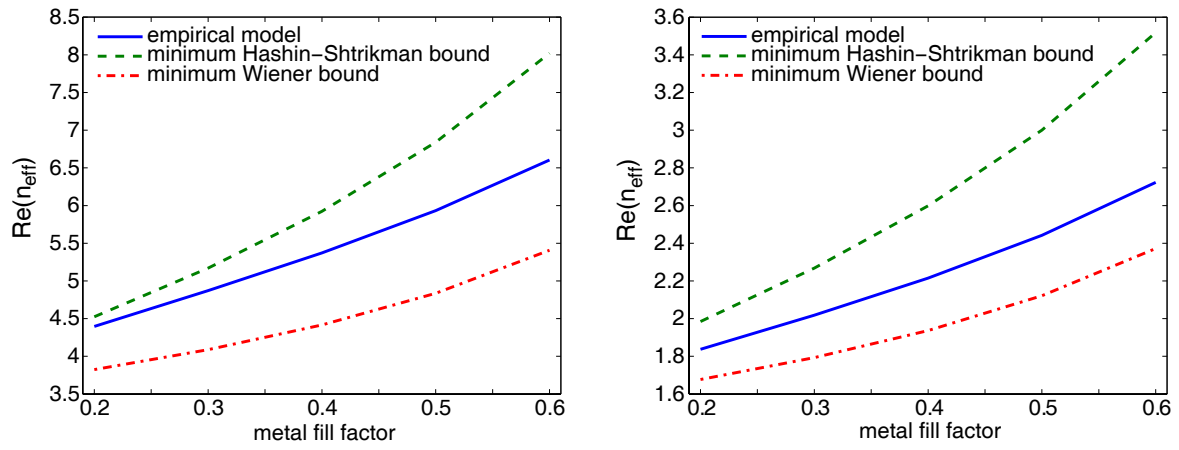

(a) *AR = 1, n = 3.42* (b) *AR = 3, n = 1.5*

Figure 4.31: *Real part of the effective permittivity of the grating structure compared with theoretical bounds for gratings with: (a) AR = 1 and n = 3.42, (b) AR = 3 and n = 1.5, where* $0.2 \leq f \leq 0.6$, $\nu = 5\,GHz$, $\Lambda = 100\,\mu m$.

4.7.2 Angle of Incidence

Since the empirical model for the on-chip signals frequency band (Section 4.5.4) was defined for the range of metal-dielectric grating structures illuminated by a normally incident plane wave, in this Subsection the accuracy of the model over a range of incidence directions is presented.

The TM polarised plane wave with the electric field vector $\mathbf{E}_{TM}$ coplanar with the grating vector **K**, as shown in Fig. 4.32, illuminates the grating structure with incidence angle θ within $-90° < \theta < 90°$. The grating period Λ and grating height h are also indicated. Due to the symmetry of the grating structure the response for the incidence angles with opposite sign is the same.

The reflection and transmission coefficient as a function of θ were compared for both the detailed structure and its homogenised equivalent. Plots of the data are shown in Fig. 4.33(a) and Fig. 4.33(b). The agreement is within 5% over the interval $-30° \leq \theta \leq 30°$ as is illustrated in Fig. 4.33(c) for the error in reflection coefficient estimation and in Fig. 4.33(d) for transmission coefficient.

The analysis shows that the empirical model, even if defined with respect to the normally incidence plane wave, can still be used with confidence to estimate the return and transmission losses over a relatively wide range of incidence angles.

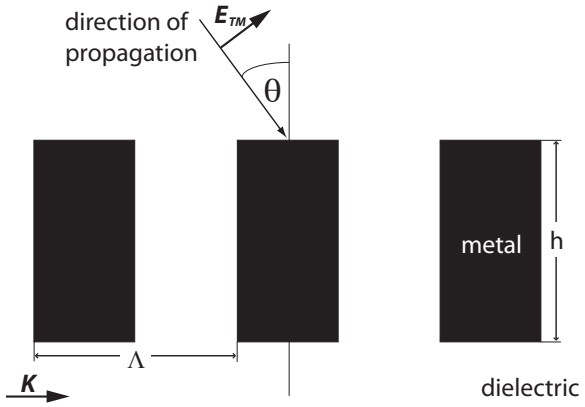

Figure 4.32: *Diagram of grating structure with rectangular profile and period Λ, grating height h, grating vector $\mathbf{K}$, TM electric field polarisation $\mathbf{E}_{TM}$, and incidence angle θ.*

4.7.3 Trapezoidal Inclusions

The empirical model defined in Section 4.5.4 for the on-chip signals frequency was based on the analysis of the grating structure with four varying parameters. Since the model can be used for the grating structure illuminated by a plane wave with incidence angle $-30^\circ \leq \theta \leq 30^\circ$ with an error less than 5% for the reflection and transmission coefficients prediction, the next consideration was focused on the validity of the model for gratings with trapezoidal cross section as is depicted in Fig. 4.34. Such gratings sometimes can be found in fabricated interconnect structures [7].

The rectangular gratings, see Fig. 4.32, were reshaped such that the metal fill factor, grating height and dielectric background were kept constant. Therefore, the only varying dimension is the sidewall angle θ_s that determines the taper of the trapezoid. The angle θ_s was considered up to a maximum of 20°. The validation was carried out over the range of studied geometries and an illustration of the agreement obtained for trapezoidal gratings with the sidewall angle of 5°, metal fill factor $f = 0.5$, aspect ratio $AR = 2$ floated in the background dielectric $n = 2.5$ is shown in Fig. 4.35. The reflection and transmission coefficients, Fig. 4.35(a) and Fig. 4.35(b), are plotted along with the errors, Fig. 4.35(c) and Fig. 4.35(d), calculated for the rectangular and trapezoidal gratings to distinguish the difference between them, and the errors between each type of grating and their homogenised equivalent obtained from the empirical model. The plots illustrate the distribution of each calculated value in terms of the changing angle of incidence. Hence, it was verified that the model, without modification, estimates

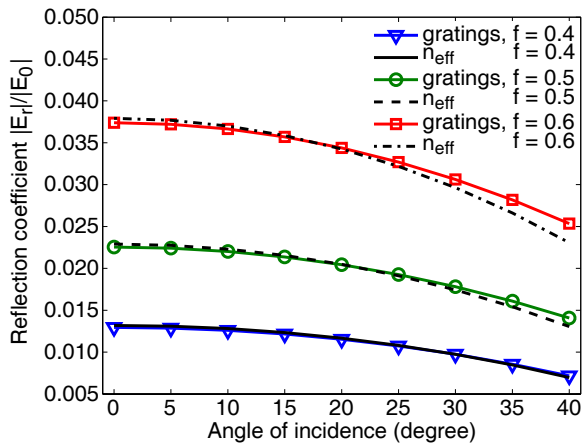

(a) *Reflection coefficient*

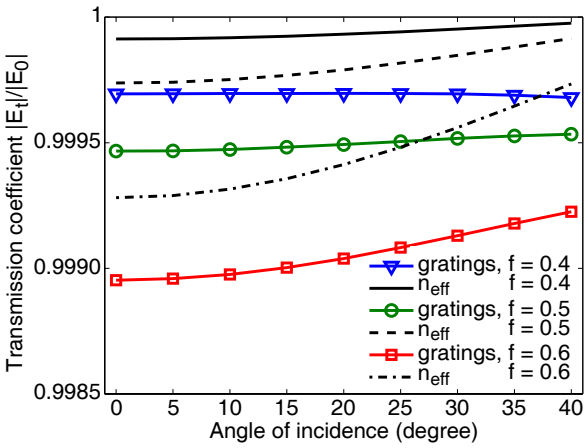

(b) *Transmission coefficient*

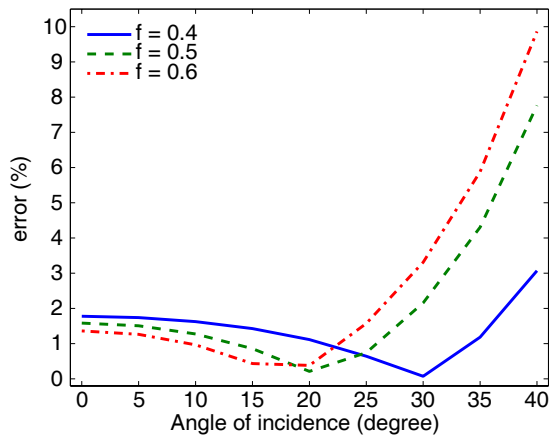

(c) *Error in reflection*

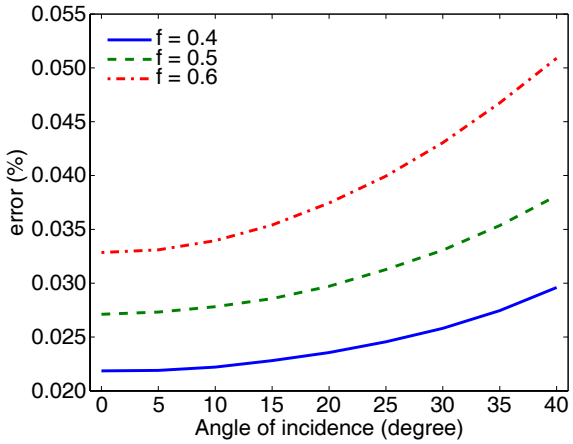

(d) *Error in transmission*

Figure 4.33: *The magnitude of the (a) reflection and (b) transmission coefficients for a grating structure compared with the homogenised equivalent. The error in (c) reflection and (d) transmission coefficients calculated between gratings and their homogeneous equivalents. Grating parameters:* $f = \{0.4, 0.5, 0.6\}$, $AR = 2$, $\Lambda = 100\,\mu m$, $\nu = 5\,GHz$, $n = 2.5$, $0° \leq \theta \leq 40°$.

the reflection and transmission coefficients with similar accuracy and for the same incidence angles range as in the case of having corresponding rectangular inclusions, for inclusions with sidewalls with an angle of up to $5°$.

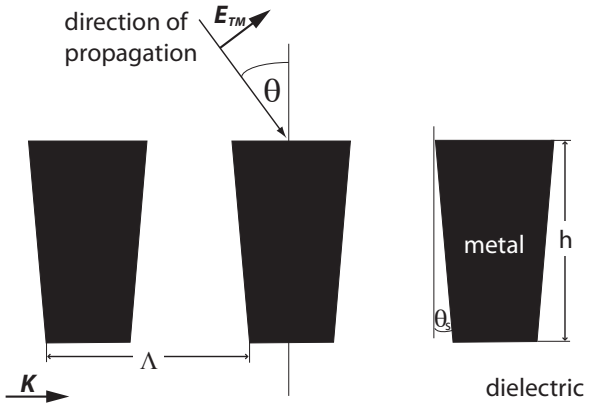

Figure 4.34: *Diagram of grating structure with trapezoidal profile and period Λ, grating height h, grating vector $\mathbf{K}$, TM electric field polarisation $\mathbf{E}_{TM}$, incidence angle θ, and sidewall angle θ_s.*

4.7.4 Comparison with Other Empirical Models

The electric fields in random dielectric mixtures of two components were studied by Karkkainen and Sihvola *et al.* [65]. The reported work shows that the effective permittivity of a mixture defined as a periodic structure with many randomly located inclusions per period can be succesfully represented by existing mixing models. The v-model, Eq. (2.36), that encompasses the Maxwell-Garnett, Bruggemann, and Coherent Potential mixing rules was used as a base to define the empirical mixing models. Since the value of the parameter v characterizes the specific mixing rule, it was used as a parameter which accounts for the change in the parameter space chosen for the mixture - inclusion volume fraction and permittivity contrast $k = \epsilon_i/\epsilon_e$. Such an approach gave more flexibility to the model and by determining the change of the parameter v with respect to the considered mixtures the two empirical models based on numerical data were defined.

It is demonstrated in Fig. 4.36 that the distribution of the value of scaling factor Ψ used to define the empirical model for on-chip signals frequency band (Section 4.5.4) has a similar trend, when expressed with respect to the change in metal volume fraction, to that presented in the quoted paper for the v parameter. The interconnects grating structure with aspect ratio $AR = 1$ has a distribution of the scaling factor Ψ, see Fig. 4.36(a), similar to that of the parameter v for the mixture with permittivity contrast $k > 1$, see Fig. 4.36(b). Furthermore, the grating structure with the maximum aspect ratio $AR = 3$ has the values of factor Ψ, see Fig. 4.36(c), similarly distributed to the values of param-

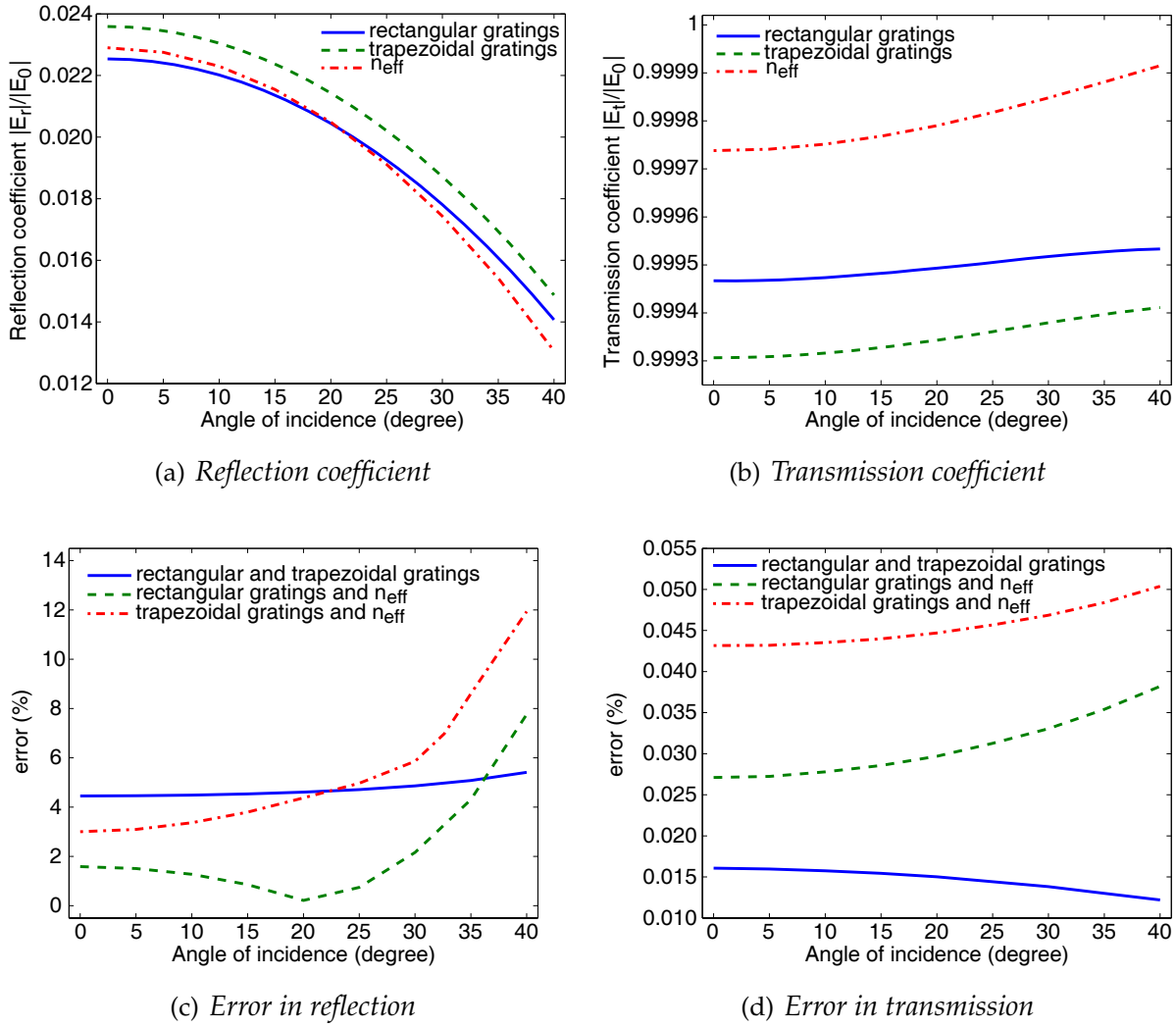

(a) *Reflection coefficient*

(b) *Transmission coefficient*

(c) *Error in reflection*

(d) *Error in transmission*

Figure 4.35: *The magnitude of the (a) reflection and (b) transmission coefficients for a grating structure with rectangular, and trapezoidal profile, and homogenised equivalent. The error in (c) reflection and (d) transmission coefficients calculated between gratings with rectangular and trapezoidal profile and between grating structures and their homogeneous equivalents. Grating parameters:* $f = 0.5$, $AR = 2$, $\Lambda = 100\,\mu m$, $\nu = 5\,GHz$, $n = 2.5$, $0° \leq \theta \leq 40°$.

eter v for mixtures with low permittivity contrast $k < 1$, see Fig. 4.36(d).
Presented results and a comparison with other empirical mixing models shows that the classical mixing rules are more widely applicable than initially envisaged.

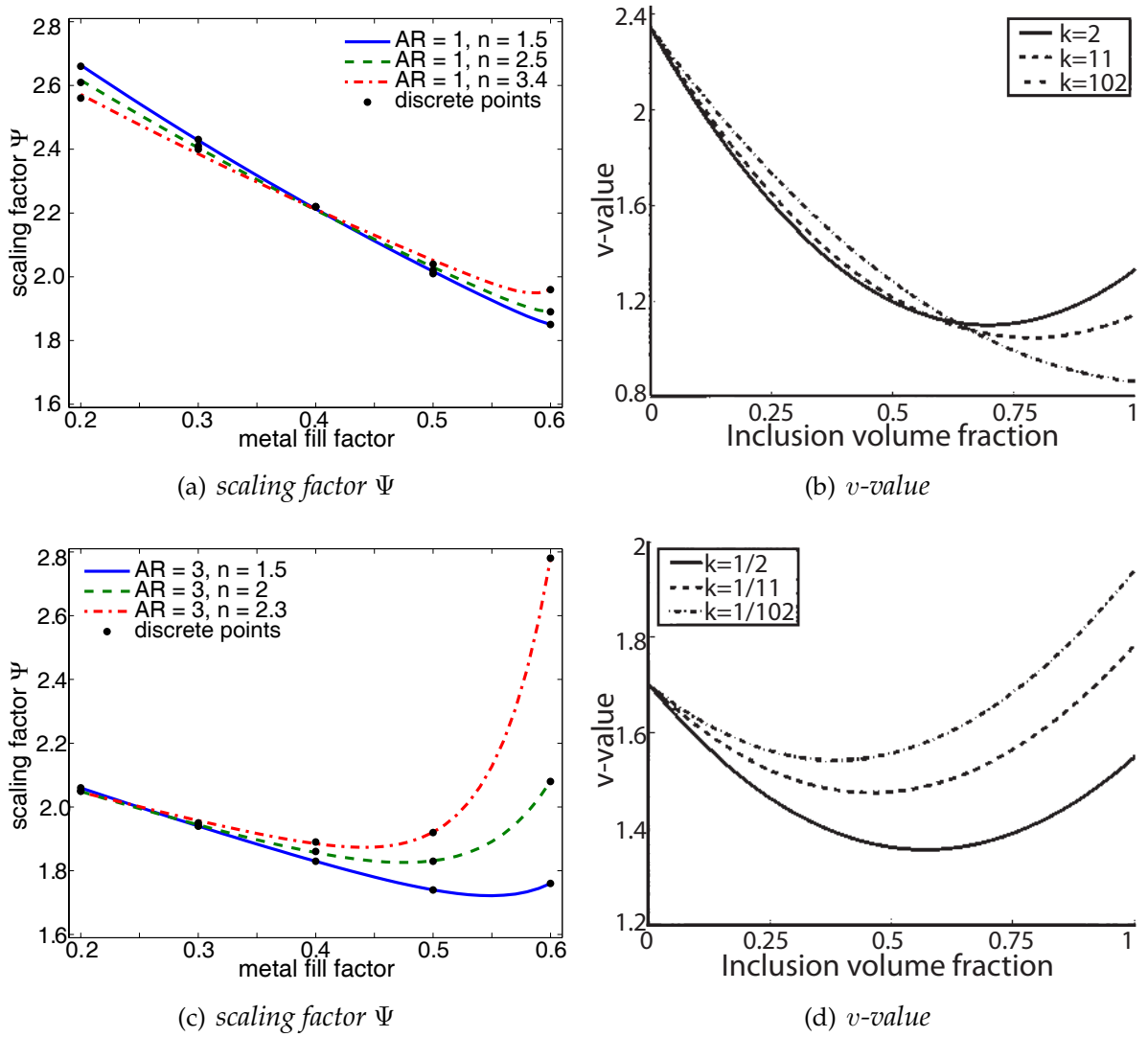

(a) *scaling factor* Ψ (b) v*-value*

(c) *scaling factor* Ψ (d) v*-value*

Figure 4.36: *The value of the scaling factor* Ψ *calculated for the grating structure with: (a)* $AR = 1$*, (c)* $AR = 3$*; and the value of the parameter* v *obtained for the permittivity contrast: (b)* $k > 1$*, (d)* $k < 1$ *(reproduced from Karkkainen et al., Fig. 5(a,b)). Grating parameters:* $0.2 \leq f \leq 0.6$*,* $AR = \{1, 3\}$*,* $\Lambda = 100\,\mu m$*,* $\nu = 100\,GHz$*,* $n = \{1.5, 2, 2.3, 2.5, 3.42\}$

4.8 Summary

New empirical mixing models based on the modified Maxwell-Garnett rule, and defined in terms of the introduced scaling factor Ψ, have been presented for interconnect structure in two frequency bands ($1 - 10\,$GHz, $30 - 200\,$GHz). A wide range of grating parameters (metal fill factor, aspect ratio, dielectric background) were considered in order to cover the likely practical interconnect geometries and clock frequencies. The

homogenisation procedure has been presented and the 'brute force' algorithm and its accuracy (error less than 0.3%) with respect to each of the considered parameters was discussed.
Each of the defined empirical models was supported with a detailed discussion on the impact of the individual parameters, and the homogenisation technique itself, on the distribution of the scaling factor Ψ. The on-chip signals frequency empirical model was defined for two sets of aspect ratio values: $0.2 - 3$ and $1.4 - 3$. The reduced interval, $1.4 - 3$, was chosen to address the typical interconnect dimensions found in ICs. Hence, for the wider range of aspect ratios the empirical model is formulated by the combination of exponential functions whereas the minimized range of aspect ratios allowed the characterisation of the model via a linear dependence.
The empirical model for the ISM band frequencies was formulated only for the reduced range of aspect ratios and due to the rapid change in the Ψ distribution, obtained from the 'brute force' algorithm, some initial limits on the individual parameters have been introduced.

The accuracy of the complex models is discussed in terms of the approximated value of the scaling factor Ψ compared with that obtained by 'brute force'. Furthermore, the models are applied to the calculation of the reflection and transmission coefficients of the homogenised structure and are compared with the adequate coefficients obtained for the detailed structure. The accuracy of the on-chip signals frequency models are better than 2.7% and for the ISM band frequency model the error is not higher than 3%.

It was validated that the effective refractive indices calculated from the empirical models are well within the Wiener bounds. Nevertheless, the upper bound, due to its relatively high magnitude, can be succesfully reduced for the studied canonical structure by adopting for the upper bound the lower Hashin-Shtrikman bound.
The model was also validated by considering non-normal angles of incidence and in the range of angles within $\pm 30^{\circ}$ the model is accurate to 5%. Finally, the model is validated with respect to the change in the grating profile and it is shown that it can still be applied to trapezoidal gratings, with sidewall angles up to 5°, with similar error not higher than 5%.
The empirical model is compared with other empirical mixing models reported in the literature. It is illustrated that the scaling factor Ψ and its equivalent, from the reported work, has a similar trend in the distribution of its value.

Chapter 5

Free-Space Measurements

5.1 Introduction

This Chapter presents measurements of metal-air gratings placed on a dielectric sheet at X-band frequencies ($8.2-12.4$ GHz). These free-space measurements are an essential step in the validation of the concept of the homogenisation of a single layer of interconnects. Free-space measurement is a challenging task due to the sensitivity of the system to the surrounding environment, therefore appropriate care needs to be taken during the calibration and measurement procedure.

The contents of this Chapter are as follows. In Section 5.2 the background for the free-space measurement technique is provided, Section 5.3 the experimental design is presented, Section 5.4 contains the description of the equipment and calibration procedure, and Section 5.5 depicts the measurement results compared with numerical calculations.

5.2 Background

In the late 19^{th} century scientist were trying to find evidence for a link between light and electromagnetic propagation. The mathematical theory given by J. C. Maxwell [81] predicted the existence of electromagnetic waves propagating through space at the speed of light and drew the conclusion that light itself is such a wave.
The first successful experimental demonstration of Maxwell's hypothesis was made by H. Hertz [82, 83, 84]. The concept of the experiment is illustrated in Fig. 5.1. Hertz

used an oscillator made of brass knobs connected to an induction coil and capacitor, and separated by a narrow gap over which sparks could discharge with an oscillation at a frequency related to the values of the capacitance and inductance of the coil. The emitted radiation was detected by a simple receiver consisting of a looped wire with small knobs separated by a tiny air gap. The receiver was designed so that current oscillating in the wire would have a natural period close to that of the transmitter. When the oscillator was turned on, the electromagnetic wave emitted by the oscillator's sparks, induced an oscillating current in the receiver loop. This was signaled by sparks occurring across the receiver air gap. This experiment was the first demonstration of the transmission and reception of electromagnetic waves. In more advanced experiments Hertz proved that the electromagnetic waves propagate with a velocity equal to the velocity of light.

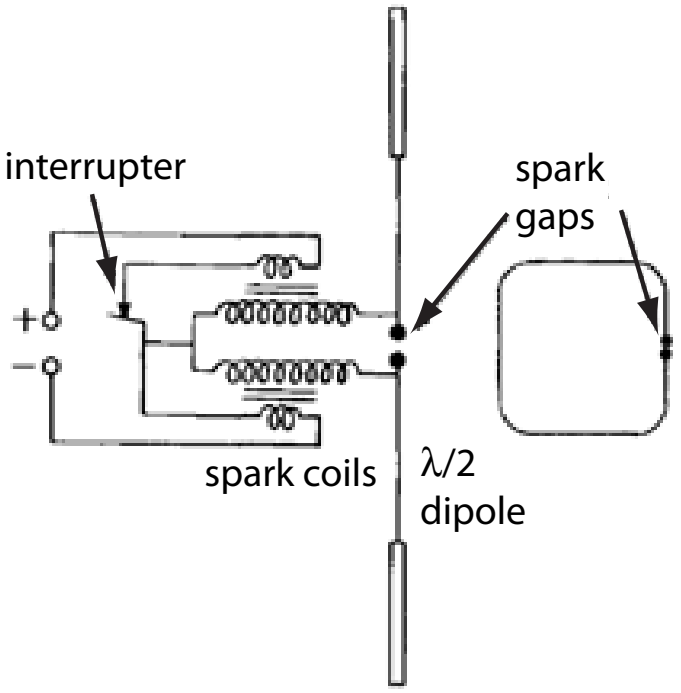

Figure 5.1: *Conceptual schematic of Hertz's experiment (reproduced from Kraus, Fig. 7).*

Since that time, more advanced techniques for the free-space measurement of electromagnetic waves have been developed. For example, the performance of radio, microwave, infrared, visible, ultraviolet, and even x-ray systems can all be measured with specialist equipment. In the case of wire grid polariser most early equipments were conducted in the optical regime.

Measurement of the reflection and transmission of a wire grid polariser (WGP) can be performed for the classical mount, when the wave vector of the incident plane wave is in the plane perpendicular to the gratings, or for the conical mount, when the wave vector is off the perpendicular plane [85]. The measurement set up is illustrated in Fig. 5.2 with the specific equipment configuration for measurement of transmission and reflection of the WGP. For the case of classical mount, the wire grid side always faces the light. Hence the transmission occurs at the glass (substrate) surface and reflection on the side with the metal wires. A polariser is mounted on the light source in order to obtain a TE and TM polarised incident wave. For the transmission measurement, illustrated in Fig. 5.2(a), the position of the detector in the plane perpendicular to the gratings changes with the change in the angle of incidence θ in order to measure the transmitted light at those angles. For the reflection measurement, shown in Fig. 5.2(b), the light source and detector are placed in the plane perpendicular to the wires. In each setting the angle of incidence θ_i and reflection θ_r are equal in order to measure the reflected light over the range of angles of interest. A similar equipment configuration for the measurement of the wire grid polariser is presented in [36, 37].

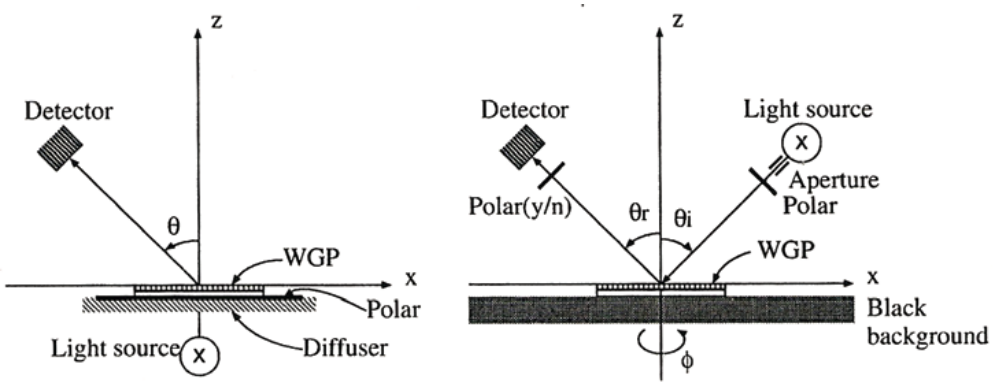

(a) *Transmission measurement* (b) *Reflection measurement*

Figure 5.2: *Experimental configuration for (a) transmission and (b) reflection measurement (reproduced from Xu et al., Fig. 6).*

Other arrangements for the measurement of the transmission through, and reflection from, the subwavelength structures for which plane wave illumination is required are presented in [27, 86, 87, 88]. There is little reported work on polarisers at radio and microwave frequencies because the antenna structures are designed to directly emit

the desired polarisation. However, it is instructive to look at an example of analysing an artificial dielectric at microwave frequencies.
In [27] Bernhard reports an adapted measurement technique and the measured transmission and reflection coefficients of the periodic structure of cones which imitate the night moth cornea. Both the geometry of the cornea and the illumination wave were scaled to microwave frequencies. A horn antenna mounted in front of the sample structure produces an electromagnetic plane wave in the far field and is shown in Fig. 5.3. The model surface was made from a mixture of beeswax and paraffin. The experimen-

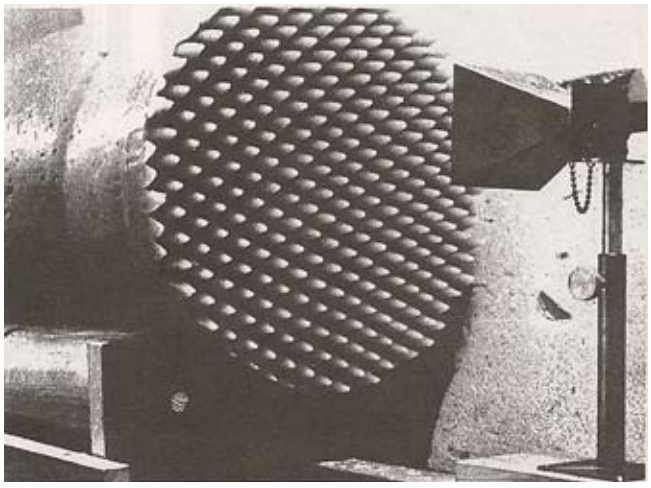

Figure 5.3: *Measurement set up of the surface imitating moth eye (reproduced from Bernhard, Fig. 6).*

tal results showed an increase in the transmission coefficient and a decrease in reflection coefficient of the wave propagating through the subwavelength periodic structure of cones in comparison to a plane featureless medium.
The free-space measurement technique for the measurement of dielectric properties of planar slabs of ceramic and composite materials at microwave frequencies was presented by D. K. Ghodgaonkar *et al.* [86, 87, 88]. The main components of the measurement system are a pair of spot-focusing horn lens antennas, a vector network analyser and a computer. The schematic diagram of the measurement system is presented in Fig. 5.4. Since this technique was adapted for the free-space measurements presented in this Thesis a detailed description of the experimental design, equipment, calibration and post-calibration processing of the data is provided in the following Subsections.

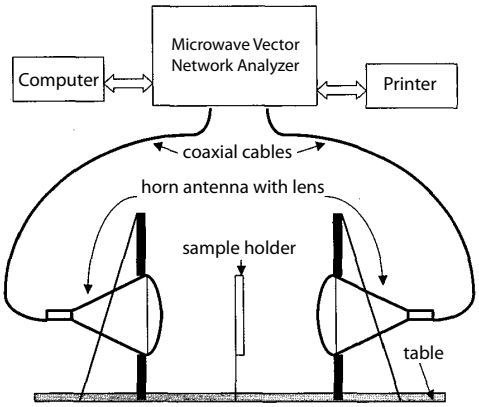

Figure 5.4: *Schematic diagram of free-space measurement system (reproduced from Ghodgaonkar et al., Fig. 1).*

5.3 Experimental Design

The key experimental aim is to measure the reflection and transmission coefficients of a grating plate attached to a dielectric substrate. The ideal experiment requires an infinite grating structure to be illuminated by a plane wave. Such a measurement configuration is difficult to approximate if not impossible, therefore a substitute approach is chosen. The plate is placed between two pyramidal horns. The pyramidal horn antenna itself transmits a quasi plane wave in the far field. The far field distance is calculated from formula [89]

$$\mathcal{D} = \frac{2 \cdot D^2}{\lambda} \tag{5.1}$$

where D is the aperture antenna maximum dimension taken to be its diagonal and λ is the wavelength of the radio wave. Therefore by choosing appropriate spacing between the horns and the grating plate, plane wave illumination can be achieved.

The distances calculated from equation Eq. (5.1) for the antennas used at X-band frequencies are within $34 - 52\,\text{cm}$. In order for the propagated plane wave to 'see' the sample at the calculated distances with no significant interferences from the surrounding environment, the sample would have to be extremely large and the experiment would have to be performed in a specially designed chamber. However, good results can be obtained from a finite grating structure with a relatively small size when illuminated by a wave transmitted from the horn antenna with a focusing lens. A schematic diagram of the free-space measurement configuration for reflection and transmission

coefficients of the grating sample is presented in Fig. 5.5.

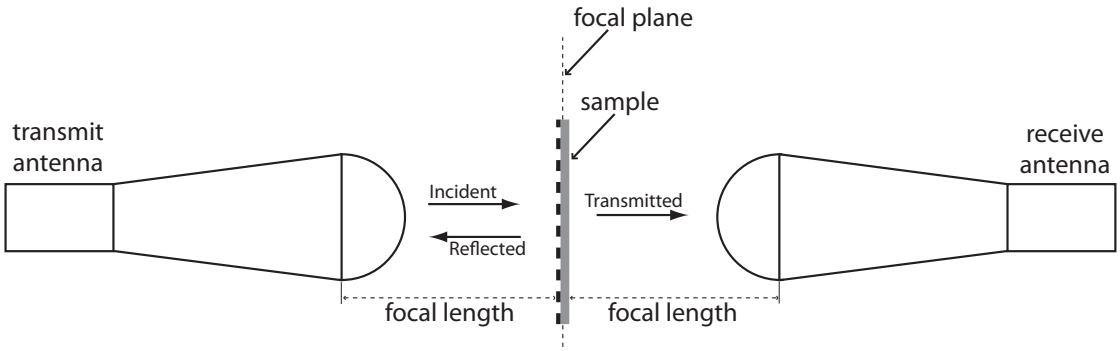

Figure 5.5: *Diagram of the plane wave reflection and transmission of a grating-dielectric sample placed in the focal plane of a pair of pyramidal antenna equipped with lens.*

Such an equipment configuration produces a plane wave at the focal plane and together with an appropriate free-space calibration of the entire system gives an accurate measurement of the response of the sample under test.

5.4 Equipment Description

This Section describes the equipment used to measure the free-space reflection and transmission coefficients of a grating plate attached to a dielectric substrate. The main components of the measurement system are pair of pyramidal horn antennas (transmit TX and receive RX) equipped with hemispherical lenses, coaxial to waveguide transition, coaxial cables and network analyser. The configuration of the free-space measurement system, calibration procedure, and measurement accuracy are also described.

5.4.1 Grating Plate

In order to explain validity of the homogenisation approach, two different grating plate prototypes were manufactured which emulate a series of parallel interconnects. Etching slots in a solid copper sheet was chosen instead of more expensive and time consuming fabrication techniques such as micro fabrication or printed circuit board manufacture. The maximum aspect ratio that can be obtained using this technique is one and is determined by the thickness (0.15 mm) of the copper sheet and the essential requirement that the structural period has to be in the deep subwavelength dimension.

With the aspect ratio fixed at one, two different proportions of the metal relative to the air-gap in the unit grating cell were chosen. In the first case gratings with metal bars of width 0.15 mm separated by air-gaps of the same width, having metal fill factor $f = 0.5$ in structural period $\Lambda = 0.3$ mm were chosen. In the second instance copper bars were separated by 0.35 mm gaps in the unit cell of $\Lambda = 0.5$ mm ($f = 0.3$).
A plan view drawing of the two types of grating plates is presented in Fig. 5.6, where a is the width of the copper bars, and b stands for the width of the air-gaps.

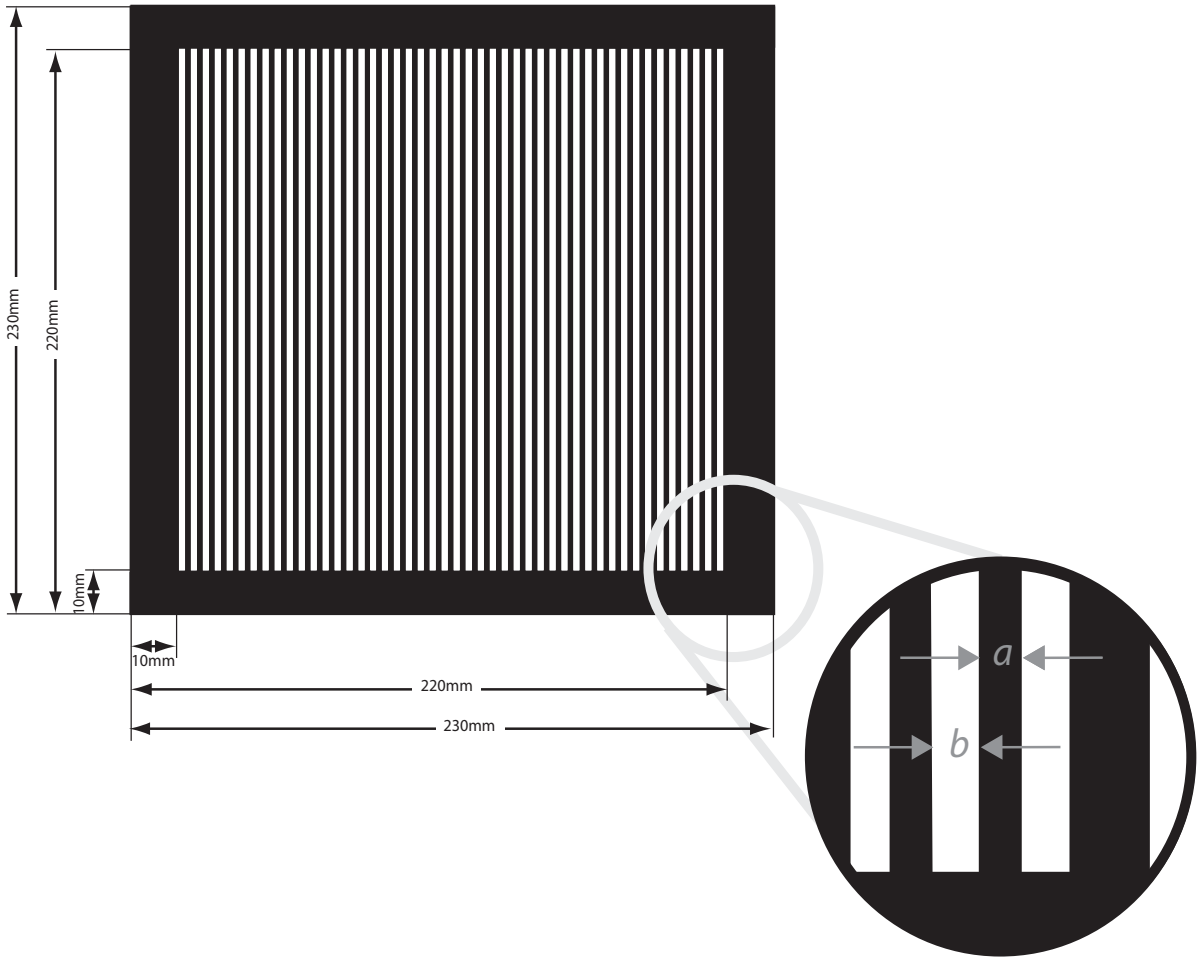

Figure 5.6: *Plan view drawing of a linear copper-air grating plate with thickness 0.15 mm and the close-up of the detail to distinguish the width of the copper bars a, and air-gaps b. There are two designs based on the drawing: (1) gratings with period $\Lambda = 0.3$ mm and metal volume fraction $f = 0.5$ with dimensions $a = 0.15$ mm, $b = 0.15$ mm, (2) gratings with period $\Lambda = 0.5$ mm and metal volume fraction $f = 0.3$ and dimensions $a = 0.15$ mm, $b = 0.35$ mm.*

As the etching process on such thin and relatively large copper sheets results in flexible

bars that cannot hold the intended geometry without assistance, a holder was designed in order to gently stretch the bars and thus hold them in the desired locations. For the measurement purpose grating plates were attached to a Rogers 4350 [90] dielectric substrate ($\epsilon_r = 3.66$) with thickness 0.762 mm and mounted on the holder as it is shown in Fig. 5.7. The three wing nut screws on the side, when tightened, move the base and at the same time stretch the copper bars.

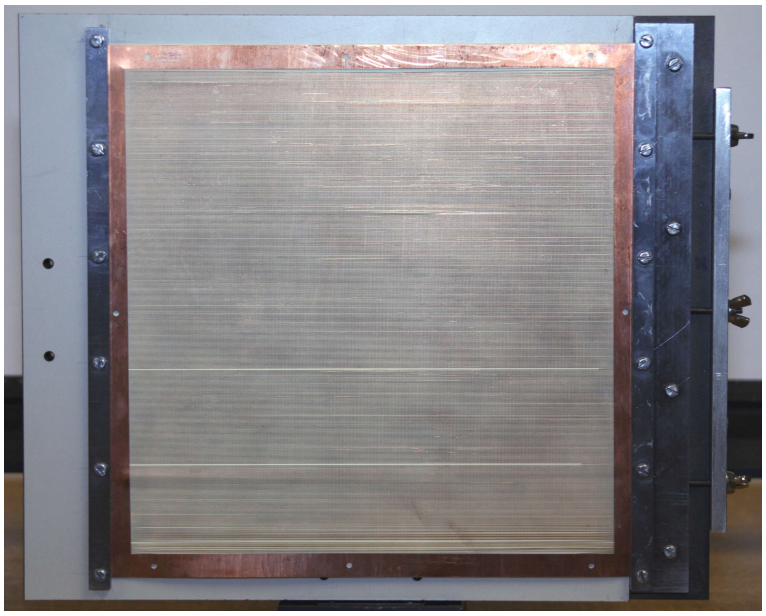

Figure 5.7: *Photograph of the grating plate mounted on the holder.*

5.4.2 X-band Free-Space Measurement Equipment

The free-space measurement system comprises a microwave network analyser, a pair of coaxial cables, two coaxial to rectangular waveguide adapters, and two pyramidal antenna with lens. A block diagram showing how these elements are connected for free-space measurement is shown in Fig. 5.8, where the device under test (DUT) is not specified. The frequency of excitation is controlled by the network analyser via the frequency synthesiser.

The Agilent Technologies E8362B PNA Microwave Network Analyser measures all four S-parameters of the two port network, and its photograph is shown in Fig. 5.9. Measurements are displayed on the integral screen in either polar or rectangular

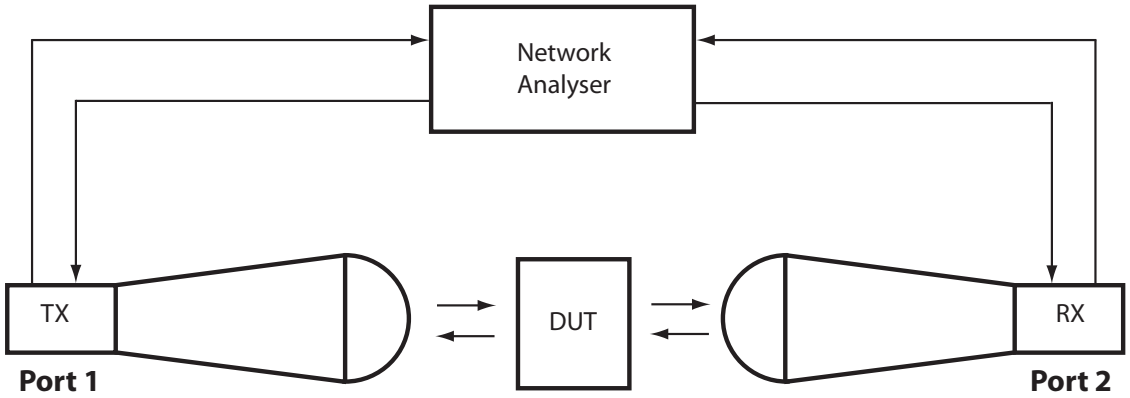

Figure 5.8: *Block diagram of the X-band equipment interconnections in free-space measurement configuration.*

co-ordinate systems, and they can also be saved for further analysis.

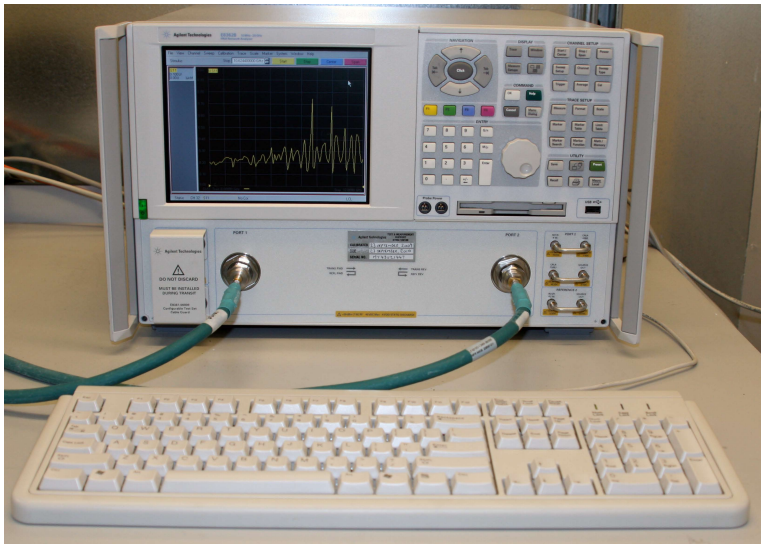

Figure 5.9: *Photograph of the Agilent Technologies E8362B PNA microwave network analyser.*

The continuous wave source is generated by a synthesised sweep over the frequency range $10\,\text{MHz} - 20\,\text{GHz}$. For this particular free-space measurement configuration the source was operated at the maximum power setting of $-5\,\text{dBm}$ in order to maximize the signal to noise ratio. The start and stop frequencies were set to the X-band range and the number of sampled frequencies taken during the frequency sweep, was set to 201 in order to cover the range with a good density of data points, sufficient to identify

expected features in the measured data.
The measurements were performed inside a microwave frequency anechoic chamber which was originally design for the near field measurements and provides the required damping of reflections at X-band frequencies. Thus multipath effects are minimised or eliminated. All surfaces inside the chamber are lined with pyramidally shaped anechoic absorber. The chamber is $4.5 \times 4.5 \times 4.0\,\mathrm{m}$.

S-parameters

The reflection and transmission coefficients are often defined by scattering parameters (S-parameters) which constitute an $n \times n$ scattering matrix [91]. The two-port network is represented by the symmetrical matrix

$$\begin{bmatrix} S_{11} & S_{12} \\ S_{21} & S_{22} \end{bmatrix}$$

with $S_{21} = S_{12}$ for linear passive devices such as those studied in this Thesis.
The diagonal elements represents reflection coefficients of the input S_{11} and output S_{22} ports, whereas the off-diagonal elements are the forward S_{21} and reverse S_{12} transmission coefficients. A schematic diagram of the S-parameters of a two-port network is presented in Fig. 5.10.

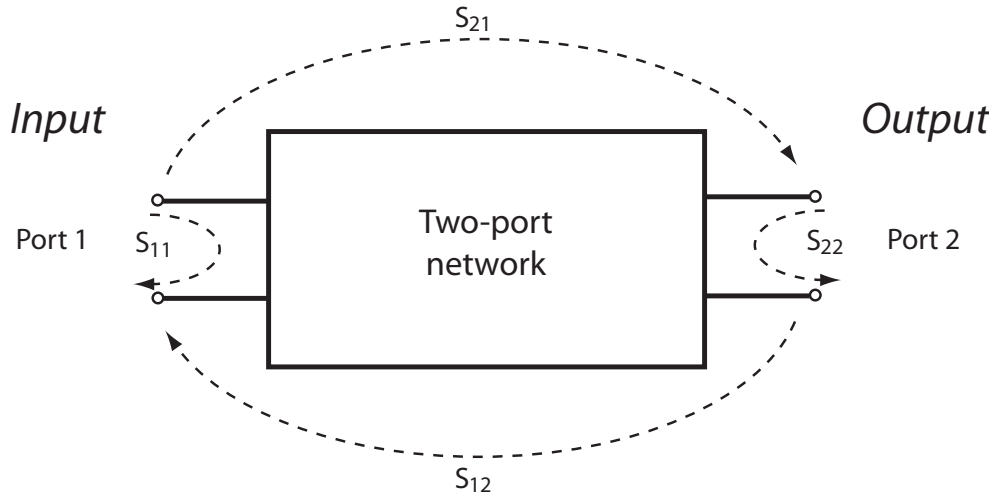

Figure 5.10: *Block diagram of the S-parameters of a two-port network.*

The S-parameters provide information about both magnitude and phase. Nevertheless in the measurement of grating structure the magnitude information is of primary interest, because it provides information about the return and transmission loss via S_{11} and S_{21} respectively. In the studied structures, the change in phase of S_{21} is minimal (less than 2°) therefore the phase data is neglected and not presented here.

5.4.3 Pyramidal Horn Antenna

A pair of waveguide-fed WR-90 (dimension $0.9" \times 0.4"$) pyramidal horn antenna (X-band Antenna from Marconi Instruments Ltd., Stevenage, England) are used for the free-space measurements. As the aim of the experiment is to measure the reflection and transmission coefficients from and through grating structure illuminated by a plane wave, the antennas are attached to focusing lenses constituting a spot-focusing lens antenna. The hemispherical lens with diameter $d = 11\,$cm is made of PTFE (polytetrafluoroethylene, $\epsilon_r = 2.1$) and mounted back to back with the transmit pyramidal horn antenna (TX), whereas for the receive antenna (RX) hemispherical lens of diameter $d = 10\,$cm made of polypropylene ($\epsilon_r = 1.8$) is used. The configuration of the two spot-focusing antennas produces an electromagnetic plane wave at the focus. The ratio of focal length ξ to the diameter of the lens (ξ/d) is equal to one in both cases. The horns are shown in place, in Fig. 5.11.

A numerical model of the pyramidal horn antenna with a PTFE lens operated at X-band frequencies was built in $1:1$ scale using HFSS software [77] and is demonstrated in Fig. 5.12(a). The pyramidal spot-focusing horn antenna is symmetrical in two planes (xy and yz) and it is possible to reduce the size of the overall model to a quarter of the original size by applying symmetry boundary conditions. To improve the accuracy of the results from the simulated model, the mesh resolution was enhanced in the areas of higher interest. This approach was applied to the lens-part of the model. The entire model was enclosed in a vacuum domain with radiation boundary conditions defined on the outside walls to allow the wave to radiate far into space without reflection. The pyramidal horn antenna was excited by a signal applied by a wave port defined at the back side of the rectangular wave guide.

An illustration of the distribution of electric and magnetic field magnitude, at frequency $\nu = 10\,$GHz, in the yz plane is given in Fig. 5.12(b) and Fig. 5.12(d) respectively. A similar distribution occurs in any cross section of the domain with axis drawn along the y-axis. The strong electromagnetic field is concentrated in the area between the

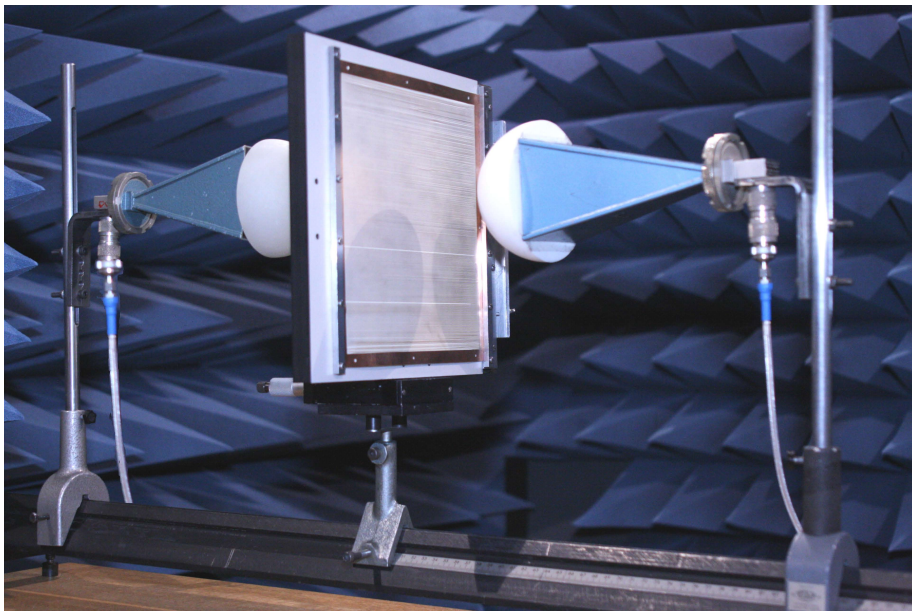

Figure 5.11: *Photograph of the pyramidal horns with lenses mounted in the transmission-reflection configuration*

tip of the lens and the focal plane, nevertheless the plane character of the wave occurs only in the focal plane region where $\xi = 11\,\text{cm}$ for the PTFE lens and $\xi = 10\,\text{cm}$ for the lens used with the receive antenna. It was verified, based on the simulated data, that the focal distance does not change when the antenna is excited by the full range of frequencies for which it was designed (X-band frequencies, $8.2 - 12.4\,\text{GHz}$).
Additional verification of the numerical model was undertaken by looking into the impedance distribution at frequency $10\,\text{GHz}$. A plot of the wave impedance calculated along a line in the y-axis and set at the end of the horn in positive y-direction is shown in Fig. 5.12(c). The fluctuating impedance within the distance of $0 - 5.5\,\text{cm}$ is calculated inside the lens and it converges to a value approximately equal to the free-space impedance $\eta_0 = 376.7\,\Omega$ when the wave passes through the vacuum. In the distance of about $11\,\text{cm}$ the impedance in the simulated model is $\sim 370\,\Omega$ as demonstrated in the close-up in Fig. 5.12(c). Further propagation of the wave into the space is characterized with a gradual divergence from the the free-space impedance value.

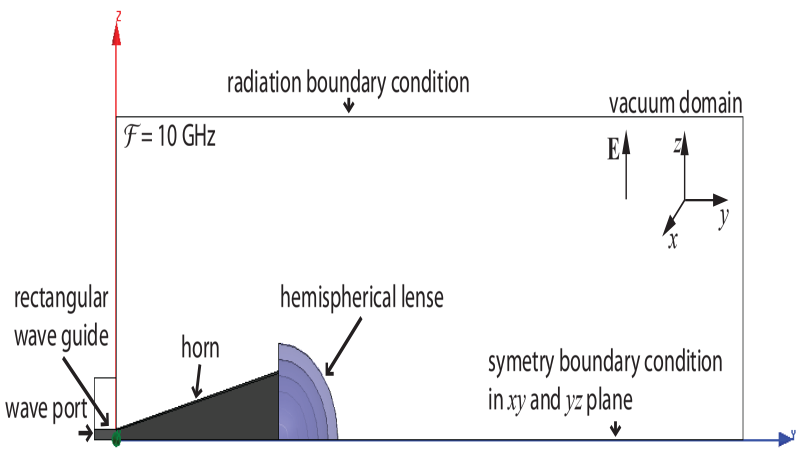

(a) *Pyramidal horn antenna model*

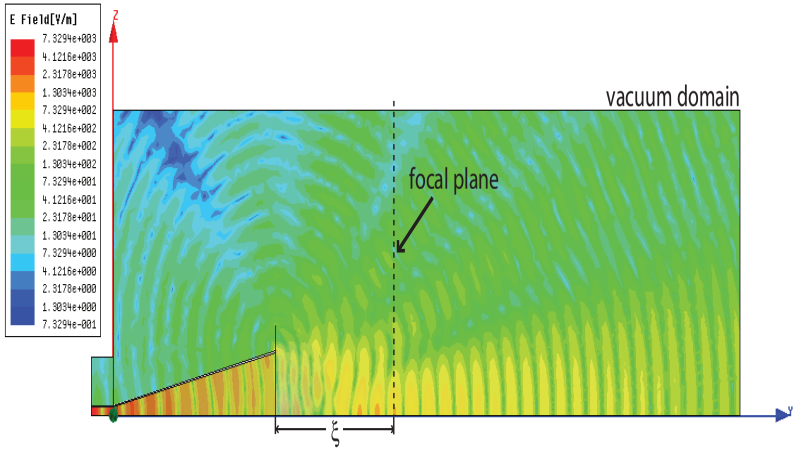

(b) *Electric field magnitude*

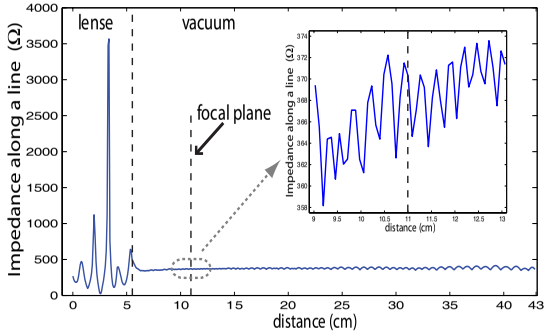

(c) *Wave impedance along a line*

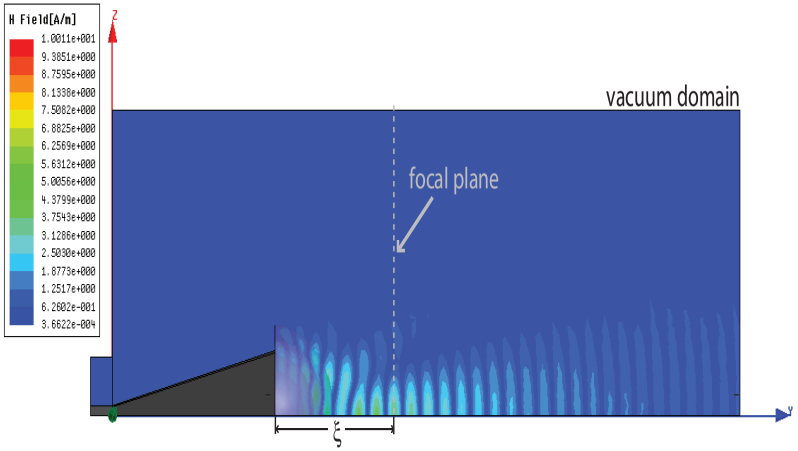

(d) *Magnetic field magnitude*

Figure 5.12: *Pyramidal horn antenna: (a) schematic diagram of numerical model, (b) electric field magnitude pattern, (c) distribution of the wave impedance along a line at frequency* 10 *GHz, (d) magnetic field magnitude pattern.*

5.4.4 Calibration Procedure

The two-port calibration was performed using the standards defined for free-space measurement of the dielectric constants and loss tangents at microwave frequencies [86, 87]. Due to the multiple reflections occurring between the coaxial-to-rectangular waveguide adapters, the rectangular-to-circular waveguide transformation and the spot-focusing horn antenna, the losses of these structures, and the errors always present in the network analyser and the cables, the measured S-parameters differ from the real response of the grating plate in free-space. It is therefore necessary to calibrate the measurement configuration with the free-space standards defined based on Through-Reflect-Line (TRL) waveguide calibration technique. This technique requires three standards: through connection, short circuit connection for each of the two ports, and transmission line connection between those ports. For the particular measurement set-up each of those three standards has its specific equivalent in free-space environment, with the principal assumption that the reference planes for the two ports are located at the focal planes of transmit (TX) and receive (RX) antennas. The through standard is defined by separating the two antennas by the distance equal to twice the focal length 2ξ as illustrated in Fig. 5.13(a). The reflect standards for port one (transmit antenna) and port two (receive antenna) are realized by placing a solid metal plate of the same thickness as the grating plate and dielectric substrate together, on the holder at the reference plane as shown in Fig. 5.13(c), and Fig. 5.13(d) respectively. The line standard is obtained by separating the focal planes of the two antennas by the distance equal to a quarter-wavelength of the signal from the middle of the frequency band as is demonstrated in Fig. 5.13(b).

A new TRL calibration kit based on that provided with the Agilent Technologies E8362B PNA Network Analyser is defined for the free-space calibration. The measurements were taken at the X-band frequency range. The mid-band frequency of $10\,\text{GHz}$ was used to calculate the quarter-wavelength distance for the line standard configuration ($\lambda = 3\,\text{cm}$, $\lambda/4 = 0.75\,\text{cm}$), and the difference between the electrical delay of the through and line connection ($\tau = 25\,\text{ps}$). For the free-space measurements the impedance in all standards is fixed at $Z_0 = 376.7\,\Omega$.
The TRL calibration technique can be applied under the condition that the difference in electrical length θ_l between the through and line standards is greater than 20° for the lowest frequency of the calibration range, and is less than 160° for the highest fre-

quency considered [92]. The electrical length θ_l is calculated from the formula

$$\theta_l = k \cdot \Delta l \tag{5.2}$$

where k is the wave number calculated as $k = \frac{2 \cdot \pi}{\lambda}$, and Δl is the difference in physical length between through and line standards.
The difference in electrical length at mid-band frequency ($10\,\text{GHz}$) is chosen to be $90°$ ($\lambda/4$). At $8.2\,\text{GHz}$ the calculated phase difference is $\sim 74°$ and for $12\,\text{GHz}$ the difference is $\sim 108°$. Therefore the calibration is valid over the entire X-band.

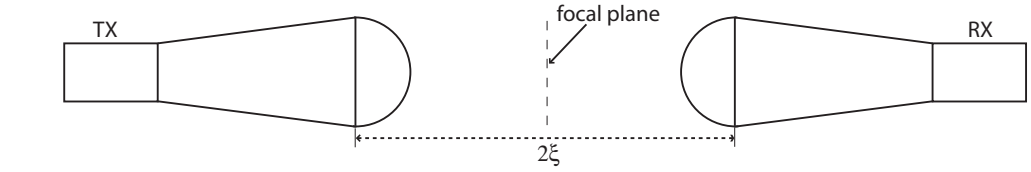

(a) *Through standard*

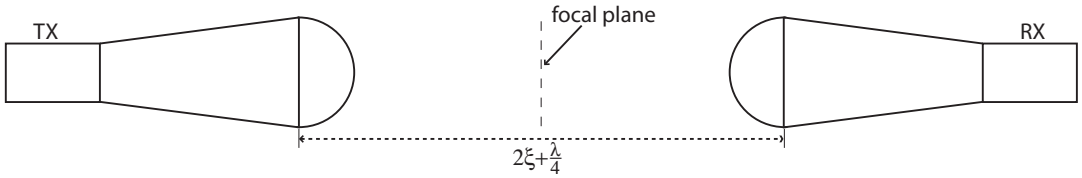

(b) *Line standard*

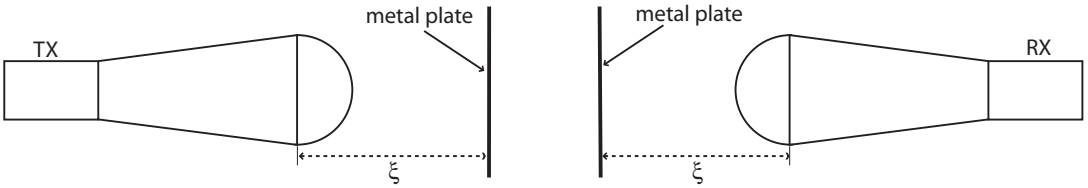

(c) *Port one reflect standard*

(d) *Port two reflect standard*

Figure 5.13: *Schematic diagram of the calibration standards and calibration procedure: (a) through line measurement, (b) second through line measurement with extra quarter-wavelength standard, (c) Port one reflect standard measurement, (d) Port two reflect standard measurement. Greek letter ξ stands for the focal length of the pyramidal horn antenna equipped with a lens.*

The through connection was measured after the calibration procedure. The magnitude of S_{11} and S_{22} was less than $-40\,\text{dB}$, whereas the amplitude and phase of S_{21} (S_{12}) was within $\pm 0.04\,\text{dB}$ and $\pm 0.32°$, respectively. The through standard respond is depicted in Fig. 5.14.

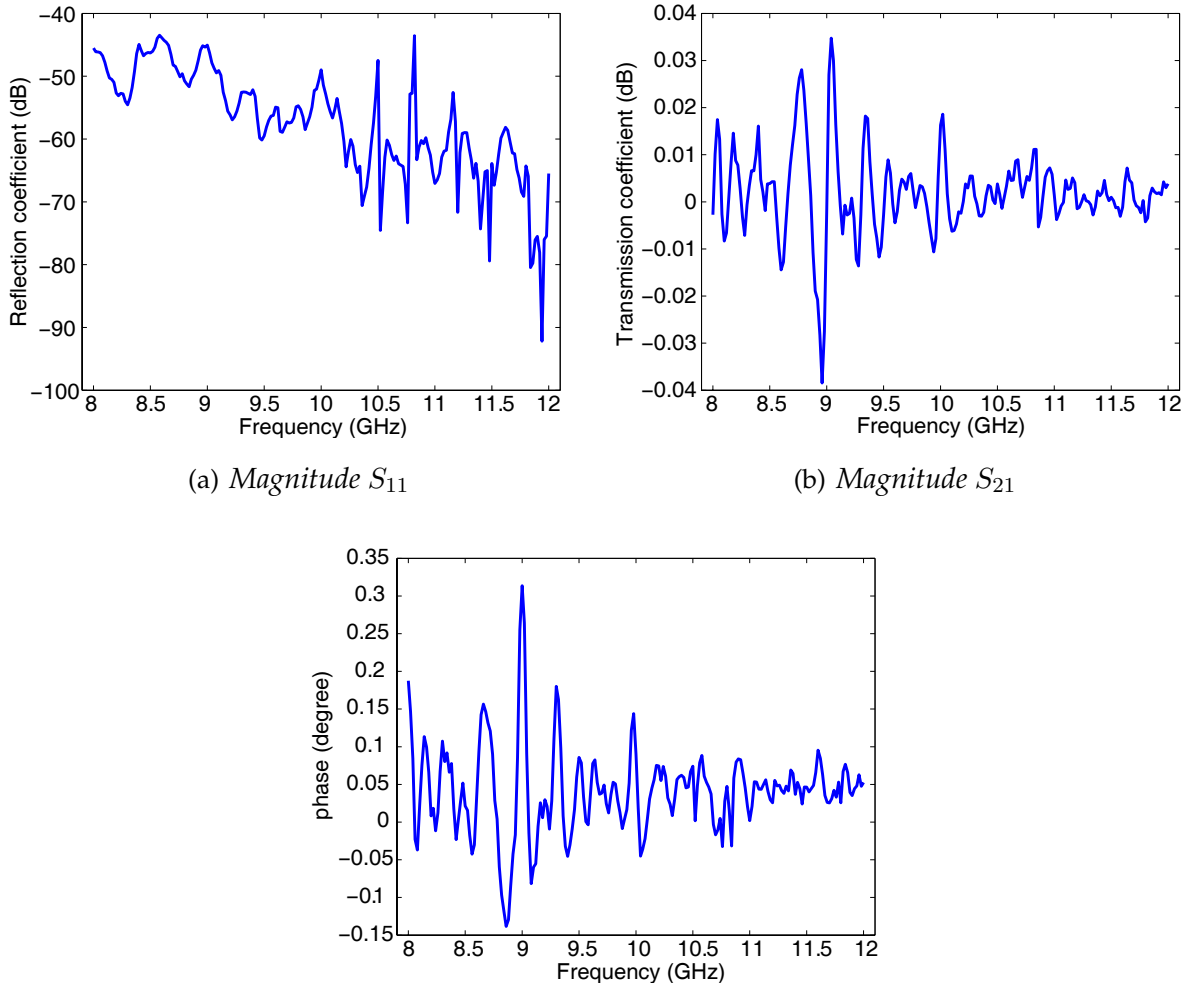

(a) *Magnitude* S_{11}

(b) *Magnitude* S_{21}

(c) *Phase* S_{21}

Figure 5.14: *Plot of the through line measurement of the free-space calibration with: (a) reflection coefficient magnitude, (b) transmission coefficient magnitude, (c) phase of transmission coefficient.*

The residual errors after calibration caused by source and load impedance mismatch can be reduced by using time domain gating [87, 86] or by the application of a smoothing function [88]. Time-domain gating for selective removal of the residual frequency response resonances, is defined as a filter in the time-domain with a pass band selected by the start and stop gate controls. The unwanted time-domain ripples are reduced by the filter but generally not completely removed [93].
Implementation of that method is given by the following steps:

1. S_{11} and S_{21} parameters are obtained from measurement in frequency-domain

2. time-domain S_{11} and S_{21} parameters are calculated by taking the inverse Fourier transform of the frequency-domain data

3. gating is applied over the time-domain response

4. the gated time-domain data are converted back to the frequency-domain by taking the Fourier transform and the unwanted resonances and multiple reflections are removed

In the presented study the smoothing procedure was applied in order to remove the postcalibration errors. The linear least squares method was used in order to obtain the approximate average of the frequency-domain data; see Appendix A.

5.4.5 Measurement Accuracy

There are two types of errors which can be distinguished when accuracy of the free-space measurement, after calibration and time-domain gating or smoothing procedure, is considered [87]. The first reflects the imprecision in calibration standards and instruments. The coaxial cables are also an issue in accuracy estimation.
The error caused by the calibration standards is mainly influenced by the difference in wave impedance between the line standard and that of free-space. The instrumentation errors, for example frequency instability, can be neglected due to the synthesised nature of the network analyser source used to take measurements. To reduce the errors caused by the coaxial cables used to connect the antennas to the ports of the apparatus, proper care needs to be taken in their set-up to ensure consistency between calibration and measurement.
The second type of error is due to the small misalignment between the position of the measured sample and the reference plane defined by the through and reflect standards in the calibration procedure. This small misalignment is caused by manually changing the samples and contributes to the error in the presented results.

The TRL calibration method can be used when the wave at the focal plane is planar in nature [86]. It was verified by numerical calculations and experimentally before the calibration procedure was taken. A numerical approach was used to predict the location of the focal plane, and hence the focal distance ξ from the horn aperture to the focal point is described in Subsection 5.4.3. Experimental validation was carried out by

placing the solid metal plate mounted on the holder parallel to the horn aperture at different distances. By measuring the S_{11} parameter it was noted that moving the reflect plate from a far distance into the horn direction, the observed return loss increases to reach its highest value when the plate is situated in the distance approximately equal to the focal length $\xi \approx 11$ cm. Those two procedures gave confidence in the correctness of the equipment configuration and further more in the correctness of the obtained experimental data.

The measurement precision and repeatability was estimated by the following approach. The system was calibrated twice and at every time a measurement of each of the two grating plates of a given type was taken. Then the errors in the return and transmission losses of the four sets of measurements data, with removed postcalibration errors, were calculated. For the gratings with structural period $\Lambda = 0.3$ mm the error in the measured magnitude of the S_{11} parameter was between $0 - 2.3\%$, and for S_{21} the error was not higher than 0.3%. Better measurement accuracy was noted for structure with period $\Lambda = 0.5$ mm with the different measurements varying only whithin $0 - 1.7\%$ for the magnitude of S_{11} parameter, and less than 0.1% for parameter S_{21}. The change in the phase of transmission coefficient was in the range $\pm 0.04^{\circ}$ and $\pm 0.015^{\circ}$ for gratings with period $\Lambda = 0.3$ mm and $\Lambda = 0.5$ mm respectivly.
The difference in experimental data is influenced by two factors. Namely, the small change in location of the holder with sample grating plates in the reference plane was manually adjusted during measurement routine. Secondly, the metal bars due to their relatively small dimensions compared to their length, gave slightly different alignment after being stretched for several times, which is also reflected in the error data.

5.5 Results for Free-Space Measurements

This Section presents the measurement results of the grating plates at X-band frequencies compared with numerical results obtained from three different methods: finite-difference time-domain method (FDTD), finite element method (FEM), and effective medium theory approach. All measurements were taken for TM and TE polarisation nevertheless here only the results for TM polarisation are presented.

5.5.1 Smoothing Procedure

The experimental results were approximated in frequency-domain by linear least squares method in order to remove the postcalibration errors. The measured reflection and transmission coefficients are plotted against its approximated average in Fig. 5.15, with results obtained for grating plates characterized by metal volume fraction $f = 0.5$ attached to Rogers substrate in Fig. 5.15(a) and Fig. 5.15(b), for gratings with metal fill factor $f = 0.3$ on dielectric plate in Fig. 5.15(c) and Fig. 5.15(d), and for the reference plate with Rogers dielectric only, in Fig. 5.15(e) and Fig. 5.15(f).

The experimental data starts to deviate from the fitted data with the increase in applied frequency. This trend is a combined effect of a few factors:

1. manufacture precision
2. the varying tension and separation between neighboring wires
3. diffraction effects at the edges of sample
4. overall size of the sample compare to the illumination wavelength

The amplitude of the ripples in experimental results increases with frequency. The overall system becomes more sensitive to any inaccuracy in the grating plates, and the arrangement of the bars after their tensioning. Hence the error in experimental data when compared with simulated is expected to become more significant for frequencies in the upper half of the X-band. The quasi-linear response of the sample is masked by ripples arising from the various reflections in the system. Overall, these reflections have the effect of degrading the measurement accuracy, but some of these can be restored by using a smoothing procedure.

5.5.2 Experimental Results

The experimental results for the free-space measurements of the two types of grating plates attached to a Rogers dielectric plate appears to be affected by factors discussed in the previous Subsection to an expected extent. The general trend in the measured data is qualitatively close to those obtained from simulated numerical models and the observed deviation tends to increase simultaneously with frequency increase. Considering the influence of each factor on the measured data those effects could be cor-

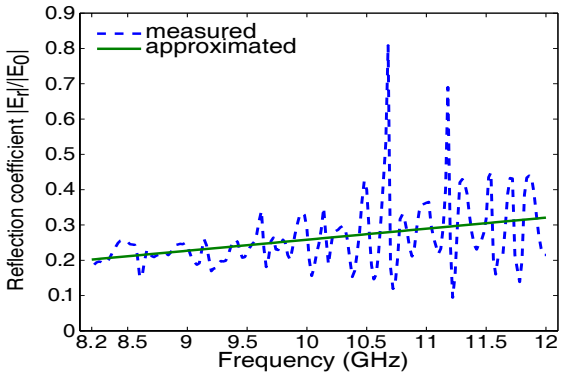

(a) *Reflection coefficient*

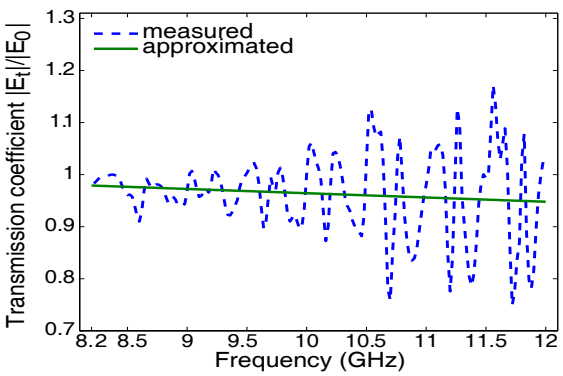

(b) *Transmission coefficient*

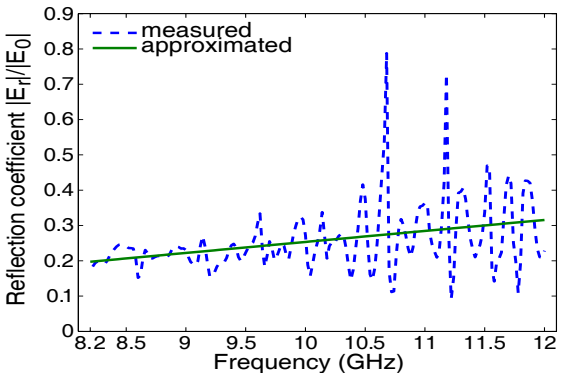

(c) *Reflection coefficient*

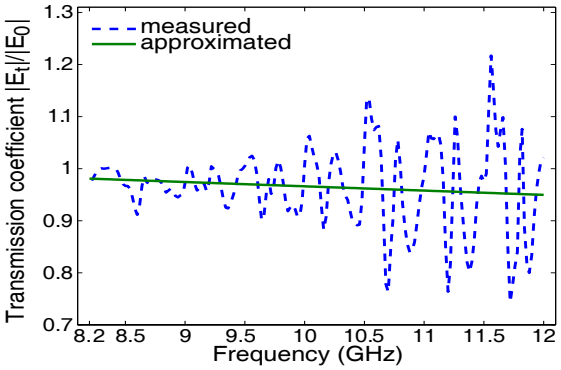

(d) *Transmission coefficient*

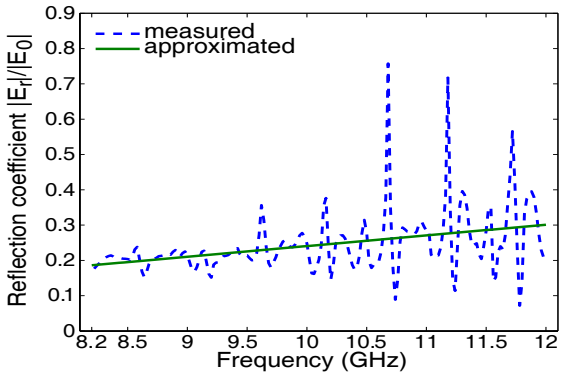

(e) *Reflection coefficient*

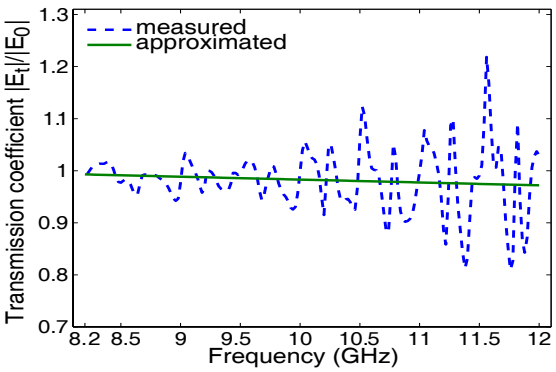

(f) *Transmission coefficient*

Figure 5.15: *The magnitude of the reflection and transmission coefficients of a grating structure attached to the Rogers dielectric of thickness* $762\,\mu m$*. The raw experimental results (dash line) are plotted against its approximated average (continuous line) for: (a,b) gratings with period* $\Lambda = 300\,\mu m$*, (c,d) gratings with period* $\Lambda = 500\,\mu m$*, (e,f) reference plate.*

rected by repositioning the feed slightly or by moving the reference plane of the measurement. Apart from the discussed errors influenced by manufacturing process and measurement set-up there is another aspect which can cause the difference between measured (real model) and simulated (ideal model) results. Specifically, in the real experiment the available sample was limited by its size, whereas its numerical equivalent was defined by an infinitely extended periodic structure.

A 2-dimensional FDTD domain was defined as shown in Fig. 5.16, with the case of detailed grating structure in Fig. 5.16(a) and its homogenised equivalent in Fig. 5.16(b). The domain size was 60 cells in x by 8203 cells in z direction for grating period $300\,\mu$m, and 100 by 8203 cells for grating period $500\,\mu$m, and 1 cell in y direction. The modeled structure extends to infinity in the y direction with no change in the shape of its transverse cross section in xz plane. In each case the space increment in all directions was set to $5\,\mu$m and it was ensured that the domain size in the z-direction was at least a half wavelength from each of the absorbing Perfect Matched Layer (PML) boundaries as the behavior of these boundaries is not reliable in the presence of evanescent fields. Periodic boundary conditions were defined on four sides of the computational domain in xz and yz planes.

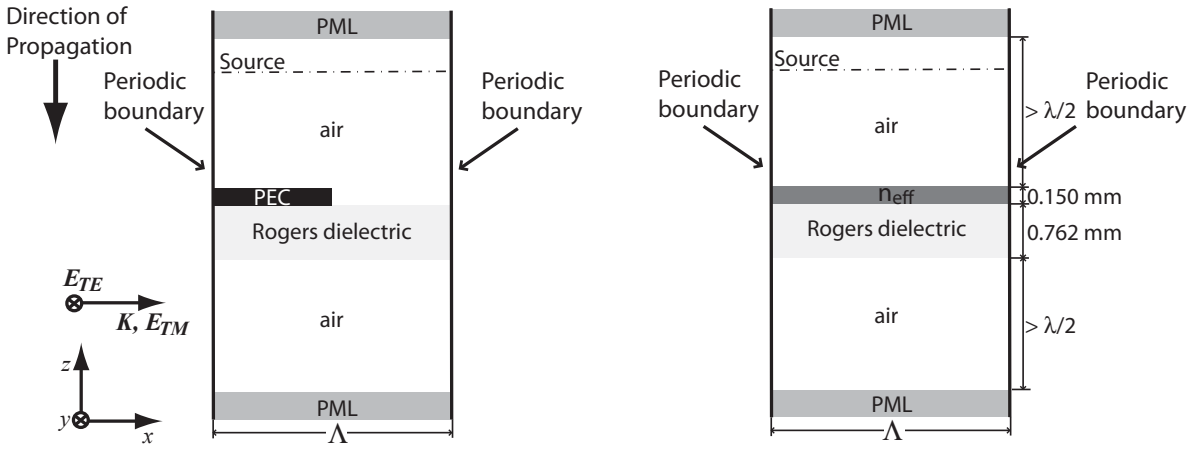

(a) *cross section in xz-plane* (b) *homogenised equivalent*

Figure 5.16: *Diagram of the 2-D FDTD simulation domain. The domain is one period wide and periodic in (a) x direction, with its (b) homogenised equivalent. The incident plane wave propagates in the negative z direction. PML absorbing boundary conditions are defined. The TM and TE directions are shown.*

The grating structure is periodic in the x direction, with one period of the grating defined in the domain. The structure was illuminated by a wave with frequencies ν within $8 - 12\,\text{GHz}$ in steps of $1\,\text{GHz}$ applied at the top of the domain and propagated in the negative z direction. Continuous plane wave illumination was defined and separate computations were performed for each of the frequencies. As an alternative approach, transient simulations involving a Gaussian pulse could also be employed. Post-processing of the numerical data for each of those cases requires different approaches. Since field plots at certain frequencies of illumination were required, continuous wave illumination was chosen to reduce post-processing although this did incur extra computation cost up front.

Among the effective medium approximations presented in Section 2.5 for the sub-wavelength dielectric gratings, only the zeroth-order approximation (Eq. (2.17)-(2.18)) is, sometimes, applied to the analysis of metallic gratings - even though it is not accurate, as it was discussed in Section 2.2 with respect to the wire grid polariser. The second-order effective medium theory given by formulas Eq. (2.19)-(2.20) is defined for gratings that do not meet the long wavelength limit. Therefore, it is not applicable to structures with structural period much smaller than the illumination wavelength. Finally, the depth dependent formulation of the effective permittivity given by Eq. (2.25) is not valid for rectangular gratings illuminated by a TM polarised electromagnetic wave. With regard to the above discussion, the simulated data obtained for the grating structure are plotted along with the zeroth-order approximation in Fig. 5.17 for gratings with structural period $300\,\mu$m and in Fig. 5.18 for gratings with period $500\,\mu$m. There is significant deviation between the reflection and transmission coefficients calculated for the grating and those calculated for the homogenised structure. Hence a new approach is required

Good accuracy was obtained by adopting the Maxwell-Garnett effective medium theory. The homogenised equivalent structure was obtained by replacing the grating layer with a solid dielectric. The dielectric properties were calculated from the modified Maxwell-Garnett mixing rule. The value of scaling factor Ψ was empirically found as due to the structural difference between experimental settings and the structure studied in order to define the empirical model, the straightforward application of the empirical model underestimated factor Ψ. It was verified that Ψ, when equal to 2.5, gives good approximation of the calculated effective refractive index n_{eff}.

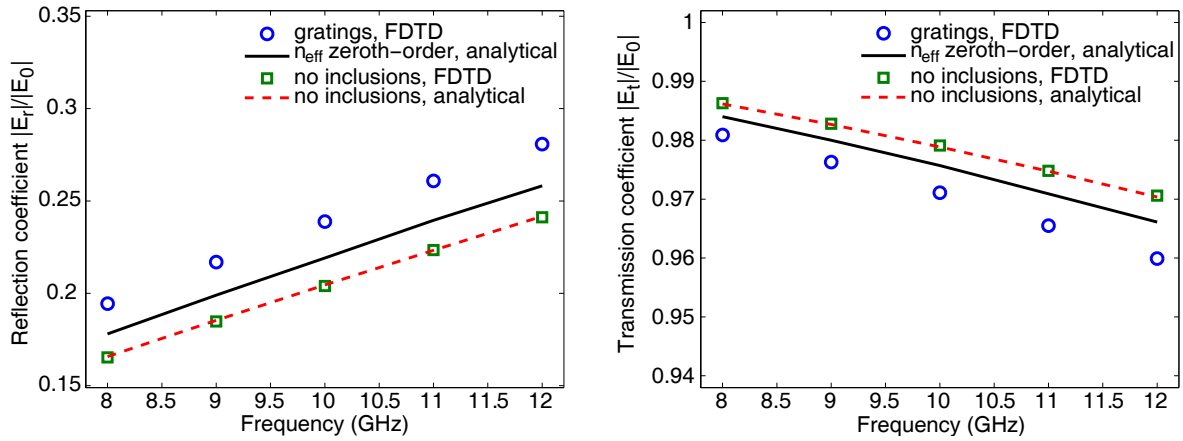

(a) *Reflection coefficient* (b) *Transmission coefficient*

Figure 5.17: *The magnitude of the reflection and transmission coefficients for a grating structure. The zeroth-order EMT deviates from the numerical FDTD data (markers) obtained for the grating. The FDTD and analytical results obtained for the reference structure are included. [gratings:* $f = 0.5$*,* $\Lambda = 300\,\mu m$*,* $AR = 1$*; substrate: Rogers dielectric of thickness* $762\,\mu m$*]*

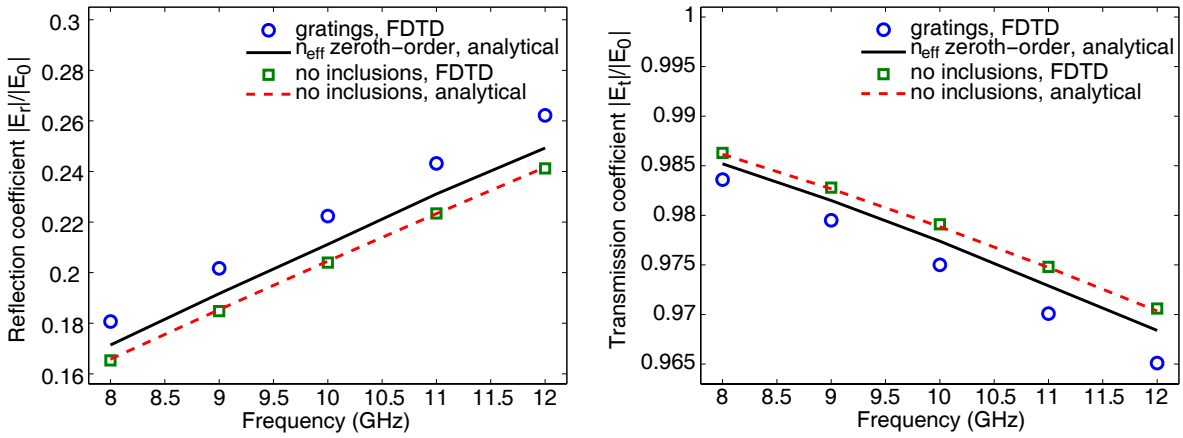

(a) *Reflection coefficient* (b) *Transmission coefficient*

Figure 5.18: *The magnitude of the reflection and transmission coefficients for a grating structure. The zeroth-order EMT deviates from the numerical FDTD data (markers) obtained for the grating. The FDTD and analytical results obtained for the reference structure are included. [gratings:* $f = 0.3$*,* $\Lambda = 500\,\mu m$*,* $AR = 1$*; substrate: Rogers dielectric of thickness* $762\,\mu m$*]*

The FDTD and analytical calculations, based on characteristic matrix method, of reflection and transmission coefficients for the gratings with structural period $300\,\mu$m and its homogenised equivalent are plotted in Fig. 5.19 along with measured return and transmission losses. Similar arrangement of results obtained for the grating with period $500\,\mu$m is shown in Fig. 5.20.

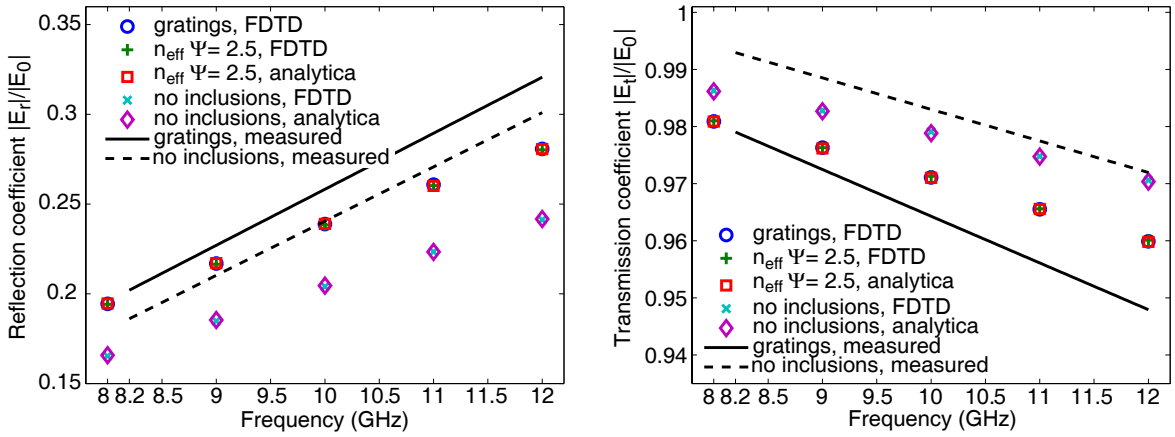

(a) *Reflection coefficient* (b) *Transmission coefficient*

Figure 5.19: *The magnitude of the reflection and transmission coefficients for a grating structure. The experimental data (lines) follows the same trend as the numerical FDTD calculations (markers) obtained for grating, homogenised and reference structure. [gratings: $f = 0.5$, $\Lambda = 300\,\mu m$, $AR = 1$; substrate: Rogers dielectric of thickness $762\,\mu m$]*

Furthermore, in order to validate the proposed approach for a wider range of frequencies, $1 - 18\,$GHz, numerical calculations were performed using the FEM method. The 3-dimensional FEM simulation domain was configured as shown in Fig. 5.21 with cross sections and dimensions of the unit cell defined in xz- and yz-plane illustrated in Fig. 5.21(a) and Fig. 5.21(b) respectively. The homogenised equivalent structure was configured as shown in Fig. 5.21(c) with effective refractive index n_{eff} calculated from mixing rule with scaling factor $\Psi = 2.5$. The domain size was determined by the recommended standards that the PML boundaries should be placed at least one-tenth of a wave length from strong radiators, and the thickness of the PML-box should also be equal to at least one-tenth of a wave length.

This analysis shows that the results of the two numerical techniques and measured

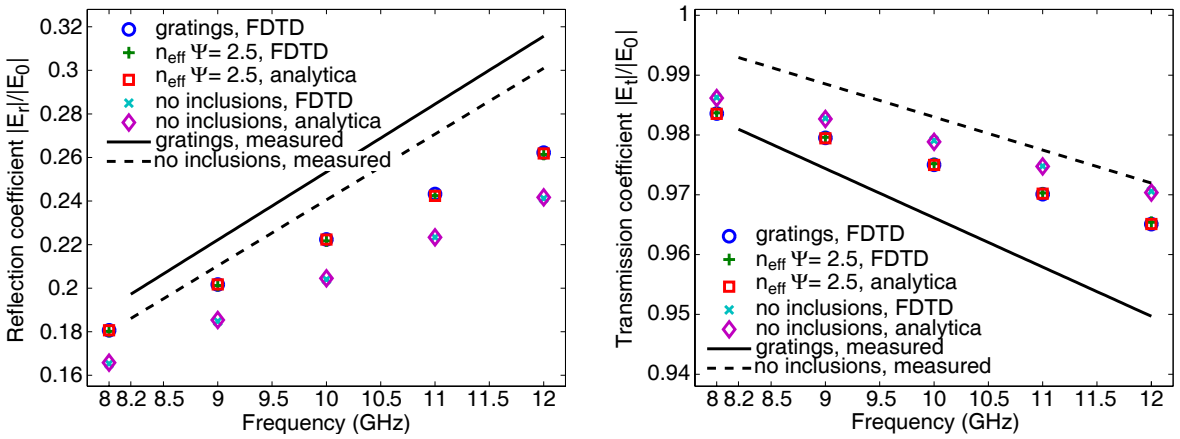

(a) *Reflection coefficient* (b) *Transmission coefficient*

Figure 5.20: *The magnitude of the reflection and transmission coefficients for a grating structure. The experimental data (lines) follows the same trend as the numerical FDTD calculations (markers) obtained for grating, homogenised and reference structure. [gratings: $f = 0.3$, $\Lambda = 500\,\mu m$, $AR = 1$; substrate: Rogers dielectric of thickness $762\,\mu m$]*

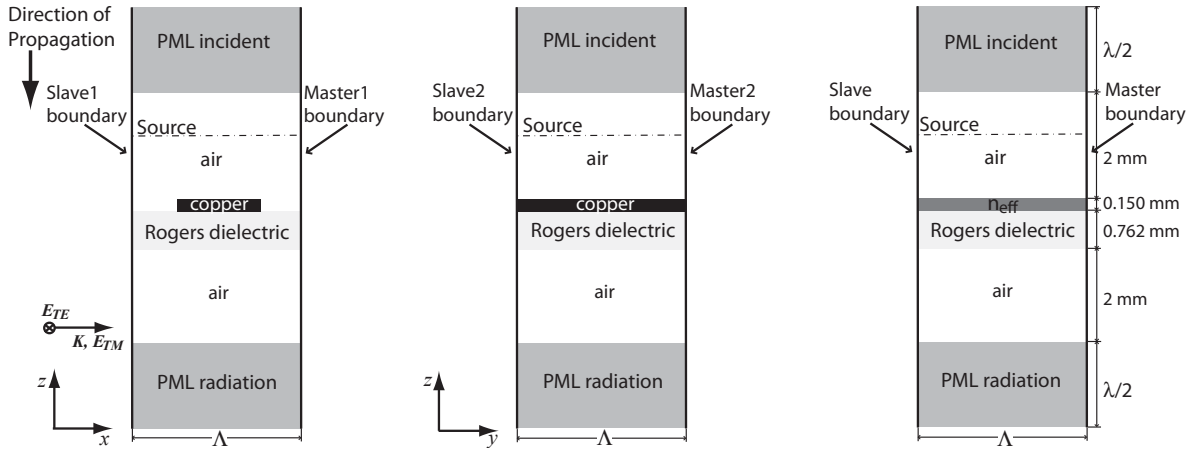

(a) *cross section in xz-plane* (b) *cross section in yz-plane* (c) *homogenised equivalent*

Figure 5.21: *Diagram of the 3-D FEM simulation domain. The domain is one period wide and periodic in: (a) x, and (b) y direction, with (c) homogenised equivalent. The incident plane wave propagates in the negative z direction. PML absorbing boundary conditions are defined. The TM and TE directions are shown.*

results follow the same trend over a wide range of frequencies and allow extrapola-

tion of the measured reflection and transmission coefficients outwith the measured domain. The FDTD method is not efficient for simulations of structures with features small compared to the illumination wavelength due to the Courant-Friedrich-Lewy constraint (Eq. 3.19), but the FEM is readily applied to such geometries. As further validation of the homogenisation method, the data extrapolated from the measurement range was compared with the FEM data and found to agree closely. The error between the FDTD and FEM results are not higher then 0.3% for the simulations of homogenised and reference structures (uniform surface), and with the error approaching 1.5% for the grating (rough surface). The accuracy of these two methods, for the case of grating structure, can be improved by reducing the space increment in FDTD domain or by manual assignment of the mesh operation in FEM domain. Both operations will reduce the error at the expense of increased computation time and memory requirement.

The results obtained from these two numerical methods and measured return and transmission losses are compared in Fig. 5.22 for the gratings characterized by metal volume fraction 0.5, and for the second case, where metal fill factor was reduced to 0.3 in Fig. 5.23.

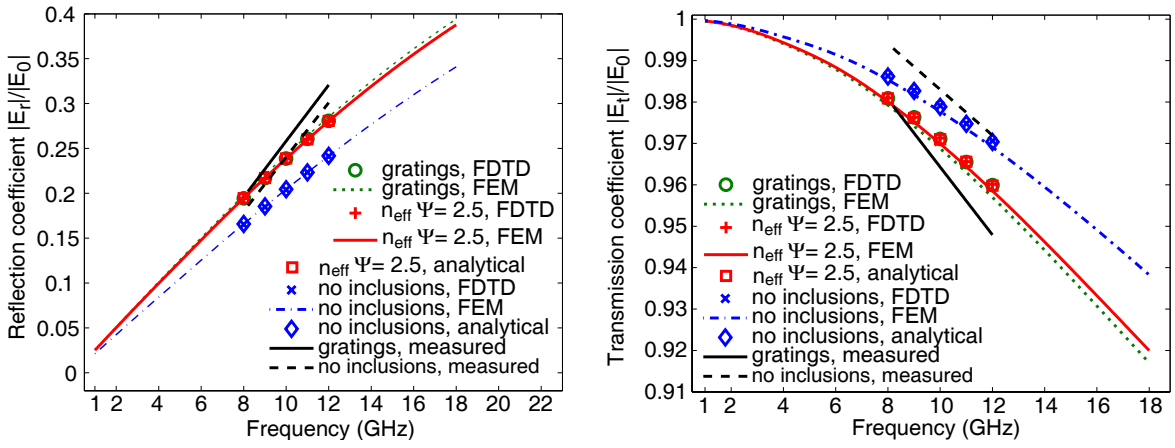

(a) *Reflection coefficient* (b) *Transmission coefficient*

Figure 5.22: *The magnitude of the reflection and transmission coefficients for a grating structure. The experimental data follows the same trend as the numerical calculations, from FDTD and FEM methods, obtained for grating, homogenised and reference structure. [gratings: $f = 0.5$, $\Lambda = 300\,\mu m$, $AR = 1$; substrate: Rogers dielectric of thickness $762\,\mu m$]*

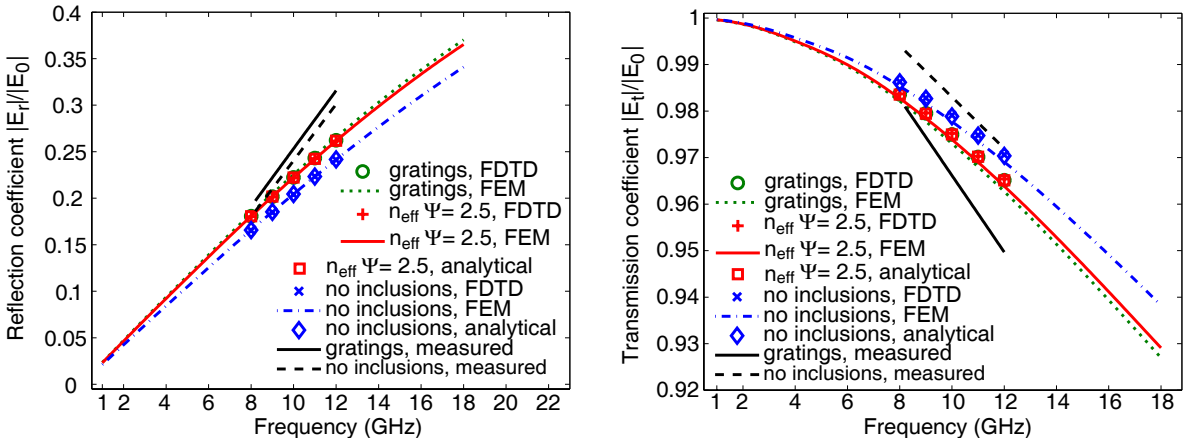

(a) *Reflection coefficient* (b) *Transmission coefficient*

Figure 5.23: *The magnitude of the reflection and transmission coefficients for a grating structure. The experimental data follows the same trend as the numerical calculations, from FDTD and FEM methods, obtained for grating, homogenised and reference structure. [gratings:* $f = 0.3$, $\Lambda = 500\,\mu m$, $AR = 1$; *substrate: Rogers dielectric of thickness* $762\,\mu m$*]*

5.6 Summary

The free-space measurements were taken at X-band ($8.2 - 12.4\,$GHz) frequencies using a network analyser with two horn antennas, each with lens. The plane wave illumination, focused on a relatively small area, was achieved by a special arrangement of the equipment. A free-space calibration method was implemented in order to eliminate the systematic errors occurring in the measurement data. The experimental data supports the concept that the grating structure can be homogenised. The validation was carried out by comparing the two different numerical results with experimental data. The obtained results were extrapolated outwith the measured domain using the FEM software. Hence the homogenisation procedure can be performed over the range of frequencies $1 - 18\,$GHz. The data obtained from FDTD and FEM simulators are in good agreement with an error less than 1.5%.

Chapter 6

Microstrip Analysis and Measurements

6.1 Introduction

So far, this Thesis has been concerned with the reflection (and transmission) of plane waves from a layer of interconnects. Now, the focus is shifted somewhat, to consider the question of whether neighbouring interconnects in the vicinity of a signal-carrying interconnect can also be homogenised to reduce the burden of physical verification tools. Hence this Chapter presents numerical and experimental results for the application of the homogenisation approach to the analysis of the lower layers of interconnects in an interconnect stack. The concept is based on the study of electromagnetic performance of a microstrip line, as it is a good analogue to signals transmitted over single interconnects. The prototype microstrip line contains a set of periodically aligned metal bars embedded in the substrate in order to examine the influence of adjacent layer on the performance of the microstrip.

This Chapter is organised as follows. In Section 6.2 the experimental design is presented, Section 6.3 covers the description of homogenisation procedure for the prototype microstrip line, model geometry, and numerical results; and Section 6.4 presents the measurement equipment and calibration issue, as well as measurement results.

6.2 Experimental Design

The microstrip transmission line was chosen in order to demonstrate the application of the homogenisation approach to an analysis of the electromagnetic performance at

the lower layers of interconnects in an interconnect stack. The effective medium approximation used in this Section is based on an analysis of the influence of metal rods embedded in substrate on the wave propagated along the strip. In order to reflect the most common arrangement of interconnects in an integrated circuits (IC), the mutually parallel rods were embedded in a dielectric medium and aligned perpendicular to the signal line. Two different configurations of periodically distributed metal rods were chosen. Specifically, miscrostrip lines with either 5 or 10 inclusions embedded in the substrate. The number of chosen inclusions was motivated by the fact that 5 regularly distributed rods can be considered as a periodic alignment, whereas 10 gives the possibility to assess the difference in the response with respect to the number of embedded inclusions. A schematic diagram of the homogenisation approach is shown in Fig. 6.1 with a microstrip line where the metal inclusions are surrounded by the virtual homogenisation boundary in Fig. 6.1(a), and a microstrip line where the area of interest is replaced by its homogenised equivalent in Fig. 6.1(b).

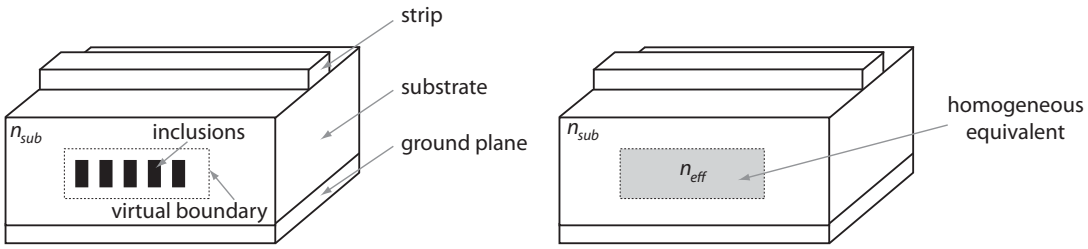

(a) *Microstrip with inclusions* (b) *Microstrip with homogenised equivalent*

Figure 6.1: *Diagram representing the microstrip model with (a) metal inclusions surrounded by the virtual homogenisation boundary, (b) homogenised equivalent.*

The distance between neighbouring interconnect layers is determined by the design rules of the particular process used. Following the general design conventions the ratio of the distance between interconnect layers to the interconnect height is in the range $0.7 - 1.5$. The lower limit generally applies to global interconnects, whereas the semiglobal and intermediate lines are designed to satisfy the upper half of the interval. However, in exceptional circumstances the intermediate lines are separated by a distance lower than the interconnect height. In order to take an average approach the distance was chosen to be in the middle of the range and the numerical models studied in this Chapter are defined with the separation of the embedded metal bars

from both signal line and ground plane by a distance equal to the height of the metal inclusions.

Numerical and experimental results for the reflection and transmission coefficients are obtained, and the homogenisation approach based on numerical simulations is validated by measurement.

6.3 Analysis

This Section presents a short introduction to microstrip theory and the homogenisation procedure for a microstrip structure with a number of rods embedded in the substrate. The geometry of the numerical model is also described and the numerical results are discussed.

6.3.1 Microstrip Theory

Microstrip is a commonly used transmission line in microwave circuits. It can be easily fabricated using printed circuit board (PCB) technology and its key advantage is that the impedance can be tuned by altering only the geometry of the metal whereas the substrate does not require altering. Microstrip is also a useful analogue to IC transmission lines. A schematic diagram of microstrip line with its dimensions is shown in Fig. 6.2(a). The conducting strip with width W, height T and length L carries the signal and is separated from the ground plane by a dielectric substrate with relative permittivity ϵ_r and thickness h. The electromagnetic field lines are depicted in Fig. 6.2(b).

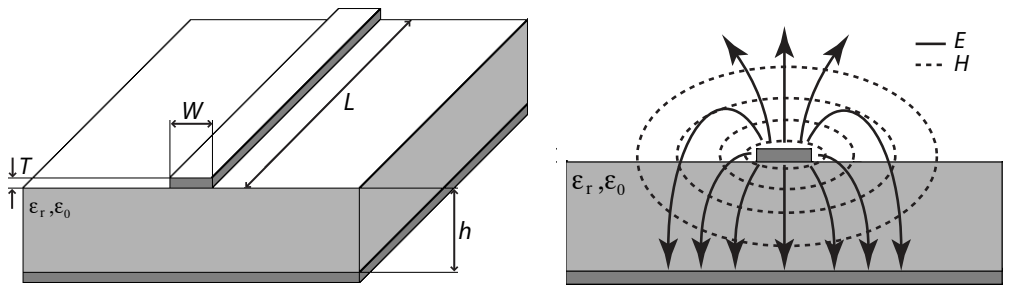

(a) *Microstrip configuration* (b) *E and H field lines*

Figure 6.2: *Microstrip transmission line: (a) configuration, (b) electric and magnetic field lines*

Two main electrical parameters are used when characterizing microstrip line circuit design: characteristic impedance Z_0 and effective permittivity $\epsilon_{<e>}$. These parameters are applied under the assumption that the propagating mode is a quasi-transverse electromagnetic mode (quasi-TEM).
The formulas presented in the rest of Section 6.3.1 come from standard text books [94, 95]. The characteristic impedance is determined by the microstrip line dimensions according to the formula

$$Z_0 = \begin{cases} \frac{60}{\sqrt{\epsilon_{<e>}}} \cdot \ln\left(\frac{8h}{W} + \frac{W}{4h}\right) & \text{for } W/h \leq 1 \\ \frac{120\pi}{\sqrt{\epsilon_{<e>}}[W/h + 1.393 + 0.667\ln(W/h + 1.444)]} & \text{for } W/h \geq 1 \end{cases} \tag{6.1}$$

where the effective permittivity $\epsilon_{<e>}$ is equal to

$$\epsilon_{<e>} = \frac{\epsilon_r + 1}{2} + \frac{\epsilon_r - 1}{2} \cdot \frac{1}{\sqrt{1 + 12h/W}} \tag{6.2}$$

The guided wavelength λ_g of a microstrip line is the ratio of the free-space wavelength λ_0 to the square root of the effective dielectric constant $\lambda_g = \lambda_0/\sqrt{\epsilon_{<e>}}$. The propagation constant is obtained from the relation $\beta = k_0\sqrt{\epsilon_{<e>}}$, where $k_0 = 2\pi/\lambda_0$ is the wave number in free-space.

Also of interest are the dielectric and conductor losses. The attenuation due to dielectric loss α_d in microstrip line operating in quasi-TEM mode can be obtained from

$$\alpha_d = \frac{k_0\epsilon_r(\epsilon_{<e>} - 1)\tan\delta}{2\sqrt{\epsilon_{<e>}}(\epsilon_r - 1)} \quad [\text{Np/m}] \tag{6.3}$$

where $\tan\delta$ is the loss tangent of the dielectric, $\delta = \epsilon^{''}/\epsilon^{'}$, and $\epsilon = \epsilon^{'} - j\epsilon^{''}$ is the permittivity of the dielectric.
The attenuation due to the conductor loss α_c is more significant than dielectric loss and is given by

$$\alpha_c = \frac{R_s}{Z_0 W} \quad [\text{Np/m}] \tag{6.4}$$

where $R_s = \sqrt{\omega\mu_0/2\sigma}$ is the surface resistivity of the conductor, ω is angular frequency, σ is conductivity, and μ_0 is permeability of free-space.

6.3.2 Homogenisation Procedure

The microstrip analysis requires an alternative homogenisation model to that presented in Chapter 4. It was verified that the straightforward application of the pre-

viously defined empirical model for on-chip frequencies with the homogenisation boundaries tightly surrounding the grating structure results in relatively high error, up to 4%, in the estimation of the reflection coefficient. Due to the small variation in the value of the transmission coefficient it is always predicted with an error less than 1%. Neverthless, the error is higher compared to the error calculated for the grating with plane wave illumination, where the error does not exceed 0.2%. The increasing error in the reflection and transmission coefficient estimation is related to the change in the character of illumination from plane wave to quasi-TEM wave and also the change in the propagation direction of the wave with respect to the grating vector. The difference can be accounted for in the homogenised equivalent structure by an averaging procedure. The averaging procedure is applied by resizing the area where the homogeneous equivalent block is defined. In the horizontal direction the virtual boundary is defined at the distance $\Lambda/2$ from the periodic structure whereas the vertical direction is adjusted in terms of the height of the metal rods. Since the rods are separated by a distance equal to their height from the signal line and the ground plane the virtual homogenisation boundary is considered in 10 different positions extending the homogeneous block between the signal and the ground. The homogenisation is applied in two steps as is illustrated in Fig. 6.3.

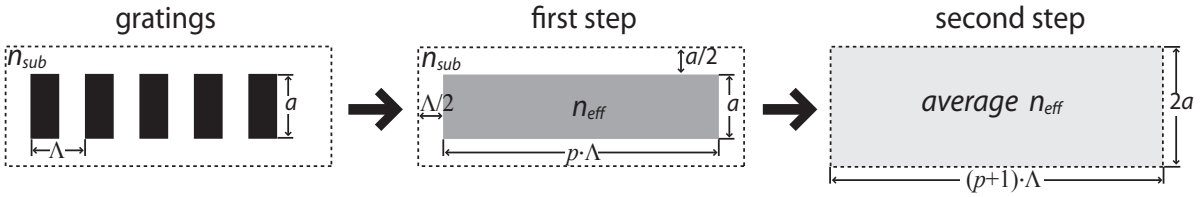

Figure 6.3: *Diagram representing the two steps of the homogenisation procedure.*

Firstly, the grating part (periodically aligned metal rods) is homogenised using the empirical model defined in Section 4.5.4. Secondly, the effective refractive index of the area enclosed by the virtual boundary is averaged in terms of the fraction occupied by a given material and material properties (effective dielectric and dielectric substrate) using Eq. (6.5)

$$< n_{eff} >= \left(n_{eff} \cdot \frac{p \cdot \Lambda}{(p+1) \cdot \Lambda} + n_{sub} \cdot \frac{\Lambda}{(p+1) \cdot \Lambda} \right) \cdot \frac{a}{2 \cdot a} + n_{sub} \cdot \frac{a}{2 \cdot a} \qquad (6.5)$$

where Λ is the grating period, p is the number of periods in a grating series, a stands for the height of the grating layer, n_{eff} is the effective refractive index calculated from

the modified Maxwell-Garnett mixing rule, and n_{sub} is the substrate refractive index. The first term in Eq. (6.5) accounts for the average effective refractive index in the horizontal direction over the distance $(p+1)\cdot\Lambda$ and grating height a. The second term accounts for the distance at which the horizontal virtual boundaries are separated from the grating. Here the distance is set to be half of the grating height.

It is shown in Fig. 6.4 that an increase of applied frequency significantly exceed the error in reflection and transmission coefficients estimated by the homogenised equivalent structure whereas the change of the size of the homogenised area does not influence the accuracy as much. The results are presented for the microstrip prototype structure with 5 inclusions embedded in the dielectric substrate with refractive index $n = 1.6$, the metal fill factor is $f = 0.51$ and the aspect ratio is $AR = 1.9$.

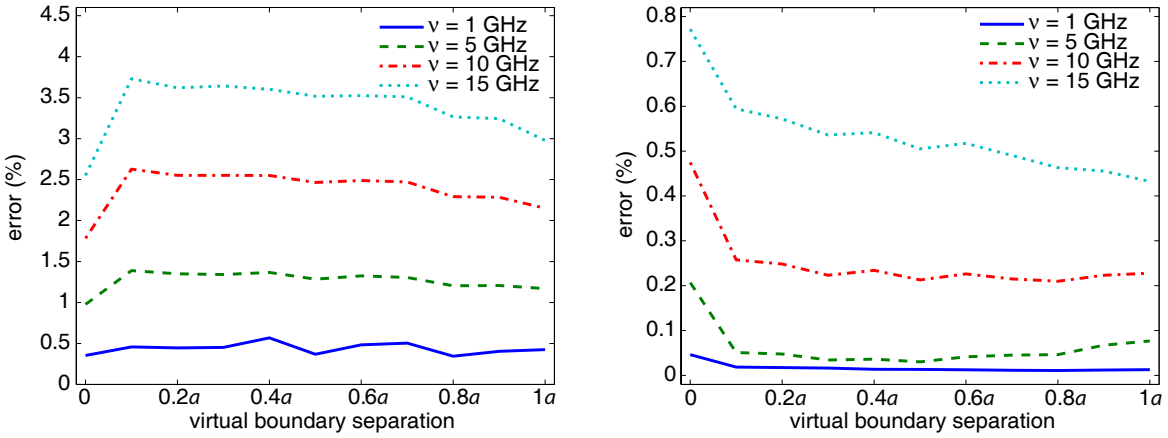

(a) *error in reflection* (b) *error in transmission*

Figure 6.4: *The error (%) in the magnitude of (a) reflection and (b) transmission coefficients calculated between the real and the homogenised structures where the empirical model is used to obtain n_{eff}. The error is plotted in terms of the changing virtual homogenisation boundaries in vertical direction.*

Since the value of the reflection and transmission coefficients in the studied structures is very low, with small differences between the response of the line with and without metal inclusions, such an increase of the error in the homogenisation procedure masks the difference between those responses. Therefore, the defined empirical model for on-chip frequencies needs to be reformulated. Nevertheless, for the microstrip prototype structures studied in this Chapter the presented results will demonstrate that the homogenisation for such structures is valid but the specific empirical model will

not be defined. The averaging procedure is slightly modified by tuning the value of the coefficient Ψ in the modified Maxwell-Garnett mixing rule. It was found that the value of $\Psi = 15$ gives good approximation for both reflection and transmission coefficients over the range of studied structures and with the horizontal virtual boundaries set within the distance of $0.6a$ the error less than 2%. This is depicted in Fig. 6.5. In the results presented in the following Sections the virtual boundaries are set at a distance of half the height a the metal rods. For simplicity in the notation in the remaining part of this Chapter the effective refractive index n_{eff} will stand for $< n_{eff} >$.

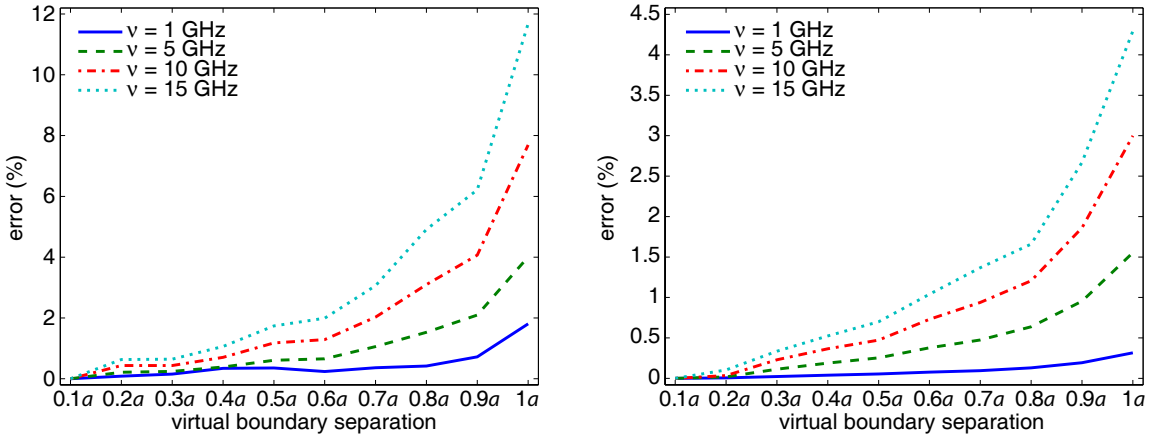

(a) *error in reflection* (b) *error in transmission*

Figure 6.5: *The error (%) in the magnitude of (a) reflection and (b) transmission coefficients calculated between the real and the homogenised structures where the n_{eff} is found based on the modified Maxwell-Garnett mixing rule. The error is plotted in terms of the changing virtual homogenisation boundaries in vertical direction.*

6.3.3 Numerical Model Geometry

The example numerical models for structures with 5 and 10 metallic inclusions are simulated using HFSS software [77]. The geometry and dimensions for the structure having 5 inclusions is shown in Fig. 6.6 with cross section in yz-plane in Fig. 6.6(a) and in xz-plane in Fig. 6.6(b). To ensure that all significant disturbances from the excitation ports are minimized the metal inclusions, defined as aluminum rods, were placed in the uniform dielectric substrate with a distance of 10Λ from each wave port. The period of the unit grating cell is $\Lambda = 35\,\mu$m and is well within the deep subwavelength

dimension, the depth η is equal to $35\,\mu$m. The metal fill factor is fixed at $f = 0.51$ and reflects the cross section of the metal rod equal to $18 \times 35\,\mu$m giving the aspect ratio $AR = 1.9$. The metal rods are separated from the signal line (copper strip) and from the ground plane (copper sheet) by the distance $35\,\mu$m. The dimension of the signal line is the same as the metal inclusions and the dielectric, used as substrate, was extended to tightly surround the line $35\,\mu$m above it. Following the HFSS guidelines for the size of the wave port for microstrip models, the height of the port was calculated and set to $6h$ whereas the width was fixed at $3h$, where $h = 3\eta$ stands for the thickness of the substrate, $630 \times 315\,\mu$m. In order to reduce the overall size of the model, symmetry boundary conditions were defined in the yz-plane whereas the model itself was surrounded by a vacuum enclosed by a radiation boundary to enable the wave to exit the domain without reflection. The radiation boundary is placed away from the microstrip line by a distance equal to one-quarter of the longest wave length in the considered range of $1 - 15\,$GHz.

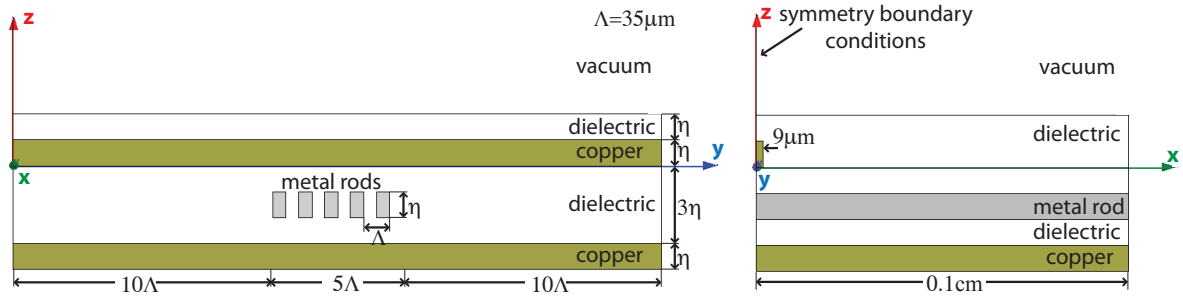

(a) *cross section in yz-plane* (b) *cross section in xz-plane*

Figure 6.6: *The numerical model of the microstrip line with five inclusions embedded in the substrate with cross section in (a) yz-plane, (b) xz-plane.*

A plot of the electric and magnetic field magnitude in the yz-plane at $10\,$GHz for the microstrip line with 5 metal bars embedded in the substrate with refractive index $n = 1.6$ is shown in Fig. 6.7(a) and Fig. 6.7(b), respectively. Compared with the standard microstrip electric field pattern, the metal rods cause a strengthening of the field in the region between the signal line and the inclusions and a weakening of the field in the region between the inclusions and the ground plane. The distribution of the magnetic field has a uniform character along the signal line. The strong electromagnetic field at such high frequencies induces a current flow along the metal

bars which generates additional heat losses. A plot of the surface current occurring at the metal bars is presented in Fig. 6.8.
The electric and magnetic field magnitudes for the homogenised structure are shown in Fig. 6.7(c) and Fig. 6.7(d), respectively. Transformation of the inclusion geometry and properties to an homogenised effective dielectric block results in a more uniform distribution of the electromagnetic field with insignificant change occurring in the area where the signal penetrates substrate consisting two different dielectrics. Nevertheless, the return and transmission loss calculated for both detailed and homogenised structures has comparable value, as will be discussed in the next Subsection.

6.3.4 Numerical Results

In this Subsection results obtained from numerical calculations based on the finite element method (HFSS software) for the microstrip lines of the type and dimensions as described in Subsection 6.3.3 are presented. The homogenisation technique is applied as discussed in Subsection 6.3.2. Presented results confirm that the homogenisation approach can be successfully applied to the analysis of structures supporting quasi-TEM modes.

Manually adjusting the value of the scaling factor to $\Psi = 15$ achieved a good agreement between the homogenised and actual structures, over the range of frequencies between $1 - 15$ GHz. Figure 6.9 shows the agreement in return and transmission loss estimation, as well as in the phase of S_{21} parameter, calculated for the real structure with 5 and 10 inclusions embedded in the substrate with dielectric constant $n = 1.6$ and compared with its homogenised equivalent. It also indicates that the performance of the microstrip line depends on the number of inclusions embedded in the substrate. The difference in phase calculated for S_{21} is less than 0.4° for the case of 5 metal bars embedded in the substrate. For the transmission line with 10 metallic inclusions the calculated difference in phase S_{21} is not higher than 0.9°. However the difference in phase between the real and the homogenised structure is so low that it does not exceed 1°. It is assumed that the small discrepancy is caused by numerical error and can be neglected. An illustration of the change in phase over the considered frequency range is shown in Fig. 6.9(c).

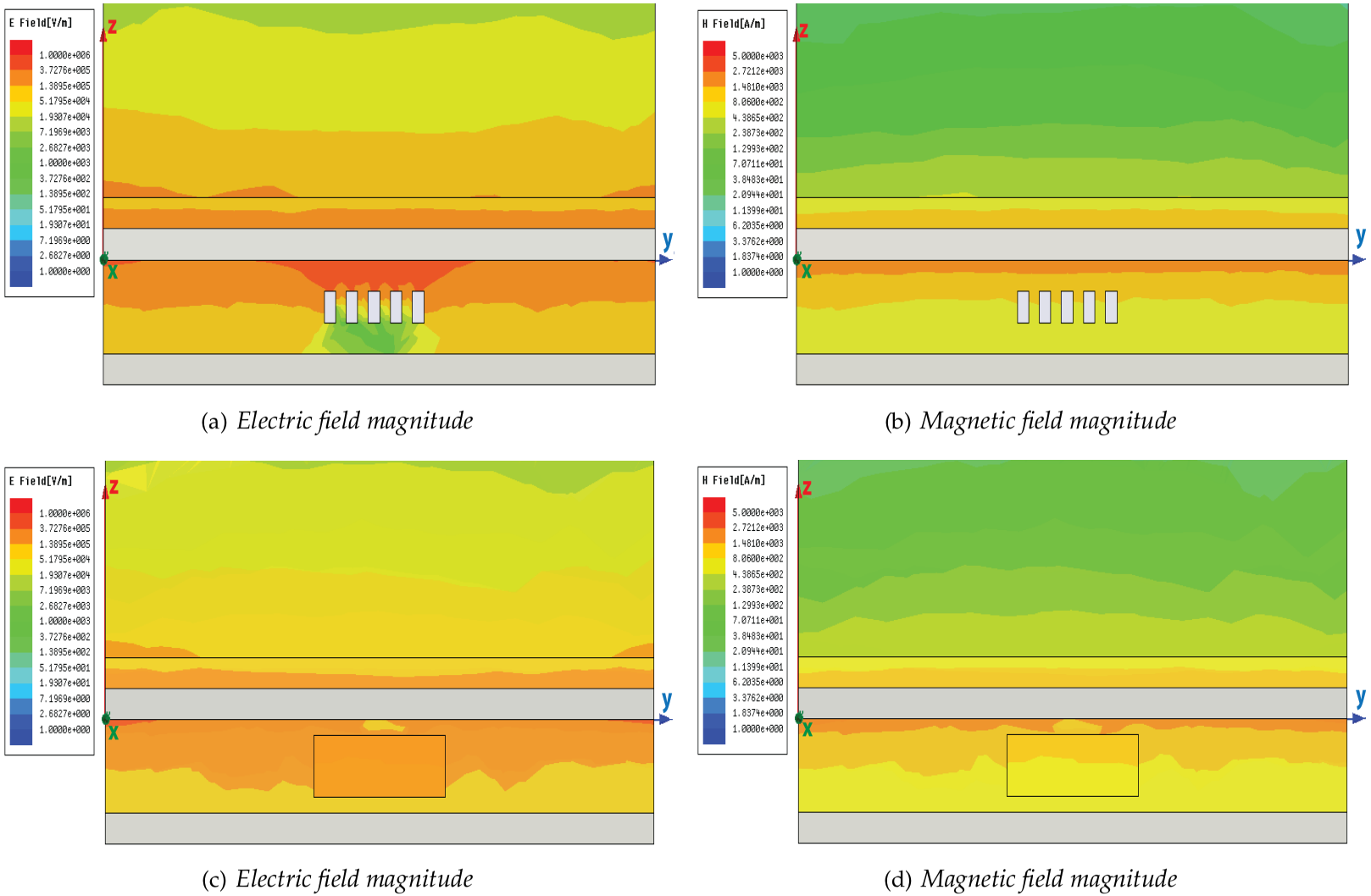

(a) *Electric field magnitude*

(b) *Magnetic field magnitude*

(c) *Electric field magnitude*

(d) *Magnetic field magnitude*

Figure 6.7: *The electromagnetic field magnitude pattern of a microstrip line with five inclusions embedded in the substrate (a) electric field, (b) magnetic field; and for its homogenised equivalent (c) electric field, (d) magnetic field.*

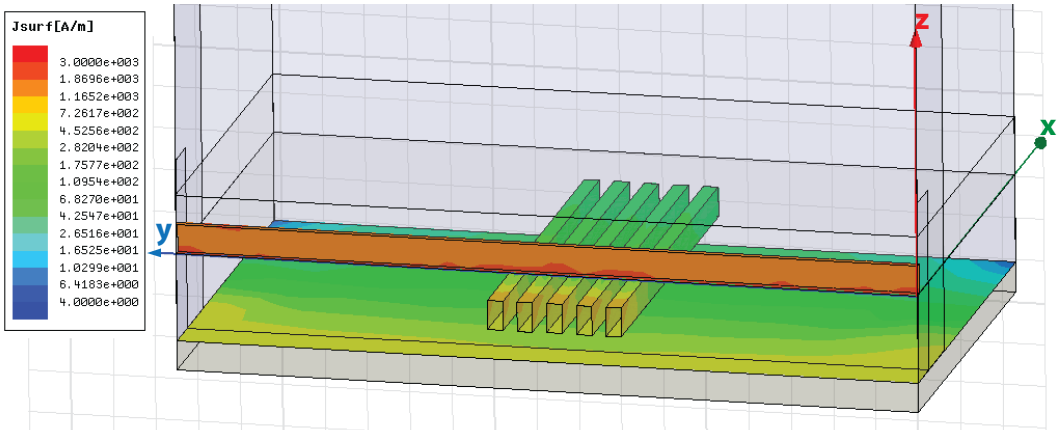

Figure 6.8: *The surface current occurring at the metal inclusions.*

Further, the analysis was performed for the microstrip lines with the same geometry but with changing properties of the dielectric substrate. The range of considered substrates was within $1 \leq n \leq 1.9$. This is within the range of low-k dielectric materials. Figure 6.10 demonstrates the good agreement in the return and transmission loss estimation for 5 inclusions embedded in different dielectric substrates. Figure 6.11 shows the agreement for 10 inclusions. In both cases the error between the reflection and transmission coefficients predicted by the homogenised equivalent and the real structure is not higher than 1% with a tendency to decrease as the frequency is reduced.

6.4 Measurement

This Section describes the equipment used in the experimental measurement of the reflection and transmission coefficients of microstrip lines with 5 and 10 metal bars placed in the dielectric substrate. The main components of the measurement system are a pair of SubMiniature version A (SMA) connectors, coaxial cables and a vector network analyser. The experimental results compared with numerical calculations for equivalent structures are also presented.

6.4.1 Microstrip Prototype

Prototypes of the microstrip lines with metal inclusions underneath the signal strip were manufactured as three-layer PCBs with two different configurations - one with 5 and the other with 10 metal bars. The lines were made of Rogers RO4350B high

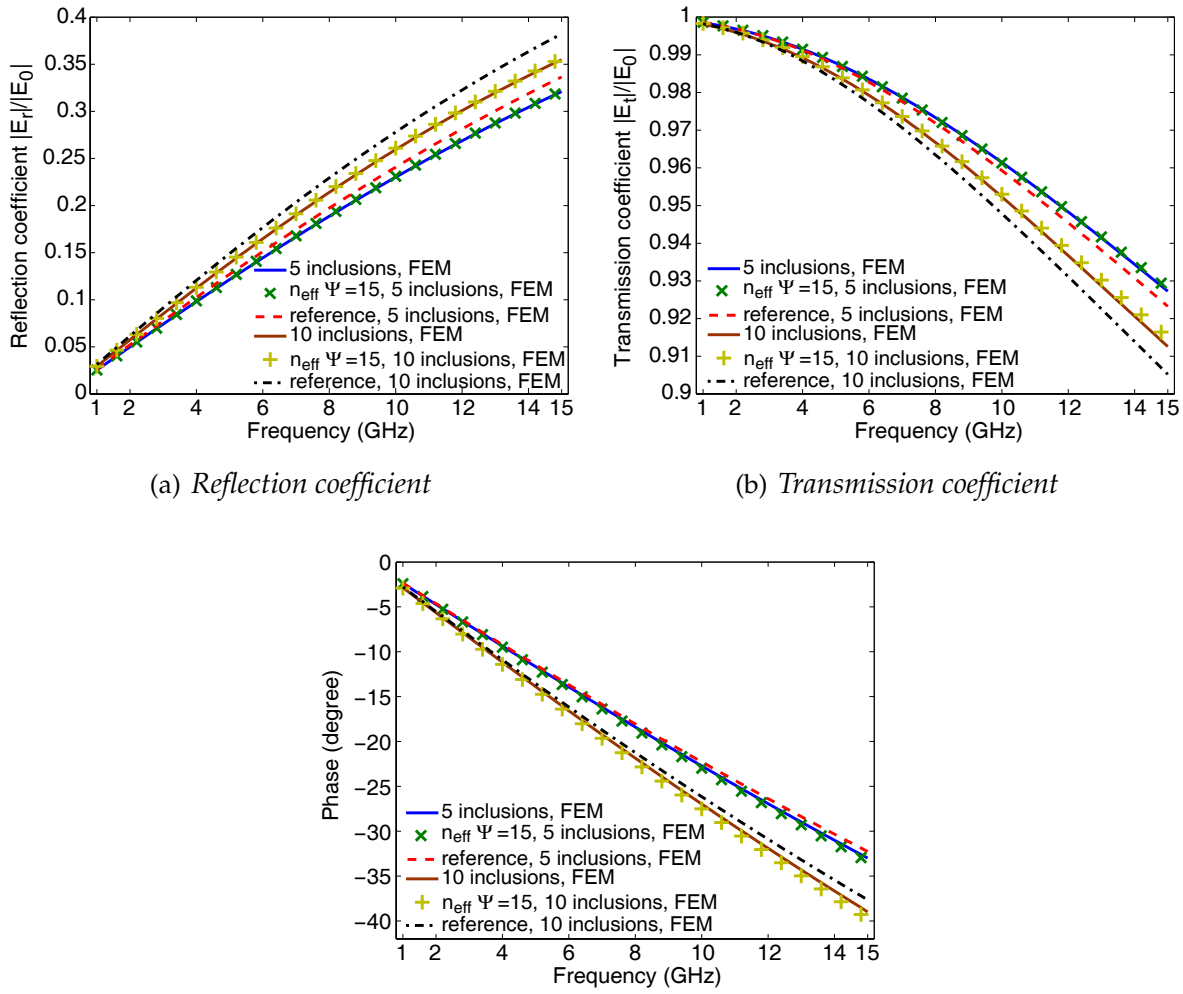

(a) *Reflection coefficient*

(b) *Transmission coefficient*

(c) *Phase* S_{21}

Figure 6.9: *The magnitude of the reflection and transmission coefficients and the phase of parameter* S_{21} *for a microstrip line with five and ten inclusions embedded in the substrate with* $n = 1.6$*. The numerical calculations from the FEM method obtained for detailed and homogenised structure are in good agreement. The plot is extended with the calculations of reference structures (with no inclusions) for each line.*

frequency laminate ($\epsilon_r = 3.66$) [90] covered with an $18\,\mu$m thick copper foil. The dimensions of the manufactured prototypes are presented in Fig. 6.12 with technical drawings for the transmission line with 5 copper bars embedded in the substrate in Fig. 6.12(a), and for the case with 10 inclusions in Fig. 6.12(b). The lines were designed such that the distance from the edges where the SMA connectors are soldered to the inclusions is fixed at $16.5\,$mm in both prototypes. For each type of microstrip

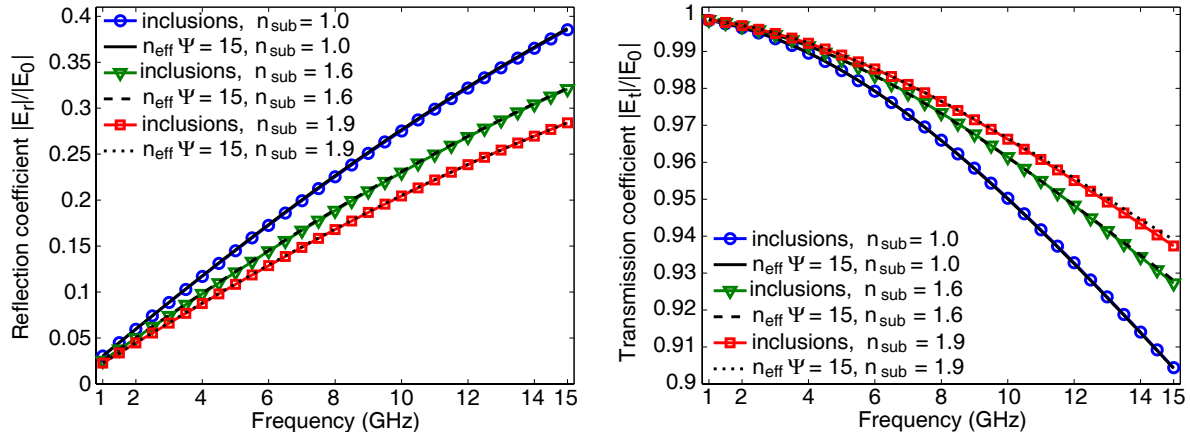

(a) *Reflection coefficient* (b) *Transmission coefficient*

Figure 6.10: *The magnitude of the reflection and transmission coefficients of a microstrip line with five inclusions embedded in different substrates. The numerical calculations from FEM method obtained for detailed and homogenised structures are shown and are in good agreement.*

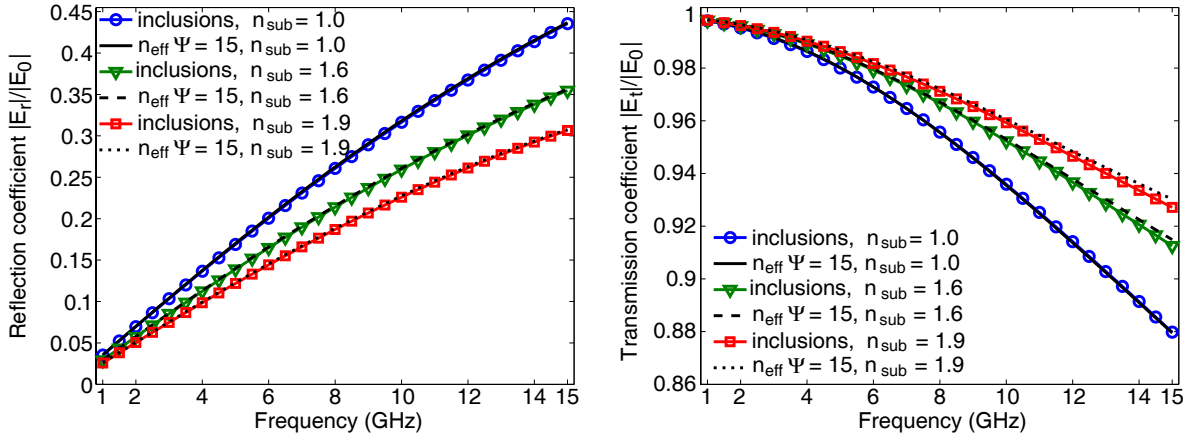

(a) *Reflection coefficient* (b) *Transmission coefficient*

Figure 6.11: *The magnitude of the reflection ($|E_r|/|E_0|$) and transmission ($|E_t|/|E_0|$) coefficients of a microstrip line with ten inclusions embedded in different substrates. The numerical calculations from FEM method obtained for detailed and homogenised structures are shown and are in good agreement.*

line, reference lines with plain substrate were manufactured in order to investigate the real change in the reflectivity and transmissivity of the line with and without metallic inclusions. Due to the limitation of the manufacturing process the highest aspect ratio

which is achievable is 0.36 with a $50\,\mu$m separation of the rods. Though interconnects with such low aspect ratios are not used in contemporary ICs, this geometry nonetheless allowed the experimental validation of this aspect of the proposed homogenisation approach to take place. The tolerance of the manufacturing process is within a range of 10%.

6.4.2 Equipment and Calibration

The microstrip measurement system contains a microwave network analyser (Agilent Technologies E8362B PNA Microwave Network Analyser), a pair of coaxial cables and SMA connectors. The measurement setup was calibrated using the guided two-port calibration for the range of frequencies $1 - 18\,$GHz. The upper limit was set according to the recommended frequency range for good electrical performance of SMA connectors (DC to $18\,$GHz). The number of sampled points in the frequency sweep was fixed at 201.

The guided SLOT (Short-Load-Open-Through) calibration process sets the reference plane to the end of the coaxial cables, therefore the SMA connectors are not removed from the measurement by the calibration procedure. This calibration procedure normalizes the measurement for increase accuracy of the measured S-parameters. It was verified that the measured response of the lines is masked by the connectors performance and to some extent by the presence of solder. Considering these issues the numerical models of the lines contains models of connectors on both its ends. The numerical model of the measured transmission line and its photograph are shown in Fig. 6.13.

6.4.3 Experimental Results

The experimental results for the two kinds of microstrip lines with metal bars located in the substrate appear to be affected by a few factors. First, the manufacturing precision for the multilayered PCB with desired dimensions and geometry needs to be within a tolerance of 10%. Therefore the deviation in the thickness of the dielectric substrate is $184\,\mu\text{m} \pm 18\,\mu$m, and in the thickness of the metal layers $18\,\mu\text{m} \pm 1.8\,\mu$m. Second, it was noted that the lines are very sensitive to any bending in the structure because of the thinness of the substrate. Hence each measured line was stabilized by attaching a solid strip to the ground plane along the signal line, in order to provide mechanical rigidity. The data obtained from the measurement are expected to be distorted because

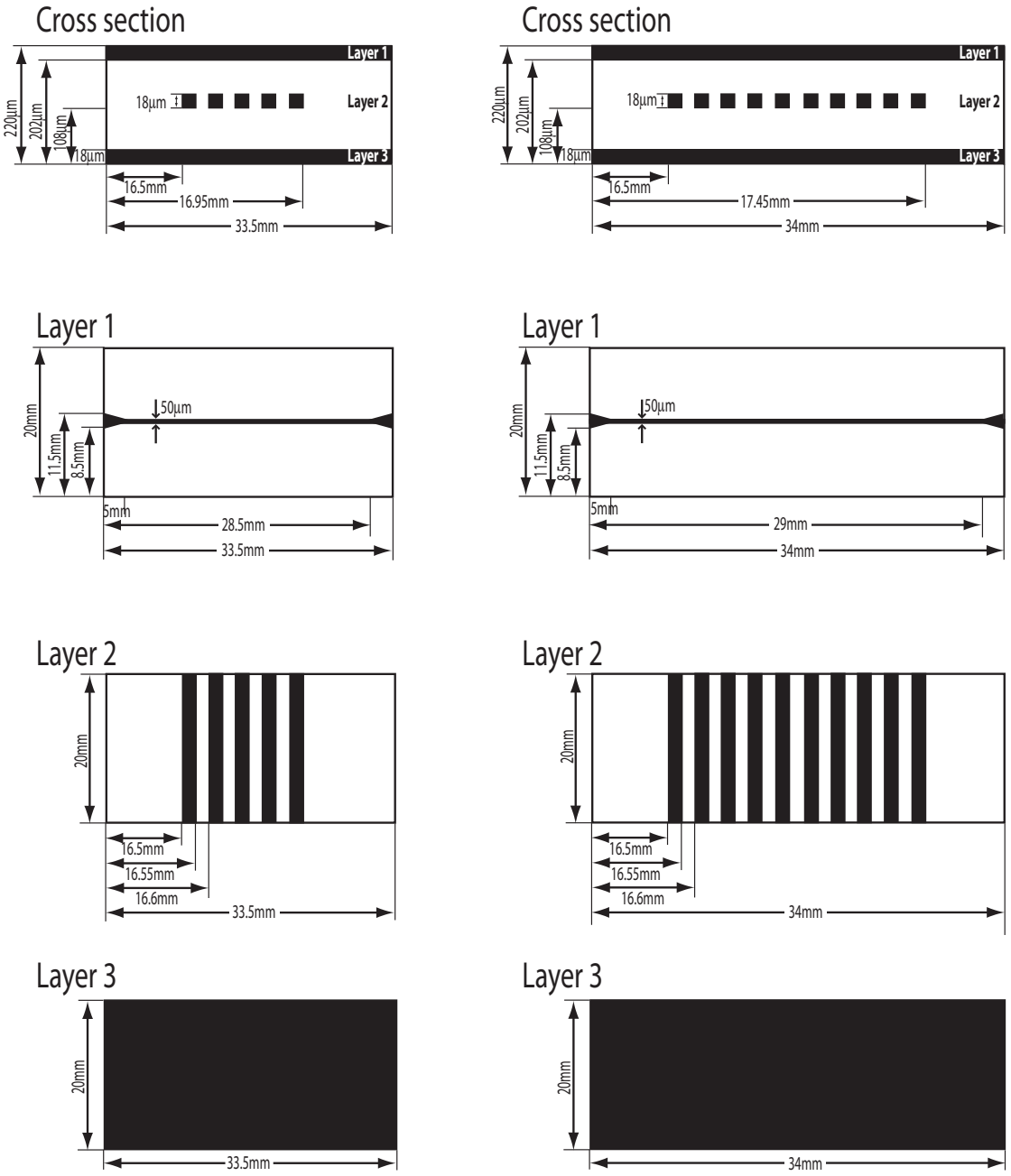

(a) *5 inclusions* (b) *10 inclusions*

Figure 6.12: *Technical drawing showing the cross section and three layers of the multilayer PCB for the microstrip prototype with: (a) five embedded copper bars, (b) ten embedded copper bars.*

of manufacturing tolerances.

In order to connect the microstrip line to SMA end-launchers, a taper is required in

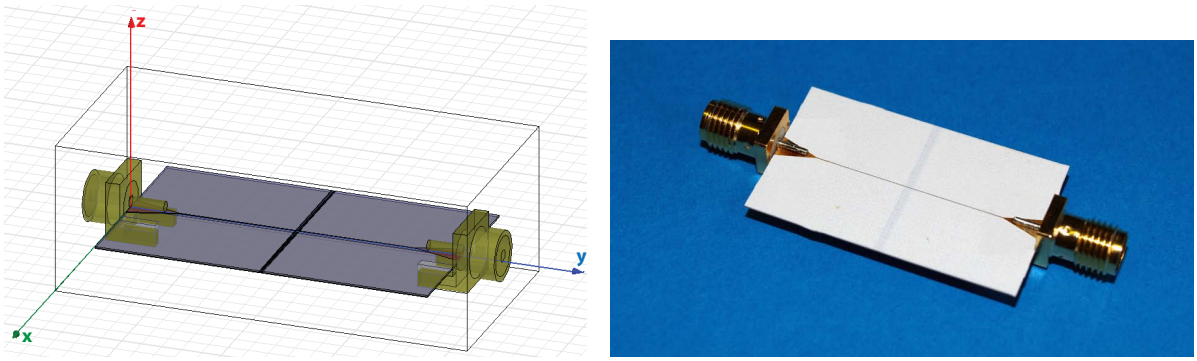

(a) *Microstrip numerical model* (b) *Microstrip prototype*

Figure 6.13: *The prototype microstrip line with metal inclusions embedded in the substrate (a) numerical model, (b) photograph of the line.*

the signal line. The rapid change in the distribution of characteristic impedance along the tapered section of the line can be reduced by an impedance matching approach. There are several methods which allow matching of the impedance along non-uniform transmission lines by designing a taper with a profile that is specified to the application [96]. However for the purpose of the presented experiment the impedance matching procedure was carried out empirically in a few steps. Since the models of the connectors have to be included into the numerical model it was verified to have the required $50\,\Omega$ characteristic impedance at the incident wave port (the obtained value was $Z_0 = 49.9 - 0.04j\,\Omega$). Then the geometry of the taper was designed considering the dimensions imposed on the microstrip line by the limitations of the manufacturing process. The reference transmission line with connectors and tapers was simulated and the obtained characteristic impedance at both wave ports was $Z_0 = 49.88 - 0.04j\,\Omega$. Nevertheless the discontinuities in impedance profile along the line between the points where the SMA connectors are fixed to the line and the points where the taper transforms into the line with characteristic impedance $Z_0 = 115\,\Omega$ result in resonances. The resonances occur in reflection and transmission coefficients with periodicity of about $3.4\,$GHz, within the range of $1 - 15\,$GHz, in both types of lines. The resonance frequencies are correlated with the length of the non-uniform transmission line and occurs at frequencies for which the length of the line is equal to a quarter or half of the illumination wavelength.

The numerical calculations and measurements were taken over the frequency range $1-$

15 GHz. Nevertheless, for the particular model the practical application of the homogenisation technique is limited to frequencies within $10 - 12$ GHz. This limitation is due to the low aspect ratio of 0.36 obtained for the embedded metal bars and the large distance between inclusions and the signal line as well as the ground plane ($\sim 90\,\mu$m $\approx 5\eta$). Hence, the significant difference between performance of the line with inclusions and reference line can be noted only in such narrow frequency range, although the effective medium theory (EMT) model gives valid results outside this range, they are the equivalent to having no inclusions. Therefore, the EMT model is useful if a structure requires modelling over a wide range of frequencies which include a frequency window where the presence of the inclusions results in a difference in performance.

Figure 6.14 illustrates the qualitative agreement between numerical and experimental data for a microstrip line with 5 inclusions floated in the substrate, and results for 10 inclusions are demonstrated in Fig. 6.15. The small displacement, by about 0.2 GHz, in obtained values of reflection and transmission coefficients is related to the non-ideal nature of the fabricated structure.

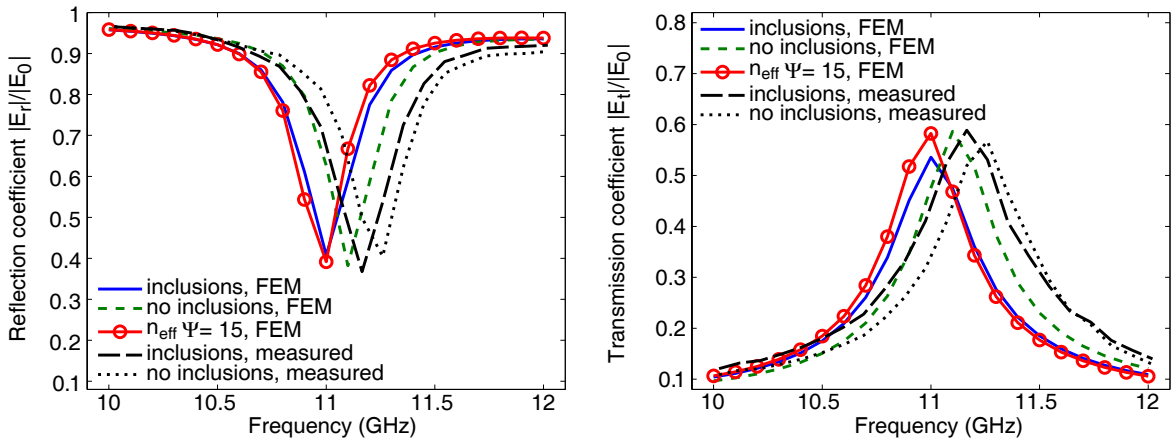

(a) *Reflection coefficient* (b) *Transmission coefficient*

Figure 6.14: *The magnitude of the reflection and transmission coefficients of a microstrip line with five inclusions embedded in the substrate. The experimental data follows the same trend as the numerical data obtained from FEM method for detailed, homogenised and reference structure.*

Further, the strength of occurring resonances is, to some extent, masked by the chosen density of sampled data points. Thus, both simulated and measured data were inter-

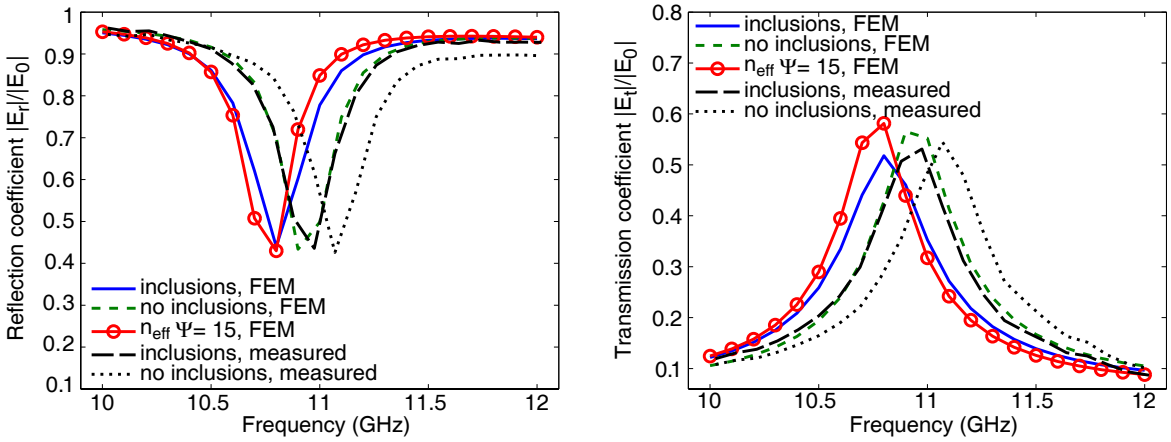

(a) *Reflection coefficient* (b) *Transmission coefficient*

Figure 6.15: *The magnitude of the reflection and transmission coefficients of a microstrip line with ten inclusions embedded in the substrate. The experimental data follows the same trend as the numerical data obtained from FEM method for detailed, homogenised and reference structure.*

polated in order to calculate the $\mathcal{Q}$ factor (quality factor) for the resonance occurring in the frequency interval $10-12\,\text{GHz}$. The $\mathcal{Q}$ factor is a value which relates the resonance bandwidth to its center frequency and is defined as

$$\mathcal{Q} = \frac{\nu_0}{\Delta\nu} \tag{6.6}$$

where ν_0 is the center frequency of the resonance and $\Delta\nu$ stands for the full width half maximum calculated at half of the maximum value of the peak. The higher the value of $\mathcal{Q}$, the narrower and sharper the resonant peak is.

The calculated $\mathcal{Q}$ factor for the prototype line in terms of the transmission coefficient has different values for the structures with and without inclusions. The quality factor of the resonance is approximately equal to 31, with the center frequency ν_0 within $10.9-11.1\,\text{GHz}$, for microstrip with 5 embedded metal bars and the homogeneous equivalent in both numerical and experimental design. Whereas $\mathcal{Q} \approx 28$ for the reference line where $\nu_0 \approx 11.2\,\text{GHz}$.

Similar agreement occurs in the value of $\mathcal{Q}$ factor calculated for the line with 10 metal bars embedded in the substrate, and also for the homogeneous equivalent. The value of $\mathcal{Q} \approx 36$ was obtained with the center frequency between $10.7-10.9\,\text{GHz}$, and for the reference line $\mathcal{Q} \approx 32$ with ν_0 within $11-11.1\,\text{GHz}$. Thus for both cases of studied

structures the resonance quality factor indicates the agreement between numerical and experimental data.

In order to demonstrate the change in the performance of the microstrip line with the change of the number of metal bars placed in the substrate the obtained results are compared in Fig. 6.16. For the transmission line with higher number of inclusions the center frequency of the resonance is lower with a narrower and sharper resonance peak than for the line with shorter series of metal-dielectric gratings embedded in the substrate.

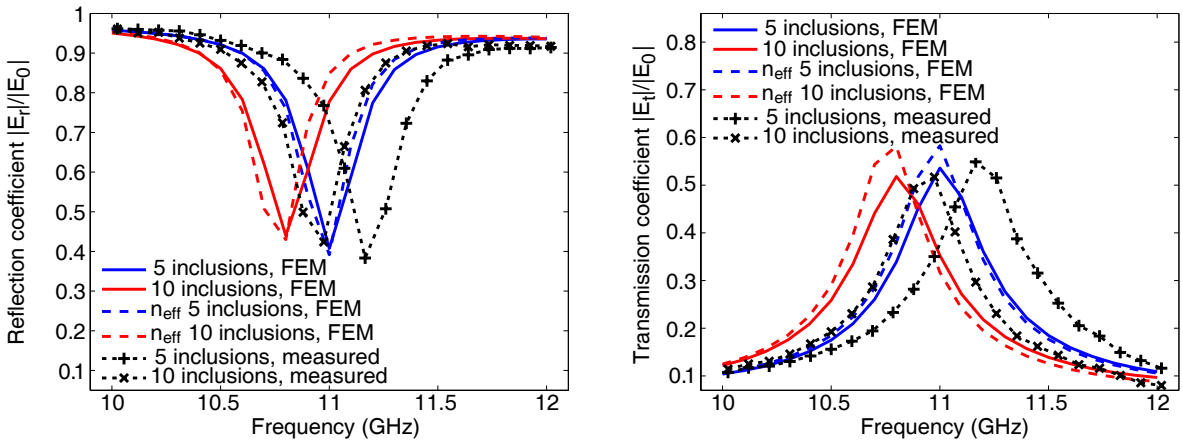

(a) *Reflection coefficient* (b) *Transmission coefficient*

Figure 6.16: *The comparison of the magnitude of the reflection and transmission coefficients of a microstrip with five and ten inclusions embedded in the substrate. The number of inclusions determine the value of the center frequency of the resonance peak.*

6.5 Summary

A study of a microstrip line with metal inclusions embedded in the substrate shows that the homogenisation approach can be applied to the analysis of the lower layers of interconnects in an interconnect stack. For the homogenisation procedure the averaging method for the calculation of the effective dielectric constant is presented. It is shown that the value of scaling factor $\Psi = 15$ in the modified Maxwell-Garnett mixing rule gives good estimation of the averaged effective dielectric constant. The homogenisation concept is based on numerical simulations and validated experimentally.

For the range of considered dielectric substrates the error in the reflection and transmission coefficient estimation between detailed and homogenised structure is less than 1% with tendency to increase proportionally to the increase of the applied frequency.
The experimental validation was carried out by the measurement of S-parameters of the prototype line with five and ten metal rods embedded in the substrate. The obtained results show that the performance of the line is influenced by the number of metal inclusions. The measured data compared with numerical results obtained for the equivalent detailed and homogenised microstrip line are in good agreement.

Chapter 7

Conclusions and Further Work

The work presented in this Thesis involves the application of effective medium theory to allow a single layer of interconnects to be replaced by a homogeneous material. The final goal was to develop an empirical model, given by a mathematical formulation, to calculate the effective refractive index of the homogeneous material equivalent to the interconnect grating structure. The main achievements of this study may be listed as follows:

- showed that the single layer of interconnects can be homogenised using effective medium theory including the development of the 'brute force' algorithm;
- applied the modified Maxwell-Garnett mixing rule in order to predict the effective refractive index of the homogenised equivalent structure so that the 'brute force' algorithm is no longer required; and proposed the empirical models to calculate the effective refractive index from a complete set of mathematical formulas for two frequency bands: $1 - 10$ GHz for the typical on-chip signals frequencies, $30 - 200$ GHz related to the ISM frequency bands;
- experimentally demonstrated the validity of the homogenisation approach via free-space measurement of the metallic grating structure at X-band ($8.2 - 12.4$ GHz) frequencies and through agreement with numerical results obtained from simulators based on numerical methods: finite-difference time-domain method, rigorous coupled wave analysis, finite element method;
- extended approach to deal with microstrip lines with interconnects located between signal line and ground plane and experimentally demonstrated the validity of the homogenisation approach by the measurement of a prototype mi-

crostrip line with metal rods embedded in the substrate and the agreement with numerical results obtained from the simulator based on the finite element method;

This work presents the first application of effective medium theory to the analysis of the performance of interconnects in integrated circuits. The contributions of the presented research have established a strong starting point for this approach in which, by introducing the homogeneous equivalent for the interconnect layer, a tool is provided for dealing with the complexity of contemporary electronic devices during the design process and physical verification of the system. Using the empirical models developed in this work, it is expected that computationally-demanding electromagnetic simulations of congested interconnect networks can be simplified whilst at the same time retaining their precise nature.

To give an understanding of the research carried out in this project, the coverage of the related background material was outlined. The essence of the artificial dielectrics and metamaterials along with the effective medium theory defined for the periodic laminated structures and a review of the work in which the modified classical mixing rules are used was provided. Since the Maxwell-Garnett rule was of the main interest in the presented study, a detailed description of this rule was given.
The numerical data were generated using solvers based on numerical techniques: FDTD, RCWA and FEM, principles of which are briefly reviewed. The validation of these techniques against the analytical method, where the reflection and transmission coefficient of a solid silicon slab was calculated, was also described.

In order to provide a general model which will account for the precise geometry and nature of interconnects layers a canonical structure has been introduced. The canonical structure, defined as a metal-dielectric grating, represents a single layer of interconnects and was successfully homogenised using the defined empirical models for the specified frequency bands. The considered parameters span a four dimensional domain, namely the values of the metal fill factor, aspect ratio, dielectric refractive index and frequency. A detailed discussion on the validity of the defined empirical model for on-chip signal band was presented. The empirical model estimates the reflection and transmission coefficients with an error not higher than 2.7% when the structure is illuminated by a normally incident plane wave. The model can be applied with confidence over a range of incident angles within $\pm 30^{\circ}$ with plane wave illumination

where the agreement is better than 5%. Further it is valid, without modifications, for a range of trapezoidal profiles of the grating with sidewall angles up to 5° and incidence angles within $\pm 30^\circ$ with similar error of 5%. It was discussed that the effective refractive indices obtained from the defined empirical model are well within the theoretical Wiener bounds and the upper limit can be succesfully reduced and estimated by the lower Hashin-Shtrikman bound.

The homogenisation approach was experimentally validated for the two main applications. The free-space measurement was performed at X-band frequencies where the reflectivity of the metallic grating structure was of the main interest. Such a measurement configuration was considered with specific reference to the estimation of the reflectivity of the whole chip in a System-in-Package. Further, the obtained results were numerically extrapolated over the range of frequencies $1 - 18\,\mathrm{GHz}$ using the FEM simulator, hence the homogenisation approach is valid over a wider frequency interval.
The second measurement was designed to validate the homogenisation concept for the estimation of the interconnect performance at the lower layers of interconnects in interconnect stacks. For this purpose the prototype microstrip line with a number of metal rods embedded in the substrate was manufactured. Both experiments together with the numerical simulations performed for the effective medium theory application showed that the homogenisation concept is valid for the analysis of interconnects.

7.1 Future Work

Further research needs to be conducted into extending the approach to the analysis of multilayered interconnect structures where the difference in the geometry of the interconnects depend on their location in the interconnect stack. Since the features differ in terms of the size of the pitch, the ratio period-to-wavelength, a more thorough investigation in terms of the influence of the period of the relevant grating structure is needed. The other issue which needs to be considered is the effect of coupling between layers, namely how the homogeneous equivalent with effective properties can account for the undesirable transfer of energy from one layer to the neighbouring ones. The perpendicular orientation of successive layers in a typical stack constrains the problem somewhat.

The study of the multilayered interconnect grating structure formed by mutually orthogonal non-connected interconnect layers can be conducted by an analysis adapted from that of two-dimensional wire media. The geometry of the periodic structure formed by 2D wire media is illustrated in Fig. 7.1(a). This structure is composed of an array of metallic wires of infinite length embedded in a dielectric. In other words, the wires are organized in a cubic lattice with a unit cell depicted in Fig. 7.1(b). The metallic crystal is created by a periodic distribution of the unit cell along three directions defined by the rectangular coordinate system.

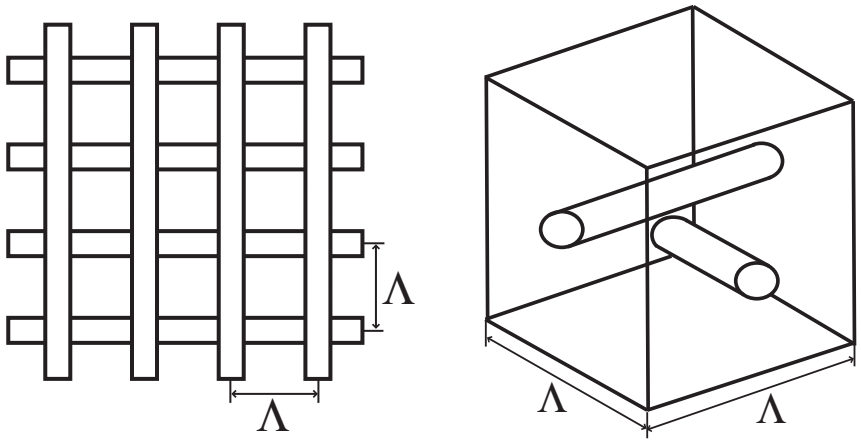

(a) *2D wire medium* (b) *unit cell*

Figure 7.1: *Geometry of the (a) two-dimensional wire media, and (b) unit cell.*

In effective medium theory the 2D wire medium is examined as a homogeneous anisotropic medium. The electromagnetic waves in such a structure experience spatial dispersion, even in the very long wavelength limit, which causes the presence of evanescent waves with complex propagation constant. This introduces anisotropy to the material's permittivity, even to the cubic lattice which would be expected to behave as an isotropic electromagnetic crystal [97, 98, 99, 100]. The artificial medium is characterised by a permittivity dyadic that depends on both the frequency and wave vector. The wire media structures have negative material parameters (permittivity and permeability) and are called double negative materials [101].

Hence the work presented in this Thesis was restricted to the study of uniform metal-dielectric gratings further research needs to extend the method to the analysis of non-

uniform density structures, quasi-periodic alignments, in order to define a homogenisation approach appropriate to encompassing larger areas consisting of interconnects in electronic components.

In some niche applications enhanced empirical models for the defined canonical structure could be formulated where wider (non-normal) incident angles of the plane wave are considered. Such an approach may provide an empirical model valid over a wider range of incident angles. Possibly, it may even cover the whole range within $\pm 90^{\circ}$.

Since the empirical models for the plain wave illumination of a grating structure (single layer of interconnects) has already been presented in this Thesis and the homogenisation approach has been validated for the structures supporting the quasi-TEM modes, appropriate future work may include the formulation of empirical models for non-TEM modes. This is important because the studied microstrip prototype lines illustrate the principle that the effect of interconnects on adjacent layers should be considered. Furthermore, the accuracy with which crosstalk can be predicted using effective medium theory needs to be evaluated.

Appendix A

Least Squares Method

The least squares method is a procedure to determine the line (curve) giving the best fit between the modelled and measured (observed) data. In the least squares scheme the best fit is obtained when the modelled values have the minimal sum of the deviations squared (least squared error) from the given set of measured data.
Assuming that the measured data points are $(x_1, y_1),\ (x_2, y_2), \ldots, (x_N, y_N)$ where $x_i, i = \{1, 2, \ldots, N\}$ is the independent variable and $y_i, i = \{1, 2, \ldots, N\}$ is the dependent (measured) variable. The fitting curve $f(x)$ has the deviation (error) e from each data point defined as the difference between the value of the dependent variable and the predicted value from the model

$$e_1 = y_1 - f(x_1),\ e_2 = y_2 - f(x_2), \ldots, e_N = x_N - f(x_N). \tag{A.1}$$

The least squares method estimates the optimum fitting curve such that the sum of the squared residuals

$$S = e_1^2 + e_2^2 + \ \ldots \ + e_N^2 = \sum_{i=1}^{N} e_i^2 = \sum_{i=1}^{N} \left[y_i - f(x_i)\right]^2 \tag{A.2}$$

is a minimum.

Figure A.1 shows a graphical illustration of the least squares estimation where the set of data points is approximated by a straight line $y = f(x; a)$ and the errors e_i are also depicted.

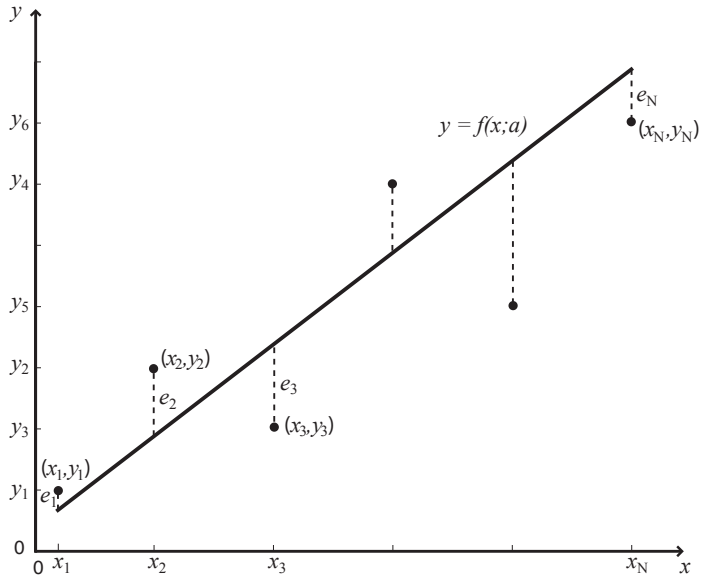

Figure A.1: *The least squares estimation.*

A.1 Multidimensional Taylor Series

Assuming that the multi-variable function $f(\mathrm{x})$, where $\mathrm{x} = (x_1, x_2, \ldots, x_N)$ and N indicates the dimension of the position vector x, is differentiable over its domain then the gradient $\nabla f(\mathrm{x})$ vanishes at points where the minimum occurs. Hence, the minimisation problem is transformed to the root finding of the following system of N equations

$$\nabla f(\mathrm{x}) = 0. \tag{A.3}$$

Denoting the origin of the coordinate system by $\mathbf{0}$, the quadratic multidimensional Taylor series of the function $f(\mathrm{x})$ about the origin is

$$f(\mathrm{x}) = f(\mathbf{0}) + \sum_{i=1}^{N} \left.\frac{\partial f}{\partial x_i}\right|_{\mathbf{0}} x_i + \frac{1}{2} \sum_{i,j=1}^{N} \left.\frac{\partial^2 f}{\partial x_i \partial x_j}\right|_{\mathbf{0}} x_i x_j + O(\delta x^3). \tag{A.4}$$

In matrix notation, Eq. (A.4) has the form

$$f(\mathrm{x}) = c - \mathbf{b} \cdot \mathrm{x} + \frac{1}{2} \mathrm{x} \cdot \mathbf{H} \cdot \mathrm{x} + O(\delta x^3), \tag{A.5}$$

where

$$c = f(\mathbf{0}), \tag{A.6}$$

$$\mathbf{b} = -\nabla f|_{\mathbf{0}}, \tag{A.7}$$

and **H** is the Hessian matrix of f with elements

$$H_{ij} = \left.\frac{\partial^2 f}{\partial x_i \partial x_j}\right|_{\mathbf{0}}. \tag{A.8}$$

It is assumed that **H** is a positive definite matrix, hence the minimum of function f exists. If the $O(\delta x^3)$ is negligible then the gradient of f is given by

$$\nabla f = \mathbf{H}\mathrm{x} - \mathbf{b}. \tag{A.9}$$

To solve Eq. (A.9), the gradient is required to vanish $\nabla f = 0$. Hence, the problem reduces to solving the linear system of equations

$$\mathbf{H}\mathrm{x} = \mathbf{b}. \tag{A.10}$$

The minimum of function f can be found in a single step or, in the case when $O(\delta x^3)$ terms are not negligible, using the iterative Newton-Raphson method.

A.2 General Description of the Least Squares Method

The curve fitting procedure is to determine a function $y = f(x)$ based on the number N of measured or observed values $y_1, \ldots, y_N$ at the corresponding x values $x_1, \ldots, x_N$. The curve fitting requires a model function

$$y = f(x, \mathbf{a}) \tag{A.11}$$

where the M $(N \geq M)$ adjustable parameters are stored in the vector $\mathbf{a} = (a_1, a_2, \ldots, a_M)$. The values of these parameters are estimated for the best fit to the data (x_i, y_i), $i = \{1, \ldots, N\}$.
The fitting procedure is executed by varying the parameters a_j, $j = \{1, \ldots, M\}$ in order to estimate the modelled vector

$$\mathbf{D}(\mathbf{a}) = (f(x_1, \mathbf{a}), f(x_2, \mathbf{a}), \ \ldots \ , f(x_N, \mathbf{a})) \tag{A.12}$$

as close as possible to the vector

$$\mathbf{D}_0 = (y_1, y_2, \ \ldots \ , y_N) \tag{A.13}$$

created from the provided measured data.
In the least squares method the deviation is reduced by minimising the function

$$\Phi(\mathbf{a}) = \frac{1}{2} \left|\mathbf{D}(\mathbf{a}) - \mathbf{D}_0\right|^2. \tag{A.14}$$

The function $\Phi(\mathbf{a})$ can be approximated by a second order Taylor series expansion about the origin of the parameter space denoted by $\mathbf{0}$ and is given by

$$\Phi(\mathbf{a}) = \Phi(\mathbf{0}) + (\nabla\Phi)(\mathbf{0}) \cdot \mathbf{a} + \frac{1}{2}\mathbf{a} \cdot \mathbf{H}(\mathbf{0}) \cdot \mathbf{a} \tag{A.15}$$

where the gradient

$$(\nabla\Phi)_i = \frac{\partial\Phi}{\partial a_i} = \frac{\partial\mathbf{D}}{\partial a_i} \cdot (\mathbf{D} - \mathbf{D}_0) = \sum_{k=1}^{N} \frac{\partial D_k}{\partial a_i}(D_k - D_{0k}) \tag{A.16}$$

and the Hessian

$$H_{ij} = \frac{\partial^2\Phi}{\partial a_i \partial a_j} = \sum_{k=1}^{N} \frac{\partial D_k}{\partial a_i}\frac{\partial D_k}{\partial a_j} + \sum_{k=1}^{N} \frac{\partial^2 D_k}{\partial a_i \partial a_j}(D_k - D_{0k}). \tag{A.17}$$

The above equations can be expressed in terms of the Jacobian matrix $\mathbf{J}$ with components $J_{ij} = \frac{\partial D_i}{\partial p_j}$

$$\nabla\Phi = \mathbf{J}^T(\mathbf{D} - \mathbf{D}_0), \tag{A.18}$$

$$(\mathbf{H})_{ij} = (\mathbf{J}^T\mathbf{J})_{ij} + \sum_{k=1}^{N} \frac{\partial^2 D_k}{\partial a_i \partial a_j}(D_k - D_{0k}). \tag{A.19}$$

If vector $\mathbf{D}(\mathbf{a})$ is linear in $\mathbf{a}$ ($\Phi(\mathbf{a})$ is quadratic in $\mathbf{a}$) then the second derivatives in $\mathbf{D}$ vanish and the Hessian $\mathbf{H}$ of Φ is given by

$$\mathbf{H} = \mathbf{J}^T\mathbf{J}. \tag{A.20}$$

The least squares method is classified into two groups, namely, linear and nonlinear least squares. In the linear least squares the model function $y = f(x, \mathbf{a})$ is a linear combination of parameters a_j, $j = \{1, \ldots, M\}$, and the formula may represent a line, a parabola or higher order polynomial. In the case of nonlinear least squares the parameters can have a form of e.g. $a_j^2,\ e^{a_j x}$.

A.3 Linear Least Squares

The linear least squares is very often used to fit a straight line to the considered data. In such a case the model function is a linear function

$$y = f(x, \mathbf{a}) = a_1 x + a_2 \tag{A.21}$$

with two parameters $a_1,\ a_2$. The parameters are estimated such that the straight line is fitted to the N data points.
The vector $\mathbf{D}(\mathbf{a})$ depending on the parameters $\mathbf{a} = (a_1, a_2)$ of the model function is

$$\begin{aligned}\mathbf{D}(\mathbf{a}) &= (f(x_1; a_1, a_2), f(x_2; a_1, a_2),\ \dots\ , f(x_N; a_1, a_2)) \\ &= (a_1 x_1 + a_2, a_1 x_2 + a_2,\ \dots\ , a_1 x_N + a_2)\end{aligned} \tag{A.22}$$

and the vector depending on the provided measured data is

$$\mathbf{D}_0 = (y_1, y_2,\ \dots\ , y_N). \tag{A.23}$$

According to the Eq. (A.14) and Eq. (A.15) the gradient $\nabla\Phi(\mathbf{a})$ with both the Hessian $\mathbf{H}$ of $\Phi(\mathbf{a})$ and $\nabla\Phi$ evaluated about the origin $\mathbf{0}$ ($a_1 = 0,\ a_2 = 0$) has the form

$$\nabla\Phi(\mathbf{a}) = \mathbf{H}\mathbf{a} - \mathbf{b} \tag{A.24}$$

where

$$\mathbf{b} = -\nabla\Phi(\mathbf{0}). \tag{A.25}$$

The parameters $\mathbf{a}$ are determined using the zero-gradient conditions $\nabla\Phi(\mathbf{a}) = 0$.
Hence

$$\mathbf{a} = \mathbf{H}^{-1}\mathbf{b}. \tag{A.26}$$

Furthermore, the $\mathbf{H}$ and $\mathbf{b}$ are evaluated in terms of the Jacobian matrix $\mathbf{J}$ with components $J_{i1} = \frac{\partial D_i}{\partial a_1} = x_i$ and $J_{i2} = \frac{\partial D_i}{\partial a_2} = 1$. Since $\mathbf{H} = \mathbf{J}^T\mathbf{J}$ and $\mathbf{b} = -\nabla\Phi(\mathbf{0}) = -\mathbf{J}^T(\mathbf{D} - \mathbf{D}_0)(\mathbf{0})$ the least squares parameters are calculated from Eq. (A.26).
The presented linear least squares scheme can be applied, by analogy, to a fitting procedure with a model function defined by a quadratic or higher order polynomial function.

Figure A.2 shows the results of fitting a linear function to a set of data points.

A.4 Nonlinear Least Squares

The nonlinear least squares method is based on fitting the general model function

$$y = f(x, \mathbf{a}) \tag{A.27}$$

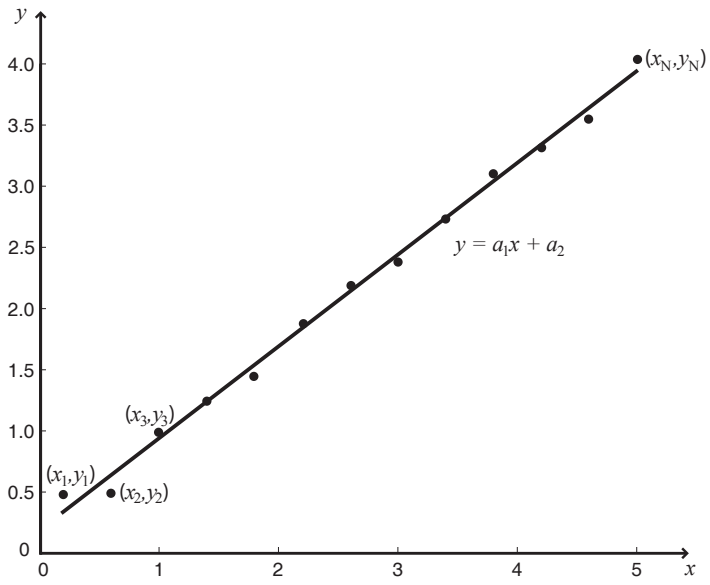

Figure A.2: *The linear least squares estimation.*

with a nonlinear dependence on the parameter vector $\mathbf{a} = (a_1, a_2, \ \ldots \ , a_M)$ to the measured data **y** at the corresponding N independent values **x**.
In the nonlinear least squares the non-quadratic function defined by Eq. (A.14) is minimised with respect to the parameter **a**. The zero-gradient conditions

$$\nabla\Phi(\mathbf{a}) = \mathbf{J}^T(\mathbf{D}(\mathbf{a}) - \mathbf{D}_0) = 0 \tag{A.28}$$

needs to be held at a minimum. Since the vector **b** is defined in the form

$$\mathbf{b}(\mathbf{a}) = -\nabla\Phi(\mathbf{a}) = -\mathbf{J}^T(\mathbf{D}(\mathbf{a}) - \mathbf{D}_0) \tag{A.29}$$

the zero-gradient condition is given by

$$\mathbf{b}(\mathbf{a}) = 0. \tag{A.30}$$

The algorithm starts with initial values for the parameter vector **a**. Then, the parameters a_j, $j = \{1, \ldots, M\}$ are refined iteratively with values incremented by parameter vector $\Delta\mathbf{a}$ satisfying the linear dependence

$$\mathbf{J}^b(\mathbf{a}) \cdot \Delta\mathbf{a} = -\mathbf{b}(\mathbf{a}) \tag{A.31}$$

where the Jacobian of the vector **b**, $\mathbf{J}^b(\mathbf{a})$, is given by

$$\mathbf{J}^b_{ij} = \frac{\partial b_i}{\partial a_j} = -\frac{\partial^2\Phi}{\partial a_i \partial a_j} = -H_{ij}. \tag{A.32}$$

Hence

$$\mathbf{J}^b = -\mathbf{H} \tag{A.33}$$

the values of the increment, $\Delta\mathbf{a}$, are determined from the system of linear equations

$$\mathbf{H} \cdot \Delta\mathbf{a} = \mathbf{b} \tag{A.34}$$

and are in the form

$$\Delta\mathbf{a} = -\mathbf{H}^{-1}\mathbf{J}^T(\mathbf{D}(\mathbf{a}) - \mathbf{D}_0). \tag{A.35}$$

The fitted curve obtained for a set of data points by applying the nonlinear least squares algorithm is shown in Fig. A.3.

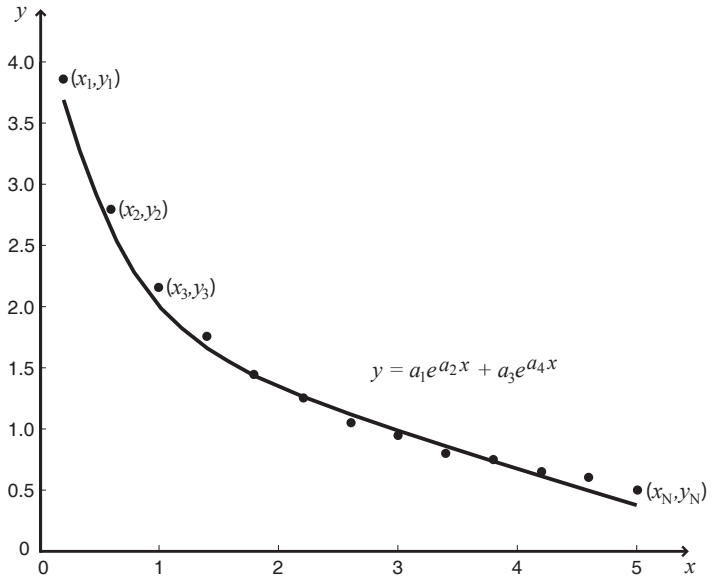

Figure A.3: *The nonlinear least squares estimation.*

The presented description of the least squares method is based on the mathematical definitions and explanations presented in [102, 103].

A.5 Matlab Code for Linear and Nonlinear Least Squares Method

This Section contains the Matlab functions used in this Thesis for the linear and nonlinear curve fitting.

The function CurveFitting.m (see Fig. A.4) implements the Newton-Raphson method

and can be used for both linear and nonlinear curve fitting by choosing the appropriate model function. The model functions are defined and presented in Fig. A.5 for the linear curve fitting and in Fig. A.6 for the exponential fitting in which the model function is defined as the sum of two exponents. The chosen model function is recalled in variable f. The input values for the CurveFitting function are defined as:

- x - array containing input independent variable values.
- y - array containing input dependent (measured) variable values.
- p0 - array containing input adjustable parameters estimated for the best fit to the data. The length of this array is equal to the number of parameters required for the particular model function, e.g. two for the linear fit ($y = p_1 + p_2 \cdot x$) and four for the sum of the two exponents ($y = p_1 \cdot exp(p_2 \cdot x) + p_3 \cdot exp(p_4 \cdot x)$). Initial values of p0 were always set to zero.
- tol - the tolerance which determines the accuracy of the fitting procedure. The smaller the value, the better the accuracy that can be obtained.

```
function p = CurveFitting(x,y,p0,tol)
        % function call: p = CurveFitting(x,y,p0,tol)
        % p - output row of optimised parameters
        % x - input row of x-data
        % y - input row of y-data
        % p0 - input row of initial parameters
        % tol - tolerance
N = length(x);
        % Choose a model function:
%f = @model_function_sum_exp;
f = @model_function_line;
        % F0 - vector F0 contains the y-data
F0 = y;
        % M - number of parameters
M = length(p0);
        % p - parameter vector, initialised to be p0
p = p0;
        % norm_dp is the norm of the increment parameter vector p
        % and is initialised to be greater than tol so that the
        % iteration will be done at least once
norm_dp = 10*tol;
while norm_dp > tol
    for i = 1:N
        F(i) = f(x(i), p, 0);
        for j = 1:M
        J(i,j) = f(x(i), p, j);
    end
end
H = J'*J;
b = -J'*(F-F0)';
dp = (H\b)';
norm_dp=sqrt(dp*dp');
p = p + dp;
end
```

Figure A.4: *Matlab function for least squares method.*

```
function y = model_function_line(x, p, k)
        % y = model_function_line(x, p, k)
        % y - output y-value
        % x - input x-value
        % k - differentiation index:
        % if k=0 then y = f(x,p) = p(1)+p(2)*x
        % if k=i>0 then y = d f(x,p)/d p(i)
if k==0 % model function for fitting
    y = p(1)+p(2)*x;
elseif k==1 % differential in terms of p(1)
    y = 1;
elseif k==2 % differential in terms of p(2)
    y = x;
end
```

Figure A.5: *Matlab function for linear curve fitting.*

```
function y = model_function_sum_exp(x, p, k)
        % y = model_function_sum_exp(x, p, k)
        % y - output y-value
        % x - input x-value
        % k - differentiation index:
        % if k=0 then y = f(x,p) = p(1)*exp(p(2)*x) + p(3)*exp(p(4)*x)
        % if k=i>0 then y = d f(x,p)/d p(i)
if k==0  % model function for fitting
    y = p(1)*exp(p(2)*x) + p(3)*exp(p(4)*x);
elseif k==1  % differential in terms of p(1)
    y = exp(p(2)*x);
elseif k==2  % differential in terms of p(2)
    y = p(1)*x*exp(p(2)*x);
elseif k==3  % differential in terms of p(3)
    y = exp(p(4)*x);
elseif k==4  % differential in terms of p(4)
    y = p(3)*x*exp(p(4)*x);
end
```

Figure A.6: *Matlab function for exponential curve fitting with model function being the sum of two exponents.*

Bibliography

[1] R. R. Schaller. Moore's law: past, present, and future. *IEEE Spectrum*, 34(6):51 – 59, 1997.

[2] A. Fontanelli. System-in-Package technology: opportunities and challenges. *Proc. ISQED*, pages 589 – 593, 2008.

[3] C. Trigas. Design challenges for system-in-package vs system-on-chip. *Proc. CICC'03*, pages 663–666, 2003.

[4] M. L. Sham, Y. C. Chen, J. R. Leung, and T. Chung. Challenges and opportunities in system-in-package business. *Proc. ICEPT'06*, pages 1–5, 2006.

[5] H. H. Happ. Diakoptics - the solution of system problems by tearing. *Proc. IEEE*, 62(7):930 – 940, 1974.

[6] T. W. Huang, B. Houshmand, and T. Itoh. The implementation of time-domain diakoptics in the FDTD method. *IEEE Trans. Microwave Theory Tech.*, 42(11):2149 – 2155, 1994.

[7] P. Bai et al. A 65nm logic technology featuring 35nm gate lengths, enhanced channel strain, 8 Cu interconnect layers, low-k ILD and $0.57\,\mu$m^2 SRAM cell. *IEEE IEDM*, pages 657 – 660, 2004.

[8] *International Technology Roadmap for Semiconductors, Interconnect, 2008 Edition*. http://www.itrs.net/, retrieved on 20th November 2009.

[9] D. D. Antono, K. Inagaki, H. Kawaguchi, and T. Sakurai. Trends of on-chip interconnects in deep sub-micron VLSI. *IEICE Trans. Electron.*, E89-C(3):392 – 394, 2006.

[10] J. Gambino. 22nm CMOS technology. BEOL technology for 22nm technology node. *IEDM Course Materials, San Francisco, 2008*.

[11] R. H. Havemann and J. A. Hutchby. High-performance interconnects: an integration overview. *Proc. IEEE*, 89(5):586 – 601, 2001.

[12] B. Kleveland, C. H. Diaz, D.Vook, L. Madden, T. H. Lee, and S. S. Wong. Exploiting CMOS reverse interconnect scaling in multigigahertz amplifier and oscillator design. *IEEE J. Solid-State Circuits*, 36(10):1480 – 1488, 2001.

[13] X. Yang, R. Kastner, and M. Sarrafzadeh. Congestion estimation during top-down placement. *IEEE Trans. Circuits and Systems*, 21(1):72 – 80, 2001.

[14] C. K. Cheng, J. Lillis, S. Lin, and N. Chang. *Interconnect analysis and synthesis*. Wiley-Interscience, 2000.

[15] D. Sylvester and C. Hu. Analytical modeling and characterization of deep-submicrometer interconnect. *Proc. IEEE*, 89(5):634–664, 2001.

[16] I. M. Golio. *RF and microwave semiconductor device handbook*. CRC Press, 2001.

[17] L. G. Gosset, F. Gaillard, D. Bouchu, R. Gras, J. de Pontcharra, S. Orani, O. Cueto, P. Lyan, O. Louveau, G. Passemard, and J. Torres. Multi-level Cu interconnects integration and characterization with air gap as ultra-low k material formed using a hybrid sacrificial oxide/polymer stack. *Proc. of the IITC'07*, pages 58 – 60, 2007.

[18] S. Lakshminarayanan, P. Wright, and J. Pallinti. Design rule methodology to improve the manufacturability of the copper CMP process. *Proc. IITC*, pages 99 – 102, 2002.

[19] P. Zarkesh-Ha, S. Lakshminarayanan, K. Doniger, W. Loh, and P. Wright. Impact of interconnect pattern density information on a 90nm technology ASIC design flow. *Proc. ISQED*, pages 405 – 409, 2003.

[20] O. Acher, G. Perrin P. L. Gourrierec, P. Baclet, and O. Roblin. Demonstration of anisotropic composites with tunable microwave permeability manufactured from ferromagnetic thin films. *IEEE Trans. Microwave Theory Tech.*, 44(5):674–684, 1996.

[21] Lord Rayleigh. On the influence of obstacles arranged in rectangular order upon the properties of a medium. *Phil. Mag.*, 34:481 – 502, 1892.

[22] H. A. Lorentz. *The theory of electrons and its applications to the phenomena of light and radiant heat, 2nd Edition*. Dover Publications, 1952.

[23] J. C. Maxwell Garnett. Colours in metal glasses and in metallic films. *Philos. Trans. R. Soc. London Ser. A*, 203:385 – 420, 1904.

[24] J. C. Maxwell Garnett. Colours in metal glasses, in metallic films, and in metallic solutions, II. *Philos. Trans. R. Soc. London Ser. A*, 205:237 – 288, 1906.

[25] J. Fraunhofer. *Gesammelte Schriften*. Verlag der K. Akademie, edited by E. Lommel, 1888.

[26] S. R. Kennedy and M. J. Brett. Porous broadband antireflection coating by glancing angle deposition. *Appl. Opt.*, 42(22):4573 – 4579, 2003.

[27] C. G. Bernhard. Structural and functional adaptation in a visual system. *Endeavour*, 26:79–84, 1967.

[28] C. G. Bernhard, G. Gemne, and J. Sallstrom. Comparative ultrastructure of corneal surface topography in insects with aspects on phylogenesis and function. *Z. vergl. Physiologie*, 67:1–25, 1970.

[29] P.B. Clapham and M.C. Hutley. Reduction of lens reflexion by the 'moth eye' principle. *Nature*, 244:281–282, 1973.

[30] A. Sihvola. Metamaterials in electromagnetics. *Elsevier, Metamaterials*, 1:2 – 11, 2007.

[31] Z. Vertesy, K. Kertesz, Zs. Balint, G. Mark, L. Tapaszto, J. P. Vigneron, and L. P. Biro. Photonic crystal type nanoarchitectures in butterfly wing scales. *Proc. EMC'08*, 3:101–102, 2008.

[32] P. Yeh, A. Yariv, and C. S. Hong. Electromagnetic propagation in periodic stratified media. I. General theory. *Opt. Soc. Am.*, 67(4):423 – 438, 1977.

[33] P. Yeh. A new optical model for wire grid polarizers. *Opt. Commun.*, 26(3):289 – 292, 1978.

[34] P. Yeh. Generalized model for wire grid polarizers. *Proc. SPIE, Polarizers and Applications*, 307:13 – 21, 1981.

[35] Z. Hua-Jun, P. Yong-Jun, T. Ju, L. Chang-Rong, L. Peng, and R. Xiao-Xia. Optimal design of sub-wavelength metal rectangular gratings for polarizing beam splitter based on effective medium theory. *Chin. Phys. B*, 18(12):5326 – 5330, 2009.

[36] T. Sergan, M. Lavrentovich, and J. Kelly. Measurement and modelling of optical performance of wire grids and liquid-crystal displays utilizing grid polarizers. *J. Opt. Soc. Am. A*, 19(9):1872 – 1885, 2002.

[37] X. J. Yu and H. S. Kwok. Optical wire-grid polarizers at oblique angles of incidence. *J. Appl. Phys.*, 93(8):4407 – 4412, 2003.

[38] A. Lehmuskero, B. Bai, P. Vahimaa, and M. Kuittinen. Wire-grid polarizers in the volume plasmon region. *Opt. Exp.*, 17(7):5481 – 5489, 2009.

[39] E. Cojocaru. Antireflection quarter-wave-thick, high-spatial-frequency, surface-relief gratings at oblique incidence. *J. Appl. Opt.*, 35(31):6231 – 6235, 1996.

[40] C. W. Haggans and L. Li. Effective-medium theory of zeroth-order lemellar gratings in conical mountings. *J. Opt. Soc. Am. A*, 10(10):2217 – 2225, 1993.

[41] D. Maystre and R. Petit. Brewster incidence for metallic gratings. *Opt. Commun.*, 17(2):196 – 200, 1976.

[42] S. Collin, F. Pardo, R. Teissier, and J. L. Pelouard. Horizontal and vertical surface resonances in transmission metallic gratings. *J. Opt. A: Pure Appl. Opt.*, 4:S154 – S160, 2002.

[43] J. A. Porto, F. J. Garcia-Vidal, and J. B. Pendry. Transmission resonances on metallic gratings with very narrow slits. *Phys. Rev. Lett.*, 83(14):2845 – 2848, 1999.

[44] L. Pilozzi, A. D'Andrea, and H. Fenniche. Mirror effect at the Brewster angle in semiconductor rectangular gratings. *Phys. Rev. B*, 64:235319(1 – 8), 2001.

[45] S. Enoch, G. Tayeb, P. Sabouroux, N. Guerin, and P. Vincent. A metamaterial for directive emission. *Phys. Rev. Lett.*, 89(21):213902(1–4), 2002.

[46] W. Cai, D. A. Genov, and V. M. Shalaev. Superlens based on metal-dielectric composites. *Phys. Rev. B*, 72(19):193101(1–4), 2005.

[47] P. Chylek and V. Strivastava. Dielectric constant of a composite inhomogeneous medium. *Phys. Rev. B*, 27(8):5098 – 5106, 1983.

[48] P. Chylek and V. Strivastava. Effective dielectric constant of a metal-dielectric composite. *Phys. Rev. B*, 30(2):1008 – 1009, 1984.

[49] M. Born and E. Wolf. *Principles of optics: electromagnetic theory of propagation, interference and diffraction of light, 7th Edition*. Cambridge University Press, 1999.

[50] D. H. Raguin and G. M. Morris. Antireflection structured surfaces for the infrared spectral region. *J. Appl. Opt.*, 32(7):1154–1167, 1993.

[51] S. M. Rytov. Electromagnetic properties of a finely stratified medium. *Soviet Physics JETP*, 2(3):466 – 475, 1956.

[52] A. M. Clogston. Reduction of skin-effect losses by the use of laminated conductors. *Proc. IRE*, 39:767–782, 1951.

[53] J. M. Bell, G. H. Derrick, and R. C. McPhedran. Diffraction gratings in the quasi-static limit. *Optica Acta*, 29(11):1475–1489, 1982.

[54] P. Lalanne and D. Lamercier-Lalenne. Depth dependence of the effective properties of subwavelength gratings. *J. Opt. Soc. Am.*, 14(2):450–458, 1997.

[55] A. Sihvola. *Electromagnetic mixing formulas and applications*. IEE Publishing, London, 1999.

[56] M. Y. Koledintseva, R. E. DuBroff, and R. W. Schwartz. A Maxwell Garnett model for dielectric mixtures containing conducting particles at optical frequencies. *Progress in Electromagnetics Research*, 63:223 – 242, 2006.

[57] O. Wiener. Zur theorie der refraktionskonstanten. *Berichte über die Verhandlungen der Königlich-Sächsischen Gesellschaft der Wisseschaften zu Leipzig*, 62:256 – 277, 1910.

[58] B. Sareni, L. Krahenbuhl, A. Beroual, and C. Brosseau. Effective dielectric constant of periodic composite materials. *J. Appl. Phys.*, 80(3):1688 – 1696, 1996.

[59] B. Sareni, L. Krahenbuhl, A. Beroual, and C. Brosseau. Effective dielectric constant of random composite materials. *J. Appl. Phys.*, 81(5):2375 – 2383, 1997.

[60] C. Brosseau, A. Beroual, and A. Boudida. How do shape anisotropy and spatial orientation of the constituents affect the permittivity of dielectric heterostructures? *J. Appl. Phys.*, 88(12):7278 – 7288, 2000.

[61] B. Sareni, L. Krahenbuhl, A. Beroual, and C. Brosseau. Complex effective permittivity of a lossy composite material. *J. Appl. Phys.*, 80(8):4560 – 4565, 1996.

[62] L. Jylha and A. Sihvola. Approximations and full numerical simulations for the conductivity of three dimensional checkerboard geometries. *IEEE Trans. Dielec. Elec. Insul.*, 13(4):760 – 764, 2006.

[63] E. Tuncer, Y. V. Serdyuk, and S. M. Gubanski. Dielectric mixtures: electrical properties and modeling. *IEEE Trans. Dielec. Elec. Insul.*, 9(5):809 – 828, 2002.

[64] L. Jylha and A. Sihvola. Numerical modeling of disordered mixture using pseudorandom simulations. *IEEE Trans. Geosci. Remote Sens.*, 43(1):59 – 64, 2005.

[65] K. Karkkainen, A. Sihvola, and K. Nikoskinen. Analysis of a three-dimensional dielectric mixture with finite difference method. *IEEE Trans. Geosci. Remote Sens.*, 39(5):1013 – 1018, 2001.

[66] K. K. Karkkainen, A. H. Sihvola, and K. I. Nikoskinen. Effective permittivity of mixtures: numerical validation by the FDTD method. *IEEE Trans. Geosci. Remote Sens.*, 38(3):1303 – 1308, 2000.

[67] A. Taflove and S. C. Hagness. *Computational electrodynamics, the finite-difference time-domain method, 3rd Edition*. Artech House, 2005.

[68] K. S. Yee. Numerical solution of initial boundary value problems involving Maxwell's equations in isotropic media. *IEEE Trans. Antennas Propag.*, AP-14(3):302 – 307, 1966.

[69] D. M. Sullivan. *Electromagnetic simulation using the FDTD method*. IEE Publishing, New York, 2000.

[70] M. G. Moharam and T. K. Gaylord. Rigorous coupled-wave analysis of metallic surface-relief gratings. *J. Opt. Soc. Am. A*, 3(11):1780 – 1787, 1986.

[71] M. G. Moharam, D. A. Pommet, and E. B. Grann. Stable implementation of the rigorous coupled-wave analysis for surface-relief gratings: enhance transmittance matrix approach. *J. Opt. Soc. Am. A*, 12(5):1077 – 1086, 1995.

[72] P. Lalanne and G. M. Morris. Highly improved convergence of the coupled-wave method for TM polarization. *J. Opt. Soc. Am. A*, 13(4):779 – 784, 1996.

[73] *Grating Solver Development Company. GSolver V5.1*. http://www.gsolver.com/, retrieved on 20th November 2009.

[74] J. B. Pendry, A. J. Holden, W. J. Stewart, and I. Youngs. Extremely low frequency plasmons in metallic mesostructures. *Phys. Rev. Lett.*, 76(25):4773 – 4776, 1996.

[75] K. H. Huebner, E. A. Thornton, and T. G. Byrom. *The finite element method for engineers, 3rd Edition*. John Wiley & Sons, New York, 1995.

[76] S. Moaveni. *Finite element analysis. Theory and application with ANSYS, 3rd Edition*. Pearson Education, 2008.

[77] *Ansoft High Frequency Structure Simulator (HFSS)*. http://www.ansoft.com/, retrieved on 20th November 2009.

[78] N. Guo, R. C. Qiu, S. S. Mo, and K. Takahashi. 60-GHz milimiter-wave radio: principle, technology, and new results. *EURASIP J. Wireless Communication and Networking*, 2007(ID 68253):1–8, 2007.

[79] Y. Uzawa, T. Noguchi, A. Kawakami, and Z. Wang. Quasi-optical log-periodic antenna SIS mixers for the 100 GHz band. *J. Supercond. Sci. Technol.*, 9:140–143, 1996.

[80] D. S. James. Some aspects related to the ISM band, especially medical. *Radio Research Advisory Committee, PRAC(01)19*, http://www.ofcom.org.uk/static/archive/ra/topics/research/rrac/members/, retrieved on 19th October 2009.

[81] J. C. Maxwell. A dynamical theory of the electromagnetic field. *Phil. Trans. Royal Soc. London*, 155:459 – 512, 1865.

[82] H. Hertz. *Electric waves: being researchers on the propagation of electric action with finite velocity through space*. Macmillan and Co, London, 1893.

[83] Z. Buchwald. *The creation of scientific effects: Heinrich Hertz and electric waves*. The University of Chicago Press, 1994.

[84] J. D. Kraus. Heinrich Hertz - theorist and experimenter. *IEEE Trans. Microw. Theory Tech.*, 36(5):824–829, 1988.

[85] M. Xu, H. P. Urbach, D. K. G. Boer, and H. J. Cornelissen. Wire-grid diffraction gratings used as polarizing beam splitter for visible light and applied in liquid crystal on silicon. *Opt. Exp.*, 13(7):2303 – 2320, 2005.

[86] D. K. Ghodgaonkar, V. V. Varadan, and V. K. Varadan. A free-space method for measurement of dielectric constants and loss tangents at microwave frequencies. *IEEE Trans. Instrum. Meas.*, 37(3):789 – 793, 1989.

[87] D. K. Ghodgaonkar, V. V. Varadan, and V. K. Varadan. Free-space measurement of complex permittivity and complex permeability of magnetic materials at microwave frequencies. *IEEE Trans. Instrum. Meas.*, 39(2):387 – 394, 1990.

[88] D. K. Ghodgaonkar, N. H. Hamzah, K. F. H. C. Kasim, and Z. Awang. Microwave nondestructive testing of coatings and paints using free-space microwave measurement system. *IEEE Proc. NCTT, Shah Alam, MY*, pages 67 – 70, 2003.

[89] C. A. Balanis. *Antenna theory, 3rd Edition*. Wiley-Interscience, 2005.

[90] *Rogers Corporation*. http://www.rogerscorp.com/, retrieved on 20th November 2009.

[91] J. D. Kraus. *Electromagnetics, 3rd Edition*. McGraw-Hill, 1984.

[92] J. Fleury and O. Bernard. Designing and characterizing TRL fixture calibration standards for device modeling. *Applied Microwave and Wireless*, 13(10):26 – 42, 2001.

[93] D. Rytting. Let time domain response provide additional insight into network behavior. *Proc. RF and Microwave Measurement Symp. Exhibition, Santa Rosa, CA*, pages 1 – 31, 1984.

[94] D. M. Pozar. *Microwave Engineering, 3rd Edition*. Wiley-Interscience, 2005.

[95] K. C. Gupta, R. Garg, I. J. Bahl, and P. Bhartia. *Microstrip lines and slotlines, 2nd Edition*. Artech House, 1996.

[96] C. Song and S. Lee. Design of a tapered impedance-matching line using inverse scattering. *Microwave Opt. Technol. Lett.*, 32(5):393 – 396, 2002.

[97] I. S. Nefedov, A. J. Viitanen, and S. A. Tretyakov. Propagating and evanescent modes in two-dimensional wire media. *Phys. Rev. E*, 71:046612, 1 – 10, 2005.

[98] I. S. Nefedov and S. A. Tretyakov. Electrically controllable metamaterials based on two-dimensional wire media. *Proc. EMC'05*, 1:433–436, 2005.

[99] I. S. Nefedov, A. J. Viitanen, and S. A. Tretyakov. Theory and application of wire media. *Proc. ICTON'06*, 2:5–8, 2006.

[100] M. G. Silveirinha and C. A. Fernandes. Homogenization of metamaterial surfaces and slabs: the crossed wire mesh canonical problem. *IEEE Trans. Antennas Propag.*, 53(1):59 – 69, 2005.

[101] V. G. Veselago. The electrodynamics of substances with simultaneously negative values of ϵ and μ. *Soviet Phys. Usp.*, 10:509 – 514, 1968.

[102] P. J. Bickel and K. A. Doksum. *Mathematical statistics: basic ideas and selected topics*. Holden-Day, San Francisco, 1977.

[103] W. H. Press, S. A. Teukolsky, W. T. Vetterling, and B. P. Flannery. *Numerical recipes in C++: the art of scientific computing, 2nd Edition*. Cambridge University Press, 2002.